STRUCTURAL STUDIES OF MEMBRANE-ASSOCIATED COMPLEXES BY SOLID-STATE NMR

BY

MARY C. CLAY

DISSERTATION

Submitted in partial fulfillment of the requirements
for the degree of Doctor of Philosophy in Chemistry
in the Graduate College of the
University of Illinois at Urbana-Champaign, 2014

Urbana, Illinois

Doctoral Committee:

Professor Chad M. Rienstra, Chair
Professor Eric Oldfield
Professor James H. Morrissey
Professor Emad Tajkhorshid

ABSTRACT

The plasma membrane is one of the most important barriers in the human body. The membrane is far more than an inert platform supporting membrane proteins and their interactions. It is a complex mixture of lipids, sterols, and proteins, the exact composition of which directly regulates all extracellular interactions and trafficking of materials. The inherent asymmetry of the plasma membrane composition is directly involved in cell signaling processes and normal biological functions of the cell. This thesis utilizes solid-state nuclear magnetic resonance spectroscopy to investigate the structure of calcium-phosphatidylserine (PS) complexes that regulate blood coagulation, and to understand how interactions of the antifungal drug amphotericin B with ergosterol are related to its toxicity.

The enzymatic activity of blood coagulation proteins is critically dependent upon the exposure of phosphatidylserine (PS) on the plasma membrane. Exposure of PS to plasma concentrations of calcium results in the formation of PS-rich nanodomains on the membrane surface, which are proposed as high affinity binding sites for coagulation factors. Phosphatidylethanolamine (PE) has been shown to enhance the pro-coagulation activity of PS membranes, and is hypothesized to play a role in the formation of PS-rich nanodomains. Despite extensive research, there is still no atomic-resolution description of these PS-rich membrane-binding sites or explanation for how they regulate blood coagulation reactions on the membrane surface. We propose the "Anything But Choline" hypothesis: GLA domain binding to lipid bilayers is facilitated by a combination of *ca*. one PS-specific interaction and *ca*. five or six phosphate-specific interactions. The PS-specific interaction can only be satisfied by L-serine, while phosphate-specific interactions can be satisfied by any phospholipid with an accessible phosphate group, with the exception of PC, because the choline headgroup sterically hinders

GLA domain access to its phosphate group. In this study, we used a combination of magic-angle spinning solid-state NMR (MAS SSNMR) and novel ^{13}C,^{15}N-isotopic labeling of phospholipid headgroups to develop an atomic resolution description of the structure and dynamics of PS-rich nanodomains and their interaction with GLA domains.

Amphotericin B is a highly effective antimicrobial agent that has been used for over fifty years to treat life threatening systemic fungal infections with minimal development of microbial resistance, an increasingly critical feature with the rise of antimicrobial resistant pathogens. The widely accepted mechanism of AmB cytotoxicity has been the formation of ion channels in the plasma membrane. However, recent studies have shown that channel formation is not essential for cell killing. Rather, it has been shown that cell death occurs from the binding of ergosterol (Erg, Fig. 1b). Erg is the primary sterol found in fungi and regulates many key cellular functions. In this thesis, I examined AmB interactions with Erg using magic-angle spinning solid-state NMR techniques, including paramagnetic relaxation enhancement (PRE), ^{1}H spin diffusion, order parameter determination by ^{1}H-^{13}C recoupling, and homonuclear ^{13}C-^{13}C correlation spectroscopy (DARR, hChhC and SPC5). Collectively, the NMR, functional, and other biophysical data have led to the development of a new model for toxicity: the AmB sterol sponge. In this model, we propose that AmB toxicity is the result of the physical extraction of Erg from the cell membrane, thus disrupting all Erg-dependent cellular processes.

This thesis is dedicated to the Clay and Hennesse families for all their love and support
Philippians 4:13

ACKNOWLEDGEMENTS

Throughout my thesis I have received immeasurable support and encouragement from my family, friends, and co-workers. I could never have completed my thesis without them, and I thank God for sending them to support me on this journey. This acknowledgments section can never fully express my gratitude to these individuals.

I would like to thank my advisor Chad Rienstra, for giving me the opportunity to work with him in one the best labs in world dedicated to pushing the limits of solid-state NMR spectroscopy. Working for Chad has helped me to mature from an eager young graduate student to a more focused and independent researcher. Chad's dedication, attention to detail, uncompromisingly high standards have pushed and motivated me to grow as a researcher. It has not always been an easy road but I can honestly say that I would not be who I am today without Chad. I would also like to thank Prof. Martin Burke and Chad for reminding me to always question that which has come before, the literature is not always right and we should always be ready to think outside the box others have built. I would like to thank Prof. James Morrissey and Prof. Emad Tajkhorshid for their advice and reminders to look outside of the NMR for answers as well, and that patience and persistence are two of the greatest qualities a researcher can cultivate. Finally to Prof. Eric Oldfield, who did some of the first NMR studies of lipid bilayers; his work has been a constant source of inspiration throughout my time at UIUC.

Over the course of my doctorial studies, I have had the privilege of interacting with a number of past and present Rienstra group members. I would like to thank Dr. Lindsay Sperling, Dr. Gemma Comellas, and Dr. Andrew Nieuwkoop for their guidance and assistance in learning the ins and outs of solid-state NMR. I am so grateful for all the time they spent training me and helping to trouble shoot spectrometer/Spinsight issues. I would like to thank Dr. John Boettcher

who introduced me to solution NMR studies of proteins. I will never know how you managed to disappear when sitting right behind me, John, but you and Lindsay got me started and helped me to see how powerful a tool NMR is in both the solution and solid state. I would also like to thank Dr. Deb Berthold and Dr. Rebecca Davis-Harrison for your patience and guidance in the 'art' of sample preparation. To my contemporaries Kristin, Grant, Joseph, Marcus, and Mike you have been everything from comedic relief, collaborators in 'crime', to many helpful and conversations about life and research, I cannot thank you enough.

A special thank you to Dr. Jacob Lopez, Marcus Tuttle, and Joseph Courtney, my python/tech experts, thank you so much for all your help with coding/computer related issues. I could not have done it without you. To the rest of the Rienstra group members: thank you for all the back up and good times. I would also like to thank Dr. Taras Pogorelov for all the tea and stimulating conversations about science and career planning. Finally, thank you to Dr. Ben Wylie and Dr. Trent Franks; you may not have physically overlapped with me, but your legacy certainly has provided an invaluable scientific resource and humorous anecdotes.

The support staff at UIUC has also been a great source of both professional and moral support through out my time at UIUC. I would like to thank the ladies of the IMP office, Beth Myler, Connie Knight, Theresa Struss, and Karen Neumann for their constant support and encouragement. Ladies, you helped me with more than just paper work and travel planning, you were a sympathetic ear, source of confectionary treats, and many other things. The guys in the machine shop, Hodge and John, for their patience and assistance in stream lining the production of rotor parts, and being willing guinea pigs for my confectionary endeavors. Thank you so much for being there for me, and my fellow graduate students.

Finally, I would like to thank my family. My parents Mike and Jane Clay, without them I would never have embarked on this journey let alone completed it. Growing up they told me I could do anything that I wanted to, and offered unwavering emotional, spiritual, financial, and physical support. To my brother, Jonathan, and sister, Rachel, I hope that I can be there for you the way you have always been there for me, reminding you to reach for the stars but never forget the ones you love. Their constant support is the cornerstone of my life, and I can never thank them enough.

Table of Contents

List of Figures ..... **x**

List of Tables ..... **xii**

Chapter 1 Introduction **1**
1.1 Preface **1**
1.2 The Membrane Bilayer **2**
1.2.1 The Plasma Membrane 2
1.2.2 Phospholipid Structure 4
1.2.3 Effect of Sterols on Membrane Structure 6
1.3 Solid-State NMR Structure and Dynamics Determination **7**
1.3.1 Chemical Shift 7
1.3.2 Dipolar Couplings 8
1.3.3 ^{1}H spin diffusion 9
1.4 Systems Studied **11**
1.4.1 Phosphatidylserine-Ca^{2+} Complex. 11
1.4.2 Amphotericine B Extraction of Ergosterol. 16
1.5 References **17**

Chapter 2 Atomic View of Calcium-Induced Clustering of Phosphatidylserine in Mixed Lipid Bilayers **27**
2.1 Notes and Acknowledgements **27**
2.2 Abstract **27**
2.3 Introduction **28**
2.4 Materials and Methods **32**
2.4.1 Isotopically Labeled POPS. 32
2.4.2 Nanodisc Preparation. 33
2.4.3 Liposome Preparation. 33
2.4.4 Solid-State NMR Spectroscopy 33
2.4.5 Molecular Dynamics Simulations 34
2.5 Results **34**
2.5.1 Effects of Ca^{2+} Binding on ^{13}C Chemical Shifts in PS Headgroups. 34
2.5.2 Ca^{2+}-PS Interactions Alter the Phase Transition and Dynamics of Lipids within the Bilayer 37
2.5.3 Ca^{2+}-PS Interactions Observed in All-Atom Simulations. 41
2.5.4 Two-Dimensional Spectra of POPS*:POPC Nanodiscs. 43
2.6 Discussion **46**
2.7 References **49**

Chapter 3 Progress Toward Solid-State NMR Structure of Ca^{2+}-Phosphatidylserine-rich Membrane Binding Domains **56**
3.1 Notes and Acknowledgements **56**
3.2 Abstract **56**
3.3 Introduction **57**
3.4 Materials and Methods **59**
3.4.1 Sample Preparation 59
3.4.2 SSNMR Spectroscopy 60
3.4.3 XPLOR-NIH Structure Calculations 62
3.5 Results **64**
3.5.1 Phospholipid Nanodisc and PS Cluster Formation 64

3.5.2 Internuclear ^{13}C-^{15}N constraints 68
3.5.3 XPLOR-NIH Structure Calculations 72
3.6 Discussion 75
3.7 Supplementary Information 79
3.8 References 80

Chapter 4 Molecular Determinants of Phospholipid Synergy in Blood Clotting 85
4.1 Notes and Acknowledgements 85
4.2 Abstract 85
4.3 Introduction 86
4.4 Materials and Methods 90
4.4.1 Materials 90
4.4.2 TF-Liposome Preparation and Measurement of FX Activation 90
4.4.3 SPR Analyses of FX Binding to Nanoscale Bilayers 91
4.4.4 MAS-SSNMR Spectroscopy 91
4.4.5 MD Simulation 91
4.5 Results 92
4.5.1 Many Phospholipids Synergize with PS to Enhance FX Activation by TF:FVIIa 92
4.5.2 PG and D–PS Synergize with L–PS to Enhance FX Binding to Membranes 94
4.5.3 Methylation of PE Headgroups Diminishes Synergy 95
4.5.4 Importance of the Phosphate Groups of Phospholipids for Synergy 96
4.5.5 MD Simulations of Phosphate Accessibility in Bilayers 97
4.5.6 SSNMR Evidence for a New PS Chemical Environment Induced by GLA Domains 98
4.6 Discussion 100
4.7 References 104

Chapter 5 Amphotericin Forms an Extramembranous and Fungicidal Sterol Sponge 107
5.1 Notes and Acknowledgements 107
5.2 Abstract 107
5.3 Introduction 108
5.4 Materials and Methods 111
5.4.1 General Methods 111
5.4.2 Biosynthesis and Characterization of U-^{13}C-Amphotericin 113
5.4.3 Solid-State NMR Spectroscopy 115
5.4.4 Preparation of Samples for SSNMR 117
5.4.5 Electron Microscopy 119
5.4.6 In Vivo Sterol Extraction Studies and Membrane Isolation 119
5.4.7 Preparation of an Amphotericin/Ergosterol Complex 122
5.5 Results 123
5.5.1 SSNMR Paramagnetic Relaxation Enhancement Experiments 123
5.5.2 AmB Primarily Exists as Large Extramembranous Aggregates 127
5.5.3 Extramembranous Aggregates of AmB Extract Ergosterol From Lipid Bilayers 129
5.5.4 AmB Extracts Ergosterol From and Thereby Kills Yeast Cells 132
5.6 Discussion 134
5.7 Supplementary Figures 139
5.8 References 155

List of Figures

Figure 1.1 Eukaryotic plasma membrane phospholipid asymmetry..... 3
Figure 1.2 Blood Clotting Cascade and GLA domains 12
Figure 1.3 ^{13}C-^{13}C 2Ds of POPS/POPC Nanodisc and multi lamellar vesicles. 15
Figure 2.1 Effect of Ca^{2+} and temperature on cross-polarized 13C one-dimensional spectra of phospholipid bilayers 36
Figure 2.2 Lipid phase transition and mobility in Nanodisc..... 38
Figure 2.3 POPS dynamics 40
Figure 2.4 MD Simulations of DOPS membranes..... 42
Figure 2.5 ^{13}C-^{13}C, ^{15}N-^{13}C, ^{31}P-^{13}C Correlation spectra fo 70% POPS* 30% POPC Nanodisc ... 44
Figure 2.6 (^{1}H)-^{13}C-(^{1}H-^{1}H)-^{13}C Spectra above and below phase transition rule out chemical exchange on the NMR timescale 45
Figure 2.7 ^{31}P-^{15}N ZF-TEDOR PS2-P-PS1N Trajectory 46
Figure 3.1 Effect of Ca^{2+} on PS Cα and β in Nanodiscs and Liposomes 66
Figure 3.2 POPS Titration ^{31}P CP-1D spectra 67
Figure 3.3 Unambiguous ^{13}C-^{15}N distance constraints..... 70
Figure 3.4 Intramolecular ^{13}C-^{15}N constraints..... 71
Figure 3.5 $Ca(PS)_2$ dimer structures. 74
Supplementary Figure 3.1 Distribution of Intramolecular ^{15}N-^{31}P and ^{13}C-^{31}P distance in 10 lowest energy structures of $Ca(PS)_2$ dimers ……..……79
Figure 4.1 GLA domain-PS interactions. 89
Figure 4.2 All tested glycerophospholipids synergize with L-PS to enhance fX activation by TF:fVIIa on liposomes, but PE does not synergize with PG. 94
Figure 4.3 PG and D-PS synergize with L-PS to enhance fX membrane binding. 95
Figure 4.4 Influence of PC methyl groups and PA phosphate on fX activation by TF:fVIIa. 96
Figure 4.5 MD simulations show that PC has restricted phosphate accessibility..... 98
Figure 4.6 SSNMR spectroscopy demonstrates a novel PS headgroup environment induced upon GLA domain binding to bilayers. 99
Figure 5.1 Models for the structure and function of AmB in the presence of lipid bilayers. 110
Figure 5.2 AmB primarily exists as large extramembranous aggregates. 125
Figure 5.3 Direct visualization of large extramembranous aggregates of AmB by transmission election microscopy. 128
Figure 5.4 AmB extracts Erg from lipid bilayers. 130
Figure 5.5 AmB extracts Erg from and thereby kills yeast cells. 133
Supplementary Figure 5.1 Phase transition behavior of 5% 5 and 16-DXYL-PC 139
Supplementary Figure 5.2 CC2D of AmB with and without ergosterol..... 140
Supplementary Figure 5.3 CC2Ds AmB with and without 5-DOXYL-PC..... 141
Supplementary Figure 5.4 AmB ^{1}H spin diffusion 143
Supplementary Figure 5.5 Supplemental transmission electron microscopy images..... 144
Supplementary Figure 5.6 AmB potassium efflux 146
Supplementary Figure 5.7 16-DOXYL PRE effects..... 147
Supplementary Figure 5.8 AmB extracts Erg from lipid bilayers. 148
Supplementary Figure 5.9 Effects of AmB of Erg linewidth, T1, and CC2D. 149
Supplementary Figure 5.10 ^{1}H spin diffusion to Erg in absence of AmB 150
Supplementary Figure 5.11 ^{1}H spin diffusion to Erg in presence of AmB..... 151

Supplementary Figure 5.12 Effects of AmdeB of Erg linewidth, T_1, and CC2D 152
Supplementary Figure 5.13 AmB T-MREV dipolar lines shapes and order parameters..... 153
Supplementary Figure 5.14 Erg T-MREV dipolar lines shapes and order parameters 153
Supplementary Figure 5.15 ^{13}C1D and UV-Vis spectra of AmB preparations 154
Supplementary Figure 5.16 Monomeric AmB in PBS:methanol and AmB aggregate in PBS buffer demonstrate spectral signatures by UV spectroscopy.[60] 155

List of Tables

Table 1.1. Structural Parameters Derived from X-ray Diffraction Studies of Fully Hydrated Phosphatidylcholine Lipids 6
Table 2.1 Carbon, nitrogen and phosphorus chemical shift values for PS headgroups bound to Ca^{2+} in mixed POPS:POPC bilayers. [a] 43
Table 3.1 ^{13}C-^{15}N BASE-TEDOR Results 72
Table 3.1 Comparison of Internuclear Distances Observed in XPLOR-NIH $Ca(PS)_2$ Dimer Calculations 75
Supplementary Table 3.1 List SSNMR Constraints 80
Supplementary Table 5.1 ^{13}C resonance assignments for AmB. 142
Supplementary Table 5.2 ^{13}C Line widths and order parameters 145
Supplementary Table 5.3 ^{13}C Chemical Shifts of ^{13}C Skip Labeled Ergosterol (^{13}C-Erg) 146

CHAPTER 1

Introduction

1.1 Preface

The function of a molecule directly depends upon its three-dimensional structure. A denatured enzyme or substrate can no longer support its catalytic activity because the enzyme cannot properly interact with the target substrate and *vice versa*. Understanding molecular structure allows us to better understand the nature of molecular interactions and their relationship to cellular function and disease. The majority of structural studies focus primarily on proteins using X-ray crystallography, electron microscopy, and nuclear magnetic resonance (NMR). This is not surprising given that the functional state of most proteins is well ordered. However, the lipid membrane is naturally dynamic and the bulk of the individual molecules are disordered, making characterization of biologically relevant states by crystallography impossible. For a long time, the membrane was viewed as nothing more than an inert fluid support matrix for membrane-associated processes[1], but it has become clear that while the membrane is quite dynamic, in nature it is by no means an inert platform.[2,3] It now clear that membrane structure and dynamics influence the structure and function of peripheral and integral membrane proteins just as much as these membrane proteins influence the structure and function of the membrane.

The plasma membrane is the most important interface/barrier in the body. The inherent asymmetry of the plasma membrane composition is directly involved in cell signaling processes, and normal biological function of the cell. Exposure of the anionic phospholipid phosphatidylserine on the plasma membrane of normal cells only occurs when the cell is ready for apoptosis or activated for blood coagulation. Phosphatidylserine is also a pathological marker

for the majority of cancer cells.[4] Sterols reduce the mobility of the phospholipid tails, and interact with sphingolipdis to form dense regions on the membrane surface. This dissertation focuses on understanding how interactions of extracellular ligands like calcium and amphotericin B interact with phosphatidylserine (chapters 2-4) and ergosterol (chapter 5) alter membrane altering membrane structure and dynamics.

1.2 The Membrane Bilayer

1.2.1 The Plasma Membrane

All eukaryotic cells are encapsulated by a semipermeable membrane composed of a complex double layer of lipids with proteins embedded separating the cytosol from the external environment. Similar membranes separate the various organelles of the cell creating regions of varying ionic strength and pH throughout the cell. The primary components of the membrane bilayer are phospholipid and sphingolipids, over 70% of the membrane. The amphipathic nature of phospholipids naturally fosters the spontaneous formation of bilayers with the hydrophilic, polar headgroups facing the aqueous environments and the hydrocarbon tails interacting to form the hydrophobic core. It is the hydrophobic nature of the core that prevents the free diffusion of water, ions, and other materials across the bilayer, effectively isolating the cell interior. The membrane proteins embedded in the plasma membrane regulate the trafficking of material across the membrane, cell signaling, and intracellular interactions. In 1972 Singer and Nicolson proposed the fluid mosaic model, which describes the lipid membrane an inert fluid like platform for membrane protein regulated processes.[1] While the fluid mosaic model remains the primary model for describing the structure of the membrane bilayer, it is now clear the membrane is more mosaic than fluid and that the lipid composition directly regulates the activities of the membrane associated proteins.[3,5,6]

The composition of the plasma membrane in healthy cells is asymmetric, with the exterior surface composed almost exclusively of zwitterionic choline lipids such as phosphatidylcholine (PC) and sphingomyelin (SM), and the interior leaflet containing higher levels of aminophospholipids like phosphatidylethanolamine (PE) and phosphatidylserine (PS) as shown in Figure 1.1.[5-10] This asymmetry is actively maintained by adenosine triphosphate (ATP) dependent transport proteins that shuttle phospholipids between the cytosolic and luminal

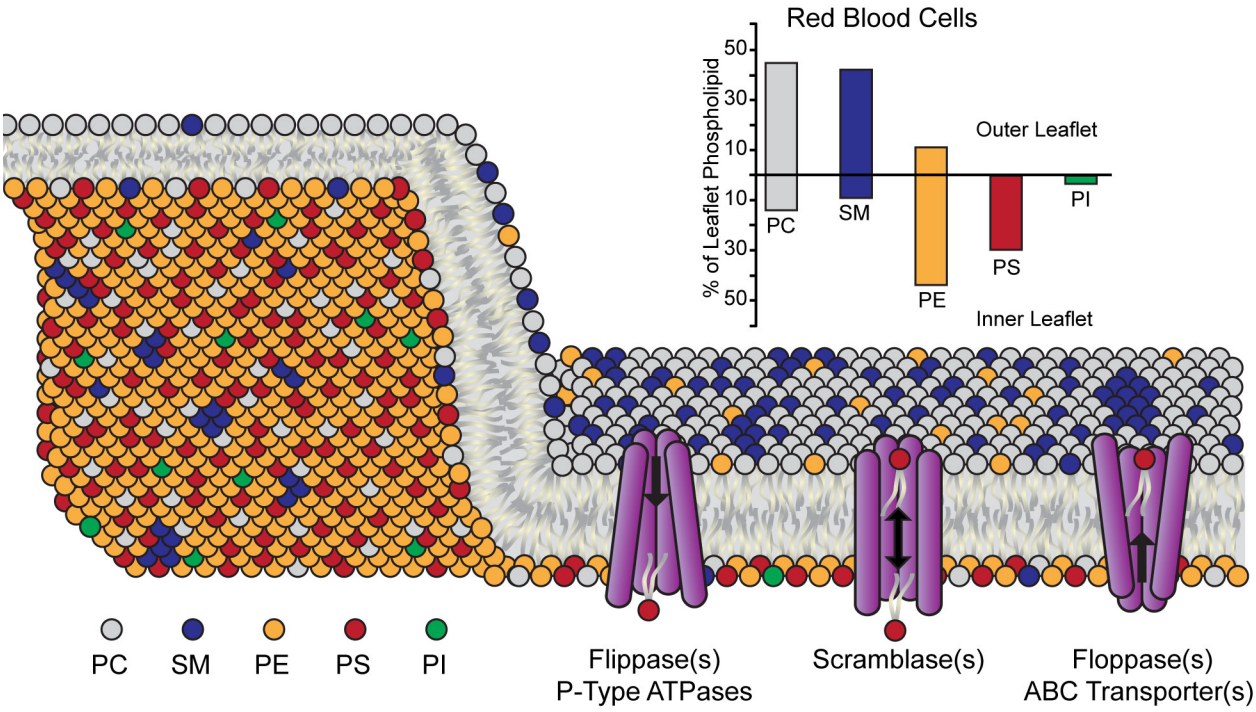

Figure 1.1 Eukaryotic plasma membrane phospholipid asymmetry.
In normal quiescent cells, the exterior leaflet of the plasma membrane is composed predominantly of the zwitterionic choline lipids phosphatidylcholine (PC) and sphingomyelin (SM) while the interior leaflet is comprised predominantly of aminophospholipids phosphatidylethanolamine (PE) and phosphatidylserine (PS) with trace amounts (>5%) of other anionic phospholipids such as phosphatidylinositol (PI) and phosphatidic acid (PA). The phospholipid asymmetry is actively maintained by the cell which uses Flippases, P-type ATPases, to transport lipids interior leaflet, Floppase, ATP-binding cassette transporters, to move lipids to the exterior leaflet, and finally Scramblases which are capable of bi-directional movement of lipids between the with leaflets. The above is a graphical representation of the phospholipid asymmetry prepared using data and inspired by images presented in Zwaal & Schroit 1997 and Fadeel & Xue 2009.[5,6]

surfaces of the plasma membrane. Flippases, like ATP8A1, selectively moves PS and PE to the cytosolic leaflet of the plasma membrane,[6,11] while floppases, are less selective and transports both amino- and choline-phospholipids to the extracellular leaflet. The activity of both flippases and floppases are ATP dependent and are sensitive to the cytosolic calcium concentrations but their action is tied to maintaining the phospholipid asymmetry characteristic to healthy cells. The loss of asymmetry is attributed to the activity of scramblases, which are capable of bidirectional transport of lipids between the inner and outer leaflets in a calcium dependent manner. In erythrocytes and platelets the activity of these lipid transport proteins is tied to the natural calcium gradient between the lumen and the cytosol, and activity of flippases and floppases is halted in the presence of micro molar calcium, which in turn stimulates the scramblase activity leading to the rapid loss of membrane asymmetry.[5,6,10] Exposure of PS on the plasma membrane facilitates coagulation reactions and prompts apoptosis.

1.2.2 Phospholipid Structure

The lipids asymmetry also directly impacts the structure and dynamics of the bilayer. Bilayers are typically described as occupying one of three lamellar phases. The lamellar liquid crystalline (Lα) phase, in which the acyl chains are completely disordered and highly mobile. The lamellar gel phase, or ordered phase, (Lβ, S_0) in which the acyl chains are still disordered but the acyl chains are no longer dynamic. Finally the lamellar crystalline phase (Lc) in which the bilayer is dehydrated, well ordered, and rigid. Each of these phases is characterized by difference in the order parameter (S), which is a measure of the orientational mobility of the ^{13}C-^{1}H, or ^{13}C-^{2}H (^{13}C-D) bond. Order parameters range from 0 (in completely disordered systems) to 1 (in rigid lattice systems).[12-15] In the liquid crystalline phase, the acyl chain order parameter ranges from ~0.05 at the terminal methyl groups to ~0.25 near the glycerol backbone.[14,16,17] the

glycerol linker is consistently the least mobile region in all the phospholipid types, serving as an anchor point in the membrane. Traditionally order parameters are measured using deuterium NMR to measure the order parameter via the deuterium quadrupolar splitting, or the ^{1}H-^{13}C dipolar line shape great progress has been made in the molecular dynamics community, which can now reproduce experimentally determined order parameters.[18-23]

Based on the low order parameters determined for the majority of pure phospholipid systems studied, it is clear that lipid membranes are a very dynamic system, not structurally well ordered. In fact, it is the dynamic nature of the liquid crystalline phase that prevents high-resolution structural studies by X-ray crystallography and neutron diffraction, which rely on the presence of a regular repeating structural elements. However, these techniques can still be used to study the liquid crystalline phase, as the diffraction patterns and electron density profiles still provide a wealth of structural information regarding the average bilayer thickness (D), area per lipid (A), hydrocarbon thickness ($2D_C$), and amount of interfacial water (n_w').[24-31] As shown in Table 1.1, the bilayer thickness is a direct function of the hydrocarbon chain length, which in cells would result in varying membrane thickness depending on the local lipid composition. Electron density profiles provide information regarding the relative distribution of various membrane components. This information can be used in solid-state NMR (SSNMR) and other structure calculations to help guide position of the plane potentials that constrain the relative position of lipids and molecules relative to the lipid normal.

Table 1.1. Structural Parameters Derived from X-ray Diffraction Studies of Fully Hydrated Phosphatidylcholine Lipids

Lipid	DLPC[a] (12:0; 12:0)	DMPC[b] (14:0; 14.0)	DPPC[c] (16:0; 16:0)	DOPC[c] (18:1; 18:1)	POPC[c] (16:0; 18:1)	di22:1PC[c] (22:1; 22:1)
V_L (Å^3)	991	1101	1232	1303	1256	1522
D (Å)	61.1	62.7	67.0	63.2	64.0	70.0
A (Å^2)	63.2	59.6	64.0	72.4	68.3	69.3
$2D_C$ (Å)	20.9	26.2	28.5	26.8	27.1	34.4
D_{HH} (Å)	30.8	36.0	38.3	36.7	37.0	44.3
D_B (Å)	31.4	36.9	38.5	36.0	36.8	44.0
$D_{B'}$ (Å)	38.9	44.2	46.5	44.8	45.1	52.4
$D_{W'}$ (Å)	22.2	18.5	20.5	18.4	1	17.6
n_w	31.3	25.6	30.1	32.8	31.0	30.0
n_w'	7.9	7.2	8.6	10.7	9.4	9.7

V_L Lipid molecular volume; D, lamellar repeat spacing; A, average interfacial area/lipid; $2D_C$, thickness of hydrocarbon core; DHH, headgroup peak-peak distance; D_B; Gibbs-Luzzati bilayer thickness (D_B-$2V_L$/A); $D_{B'}$, steric bilayer thickness ($D_{B'}$= $2(D_C+D_{H'})$); $D_{W'}$, steric water thickness ($D_{w'}$=D-$D_{B'}$); nw; number of water molecules/lipid ($n_w = AD_w.2V_w$), $n_{w'}$, number of waters between D_C and $D_{B'}/2$.
[a] Results from ref 25 , [b] results from ref 26, [c] results form ref 24.

1.2.3 Effect of Sterols on Membrane Structure

Cholesterol also plays a substantial regulatory role in the structure and dynamics of the plasma membrane, and accounts for ~30% of the total lipid. Unlike phospholipids, it is unclear whether cholesterol is asymmetrically distributed between the inner and out leaflets of the plasma membrane. Incorporation of sterols such as cholesterol and ergosterol result in an increase in the experimentally determined order parameter by a factor of two along the acyl chains with the exception of the terminal methyl groups with appear unaffected, in bilayers containing 20% or more sterol.[14,32-34] This effect is postulated to be the result of the parallel orientation of the sterol rings relative to the fatty acid acyl chains and perpendicular to the membrane normal with the C3-OH group located close to the glycerol/sphingosine linkers, and

the flexible hydrocarbon tail near the hydrophobic core. Coupled with the reduced mobility is a reduction in the effective area/lipid creating a tighter less permeable membrane.[34,35]

Sterols induced similar changes in membrane fluidity in the presence of either phospholipids or sphingolipids. However, it takes considerably less sterol to induce ordering of sphingolipids tails.[32] It is proposed that hydrogen bonding between the sterol C3-OH and the NH group on sphingolipids fosters the interaction of sphingolipids and sterols to form micro/ nanodomains on the membrane surface.[32-34,36,37]

1.3 Solid-State NMR Structure and Dynamics Determination

The dynamic nature of the phospholipid bilayer hinders structural studies by X-ray and neutron diffraction, and unique atom positions cannot be extracted from the diffraction patterns observed for hydrated lipid bilayers. Diffraction studies have difficulty distinguishing between the different components of the mixed lipid membranes. SSNMR can and has provided insights into the structure and dynamics of lipid mixtures under biologically relevant conditions. This dissertation focuses on using chemical shifts, dipolar couplings, paramagnetic relaxation enhancement, spin diffusion, and dynamics measurements to determine changes to the structure and dynamics of PS headgroup in the presence of Ca^{2+} and ergosterol in the presence of amphotericin B (Chapter 5).

1.3.1 Chemical Shift

The chemical shift parameter is one of the most basic and enabling of all the NMR observables. Chemical shift is a reflection of the interactions of the local magnetic flied induced by the electrons shielding or deshielding of the nucleus, relative to the bare nucleus. The magnitude of the shielding or deshielding effect is a direct function of the local electronic/chemical environment, which is determined by the ionic strength of solution, bond

type, and three-dimensional arrangement (bond and torsion angles). The chemical shift can be used to identify amino acid type or other molecules, that can be related to secondary structure, via empirical or quantum mechanical methods.

The relationship between chemical shift and secondary structure can be exploited to monitor structural changes induced by ligand binding. Chemical shift perturbation mapping is often used in solution NMR to identify ligand-binding sites, by monitoring changes in a fingerprint spectrum like an ^{1}H-^{15}N HSQC[38], or ^{13}C-^{13}C two-dimensional correlation spectrum[39] of ^{15}N or ^{13}C-labeled target in the presence and absence of ligand. Perturbations in the fingerprint spectrum can then be mapped as a function of ligand concentration and used to determine binding constants and other kinetic properties. These perturbations can also be mapped site specifically on the binding partners structure allowing for the identification and structural characterizing of bound state of the complex.

1.3.2 Dipolar Couplings

In the case were two or more NMR active nuclei are present couplings arise via through space interaction of their magnetic moments are called dipolar interactions. Dipolar coupling between and I and S spins are described by the dipolar Hamiltonian ($\hat{H}_D$):

$$\hat{H}_D = -\left(\frac{\mu_0}{4\pi}\right)\gamma_I\gamma_S\hbar\left(\frac{\mathbf{I}\cdot\mathbf{S}}{r^3} - 3\frac{(\mathbf{I}\cdot r)(\mathbf{S}\cdot r)}{r^5}\right) \tag{1.1}$$

Where ***I*** and ***S*** are the spin operators for the *I* and *S* spins respectively. Expansion of the scalar products followed by considerable simplification, yields the dipolar Hamiltonian defined in terms of the dipolar alphabet:

$$\hat{H}_D = -\left(\frac{\mu_0}{4\pi}\right)\frac{\gamma_I\gamma_S\hbar}{r^3}\left[A + B + C + D + E + F\right] \tag{1.2}$$

$$
\begin{aligned}
A &= \hat{I}_z\hat{S}_z\left(3\cos^2\theta - 1\right) \\
B &= -\frac{1}{4}\left[\hat{I}_+\hat{S}_- + \hat{I}_-\hat{S}_+\right]\left(3\cos^2\theta - 1\right) \\
C &= -\frac{3}{2}\left[\hat{I}_z\hat{S}_- + \hat{I}_-\hat{S}_z\right]\sin\theta\cos\theta e^{-i\phi} \\
D &= -\frac{3}{2}\left[\hat{I}_z\hat{S}_- + \hat{I}_-\hat{S}_z\right]\sin\theta\cos\theta e^{+i\phi} \\
E &= -\frac{3}{4}\left[\hat{I}_+\hat{S}_+\right]\sin^2\theta e^{-2i\phi} \\
F &= -\frac{3}{4}\left[\hat{I}_-\hat{S}_-\right]\sin^2\theta e^{+2i\phi}
\end{aligned}
\tag{1.3}
$$

Only the *A* term commutes with the Zeeman Hamiltonian ($\hat{H}_z = -\hbar\gamma_I\vec{B}_0\hat{I}_z = -\hbar\omega_0\hat{I}_z$), in the case of both homo and heteronuclear *I-S* couplings, and therefore is the only term that directly contributes to the energy of the spin system. In the case of homonuclear dipolar interactions the B term will also commute with the Zeeman Hamiltonian. The remaining terms make insignificant contributions to the energy of the system, but can contribute to relaxation processes. Thus for heteronuclear *I-S* spin system the dipolar Hamiltonian simplifies to:

$$
\hat{H}_D = -\left(\frac{\mu_0}{4\pi}\right)\frac{\gamma_I\gamma_S\hbar}{r^3}2\hat{I}_z\hat{S}_z\left(3\cos^2\theta - 1\right) \tag{1.4}
$$

Molecular tumbling in solution NMR and magic angle (54.74 °) spinning (MAS) in SSNMR averages out or significantly attenuates dipolar couplings. There are a number of pulse sequences in SSNMR designed to recouple the dipolar couplings, in a quantitative or semi-quantitative manner. [40-50]

1.3.3 ^{1}H spin diffusion

The overall structure and function of peripheral and membrane proteins plays a critical role in the regulation of their structure and function. The proximity of specific amino acids or sites in small molecules relative the lipid-water interface can aid in the elucidation of the

mechanism of membrane insertion, extraction, or accessibility of surface residues for intermolecular interactions. This can be particularly probative when characterizing changes in water and lipid accessibility in the presence and absence on an antagonist, as shown in Chapter 5 with amphotericin B and ergosterol.

In ^{1}H spin diffusion, magnetization is transferred from a source spin to a target spin via ^{1}H-^{1}H dipolar couplings. The source spin can be selected based on the relative mobility of the source spins, using a ^{1}H T_2 filter, prior to storage of magnetization along the z-axis where ^{1}H-^{1}H magnetization is transferred via spin diffusion. The magnetization is then transferred the X spin (typically ^{13}C or ^{31}P) prior to detection.[51] The T_2 filter attenuates magnetization from the more rigid protons, thus selecting magnetization from the more mobile lipid/water baths. The build-up curves can be described according to the discrete diffusion equation:

$$\frac{\Delta Mi}{\Delta t} = -2\Omega M_i + \Omega M_{i+1} + \Omega M_{i-1} \tag{1.5}$$

where the rate of magnetization transfer $\Omega = D/a^2$ depends on the distance between spins, a, and the diffusion coefficient D.[52] Distance determination requires knowledge of the diffusion constants within the matrixes involved. Therefore, to determine the rates of lipid-protein spin diffusion, the diffusion rates within the lipid matrix (D_L) and the protein matrix (D_P) are needed. Distances up to 25 Å can be estimated, based in the build-up trajectories.[51,52]

Proton spin diffusion is a very useful tool, and it can be used to probe multiple correlations simultaneously between source sites with unique ^{1}H chemical shifts and the target. The most common choices are the terminal methyl groups of the lipid acyl chains, the lipid methylene (CH_2) groups, water, and occasionally the choline methyl groups, serving as probes for the center, middle, and surface of the bilayer respectively. Care must be taken when

normalizing the data to correct for ^{1}H T_1 relaxation and the relative intensity of all source protons to the same target site.

1.4 Systems Studied

1.4.1 Phosphatidylserine-Ca^{2+} Complex.

Thrombotic disorders represent a leading cause of death and disability in the United States. Approximately 7-10% all deaths in the United States can be directly attributed to the formation of blood clots in the vasculature, e.g. deep vein thrombosis, pulmonary embolism, or cerebrovascular disease (stroke). As shown in Figure 1.3, both the intrinsic and extrinsic clotting pathways depend on the activity of factors VII, IX, X and prothrombin (PT, also called factor II). These proteins all have N-terminal membrane binding domain rich in γ-carboxylated glutamates (Gla) residues, GLA domains, that bind to PS-rich regions on the plasma membrane in a Ca^{2+}-dependent manner. The *N*-terminus glutamate residues are carboxylated by gamma glutamyl carboxylase using reduced vitamin K_1, which then forms vitamin K_1-epoxide. The vitamin K_1-epoxide is reduced by vitamin K_1-epoxide-reductase to regenerate vitamin K_1 and complete the vitamin K cycle, which is responsible for the generation of effective clotting factors and other proteins involved in bone metabolism.[53-56] Oral anticoagulants coumarin and indandione derivatives are anti-vitamin K anticoagulants (AVK) that block the activity of vitamin K_1-epoxide and vitamin K_1-epoxide-reductase.[53,54] It is believed that coagulation factors' Gla residues interact with the anionic membrane in the presence of Ca^{2+} to facilitate partial insertion of the GLA domain into the bilayer. Association of the prothrombinase complex (Factor Xa: Factor Va) with anionic (PS-rich) membranes increases the rate of prothrombin cleavage *several thousand-fold,* resulting in a local propagation of blood coagulation.[57-60] Similar enhancements in

procoagulant activity have been noted for other coagulation factors when associated with PS-containing membranes.[61-64]

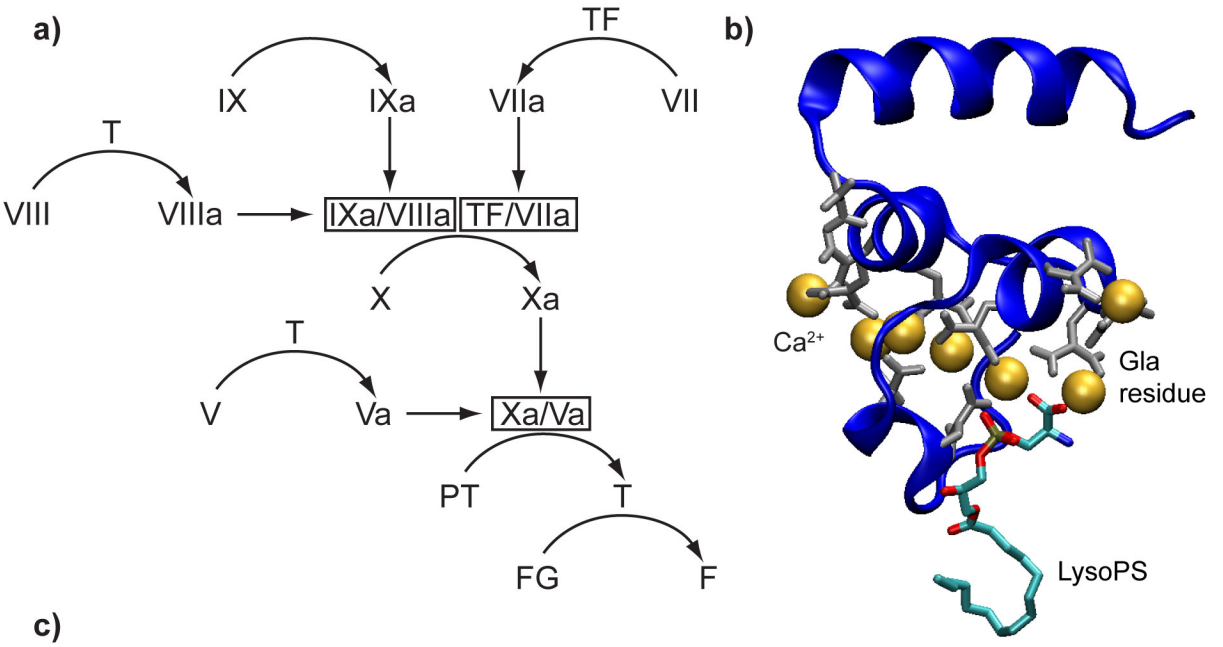

Figure 1.2 Blood Clotting Cascade and GLA domains
(a) The extrinsic and intrinsic blood clotting pathways converge with the activation of factor X which then binds to activated factor V to form the prothrombinase complex which cleaves prothrombin (PT) to form thrombin which later interacts with fibrinogen (FG) to for fibrin (F) and ultimately a fully formed fibrin clot. Clotting factors IX, VII, X, and PT are vitamin-K dependent serine protease that contain a common membrane biding domain rich in γ-carboxylated glutamates (Gla) residues called a GLA domain. As shown in panel (b) the crystal structure of bovine prothrombin fragment 1 (bPT-F1, 1NL2) bound lysophosphatidylserine (LysoPS) the fold of the GLA domain depends on the interaction of the Gla residues with Ca^{2+} and its activity is directly tied association with PS. [65] Panel (c) shows the sequence homology between the clotting factor GLA domains.

The conserved activity of these lipid transport proteins underlines the significance of the membrane composition in biological function of the cell. As is the case with case proteins, the

dynamics and structures of lipids are tied to their environment, and the presence of specific cofactors. The activity of the lipid transport proteins sequesters PS to the cytosolic leaflet, away from the extracellular proteins, and millimolar levels of Ca^{2+} found in plasma. Phosphatidylserine is only exposed on the outer leaflet of the membrane during cell activation for blood clotting and apoptosis. [66,67] Studies have shown that exposure of PS and other anionic lipids to millimolar Ca^{2+} and proteins induces clustering/aggregation on the bilayer surface into microdomains visible by fluorescence microscopy.[68-70] Further investigations of PS enriched bilayers have shown that Ca^{2+} induces a lateral reorganization and rigidification of the PS headgroups, *possibly* resulting from conformational changes in the PS headgroup.[71-74] In addition, PE has been shown to enhance the procoagulant activity of PS membranes[62,75,76], and is hypothesized to play a role in the formation of PS-rich nanodomains.[61,77] These PS rich regions serve as high affinity binding sites for zymogenic coagulations factors that are circulating in the blood, like factor VII, Factor X, and PT.[59,77,78]

Membrane binding is of critical importance in regulating blood-clotting reactions, and despite much work in the field[64,77,79,80], we still do not understand how these membrane-binding domains interact with PS-microdomains at atomic resolution. Biophysical studies and MD simulations have shown that on average there are six to eight phospholipids interacting with a membrane associated GLA domain.[64,79,81] The crystal structure of LysoPS-bPT Fragment 1 (Figure 1.2b) identified a potential PS specific interaction, which was also observed in MD simulations of GLA domains in pure DOPS membranes.[79,80] We propose that GLA domain binding to lipid bilayers is facilitated by a combination of *ca*. one PS-specific interaction and *ca*. five to seven phosphate-specific interactions. SSNMR spectroscopy is a powerful technique that can be used

to directly probe the details of both the PS-rich binding domains and lipid-protein interactions at the atomic level, in the context of a fluid membrane as shown in Chapter 4.[63]

The use of Nanodiscs as a membrane mimetic in these studies offers many advantages to alternative synthetic membranes.[82-86] In order to probe the details of how anionic membrane binding domains regulate and enhance blood coagulation, we must have precise control of membrane composition at the nanoscale. Because Nanodiscs can be prepared with specific phospholipid composition, we can essentially reconstruct the membrane binding nanodomains, which catalyze blood coagulation. Notably, vesicles cannot be reliably prepared with more than ~20% POPS and Ca^{2+}, since Ca^{2+} phosphate coordination initiates a process of fusion, aggregation and collapse of the vesicles.[87] This is reflected in the poor spectral quality relative to Nanodisc samples, as shown in Figure 1.3b. In contrast, with Nanodiscs, the lipid composition can be varied as desired, and we can prepare samples with very high PS concentrations, providing high SSNMR sensitivity and thereby enabling efficient measurement of correlation spectra and distances through multidimensional NMR and dipolar recoupling methods. We have performed control studies with membrane vesicles (Figure 1.3a, b) confirming that we observe the similar effects in both Nanodisc and liposomes. The primary differences are that the data collected above the phase transition in MLVs show a more significant contribution from natural abundance lipids, specifically the choline headgroup and glycerol carbons in the PS alpha and beta carbon region between 70 and 55 ppm; however, below the phase transition they are identical to Nanodisc spectra below the phase transition (Figure 2.1). Difference in the spectra collected above the phase transition are most likely due to the differences in the phase transition temperatures as exemplified by the relative intensity and line width of the lipid acyl chains

collected at 10 °C (Figure 2.1b, d, e, h), and the increased probability that not all PS molecules are involved in the cluster given the differences in surface area.

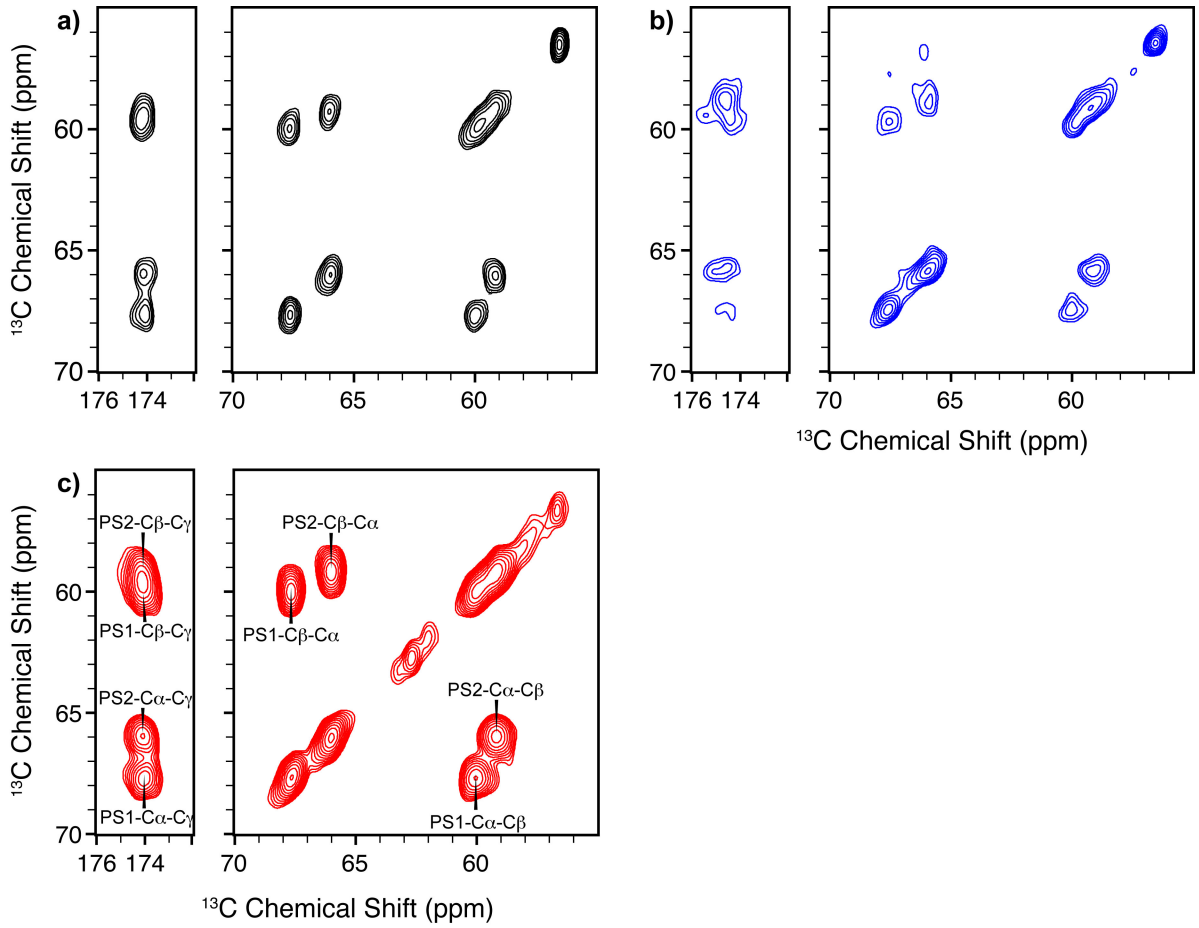

Figure 1.3 ^{13}C-^{13}C 2Ds of POPS/POPC Nanodisc and multi lamellar vesicles.
Multi lamellar vesicles (MLVs) are a commonly used membrane mimetic; however, for studies of anionic lipids in the presence of divalent cations, MLVs exhibit technical limitations. As shown in the panels (a) ^{13}C-^{13}C 2D of 10% POPS* 90% POPC with Ca^{2+} with 50 ms DARR mixing acquired at -20 °C at an MAS rate of 10.000 kHz, signal averaged for 39 hours, average cross peak signal to noise 15. (b) ^{13}C-^{13}C 2D of 30% POPS* 70% POPC MLVs with Ca^{2+} with 25 ms DARR mixing acquired at -20 °C at an MAS rate of 11.111 kHz, signal averaged for 18 hours, average cross peak signal to noise 15. (c) ^{13}C-^{13}C 2D of 30% POPS* 70% POPC Nanodisc with Ca^{2+} with 50 ms DARR mixing acquired at -20 °C at an MAS rate of 10.000 kHz, signal averaged fro 4 hours, average cross peak signal to noise 45. Nanodisc samples have both superior signal to noise and sample life time compared to the 30% MLVs which are already showing signs of degradation after 1 month, with the majority of that time spent in storage at -20 °C.

1.4.2 Amphotericine B Extraction of Ergosterol.

Fungal infections affect ~25% of the world population (1.3 billion). Most of these infections are the caused by dermatophytes resulting in common infections like athlete's foot, ringworm, and infections of the nails. The majority of these superficial infections are caused by various *Candida* fungi and are easily diagnosed and treated. However, approximately 2 million people die every year as a result of invasive, systemic, fungal infections. These infections are opportunistic in nature and typically the result of exposure to *Cryptococcus, Candida, Aspergillus, and Pneumocystis*, and affect primarily immunocompromised individuals *i.e.*, HIV/AIDS, cancer, transplant patents and the elderly. While the exact mortality rate as a result of fungal infections is hard to track due to poor epidemiology, rates of *ca.* 50% are reported for the four most common fungi.[88] The incidence of life-threatening systemic fungal infections continues to rise in parallel with expanding populations of immunocompromised patients and concomitant rise in pathogen resistance to most antifungals.

Ergosterol is the primary sterol found in fungal cells, and like cholesterol, it regulates membrane fluidity, integrity, and sterol-regulated processes. The two main classes of antifungal drugs azoles and polyenes all work by either inhibiting ergosterol synthesis or direct interaction with ergosterol. One of the final stages of sterol preparation in both human and fungal cells is the removal of C4 methyl groups by the cytochrome P450-depended 14α-demethylase. Azoles, like fluconazole, work by inhibiting the activity of cytochrome P450-depended 14α-demethylase, depleting ergosterol and thereby altering the membrane structure and functionality. Azoles also affect cholesterol production, but at a much higher dosage than that required for treatment fungi.[89,90] However, microbial resistance to azoles is on the rise, while resistance to amphotericin B remains minimal even after 50 years of use.[91]

Amphotericin B, a member of the polyene macrolide class of antimicrobial agents, is the most efficacious of the antifungals for treatment of life threatening systemic fungal infections. It has been in clinical use for over 50 years with minimal development of microbial resistance. AmB is the gold standard for the treatment of the majority of life threatening systemic fungal infections, but its clinical use is limited to more extreme cases. The main barriers to the effective administration are its inherent nephrotoxicity, and the fact that it can only be administered intravenously, due to its poor solubility, limiting its use in more resource poor regions, were systemic fungal infections are more prevalent. For nearly 50 years, the proposed mechanism of action for AmB is that it binds to ergosterol in the fungal membrane forming ion channels that result in the leakage of monovalent ions like K^+ leading to cell death.[92-110] However, the solid state NMR studies outline in chapter 5, along with extensive research by collaborators in the Burke group, have shown that AmB's fungicidal activity is primarily the result of the extraction of ergosterol from the membrane into a large extramembranous sponge.

1.5 References

1 Singer, S. J. & Nicolson, G. L. The fluid mosaic model of the structure of cell membranes. *Science* **175**, 720-731, (1972).

2 Engelman, D. M. Membranes are more mosaic than fluid. *Nature* **438**, 578-580, (2005).

3 Phillips, R., Ursell, T., Wiggins, P. & Sens, P. Emerging roles for lipids in shaping membrane-protein function. *Nature* **459**, 379-385, (2009).

4 Riedl, S., Zweytick, D. & Lohner, K. Membrane-active host defense peptides--challenges and perspectives for the development of novel anticancer drugs. *Chem. Phys. Lipids* **164**, 766-781, (2011).

5 Fadeel, B. & Xue, D. The ins and outs of phospholipid asymmetry in the plasma membrane: roles in health and disease. *Crit. Rev. Biochem. Mol. Biol.* **44**, 264-277, (2009).

6 Zwaal, R. F. & Schroit, A. J. Pathophysiologic implications of membrane phospholipid asymmetry in blood cells. *Blood* **89**, 1121-1132, (1997).

7 Leventis, P. A. & Grinstein, S. The Distribution and Function of Phosphatidylserine in Cellular Membranes. *Annu. Rev. Biophys.* **39**, 407-427, (2010).

8 Zwaal, R. F. A., Comfurius, P. & Vandeenen, L. L. M. Membrane Asymmetry and Blood-Coagulation. *Nature* **268**, 358-360, (1977).

9 Virtanen, J. A., Cheng, K. H. & Somerharju, P. Phospholipid composition of the mammalian red cell membrane can be rationalized by a superlattice model. *Proc. Natl. Acad. Sci. USA* **95**, 4964-4969, (1998).

10 Zwaal, R. F., Comfurius, P. & Bevers, E. M. Scott syndrome, a bleeding disorder caused by defective scrambling of membrane phospholipids. *Biochim. Biophys. Acta* **1636**, 119-128, (2004).

11 Paterson, J. K., Renkema, K., Burden, L., Halleck, M. S., Schlegel, R. A., Williamson, P. & Daleke, D. L. Lipid specific activation of the murine P4-ATPase Atp8a1 (ATPase II). *Biochemistry* **45**, 5367-5376, (2006).

12 Seelig, J. Deuterium magnetic resonance: theory and application to lipid membranes. *Q. Rev. Biophys.* **10**, 353-418, (1977).

13 Smith, R. L. & Oldfield, E. Dynamic structure of membranes by deuterium NMR. *Science* **225**, 280-288, (1984).

14 Urbina, J. A., Pekerar, S., Le, H. B., Patterson, J., Montez, B. & Oldfield, E. Molecular order and dynamics of phosphatidylcholine bilayer membranes in the presence of cholesterol, ergosterol and lanosterol: a comparative study using ^{2}H-, ^{13}C- and ^{31}P-NMR spectroscopy. *Biochim. Biophys. Acta* **1238**, 163-176, (1995).

15 Haberkorn, R. A., Griffin, R. G., Meadows, M. D. & Oldfield, E. Deuterium nuclear magnetic resonance investigation of the dipalmitoyl lecithin-cholesterol-water system. *J. Am. Chem. Soc.* **99**, 7353-7355, (1977).

16 Browning, J. L. & Seelig, J. Bilayers of phosphatidylserine: a deuterium and phosphorus nuclear magnetic resonance study. *Biochemistry* **19**, 1262-1270, (1980).

17 Leftin, A. & Brown, M. F. An NMR database for simulations of membrane dynamics. *Biochim. Biophys. Acta* **1808**, 818-839, (2011).

18 Vermeer, L. S., de Groot, B. L., Reat, V., Milon, A. & Czaplicki, J. Acyl chain order parameter profiles in phospholipid bilayers: computation from molecular dynamics simulations and comparison with 2H NMR experiments. *Eur. Biophys. J.* **36**, 919-931, (2007).

19 Lopez Cascales, J. J., Otero, T. F., Smith, B. D., Gonzalez, C. & Marquez, M. Model of an asymmetric DPPC/DPPS membrane: effect of asymmetry on the lipid properties. A molecular dynamics simulation study. *J. Phys. Chem. B* **110**, 2358-2363, (2006).

20 Bhide, S. Y., Zhang, Z. & Berkowitz, M. L. Molecular dynamics simulations of SOPS and sphingomyelin bilayers containing cholesterol. *Biophys. J.* **92**, 1284-1295, (2007).

21 Vernier, P. T., Ziegler, M. J. & Dimova, R. Calcium binding and head group dipole angle in phosphatidylserine-phosphatidylcholine bilayers. *Langmuir* **25**, 1020-1027, (2009).

22 Yang, H., Xu, Y., Gao, Z., Mao, Y., Du, Y. & Jiang, H. Effects of Na^+, K^+, and Ca^{2+} on the structures of anionic lipid bilayers and biological implication. *J. Phys. Chem. B* **114**, 16978-16988, (2010).

23 Slochower, D. R., Huwe, P. J., Radhakrishnan, R. & Janmey, P. A. Quantum and all-atom molecular dynamics simulations of protonation and divalent ion binding to phosphatidylinositol 4,5-bisphosphate (PIP2). *J. Phys. Chem. B* **117**, 8322-8329, (2013).

24 Kucerka, N., Tristram-Nagle, S. & Nagle, J. F. Structure of fully hydrated fluid phase lipid bilayers with monounsaturated chains. *J. Mem. Biol.* **208**, 193-202, (2005).

25 Kucerka, N., Liu, Y., Chu, N., Petrache, H. I., Tristram-Nagle, S. & Nagle, J. F. Structure of fully hydrated fluid phase DMPC and DLPC lipid bilayers using X-ray scattering from oriented multilamellar arrays and from unilamellar vesicles. *Biophys. J.* **88**, 2626-2637, (2005).

26 Nagle, J. F. & Tristram-Nagle, S. Structure of lipid bilayers. *Biochim. Biophys. Acta* **1469**, 159-195, (2000).

27 Seimiya, T. & Ohki, S. Ionic structure of phospholipid membranes, and binding of calcium ions. *Biochim. Biophys. Acta* **298**, 546-561, (1973).

28 Hauser, H., Paltauf, F. & Shipley, G. G. Structure and thermotropic behavior of phosphatidylserine bilayer membranes. *Biochemistry* **21**, 1061-1067, (1982).

29 Wiener, M. C. & White, S. H. Structure of a fluid dioleoylphosphatidylcholine bilayer determined by joint refinement of x-ray and neutron diffraction data. III. Complete structure. *Biophys. J.* **61**, 434-447, (1992).

30 Petrache, H. I., Tristram-Nagle, S., Gawrisch, K., Harries, D., Parsegian, V. A. & Nagle, J. F. Structure and fluctuations of charged phosphatidylserine bilayers in the absence of salt. *Biophys. J.* **86**, 1574-1586, (2004).

31 Pan, J., Cheng, X., Monticelli, L., Heberle, F. A., Kucerka, N., Tieleman, D. P. & Katsaras, J. The molecular structure of a phosphatidylserine bilayer determined by scattering and molecular dynamics simulations. *Soft Matter* **10**, 3716-3725, (2014).

32 Bartels, T., Lankalapalli, R. S., Bittman, R., Beyer, K. & Brown, M. F. Raftlike mixtures of sphingomyelin and cholesterol investigated by solid-state 2H NMR spectroscopy. *J. Am. Chem. Soc.* **130**, 14521-14532, (2008).

33 Bunge, A., Muller, P., Stockl, M., Herrmann, A. & Huster, D. Characterization of the ternary mixture of sphingomyelin, POPC, and cholesterol: support for an inhomogeneous lipid distribution at high temperatures. *Biophys. J.* **94**, 2680-2690, (2008).

34 Aussenac, F., Tavares, M. & Dufourc, E. J. Cholesterol dynamics in membranes of raft composition: a molecular point of view from 2H and 31P solid-state NMR. *Biochemistry* **42**, 1383-1390, (2003).

35 Pan, J., Tristram-Nagle, S. & Nagle, J. F. Effect of cholesterol on structural and mechanical properties of membranes depends on lipid chain saturation. *Phys. Rev. E, Stat., Nonlinear, Soft Matter Phys.* **80**, 021931, (2009).

36 Quinn, P. J. & Wolf, C. The liquid-ordered phase in membranes. *Biochim. Biophys. Acta* **1788**, 33-46, (2009).

37 Boggs, J. M. Lipid intermolecular hydrogen bonding: influence on structural organization and membrane function. *Biochim. Biophys. Acta* **906**, 353-404, (1987).

38 Zuiderweg, E. R. Mapping protein-protein interactions in solution by NMR spectroscopy. *Biochemistry* **41**, 1-7, (2002).

39 Anderson, T. M., Clay, M. C., Cioffi, A. G., Diaz, K. A., Hisao, G. S., Tuttle, M. D., Nieuwkoop, A. J., Comellas, G., Maryum, N., Wang, S., Uno, B. E., Wildeman, E. L., Gonen, T., Rienstra, C. M. & Burke, M. D. Amphotericin forms an extramembranous and fungicidal sterol sponge. *Nature Chemical Biology* **10**, 400-406, (2014).

40 Bennett, A. E., Rienstra, C. M., Griffiths, J. M., Zhen, W. G., Lansbury, P. T. & Griffin, R. G. Homonuclear radio frequency-driven recoupling in rotating solids. *J. Chem. Phys.***108**, 9463-9479, (1998).

41 Takegoshi, K., Nakamura, S. & Terao, T. C-13-H-1 dipolar-assisted rotational resonance in magic-angle spinning NMR. *Chem. Phys. Lett.* **344**, 631-637, (2001).

42 Takegoshi, K., Nakamura, S. & Terao, T. C-13-H-1 dipolar-driven C-13-C-13 recoupling without C-13 rf irradiation in nuclear magnetic resonance of rotating solids. *J. Chem. Phys.* **118**, 2325-2341, (2003).

43 Gullion, T. & Schaefer, J. Rotational-echo double-resonance NMR. *J. Magn. Res.* **213**, 413-417, (1989).

44 Jaroniec, C. P., Lansing, J. C., Tounge, B. A., Belenky, M., Herzfeld, J. & Griffin, R. G. Measurement of dipolar couplings in a uniformly (13)C,(15)N-labeled membrane protein: distances between the Schiff base and aspartic acids in the active site of bacteriorhodopsin. *J. Am. Chem. Soc.* **123**, 12929-12930, (2001).

45 Jaroniec, C. P., Tounge, B. A., Herzfeld, J. & Griffin, R. G. Frequency selective heteronuclear dipolar recoupling in rotating solids: accurate (13)C-(15)N distance measurements in uniformly (13)C,(15)N-labeled peptides. *J. Am. Chem. Soc.* **123**, 3507-3519, (2001).

46 Jaroniec, C. P., Tounge, B. A., Rienstra, C. M., Herzfeld, J. & Griffin, R. G. Recoupling of heteronuclear dipolar interactions with rotational-echo double-resonance at high magic-angle spinning frequencies. *J. Magn. Res.* **146**, 132-139, (2000).

47 Mani, R., Tang, M., Wu, X., Buffy, J. J., Waring, A. J., Sherman, M. A. & Hong, M. Membrane-bound dimer structure of a beta-hairpin antimicrobial peptide from rotational-echo double-resonance solid-state NMR. *Biochemistry* **45**, 8341-8349, (2006).

48 Jaroniec, C. P., Filip, C. & Griffin, R. G. 3D TEDOR NMR experiments for the simultaneous measurement of multiple carbon-nitrogen distances in uniformly (13)C,(15)N-labeled solids. *J. Am. Chem. Soc.* **124**, 10728-10742, (2002).

49 Nadaud, P. S., Helmus, J. J., Hofer, N. & Jaroniec, C. P. Long-range structural restraints in spin-labeled proteins probed by solid-state nuclear magnetic resonance spectroscopy. *J. Am. Chem. Soc.* **129**, 7502-+, (2007).

50 Nieuwkoop, A. J., Wylie, B. J., Franks, W. T., Shah, G. J. & Rienstra, C. M. Atomic resolution protein structure determination by three-dimensional transferred echo double resonance solid-state nuclear magnetic resonance spectroscopy. *J. Chem. Phys.* **131**, 095101, (2009).

51 Hong, M. & Schmidt-Rohr, K. Magic-angle-spinning NMR techniques for measuring long-range distances in biological macromolecules. *Acc. Chem. Res.* **46**, 2154-2163, (2013).

52 Huster, D., Yao, X. & Hong, M. Membrane protein topology probed by (1)H spin diffusion from lipids using solid-state NMR spectroscopy. *J. Am. Chem. Soc.* **124**, 874-883, (2002).

53 Freedman, M. D. Oral anticoagulants: pharmacodynamics, clinical indications and adverse effects. *J. Clin. Pharmacology* **32**, 196-209, (1992).

54 Ansell, J., Hirsh, J., Poller, L., Bussey, H., Jacobson, A. & Hylek, E. The pharmacology and management of the vitamin K antagonists: the Seventh ACCP Conference on Antithrombotic and Thrombolytic Therapy. *Chest* **126**, 204S-233S, (2004).

55 Hauschka, P. V., Lian, J. B., Cole, D. E. & Gundberg, C. M. Osteocalcin and matrix Gla protein: vitamin K-dependent proteins in bone. *Physiol. Rev.* **69**, 990-1047, (1989).

56 Price, P. A. Role of vitamin-K-dependent proteins in bone metabolism. *Ann. Rev. Nut.* **8**, 565-583, (1988).

57 Nesheim, M. E., Taswell, J. B. & Mann, K. G. Contribution of Bovine Factor-V and Factor-Va to the Activity of Prothrombinase. *J. Biol. Chem.* **254**, 952-962, (1979).

58 Rosing, J., Vanrijn, J. L. M. L., Bevers, E. M., Vandieijen, G., Comfurius, P. & Zwaal, R. F. A. The Role of Activated Human-Platelets in Prothrombin and Factor-X Activation. *Blood* **65**, 319-332, (1985).

59 Lentz, B. R. Exposure of platelet membrane phosphatidylserine regulates blood coagulation. *Pro.g Lipid Res.* **42**, 423-438, (2003).

60 Cutsforth, G. A., Whitaker, R. N., Lentz, B. R. & Hermans, J. A New Model to Describe Extrinsic Protein-Binding to Phospholipid-Membranes of Varying Composition - Application to Human Coagulation Proteins - Appendix - a New Model to Describe Extrinsic Protein-Binding to Phospholipid-Membranes of Varying Composition - Quantitative Development. *Biochemistry* **28**, 7453-7461, (1989).

61 Gilbert, G. E. & Arena, A. A. Phosphatidylethanolamine Induces High-Affinity Binding-Sites for Factor-Viii on Membranes Containing Phosphatidyl-L-Serine. *J. Biol. Chem.* **270**, 18500-18505, (1995).

62 Neuenschwander, P. F., Biancofisher, E., Rezaie, A. R. & Morrissey, J. H. Phosphatidylethanolamine Augments Factor Viia-Tissue Factor Activity - Enhancement of Sensitivity to Phosphatidylserine. *Biochemistry* **34**, 13988-13993, (1995).

63 Tavoosi, N., Davis-Harrison, R. L., Pogorelov, T. V., Ohkubo, Y. Z., Arcario, M. J., Clay, M. C., Rienstra, C. M., Tajkhorshid, E. & Morrissey, J. H. Molecular Determinants of Phospholipid Synergy in Blood Clotting. *J. Biol. Chem.* **286**, 23247-23253, (2011).

64 Shaw, A. W., Pureza, V. S., Sligar, S. G. & Morrissey, J. H. The local phospholipid environment modulates the activation of blood clotting. *J. Biol. Chem.* **282**, 6556-6563, (2007).

65 Huang, M., Rigby, A. C., Morelli, X., Grant, M. A., Huang, G., Furie, B., Seaton, B. & Furie, B. C. Structural basis of membrane binding by Gla domains of vitamin K-dependent proteins. *Nat. Struct. Biol.* **10**, 751-756, (2003).

66 Bevers, E. M., Comfurius, P., Dekkers, D. W., Harmsma, M. & Zwaal, R. F. Transmembrane phospholipid distribution in blood cells: control mechanisms and pathophysiological significance. *Biol. Chem.* **379**, 973-986, (1998).

67 Schroit, A. J. & Zwaal, R. F. Transbilayer movement of phospholipids in red cell and platelet membranes. *Biochim. Biophys. Acta* **1071**, 313-329, (1991).

68 Haverstick, D. M. & Glaser, M. Visualization of Ca-2+-Induced Phospholipid Domains. *Proc. Natl. Acad. Sci. USA* **84**, 4475-4479, (1987).

69 Yang, L. & Glaser, M. Formation of membrane domains during the activation of protein kinase C. *Biochemistry* **35**, 13966-13974, (1996).

70 Yeung, T., Gilbert, G. E., Shi, J., Silvius, J., Kapus, A. & Grinstein, S. Membrane phosphatidylserine regulates surface charge and protein localization. *Science* **319**, 210-213, (2008).

71 Boettcher, J. M., Davis-Harrison, R. L., Clay, M. C., Nieuwkoop, A. J., Ohkubo, Y. Z., Tajkhorshid, E., Morrissey, J. H. & Rienstra, C. M. Atomic View of Calcium-Induced Clustering of Phosphatidylserine in Mixed Lipid Bilayers. *Biochemistry* **50**, 2264-2273, (2011).

72 Roux, M. & Bloom, M. Ca-2+, Mg-2+, Li+, Na+, and K+ Distributions in the Headgroup Region of Binary Membranes of Phosphatidylcholine and Phosphatidylserine as Seen by Deuterium Nmr. *Biochemistry* **29**, 7077-7089, (1990).

73 Roux, M. & Bloom, M. Calcium-Binding by Phosphatidylserine Headgroups - Deuterium Nmr-Study. *Biophys. J.* **60**, 38-44, (1991).

74 Schultz, Z. D., Pazos, I. M., McNeil-Watson, F. K., Lewis, E. N. & Levin, I. W. Magnesium-Induced Lipid Bilayer Microdomain Reorganizations: Implications for Membrane Fusion. *J. Phys. Chem. B* **113**, 9932-9941, (2009).

75 Smeets, E., Comfurius, P., Bevers, E. & Zwaal, R. Contribution of different phospholipid classes to the prothromin converting capacity of sonicated lipid vesicles. *Thromb. Res.* **81**, 419-426, (1996).

76 Smirnov, M. D. & Esmon, C. T. Phosphatidylethanolamine Incorporation into Vesicles Selectively Enhances Factor Va Inactivation by Activated Protein-C. *J. Biol. Chem.* **269**, 816-819, (1994).

77 Zwaal, R. F. A., Comfurius, P. & Bevers, E. M. Lipid-protein interactions in blood coagulation. *Biochim. Biophys. Acta –Rev. Biomembranes* **1376**, 433-453, (1998).

78 Morrissey, J. H., Pureza, V., Davis-Harrison, R. L., Sligar, S. G., Rienstra, C. M., Kijac, A. Z., Ohkubo, Y. Z. & Tajkhorshid, E. Protein-membrane interactions: blood clotting on nanoscale bilayers. *J. Thromb. Haemost.* **7**, 169-172, (2009).

79 Ohkubo, Y. Z. & Tajkhorshid, E. Distinct structural and adhesive roles of Ca^{2+} in membrane binding of blood coagulation factors. *Structure* **16**, 72-81, (2008).

80 Huang, M. D., Rigby, A. C., Morelli, X., Grant, M. A., Huang, G. Q., Furie, B., Seaton, B. & Furie, B. C. Structural basis of membrane binding by Gla domains of vitamin K-dependent proteins. *Nat. Struct. Biol.* **10**, 751-756, (2003).

81 Morrissey, J. H., Pureza, V., Davis-Harrison, R. L., Sligar, S. G., Ohkubo, Y. Z. & Tajkhorshid, E. Blood clotting reactions on nanoscale phospholipid bilayers. *Thromb. Res.* **122**, S23-S26, (2008).

82 Bayburt, T. H., Grinkova, Y. V. & Sligar, S. G. Self-assembly of discoidal phospholipid bilayer nanoparticles with membrane scaffold proteins. *Nano. Lett.* **2**, 853-856, (2002).

83 Bayburt, T. H. & Sligar, S. G. Self-assembly of single integral membrane proteins into soluble nanoscale phospholipid bilayers. *Protein Sci.* **12**, 2476-2481, (2003).

84 Denisov, I. G., Grinkova, Y. V., Lazarides, A. A. & Sligar, S. G. Directed Self-Assembly of Monodisperse Phospholipid Bilayer Nanodiscs with Controlled Size. *J. Am. Chem. Soc.* **126**, 3477-3487, (2004).

85 Denisov, I. G., McLean, M. A., Shaw, A. W., Grinkova, Y. V. & Sligar, S. G. Thermotropic phase transition in soluble nanoscale lipid bilayers. *J. Phys. Chem. B* **109**, 15580-15588, (2005).

86 Nath, A., Atkins, W. M. & Sligar, S. G. Applications of Phospholipid Bilayer Nanodiscs in the Study of Membranes and Membrane Proteins. *Biochemistry* **46**, 2059-2069, (2007).

87 Papahadjopoulos, D., Poste, G., Schaeffer, B. E. & Vail, W. J. Membrane fusion and molecular segregation in phospholipid vesicles. *Biochim. Biophys. Acta* **352**, 10-28, (1974).

88 Brown, G. D., Denning, D. W., Gow, N. A., Levitz, S. M., Netea, M. G. & White, T. C. Hidden killers: human fungal infections. *Science Translational Medicine* **4**, 165rv113, (2012).

89 Ghannoum, M. A. & Rice, L. B. Antifungal agents: mode of action, mechanisms of resistance, and correlation of these mechanisms with bacterial resistance. *Clin. Microbiol. Rev.* **12**, 501-517, (1999).

90 Kelly, S. L., Rowe, J. & Watson, P. F. Molecular genetic studies on the mode of action of azole antifungal agents. *Biochem. Soc. Trans.* **19**, 796-798, (1991).

91 Ellis, D. Amphotericin B: spectrum and resistance. *J. Antimicrob. Chemother.* **49 Suppl 1**, 7-10, (2002).

92 Andreoli, T. E. & Monahan, M. The interaction of polyene antibiotics with thin lipid membranes. *J. Gen. Physiol.* **52**, 300-325, (1968).

93 Cass, A., Finkelstein, A. & Krespi, V. The ion permeability induced in thin lipid membranes by the polyene antibiotics nystatin and amphotericin B. *J. Gen. Physiol.* **56**, 100-124, (1970).

94 Finkelstein, A. & Holz, R. Aqueous pores created in thin lipid membranes by the polyene antibiotics nystatin and amphotericin B. *Membranes* **2**, 377-408, (1973).

95 Verkleij, A. J., Dekruijf.B, Gerritse.Wf, Demel, R. A., Vandeene.Ll & Ververga.Ph. Freeze-Etch Electron-Microscopy of erythrocytes, acholeplasma-laidlawii cells and liposomal membranes after action of filipin and amphotericin-B. *Biochim. Biophys. Acta* **291**, 577-581, (1973).

96 Andreoli, T. E. Structure and function of amphotericin B-cholesterol pores in lipid bilayer membranes. *Annals of the New York Academy of Sciences* **235**, 448-468, (1974).

97 de Kruijf, B. & Demel, R. A. Polyene antibiotic-sterol interactions in membranes of acholeplasma-laidlawii cells and lecithin liposomes. 3. molecular-structure of polyene sntibiotic-cholesterol complexes. *Biochim. Biophys. Acta* **339**, 57-70, (1974).

98 Ermishkin, L. N., Kasumov, K. M. & Potzeluyev, V. M. Single ionic channels induced in lipid bilayers by polyene antibiotics amphotericin-B and nystatine. *Nature* **262**, 698-699, (1976).

99 Bolard, J. How do the polyene macrolide antibiotics affect the cellular membrane-properties. *Biochim. Biophys. Acta* **864**, 257-304, (1986).

100 Cheron, M., Cybulska, B., Mazerski, J., Grzybowska, J., Czerwinski, A. & Borowski, E. Quantitative structure-activity relationships in amphotericin B derivatives. *Biochem. Pharmacol.* **37**, 827-836, (1988).

101 Baginski, M., Resat, H. & Borowski, E. Comparative molecular dynamics simulations of amphotericin B-cholesterol/ergosterol membrane channels. *Biochim. Biophys. Acta* **1567**, 63-78, (2002).

102 Milhaud, J., Ponsinet, V., Takashi, M. & Michels, B. Interactions of the drug amphotericin B with phospholipid membranes containing or not ergosterol: New insight, into them role of ergosterol. *Biocehm. Biophys. Acta-Biomembranes* **1558**, 95-108, (2002).

103 Cereghetti, D. M. & Carreira, E. M. Amphotericin B: 50 years of chemistry and biochemistry. *Synthesis-Stuttgart*, 914-942, (2006).

104 Matsumori, N., Sawada, Y. & Murata, M. Large molecular assembly of amphotericin B formed in ergosterol-containing membrane evidenced by solid-state NMR of intramolecular bridged derivative. *J. Am. Chem. Soc.* **128**, 11977-11984, (2006).

105 Matsuoka, S., Ikeuchi, H., Umegawa, Y., Matsumori, N. & Murata, M. Membrane interaction of amphotericin B as single-length assembly examined by solid state NMR for uniformly ^{13}C-enriched agent. *Bioorgan. Med. Chem.* **14**, 6608-6614, (2006).

106 Mouri, R., Konoki, K., Matsumori, N., Oishi, T. & Murata, M. Complex formation of amphotericin B in sterol-containing membranes as evidenced by surface plasmon resonance. *Biochemistry* **47**, 7807-7815, (2008).

107 Murata, M., Kasai, Y., Umegawa, Y., Matsushita, N., Tsuchikawa, H., Matsumori, N. & Oishi, T. Ion channel complex of antibiotics as viewed by NMR. *Pure Appl. Chem.* **81**, 1123-1129, (2009).

108 Volmer, A. A., Szpilman, A. M. & Carreira, E. M. Synthesis and biological evaluation of amphotericin B derivatives. *Nat. Prod. Rep.* **27**, 1329-1349, (2010).

109 Croatt, M. P. & Carreira, E. M. Probing the role of the mycosamine C2'-OH on the activity of amphotericin B. *Org. Lett.* **13**, 1390-1393, (2011).

110 Umegawa, Y., Nakagawa, Y., Tahara, K., Tsuchikawa, H., Matsumori, N., Oishi, T. & Murata, M. Head-to-tail interaction between amphotericin B and ergosterol occurs in hydrated phospholipid membrane. *Biochemistry* **51**, 83-89, (2012).

CHAPTER 2

Atomic View of Calcium-Induced Clustering of Phosphatidylserine in Mixed Lipid Bilayers

2.1 Notes and Acknowledgements

This chapter is adapted with permission from Atomic View of Calcium-Induced Clustering of Phosphatidylserine in Mixed Lipid Bilayers, volume 50, 2011, pages 2264-2273, authors: John M. Boettcher[#], Rebecca L. Davis-Harrison[#], Mary C. Clay, Andrew J. Nieuwkoop, Y. Zenmei Ohkubo, Emad Tajkhorshid, James H. Morrissey, and Chad M. Rienstra (# these authors contributed equally to this work) copyright 2011. Copyright 2011 American Chemical Society.This work was supported by the National Institute of General Medical Sciences, NIH (R01-GM075937 and R01-GM079530 to C.M.R., and R01-GM086749 and R01-GM067887 to E.T.), the National Center for Research Resources, NIH (P41-RR05969 to E.T.), the National Heart Lung and Blood Institute, NIH (R01 HL47014 to J.H.M. and R01 HL103999 to J.H.M. and C.M.R.), and by the American Heart Association (0920045G to R.D.H.).

2.2 Abstract

Membranes play key regulatory roles in biological processes, with bilayer composition exerting marked effects on binding affinities and catalytic activities of a number of membrane-associated proteins. In particular, proteins involved in diverse processes such as vesicle fusion, intracellular signaling cascades, and blood coagulation interact specifically with anionic lipids such as phosphatidylserine (PS) in the presence of Ca^{2+} ions. While Ca^{2+} is suspected to induce PS clustering in mixed phospholipid bilayers, the detailed structural effects of this ion on anionic lipids are not established. In this study, combining magic angle spinning (MAS) solid-state NMR

(SSNMR) measurements of isotopically labeled serine headgroups in mixed lipid bilayers with molecular dynamics (MD) simulations of PS lipid bilayers in the presence of different counterions, we provide site-resolved insights into the effects of Ca^{2+} on the structure and dynamics of lipid bilayers. Ca^{2+}-induced conformational changes of PS in mixed bilayers are observed in both liposomes and Nanodiscs, a nanoscale membrane-mimetic of bilayer patches. Site-resolved multidimensional correlation SSNMR spectra of bilayers containing ^{13}C, ^{15}N-labeled PS demonstrate that Ca^{2+} ions promote two major PS headgroup conformations, which are well resolved in two-dimensional ^{13}C-^{13}C, ^{15}N-^{13}C and ^{31}P-^{13}C spectra. The results of MD simulations performed on PS lipid bilayers in the presence or absence of Ca^{2+} provide an atomic view of the conformational effects underlying the observed spectra.

2.3 Introduction

In healthy cells, phosphatidylserine (PS) resides on the inner leaflet of the plasma membrane [1] and represents 10-20% of all plasma membrane lipids.[2, 3] PS both imparts a negative surface potential for nonspecific binding of cationic proteins [4, 5] and recruits several proteins through specific interactions, frequently involving Ca^{2+} (*6*). Externalization of PS in activated platelets and apoptotic cells constitutes a signal eliciting coagulation and phagocytosis, respectively.[7, 8] It is well documented that relatively high concentrations of Ca^{2+} can exert dramatic effects on membranes containing PS, observed as alterations in phase transition and separation of lipid components leading to aggregation, fusion, and even collapse of the membrane bilayer structure.[9-12] However, Ca^{2+} in the cytoplasm is tightly controlled at much lower levels, around 100 nM for a quiescent cell, increasing 10 to 100-fold (to ~mM) for an activated cell [13], while plasma contains about 2.4 mM total Ca^{2+}. At physiologically relevant

concentrations, Ca^{2+} may exert more subtle effects on a bilayer structure that are challenging to measure but of potential importance to the timing and coordination of many cellular processes.

Microscopic and transient islands enriched in specific lipids are proposed to act as targets enhancing and/or coordinating activities such as cell signaling and blood coagulation.[14, 15] To date, most investigations of divalent cation- and protein-induced PS microdomains have either relied on perturbative methods or focused on bulk characteristics such as surface pressure.[15-17] For instance, it has been demonstrated that membrane-binding proteins, such as annexin A5 and 2, in concert with plasma concentrations of Ca^{2+} induce the lateral organization of anionic phospholipids such as PS, phosphatidic acid (PA) and phosphatidylinositol (4,5)-bisphosphate (PIP_2).[16, 18, 19] Recently, fluorescence microscopy has revealed that plasma Ca^{2+} concentrations induce clustering of PIP_2 into sub-micrometer domains, but no such effect was observed for PS.[20] Intriguingly, fluorescence microscopy previously revealed micrometer scale clustering for PA [19], and more detailed infrared vibrational spectroscopic studies using plasma levels of Mg^{2+} showed clustering of DPPS into groups of 10-100 acyl chains[17], well below the resolution of light microscopy.[17] This suggests that Ca^{2+}-induced lateral organization of PS may occur at a limited scale on the order of $\sim 10^2$ lipids. A few previous NMR studies have shown that Ca^{2+}-PS interactions in mixed bilayers cause conformational changes in PS headgroups,[21, 22] but only structures of PS headgroups in the absence of Ca^{2+} are currently available.[23] Thus, a detailed molecular model of exactly how Ca^{2+} ions interact with PS molecules at a membrane surface has yet to emerge and may provide clues important for unraveling why the lateral organization of PS seems to occur at different size scales from other anionic phospholipids.

Piecing together what is known about a few Ca^{2+}-dependent membrane-binding domains, and what is predicted about the PS lipid bilayer structure, suggests that the bulk of PS-bound

Ca^{2+} resides in the phosphodiester region of the bilayer, and that the PS headgroup rigidifies upon Ca^{2+} binding. For instance, several Ca^{2+}-dependent C2 domains penetrate the bilayer sufficiently to position their Ca^{2+} binding sites within the phosphodiester linker region of the membrane,[24-26] and a similar behavior has been predicted in a recent model for GLA domains.[27] It has also been reported that PS increases the apparent binding affinity of Ca^{2+} to the zwitterionic lipid, phosphatidylcholine (PC), if an excess of Ca^{2+} in the electrical double layer due to the formal negative charge of PS is taken into account (i.e., the amount of Ca^{2+} bound by either PS or PC is correlated with the concentration of Ca^{2+} directly adjacent to the bilayer).[28] Both observations hint that Ca^{2+} is most likely intercalated within the phosphodiester layer of the membrane, and in such a position it would rigidify not only PS headgroups but also perhaps the glycerol backbone of PS and neighboring PC headgroups. Indeed, molecular dynamics (MD) investigations concur with this hypothesis, demonstrating that Ca^{2+} predominantly resides within ~10 Å of the phosphodiester moiety, and may be found associated to a lesser extent with the PS carboxyl.[29, 30] Whether Ca^{2+} preferentially binds the PS phosphate or carboxyl has not been observed directly, and may have biological consequences in promoting or limiting the lateral organization of PS.

In this study, we investigate the interactions of Ca^{2+} with PS-containing lipid bilayers using all-atom MD simulations paired with magic angle spinning (MAS) solid-state NMR (SSNMR) studies that employ two membrane mimetics, liposomes and Nanodiscs. Nanodiscs are discoidal phospholipid bilayers of 8 nm-diameter containing ~67 lipids per leaflet which are wrapped and stabilized by two molecules of an amphipathic helical protein termed membrane scaffold protein (MSP).[31-34] Many studies have effectively used the Nanodisc system as a membrane mimetic to study membrane protein interactions,[35, 36] including SSNMR analyses of membrane protein

structures.[37-39] One advantage of the Nanodisc system, in addition to precise local control over lipid composition, is that their structural integrity is maintained in the presence of mM concentrations of Ca^{2+}, even with up to 90% PS in the bilayer—as opposed to liposomes which cannot tolerate more than ~30% PS in the presence of Ca^{2+} without undergoing vesicle aggregation, fusion and collapse. For these reasons, the Nanodisc system is an ideal experimental platform for investigating nanoscale Ca^{2+}-PS interactions on a membrane surface by SSNMR.

In the present study, the serine headgroup of PS has been isotopically labeled and incorporated into the lipid bilayers, allowing high-resolution NMR spectra of PS headgroup moieties interacting with Ca^{2+} ions. Our results indicate that Ca^{2+} ions promote the formation of a more ordered liquid phase, producing rigid conformations for PS headgroups. Mobility of the lipid acyl chains is not as affected by interactions with Ca^{2+} ions as the headgroups, although alteration of the phase transition behavior of the bilayer by Ca^{2+}-PS interactions is presented. We report carbon, nitrogen and phosphorus chemical shift values for two Ca^{2+}-induced PS conformations as well as initial estimates of intermolecular distances between the two PS conformations in the bilayer. Furthermore, all-atom MD simulations performed in conjunction with NMR measurements support the idea of the Ca^{2+}-induced lateral reorganization of PS and indicate a much tighter fluctuation radius for Ca^{2+} over Na^{2+} at the PS phosphodiester and carboxyl moieties. In the simulations, two predominant conformational species are also observed. These two PS conformations may be a basis for Ca^{2+}-induced lateral organization of PS molecules.

2.4 Materials and Methods

2.4.1 Isotopically Labeled POPS.

In a modification of the method of Iwasaki *et al*. (*40*), phospholipase D from *Streptomyces* (PLD; Sigma-Aldrich, St. Louis, MO) was used to replace the choline headgroup of POPC (1-palmitoyl-2-oleoyl-phosphatidylcholine) with U-^{13}C, ^{15}N-L-serine (Cambridge Isotopes Laboratories, Andover, MA) to yield POPS (1-palmitoyl-2-oleoyl-phosphatidylserine) isotopically labeled in the serine headgroup (termed POPS*). Briefly, 5 μg/mL PLD was added, with stirring, to a mixture of 1.5 M ^{13}C, ^{15}N-serine, 36 mg/mL POPC (Avanti Polar Lipids, Alabaster, AL) and $CaSO_4$ in 50 mM sodium acetate buffer, pH 5.6, and allowed to react overnight at 42 °C. The supernatant was collected by centrifugation, flushed with nitrogen gas and stored at 4 °C for use in subsequent reactions. The pellet was washed with water and re-suspended in 2:1 hexane:ethanol (5 mL per 1 mL original reaction volume), followed by water (1/4 the volume of hexane:ethanol) and 1 N HCl (1/10 the volume of the water). After vortexing, the hexane phase was collected, and the aqueous phase and pellet were extracted with additional hexane. The pooled hexane phases were dried under vacuum and POPS* was purified by CM52 chromatography.[41] Purity of POPS* was evaluated by two-dimensional thin-layer chromatography, using 90:54 chloroform:methanol for the first dimension and 65:25:4 chloroform:methanol:water for the second dimension. When necessary, POPS* was further purified by flash silica chromatography developed with 90:40:12:2 chloroform:methanol:acetic acid:water. Purified POPS* was stored in chloroform and its concentration determined by inorganic phosphate analysis after complete hydrolysis. POPS* purity and the level of ^{13}C, ^{15}N-serine incorporation was verified by HSQC solution NMR in chloroform.

2.4.2 Nanodisc Preparation.

Nanodiscs were prepared as previously described[33] using mixtures of POPC and POPS*. After the Nanodiscs were assembled, they were purified by size-exclusion chromatography,[33] except that the buffer was 10 mM Tris-HCl pH 7.4, 10 mM NaCl, with 2 mM $CaCl_2$. Samples were concentrated using an Amicon Ultra 10000 NMWL centrifugal filter (Thermo Fisher Scientific, Waltham, MA) to 2-3 mM phospholipid (15-22 μM Nanodiscs). The lyoprotectant, trehalose, was added in a 1:1 molar ratio to phospholipid, after which samples were frozen and lyophilized. The powders (~50% Nanodiscs by weight) were packed into 3.2 mm SSNMR rotors, after which water was added (equal to ~50% of the dry weight of packed samples).

2.4.3 Liposome Preparation.

Mixtures of dried POPC and POPS* (10 mg total) were suspended in 30 μL of 50 mM Tris-HCl pH 7.4, 100 mM NaCl, 2.5 mM $CaCl_2$ and sonicated until the solution was visually homogeneous, after which 1 mL of 2.5 mM $CaCl_2$ was added and the solution was sonicated again. Sample preparation in the absence of Ca^{2+} was identical except for the inclusion or addition of $CaCl_2$. Liposomes were collected by ultracentrifugation at 4 °C for 2.5 hours at 250,000 rcf, and the pelleted liposomes were packed into 3.2 mm SSNMR rotors.

2.4.4 Solid-State NMR Spectroscopy.

SSNMR studies were performed on four-channel Varian InfinityPlus spectrometers. POPS*:POPC Nanodisc spectra were acquired at 600 MHz with a Varian T3 ^{1}H-^{13}C-^{15}N 3.2 mm probe at an MAS rate of 10,000±3 Hz. The variable temperature gas was maintained at 90±10 scfh flow, and the reported sample temperatures take into account thermocouple calibration and frictional heating due to MAS, as calibrated with ethylene glycol.[42] All experiments utilized tangent ramped cross polarization (CP)[43] with TPPM[44] decoupling of the protons applied during

acquisition and evolution periods on average at ~80 kHz. Data were processed with NMRPipe[45] with back linear prediction and polynomial baseline (frequency domain) correction applied to the direct dimension, and zero filling and Lorentzian-to-Gaussian apodization applied to each dimension before Fourier transformation; additional processing parameters are located in the figure captions. Chemical shifts are referenced to adamantane, using the IUPAC standard gyromagnetic ratios to indirectly reference ^{15}N and ^{31}P spectra.[46] Peak picking and assignments were performed with Sparky.[47]

2.4.5 Molecular Dynamics Simulations

Two systems, each consisting of 288 1,2-dioleoyl-*sn*-glycero-3-[phospho-L-serine] (DOPS), were simulated in the presence of two different counterions. The first system included 144 Ca^{2+} ions and the other 288 Na^{+} ions. Each system was simulated for 100 ns under NP_nTA conditions using NAMD 2.6 (48) with the CHARMM27 set of force field parameters.[49] Periodic boundary conditions were assumed and the particle mesh Ewald (PME) method[50] was employed for the computation of long-range electrostatic interactions without truncation. A constant area of 9,409 $Å^2$ (97 Å x 97 Å) was imposed for both systems to maintain an experimentally obtained area-per-lipid value.[51] The details of the simulations are identical to those described elsewhere,[27,52] The last 90 ns of the trajectories were used for analysis.

2.5 Results

2.5.1 Effects of Ca^{2+} Binding on ^{13}C Chemical Shifts in PS Headgroups.

To test the effect of Ca^{2+} on PS headgroup conformation, we initially compared one-dimensional ^{13}C spectra of mixed POPS*:POPC bilayers, observing the effects of Ca^{2+} on the ^{13}C chemical shifts, which are sensitive to binding events and structural changes. (POPS* is phosphatidylserine whose L-serine headgroups are uniformly labeled with ^{13}C and ^{15}N.) One-

dimensional CP ^{13}C spectra (Figure 2.2.1) were acquired on liposomes containing 30% POPS*, 70% POPC in the absence (Figure 2.2.1a, b) and presence (Figure 2.2.1c, d) of 2.5 mM Ca^{2+}. We observe narrow resonances due to natural abundance ^{13}C on the fatty acyl chains (predominantly at 25 to 40 ppm, but also the ~132 ppm resonance ascribed to the olefinic carbons in the oleoyl chain), which are consistent with previous SSNMR assignments of lipids in bilayers (*53*). Above the phase transition (10 °C, Figure 2.2.1b) in the absence of Ca^{2+}, the POPS* headgroup signals are narrow and strong, when observed via direct (^{13}C Boltzmann) polarization in Bloch decay experiments (data not shown), yet cross polarize weakly from protons, indicative of fast-limit motions averaging dipolar couplings to a nearly isotropic limit. When frozen in the absence of Ca^{2+} (-20 °C, Figure 2.2.1a), the gel phase spectrum exhibits broad features characteristic of the inhomogeneous distribution of headgroup environments, since no particular conformation is preferred. In contrast, spectra of liposomes at -20 °C in the presence of 2.5 mM Ca^{2+} (Figure 2.2.1c) contain distinct ^{13}C resonances from POPS* headgroups, which cross polarize with high efficiency and have the typical characteristics of a rigid solid (e.g., cross polarization buildup in hundreds of microseconds and a requirement for high power decoupling to observe well-resolved spectra). Two resonances, at 66.3 and 67.9 ppm, are tentatively assigned to the POPS* alpha carbon (Cα), while upfield POPS* peak at ~60 ppm is significantly broadened (line width 190 Hz), potentially arising from two unresolved beta carbon (Cβ) signals (we remind readers that the lipid nomenclature for PS headgroups differs from that used for amino acids; i.e., the carbon proximate to the ^{31}P is called Cα). Similarly, the POPS* gamma carbon (Cγ) (at ~174.2 ppm) resonance is also slightly broadened to 131 Hz, which, while not as dramatic as the Cβ, is still consistent with two unresolved signals.

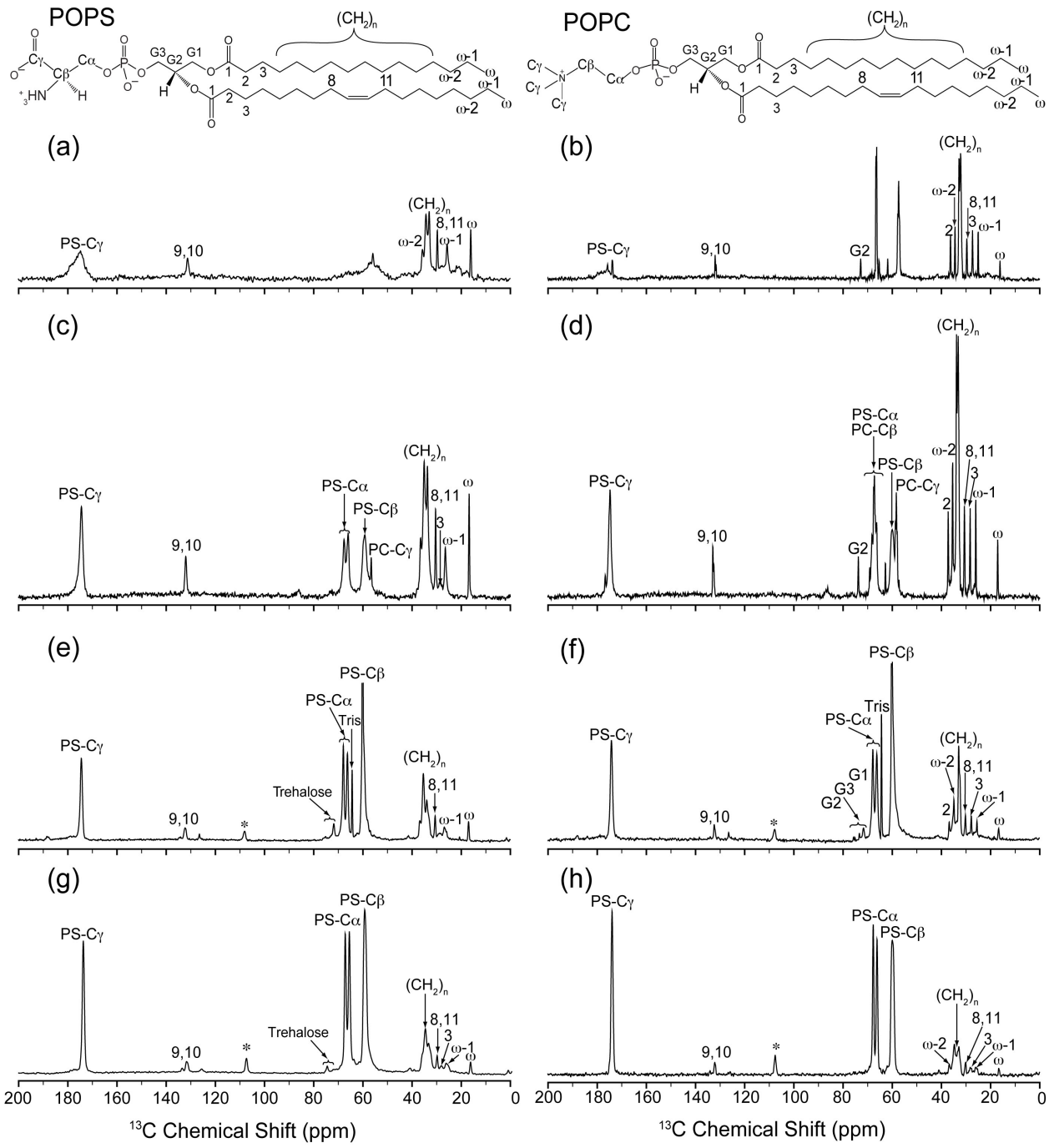

Figure 2.1 Effect of Ca^{2+} and temperature on cross-polarized 13C one-dimensional spectra of phospholipid bilayers

Spectra of 30% POPS*, 70% POPC liposomes were acquired without Ca^{2+} at (a) -20 °C or (b) 10 °C; or with 2.5 mM Ca^{2+} at (c) -20 ºC or (d) 10 ºC. Spectra of Nanodiscs were all acquired with 2 mM Ca^{2+}, using 30% POPS*, 70% POPC Nanodiscs at (e) -20 ºC or (f) 10 ºC; or 70% POPS*, 30% POPC Nanodiscs at (g) -20 ºC or (h) 10 ºC, Spectra (a)-(d) were acquired with an MAS rate of 11.111 kHz on a 500 MHz (^{1}H frequency) spectrometer. Spectra (e)-(h) were acquired with an MAS rate of 10.000 kHz on a 600 MHz (^{1}H frequency) spectrometer; asterisks indicate a carrier frequency artifact at ~108 ppm. All spectra were zero filled to twice the original data size and line broadened 0.2 ppm.

We propose that the carbon chemical shifts of the PS headgroup are the result of two distinct chemical environments in the presence of Ca^{2+} that are long-lived on NMR time scales (>10 ms). This hypothesis is compatible with earlier studies[21, 22] showing that PS headgroups, in mixed bilayers, adopt a rigid conformation in the presence of Ca^{2+}. To test whether this rigidity is sufficient to maintain near rigid-lattice behavior of the lipid headgroup above the phase transition, we also performed experiments with Ca^{2+}-treated liposomes at 10 °C (Figure 2.2.1d). Under this condition, the POPS*:POPC liposomes exhibited the same splitting of the POPS* Cα, and broadening of the POPS* Cβ and Cγ resonances, as in spectra acquired at -20 °C (Figure 2.2.1c). Again, these results agree with the results reported by Roux *et al*., where the conformational changes were observed with Ca^{2+} and membrane mimetics in solution NMR experiments at 25 °C, well above the phase transition.[22]

We also investigated the effect of Ca^{2+} on PS headgroups using POPS*:POPC Nanodiscs in the presence of 2 mM Ca^{2+}, containing either 30% POPS* (Figure 2.2.1e, f) or 70% POPS* (Figure 2.2.1g, h), both above (-20 °C, Figure 2.2.1f, h) and below (-10 °C Figure 2.2.1e, g) the phase transition. One-dimensional ^{13}C spectra are consistent with the spectra of similarly treated liposomes shown in Figure 2.2.1a-d, with identical chemical shifts observed for the POPS* headgroup carbons. These data show that the same Ca^{2+}-induced PS conformations are present in both liposomes and nanoscale bilayers over a broad range of PS concentrations.

2.5.2 Ca^{2+}-PS Interactions Alter the Phase Transition and Dynamics of Lipids within the Bilayer

A first experimental investigation of Ca^{2+}-induced PS microdomain dynamics was performed by examining the change in the apparent phase transition of the mixed POPS:POPC Nanodisc bilayers in the presence of Ca^{2+}. ^{1}H transverse relaxation (T_2) values of directly

detected ^{1}H spectra over a ±20 °C temperature range reveal acyl chain dynamics as a function of temperature (Figure 2.2a). We confirmed the expected ~3 °C phase transition of pure POPC Nanodisc bilayers observed in previous differential scanning calorimetry measurements.[54] Dynamics measurements on mixed lipid POPS*:POPC Nanodiscs with 2 mM Ca^{2+} (Figure 2.2a) display a broadened (spanning about a 30 °C range) and slightly elevated phase transition in comparison to POPC Nanodisc. This effect has been reported previously using other membrane mimetics[28, 55, 56] and is attributed to the Ca^{2+}-PS coordination.

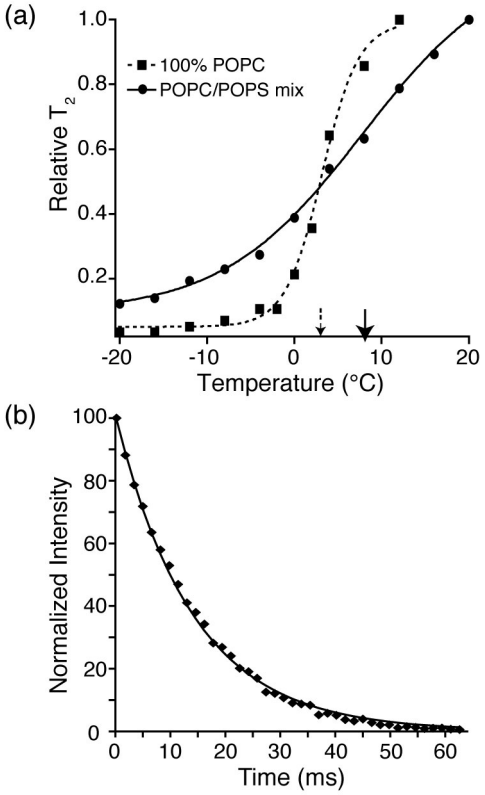

Figure 2.2 Lipid phase transition and mobility in Nanodisc
(a) Normalized ^{1}H T_2 values of the bulk fatty acyl CH_2 peaks of nanobilayers, as a function of temperature. Nanodiscs were composed of either 100% POPC (squares, dashed lines) or 30% POPS*, 70% POPC (circles, solid lines) with 2 mM Ca^{2+}. Transition temperatures were determined using acyl chain signals, with ^{1}H T_2 values used to fit the inflection point of the curve as a function of temperature. The solid arrow denotes the phase transition for 30% POPS*, 70% POPC Nanodiscs (~8 °C), while the dashed arrow denotes the phase transition for 100% POPC Nanodiscs (~3 °C). (b) ^{1}H Hahn echo was used to investigate the T_2 of the methylene protons (8 and 11; Figure 2.2.1) neighboring the olefinic bond at 25

°C. Plotted is the intensity of the methylene proton peak as a function of the echo time. A single exponential decay curve was fitted (using Spinsight 3.0); a bi-exponential fit did not yield statistically significant improvement (F test). The T_2 was determined to be 14 ms.

A control study was performed on the POPC Nanodisc bilayer to investigate the lateral diffusion and mobility of lipids inside the Nanodiscs and to identify any possible interactions between the lipid acyl chains and the MSP protein that might distort the phase transition (i.e., to identify whether a perturbed boundary layer of lipids exists in Nanodiscs). The ^{1}H T_2 (at 25°C) of the methylene protons neighboring the olefinic bond (carbon positions 8 and 11 in Figure 2.2.1), unique to the lipid acyl chain, were measured to prevent spurious contributions from MSP protons (Figure 2.2b). A single exponential fit best described the decay behavior (Figure 2.2b), indicating that all the lipids are fully mobile within the Nanodisc and diffuse freely on NMR time scales. Thus, any interactions between lipids and the membrane scaffold protein occur in the rapid exchange regime and therefore have only negligible effects on the phase transition.

To further understand the dynamics of Ca^{2+} on the POPS*:POPC bilayers, a more detailed, site-specific investigation of the bilayer dynamics was performed. Site-specific dynamics measurements using SSNMR recoupling methods were performed for POPS*:POPC Nanodisc bilayers utilizing the symmetry-based sequence $R18_1^7$ (57), which reports on ^{1}H-^{13}C dipolar couplings. The $R18_1^7$ sequence recouples the ^{1}H-^{13}C-dipolar interactions, and signal intensity measured as a function of time reports on the dynamics of the system. Observed here are the ^{1}H-Cα (Figure 2.3a) and ^{1}H-Cβ (Figure 2.3b) dephasing curves due to ^{1}H-^{13}C-dipolar interactions of the POPS* headgroup at varying temperatures. The bulk acyl chain trajectory (Figure 2.3c) shows that at -30 °C, the ^{13}C signal dephases to 30% of its original intensity within 180 microseconds and at -5 °C this happens within 190 microseconds, but at +5 °C the dephasing requires 220 microseconds and at +20 °C, 240 microseconds. In contrast, the headgroup ^{13}C

signal (Figure 2.3a, b) dephases to 30% of its original intensity within 100 microseconds, which is in the rigid lattice regime where the order parameter is ~0.9 or higher (depending on normalization of the ^{1}H-^{13}C bond length), independent of temperature. The order parameter for the acyl chain is approximately 0.5 at +20 °C. Thus, the serine headgroups have very little change in order parameter over a temperature range of -30 to +20 °C in the presence of Ca^{2+} ions (Figure 2.3). In contrast, the acyl chains' motions are activated over the same temperature range, becoming approximately twice as mobile as the temperature is increased. This result is consistent with the model in which the POPS lipids form microdomains when the headgroups are restrained in position by the presence of Ca^{2+} ions (likely also restraining lateral diffusion), while the acyl chains have fewer restrictions to motional modes such as axial diffusion and trans-gauche isomerization.

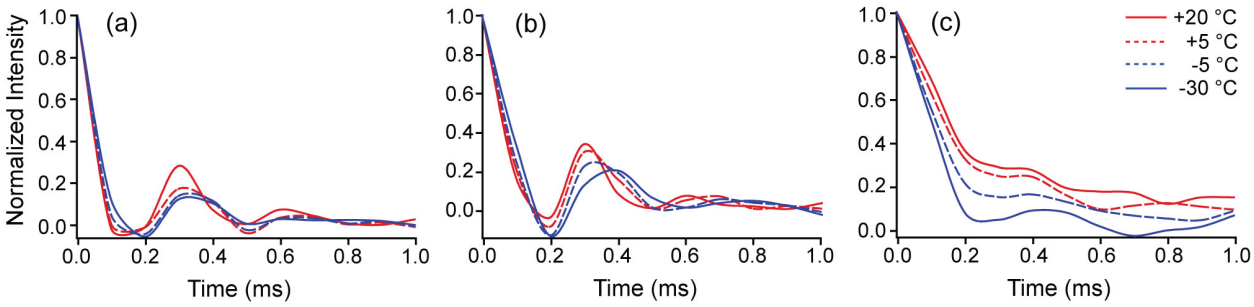

Figure 2.3 POPS dynamics
Dipolar dephasing trajectories of phospholipid headgroups and acyl chains in 30% POPS*, 70% POPC Nanodiscs with 2 mM Ca^{2+}. ^{1}H-^{13}C dipolar trajectories (plotted as normalized intensities) are presented at the indicated temperatures for (a) the Cα (CH_2) of the serine headgroup, (b) the Cβ (CH) of the serine headgroup, and (c) the bulk CH_2 (same resonance used in Figure 2.2b) of fatty acyl chains. The ^{1}H-^{13}C dipolar interaction was recoupled using $R18_1^7$ in a constant time manner. The PS headgroup maintains an order parameter near the rigid lattice limit (S = ~0.9), while the acyl chain motion is substantially activated (S = ~0.6 to 0.9) over the range from -30 °C to +20 °C.

2.5.3 Ca^{2+}-PS Interactions Observed in All-Atom Simulations.

To gain further insight into the ordering of the PS-containing membranes, we have investigated the effect of the counterion on PS headgroups by all-atom MD simulations. Pure DOPS membrane patches were prepared with either Ca^{2+} or Na^{+} as counterion and simulated each for 100 ns. Structural comparison of the two systems clearly indicates Ca^{2+}-induced organization of the PS headgroups, as demonstrated by the decrease in fluctuation of the phosphate and carboxyl groups of the lipids illustrated in Figure 2.4. Distinct patterns of Ca^{2+} and PS headgroups are evident (Figure 2.4, top right panel) indicating lateral organization of PS headgroups within the membrane environment in the presence of Ca^{2+} ions, an effect that is smaller in the Na^{+} system and in line with the fact that residence times for cation-lipid interactions are shorter for Na^{+} compared to Ca^{2+}. Even though the time scale of the simulations is shorter than the time scales that fully capture the conformational dynamics measured in the NMR measurements, structural analysis of the results can shed light on the putative conformations that might represent the two PS populations detected in the NMR measurements (which we term PS1 and PS2). In the simulations, two major conformational populations are observed for the lipid headgroups, with regard to the O-Ca-Cb-N dihedral angle. These populations are the two gauche conformations of the serine headgroup, with average dihedral angles of around -60 and 60 degrees respectively; these dihedral angels correspond to P-Cγ distances centered around ~4.5 Å and ~5.1 Å, which are the distances derived for PS1 and PS2 from the NMR measurements. A snapshot showing a PS1 and a PS2 joined by a common Ca^{2+} ion is shown as an inset in Figure 2.7. The Ca^{2+} counterions themselves are also significantly immobilized (average RMSF, 3.45 ± 1.10 Å) by interacting with the phosphate and carboxyl groups, whereas Na^{+} moves rather rapidly from one headgroup to another on the order of a few

nanoseconds, thus traveling a long range on the membrane patch within the time scale of the simulation (average RMSF, 12.41 ± 3.51 Å).

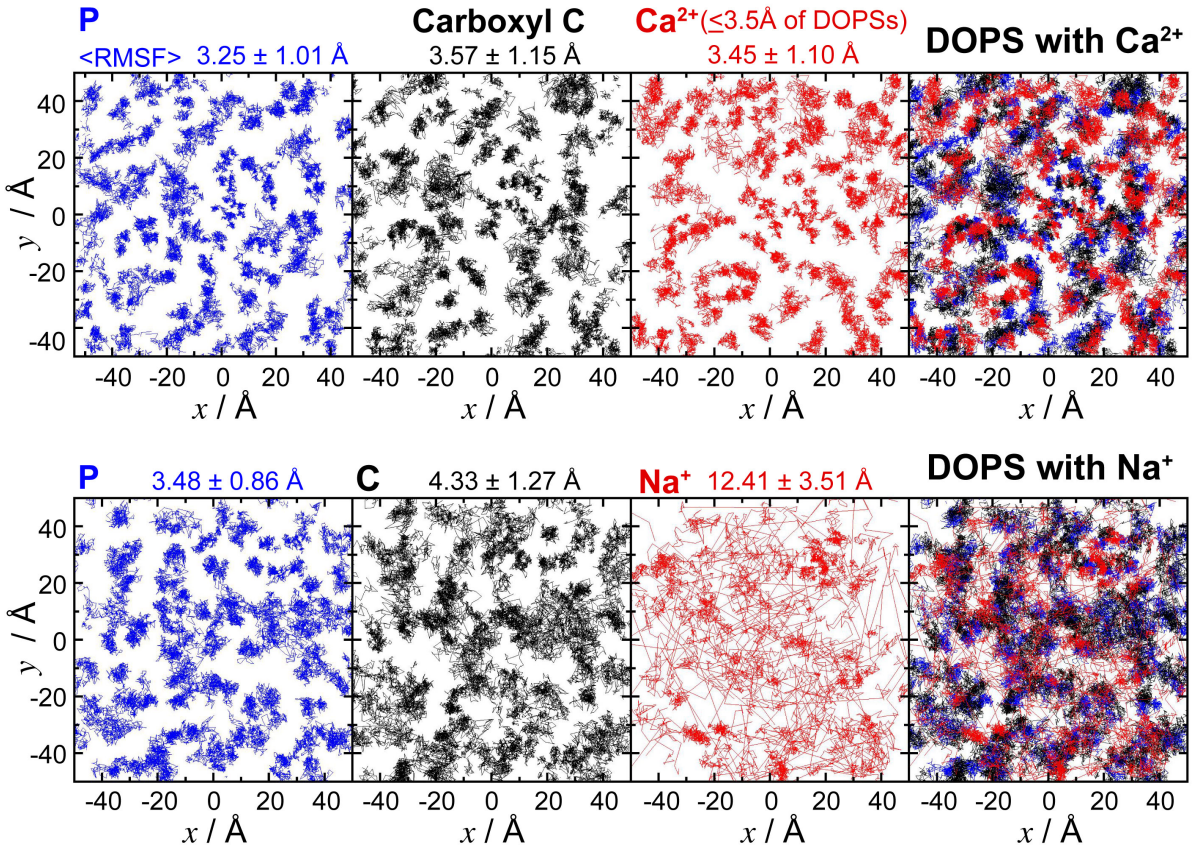

Figure 2.4 MD Simulations of DOPS membranes
Structure and dynamics of lipid molecules. Top view of one of the leaflets of the DOPS membranes simulated with either Ca^{2+} (top panel) or Na^{+} (bottom panel) as counterion. The left-most panels show the trajectories of phosphorus atoms of the phosphate groups in blue lines, using positions taken every 0.2 ns from the last 90 ns of the 100 ns simulations. Using the same snapshots, in the second panels the trajectories of the carboxyl carbons are shown in black, and in the third panels the trajectories of the counterions within 3.5 Å of DOPS lipids are depicted in red. The right-most panels show the overlap of the three sets of trajectories. The average root-mean-square fluctuations (RMSFs) of the atoms used in each panel are also shown. Due to the large number of frames included in the analysis and in order to avoid overcrowding that would mask the differences between the two systems, in each case, only half of the lipids (72 out of 144) were randomly selected for the analysis of phosphorus and carboxyl carbon atoms.

2.5.4 Two-Dimensional Spectra of POPS:POPC Nanodiscs.*

Using a series of two-dimensional spectra (Figure 2.5) acquired on 70% POPS*, 30% POPC Nanodiscs in the presence of 2 mM Ca^{2+}, we site-specifically assigned the chemical shifts of the two PS headgroup conformations and report on their intra- and intermolecular correlations. We acquired ^{13}C-^{13}C, ^{15}N-^{13}C, and ^{31}P-^{13}C two-dimensional spectra (Figure 2.5) and assigned the chemical shifts for both PS spin systems (Table 2.1) for all carbon, nitrogen and phosphorus atoms. We arbitrarily refer to the two spin systems PS1 and PS2 (Table 1). The ^{13}C-^{13}C two-dimensional spectra were acquired with 25 and 200 ms of DARR mixing (*58, 59*) (Figure 2.5a, b). The carbon signals arising from the naturally abundant ^{13}C on the acyl chains are observed along the diagonal below 40 ppm; as expected, no cross peaks observed in this region. ^{13}C-^{13}C spectra with 25 ms DARR mixing (Figure 2.5a) show intramolecular Cα-Cβ cross peaks of both PS1 and PS2. The ratio of integrated intensities of the PS1:PS2 intramolecular Cα-Cβ cross peaks is 50:50, indicating that the PS is divided approximately equally between the two conformations. Additionally, intramolecular Cα-Cγ and Cβ-Cγ correlations are observed for both conformations. Similar intramolecular correlations are observed between both ^{15}N and ^{31}P of the two PS conformations and the three carbon resonances (Cα, Cβ, Cγ) in the ^{15}N-^{13}C and ^{31}P-^{13}C two-dimensional TEDOR[60] spectra (Figure 2.5c, d).

Table 2.1 Carbon, nitrogen and phosphorus chemical shift values for PS headgroups bound to Ca^{2+} in mixed POPS:POPC bilayers. [a]

Chemical Shift Values (ppm)					
	Cα	Cβ	Cγ	N	P
PS1	67.9	60.2	174.4	41.8	-6.3
PS2	66.3	59.6	174.2	38.4	-7.4

[a]The chemical shift values were assigned using the spectra in Figure 2.5.

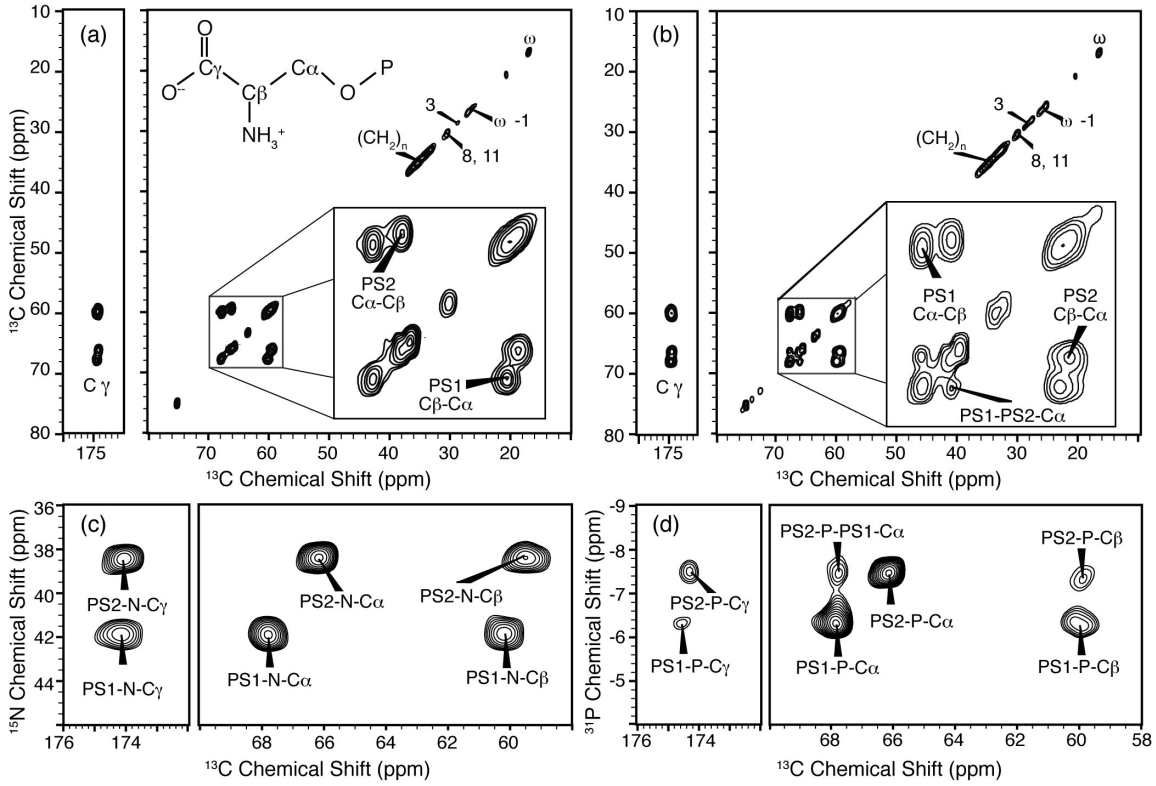

Figure 2.5 ^{13}C-^{13}C, ^{15}N-^{13}C, ^{31}P-^{13}C Correlation spectra fo 70% POPS* 30% POPC Nanodisc
Ca^{2+} induces two conformations of PS headgroups as evidenced by two-dimensional SSNMR.
Spectra were acquired of 70% POPS*, 30% POPC Nanodiscs with 2 mM Ca^{2+} using an MAS rate of 10 kHz on a 600 MHz (^{1}H frequency) spectrometer: ^{13}C-^{13}C two-dimensional DARR spectra with (a) 25 ms DARR mixing acquired at -30 °C and (b) with 200 ms DARR mixing acquired at 5 °C. Insets in panels a and b are expansions of Cα-Cβ regions. The phosphorus and nitrogen chemical shifts of the two Ca^{2+}-induced conformers are also well resolved as shown in expansions of the serine Cα-Cβ and Cγ regions of (c) ^{15}N-^{13}C TEDOR spectrum with 6.4 ms REDOR mixing acquired at -10 °C and (d) ^{31}P-^{13}C TEDOR spectrum with 2.4 ms of REDOR mixing acquired at -20 °C. All spectra were zero filled to twice the original data size. The ^{13}C-^{13}C two-dimensional spectra were line broadened 0.2 ppm in each dimension. The ^{31}P-^{13}C and ^{15}N-^{13}C spectra were line broadened 0.4 ppm in the carbon dimension and 0.25 ppm in the ^{31}P and/or ^{15}N dimensions.

Intra- and intermolecular correlations in the two-dimensional spectra reveal structural insights of individual PS headgroups and on the lateral organization of the two conformations, respectively. TEDOR (heteronuclear),[60] DARR (homonuclear, ^{13}C-^{13}C),[58, 59] and ^{1}H diffusion (CHHC) (homonuclear, ^{1}H-^{1}H)[61, 62] pulse sequences take advantage of strong dipolar interactions present in SSNMR. The dipolar interaction is a through-space interaction and therefore inherently contains information on distance ($\propto 1/r^3$) that is reflected in the intensity of the cross

peaks as a function of mixing time. Using the ^{1}H-^{1}H, ^{13}C-^{13}C, and ^{13}C-^{31}P dipolar interactions, distances up to ~6 Å can be measured between atoms. The ^{31}P-^{13}C TEDOR spectrum (Figure 2.5d) exhibits P-Cγ and P-Cβ intramolecular cross peaks with differing intensities for the PS1 and PS2 conformations.

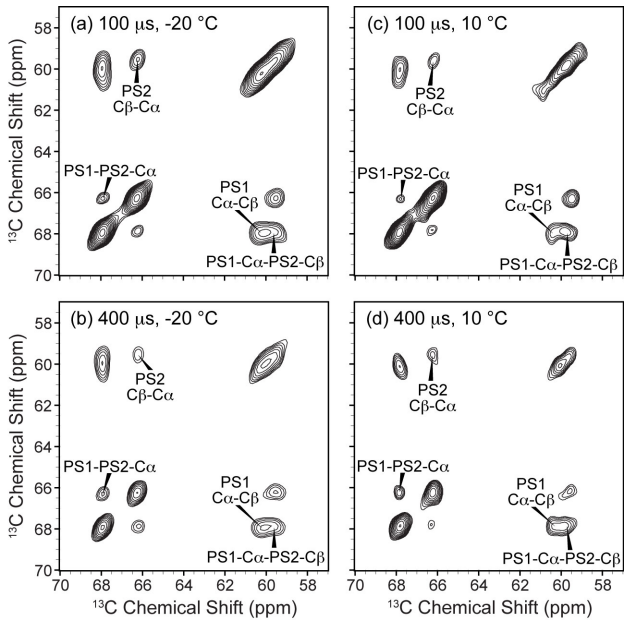

Figure 2.6 (^{1}H)-^{13}C-(^{1}H-^{1}H)-^{13}C Spectra above and below phase transition rule out chemical exchange on the NMR timescale
Close intermolecular ^{13}C-^{13}C spacing between the two configurations of the PS headgroup, demonstrated by intermolecular cross-peaks in CHHC two-dimensional correlation spectra of 70% POPS* 30% POPC Nanodisc prepared with 2 mM Ca^{2+}. Gel phase spectra (left) were acquired at -20 °C and liquid crystal phase spectra (right) were acquired at 10 °C with (a, c) 100 μs and (b, d) 400 μs of ^{1}H-^{1}H mixing. All spectra were acquired with an MAS rate of 10 kHz on a 600 MHz (^{1}H frequency) spectrometer, and processed with 0.3 ppm of line broadening in each dimension.

Finally, using ^{13}C-^{13}C DARR spectrum with 200 ms mixing (Figure 2.5b), and CHHC spectra with 100 and 400 μs mixing (Figure 2.6) we show direct evidence of Ca^{2+}-induced PS lateral organization. Both types of 2D ^{13}C-^{13}C spectra show cross peaks between the Cα of PS1 and the Cα of PS2. These experiments both support the semi-quantitative restraint on the intermolecular ^{13}C-^{13}C distance of less than 6 Å, based on previous studies that have calibrated these methods.[61, 62] The fact that such correlations are observed in the CHHC experiment at less

than 1 ms mixing time furthermore illustrates that chemical exchange could not account for the observed cross peaks, since rates of exchange on this timescale would lead to substantial line broadening in the NMR spectra. To provide a compelling quantitative measurement of the intermolecular arrangements, we collected a trajectory of mixing times from the 3D ZF-TEDOR experiment,[63] utilizing ^{31}P and ^{15}N, for which the complication of homonuclear scalar and dipolar couplings is minimized. The intermolecular ^{31}P-^{15}N distance fits to 6.1 Å (Figure 2.7). Altogether, the multiple observations of intermolecular cross peaks and dipolar coupling confirm a tight packing of the PS headgroups in the presence of Ca^{2+} ions, and give insight into the geometric arrangement of the PS conformations.

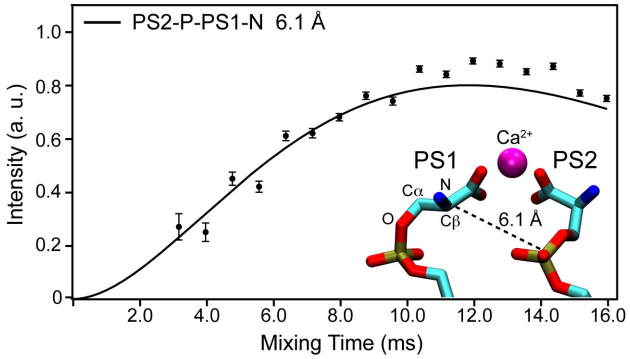

Figure 2.7 ^{31}P-^{15}N ZF-TEDOR PS2-P-PS1N Trajectory
Three-dimensional ZF TEDOR trajectories of the cross-peak observed for the ^{31}P of the PS2 and the ^{15}N of the PS1 headgroup spin systems with a T_2 of 7.0 ms. To derive distance values, experimental buildup curves were fitted using a nonlinear least-squares optimization of the analytical expression described by equations 10 & 11 in Jaroniec et al. (*63*). Also shown as an insert is a snapshot taken from the MD simulations depicting an example of a PS1 and a PS2 headgroup interacting with the same Ca^{2+} ion. The O-Ca-Cb-N dihedral angle and the Cg-P distance are -71.2° and 4.82 Å in PS1 (left), and 52.4° and 4.17 Å in PS2 (right). The distance between PS1-N and PS2-P in this snapshot is 6.05 Å.

2.6 Discussion

Ca^{2+} is thought to induce the formation of PS microdomains in mixed lipid bilayers and has previously been shown to induce rigid PS headgroup conformations (*21, 22*). The interaction of

PS with Ca^{2+} has also been shown to affect the bulk properties of the bilayer and indicate the formation of larger PS microdomains. However, observations of the phenomena have not resolved the scale of the PS assemblies formed with Ca^{2+} (in particular), nor have key features of the molecular structure of such assemblies been reported. Our observations using POPS*-enriched liposomes and Nanodiscs now demonstrate the formation of two distinct, rigid PS headgroup conformations induced upon interaction with Ca^{2+}, that are within ~6 Å of each other. We also report the site-specific assignments of headgroup nitrogen, carbon and phosphorus resonances for the two PS headgroup conformations, PS1 and PS2 (Table 1) and give preliminary distance measurements that report on their structure. Previously, Sanson *et al*. reported two headgroup conformers solved at pH 7.5 for the PS headgroup of 1,2-dimyristoyl-phosphatidylserine (DMPS) in dodecylphosphocholine (DPC) micelles (*23*). That report (*23*) focused on the conformation of the glycerol backbone of the lipids and no angular or distance data were specifically reported for the serine headgroups. This makes comparing our preliminary distance data with previous structures difficult, so we cannot exclude or confirm the existence of those structures in the Ca^{2+}-induced PS domains. Significantly, we observe a major change (reduction) in the dynamics of the conformations in the presence of Ca^{2+}. PS conformers in the presence of Na^{+} are in fast chemical exchange, sampling many conformations over the NMR chemical shift timescale (*23, 64*). Therefore, this fast exchange among conformations in the absence of Ca^{2+} results in only one chemical shift value for each of the three carbons (Cα, Cβ, Cγ) above the phase transition temperature and broad signals below it (Figure 2.2.1). Addition of Ca^{2+} to the system coordinates PS into two distinct conformations, changing the dynamics of the system, so that PS1 and PS2 are long-lived on the NMR timescale.

In addition to the change in headgroup dynamics, the results show a marked change in the bulk dynamics of the bilayer. The dynamics measurements using the Nanodisc system demonstrate that Ca^{2+} interactions observed with mixed POPS:POPC bilayers are consistent with previous studies using liposomes.[21, 22, 28, 65] Site-specific dynamics data (Figure 2.2.3) indicate that interactions of Ca^{2+} with mixed POPS:POPC bilayers cause the PS headgroups to become highly ordered, while the acyl chains are only slightly affected by this ordering. This observation has been made previously and indicates that in the presence of Ca^{2+}, the PS headgroups do not dominate the properties of the hydrophobic tails in the liquid-crystalline state.[65] This explains the increase in the liquid-crystalline to solid-gel phase transition temperature of these mixed bilayers presented here (Figure 2.2.2a) and observed by others.[28, 55, 56] The restricted motion of the headgroups translates minimally to the carbons on the acyl chains near the glycerol backbone, causing a slight increase and broadening in the transition temperature. This is what we would expect in the model where headgroups in PS microdomains are locked in position by the coordination of Ca^{2+}, while the acyl chains experience only slight restrictions on their motion. We propose that Ca^{2+} induces a more ordered liquid crystal phase in which there is increased order in the PS headgroups, while the acyl chains remain disordered as in a liquid phase. We picture this as a microdomain of PS in which diffusion of PS molecules within the microdomain is likely, and the microdomain, as a whole unit, is free to diffuse laterally in the bilayer. This is characterized in MD simulations presented in Figure 2.4 and is consistent with the dynamics data, including the increase and broadening of the liquid-crystalline to solid-gel phase transition temperature.

The intermolecular cross-peaks observed in homonuclear and heteronuclear correlation experiments (Figures 5 and 6) directly confirm a spatial reorganization of the PS headgroups.

The <6 Å distance between Cα carbons and 6.1 Å distance between the ^{31}P of PS2 and ^{15}N of PS1 are in good agreement with the two major conformational populations observed in the MD simulations. We propose that the two conformations of the PS headgroup are arranged in a two-fold symmetry around a shared Ca^{2+} coordination center (Figure 2.7). This model is also consistent with binding data and previously reported MD simulations showing a 2:1 ratio of PS:Ca^{2+} (*10, 30, 66*), although the exact stoichiometry of the coordination center is yet to be determined.

In conclusion, we have demonstrated that Ca^{2+} interacts with PS in membrane bilayers to form more ordered PS microdomains. The interaction induces a symmetric organization of the PS in the lipid bilayer, which is free to diffuse laterally through the bilayer. By studying these microscopic and transient islands of a specific PS lipid, we will be able to better understand the membrane's contribution to processes such as cell signaling and blood coagulation (*14, 15*). Specifically, we will be able to determine the conformations of the PS headgroups in Ca^{2+}-bound microdomains that may be encountered by PS-specific membrane binding proteins. Our current work is focused on completing the analysis of distance and angular restraints to use in calculations of an atomically resolved structure of the PS microdomains in membrane bilayers.

2.7 References

1. Gordesky, S. E., and Marinetti, G. V. The asymetric arrangement of phospholipids in the human erythrocyte membrane, *Biochem. Biophys. Res. Commun.* **50**, 1027-1031 (1973).

2. Buckland, A. G., and Wilton, D. C. Anionic phospholipids, interfacial binding and the regulation of cell functions, *Biochim. Biophys. Acta* **1483**, 199-216 (2000).

3. Leventis, P. A., and Grinstein, S. (2010) The distribution and function of phosphatidylserine in cellular membranes, *Annu. Rev. Biophys.* **39**, 407-427.

4. McLaughlin, S., and Murray, D. Plasma membrane phosphoinositide organization by protein electrostatics, *Nature* **438**, 605-611 (2005).

5. Yeung, T., Gilbert, G. E., Shi, J., Silvius, J., Kapus, A., and Grinstein, S. Membrane phosphatidylserine regulates surface charge and protein localization, *Science* **319**, 210-213 (2008).

6. Lemmon, M. A. Membrane recognition by phospholipid-binding domains, *Nat. Rev. Mol. Cell. Biol.* **9**, 99-111 (2008).

7. Fadok, V. A., Voelker, D. R., Campbell, P. A., Cohen, J. J., Bratton, D. L., and Henson, P. M. Exposure of phosphatidylserine on the surface of apoptotic lymphocytes triggers specific recognition and removal by macrophages, *J. Immunol.* **148**, 2207-2216 (1992).

8. Zwaal, R. F., Comfurius, P., and Bevers, E. M. Surface exposure of phosphatidylserine in pathological cells, *Cell. Mol. Life Sci.* **62**, 971-988 (2005).

9. Duzgunes, N., Nir, S., Wilschut, J., Bentz, J., Newton, C., Portis, A., and Papahadjopoulos, D. Calcium- and magnesium-induced fusion of mixed phosphatidylserine/phosphatidylcholine vesicles: effect of ion binding, *J. Membr. Biol.* **59**, 115-125 (1981).

10. Feigenson, G. W. On the Nature of Calcium-Ion Binding between Phosphatidylserine Lamellae, *Biochemistry* **25**, 5819-5825 (1986).

11. Leckband, D. E., Helm, C. A., and Israelachvili, J. Role of calcium in the adhesion and fusion of bilayers, *Biochemistry* **32**, 1127-1140 (1993).

12. Ito, T., and Ohnishi, S. I. Ca^{2+}-Induced Lateral Phase Separations in Phosphatic Acid-Phosphatidylcholine Membranes, *Biochim. Biophys. Acta* **352**, 29-37 (1974).

13. Berridge, M. J., and Irvine, R. F. Inositol trisphosphate, a novel second messenger in cellular signal transduction, *Nature 312*, 315-321 (1984).

14. Maxfield, F. R. Plasma membrane microdomains, *Curr. Opin. Cell Biol.* **14**, 483-487 (2002).

15. Laude, A. J., and Prior, I. A. Plasma membrane microdomains: organization, function and trafficking, *Mol. Membr. Biol.* **21**, 193-205 (2004).

16. Menke, M., Gerke, V., and Steinem, C. Phosphatidylserine membrane domain clustering induced by annexin A2/S100A10 heterotetramer, *Biochemistry* **44**, 15296-15303 (2005).

17. Schultz, Z. D., Pazos, I. M., McNeil-Watson, F. K., Lewis, E. N., and Levin, I. W. Magnesium-induced lipid bilayer microdomain reorganizations: implications for membrane fusion, *J. Phys. Chem. B* **113**, 9932-9941 (2009).

18. Gokhale, N. A., Abraham, A., Digman, M. A., Gratton, E., and Cho, W. Phosphoinositide specificity of and mechanism of lipid domain formation by annexin A2-p11 heterotetramer, *J. Biol. Chem.* **280**, 42831-42840 (2005).

19. Eklund, K. K., Vuorinen, J., Mikkola, J., Virtanen, J. A. & Kinnunen, P. K. Ca^{2+}-induced lateral phase separation in phosphatidic acid/phosphatidylcholine monolayers as revealed by fluorescence microscopy. *Biochemistry* **27**, 3433-3437 (1988).

20. Levental, I., Christian, D. A., Wang, Y. H., Madara, J. J., Discher, D. E., and Janmey, P. A. Calcium-dependent lateral organization in phosphatidylinositol 4,5-bisphosphate (PIP2)- and cholesterol-containing monolayers, *Biochemistry* **48**, 8241-8248 (2009).

21. Roux, M., and Bloom, M. Ca^{2+}, Mg^{2+}, Li^{+}, Na^{+}, and K^{+} distributions in the headgroup region of binary membranes of phosphatidylcholine and phosphatidylserine as seen by deuterium NMR, *Biochemistry* **29**, 7077-7089 (1990).

22. Roux, M., and Bloom, M. Calcium-binding by phosphatidylserine headgroups - Deuterium NMR study, *Biophys. J.* **60**, 38-44 (1991).

23. Sanson, A., Monck, M. A., and Neumann, J. M. 2D H-1-NMR conformational study of phosphatidylserine diluted in perdeuterated dodecylphosphocholine micelles - Evidence for a pH-Induced conformational transition, *Biochemistry* **34**, 5938-5944 (1995).

24. Frazier, A. A., Roller, C. R., Havelka, J. J., Hinderliter, A., and Cafiso, D. S. Membrane-bound orientation and position of the synaptotagmin I C2A domain by site-directed spin labeling, *Biochemistry* **42**, 96-105 (2003).

25. Rufener, E., Frazier, A. A., Wieser, C. M., Hinderliter, A., and Cafiso, D. S. Membrane-bound orientation and position of the synaptotagmin C2B domain determined by site-directed spin labeling, *Biochemistry* **44**, 18-28 (2005).

26. Verdaguer, N., Corbalan-Garcia, S., Ochoa, W. F., Fita, I., and Gomez-Fernandez, J. C. Ca^{2+} bridges the C2 membrane-binding domain of protein kinase Ca directly to phosphatidylserine, *EMBO J.* **18**, 6329-6338 (1999).

27. Ohkubo, Y. Z., and Tajkhorshid, E. Distinct structural and adhesive roles of Ca^{2+} in membrane binding of blood coagulation factors, *Structure* **16**, 72-81 (2008).

28. Sinn, C. G., Antonietti, M., and Dimova, R. Binding of calcium to phosphatidylcholine-phosphatidylserine membranes, *Colloid Surface A* **282**, 410-419 (2006).

29. Pedersen, U. R., Leidy, C., Westh, P., and Peters, G. H. The effect of calcium on the properties of charged phospholipid bilayers, *Biochim. Biophys. Acta* **1758**, 573-582 (2006).

30. Vernier, P. T., Ziegler, M. J., and Dimova, R. Calcium Binding and Head Group Dipole Angle in Phosphatidylserine-Phosphatidylcholine Bilayers, *Langmuir* **25**, 1020-1027 (2009).

31. Bayburt, T. H., and Sligar, S. G. Self-assembly of single integral membrane proteins into soluble nanoscale phospholipid bilayers, *Protein Sci*. **12**, 2476-2481 (2003).

32. Bayburt, T. H., and Sligar, S. G. Single-molecule height measurements on microsomal cytochrome P450 in nanometer-scale phospholipid bilayer disks, *Proc. Natl. Acad. Sci. U. S. A*. **99**, 6725-6730 (2002).

33. Bayburt, T. H., Grinkova, Y. V., and Sligar, S. G. Self-assembly of discoidal phospholipid bilayer nanoparticles with membrane scaffold proteins, *Nano Lett*. **2**, 853-856 (2002).

34. Bayburt, T. H., Carlson, J. W., and Sligar, S. G. Single molecule height measurements on a membrane protein in nanometer-scale phospholipid bilayer disks, *Langmuir* **16**, 5993-5997 (2000).

35. Morrissey, J. H., Pureza, V., Davis-Harrison, R. L., Sligar, S. G., Ohkubo, Y. Z., and Tajkhorshid, E. Blood clotting reactions on nanoscale phospholipid bilayers, *Thromb. Res*. **122** *Suppl 1*, S23-26 (2008).

36. Morrissey, J. H., Pureza, V., Davis-Harrison, R. L., Sligar, S. G., Rienstra, C. M., Kijac, A. Z., Ohkubo, Y. Z., and Tajkhorshid, E. Protein-membrane interactions: blood clotting on nanoscale bilayers, *J. Thromb. Haemost*. **7**, 169-172 (2009).

37. Li, Y., Kijac, A. Z., Sligar, S. G., and Rienstra, C. M. Structural analysis of nanoscale self-assembled discoidal lipid bilayers by solid-state NMR spectroscopy, *Biophys. J*. **91**, 3819-3828 (2006).

38. Frericks, H. L., Zhou, D. H., Yap, L. L., Gennis, R. B., and Rienstra, C. M. Magic-angle spinning solid-state NMR of a 144 kDa membrane protein complex: E-coli cytochrome bo_3 oxidase, *J. Biomol. NMR* **36**, 55-71 (2006).

39. Kijac, A. Z., Li, Y., Sligar, S. G., and Rienstra, C. M. Magic-Angle Spinning Solid-State NMR Spectroscopy of Nanodisc-Embedded Human CYP3A4, *Biochemistry* **46**, 13696-13703 (2007).

40. Iwasaki, Y., Mizumoto, Y., Okada, T., Yamamoto, T., Tsutsumi, K., and Yamane, T. An aqueous suspension system for phospholipase D-mediated synthesis of PS without toxic organic solvent, *J. Am. Oil Chem. Soc*. **80**, 653-657 (2003).

41. Comfurius, P., and Zwaal, R. F. A. Enzymatic-Synthesis of Phosphatidylserine and Purification by Cm-Cellulose Column Chromatography, *Biochim.Biophys. Acta* **488**, 36-42 (1977).

42. Van Geet, A. L. Calibration of the methanol and glycol nuclear magnetic resonance thermometers with a static thermistor probe. *Anal. Chem*. **42**, 2227 (1968).

43. Hediger, S., Meier, B. H., Kurur, N. D., Bodenhausen, G., and Ernst, R. R. NMR cross-polarization by adiabatic passage through the Hartmann-Hahn condition (APHH), *Chem. Phys. Lett.* **223**, 283-288 (1994).

44. Bennett, A. E., Rienstra, C. M., Auger, M., Lakshmi, K. V., and Griffin, R. G. Heteronuclear decoupling in rotating solids, *J. Chem. Phys.* **103**, 6951-6958 . (1995)

45. Delaglio, F., Grzesiek, S., Vuister, G. W., Zhu, G., Pfeifer, J., and Bax, A. Nmrpipe: a Multidimensional Spectral Processing System Based On Unix Pipes, *J. Biomol. NMR* **6**, 277-293 (1995).

46. Morcombe, C. R., and Zilm, K. W. Chemical shift referencing in MAS solid state NMR, *J. Magn. Reson.* **162**, 479-486 (2003).

47. Goddard, T. D., and Kneller, D. G. Sparky 3, 3.106 ed., University of California, San Francisco.

48. Phillips, J. C., Braun, R., Wang, W., Gumbart, J., Tajkhorshid, E., Villa, E., Chipot, C., Skeel, R. D., Kale, L., and Schulten, K. Scalable molecular dynamics with NAMD, *J. Comput. Chem.* **26**, 1781-1802 (2005).

49. MacKerell, A. D., Bashford, D., Bellott, Dunbrack, R. L., Evanseck, J. D., Field, M. J., Fischer, S., Gao, J., Guo, H., Ha, S., Joseph-McCarthy, D., Kuchnir, L., Kuczera, K., Lau, F. T. K., Mattos, C., Michnick, S., Ngo, T., Nguyen, D. T., Prodhom, B., Reiher, W. E., Roux, B., Schlenkrich, M., Smith, J. C., Stote, R., Straub, J., Watanabe, M., Wiorkiewicz-Kuczera, J., Yin, D., and Karplus, M. All-atom empirical potential for molecular modeling and dynamics studies of proteins, *J. Phys. Chem. B* **102**, 3586-3616 (1998).

50. Darden, T. A., York, D. M., and Pedersen, L. Particle mesh Ewald: An N.log(N) method for Ewald sums in large systems, *J. Chem. Phys.* **98**, 10089-10092 (1993).

51. Petrache, H. I., Tristram-Nagle, S., Gawrisch, K., Harries, D., Parsegian, V. A., and Nagle, J. F. Structure and fluctuations of charged phosphatidylserine bilayers in the absence of salt, *Biophys. J.* **86**, 1574-1586 (2004).

52. Wang, Y., Ohkubo, Y. Z., and Tajkhorshid, E. Gas conduction of lipid bilayers and membrane channels, in Current Topics in Membranes: Computational Modeling of Membrane Bilayers (Feller, S., Ed.), pp 343-367, Elsevier (2008).

53. Husted, C., Montez, B., Le, C., Moscarello, M. A., and Oldfield, E. ^{13}C Magic-angle sample-spinning nuclear-magnetic-resonance studies of human myelin, and model membrane systems, *Magnet. Reson. Med.* **29**, 168-178 (1993).

54. Denisov, I. G., McLean, M. A., Shaw, A. W., Grinkova, Y. V., and Sligar, S. G. Thermotropic phase transition in soluble nanoscale lipid bilayers, *J. Phys. Chem. B* **109**, 15580-15588 (2005).

55. Jacobson, K., and Papahadjopoulos, D. Phase-transitions and phase separations in phospholipid membranes induced by changes in temperature, pH, and concentration of bivalent-cations, *Biochemistry* **14**, 152-161 (1975).

56. Silvius, J. R., and Gagne, J. Calcium-induced fusion and lateral phase separations in phosphatidylcholine-phosphatidylserine vesicles - correlation by calorimetric and fusion measurements, *Biochemistry* **23**, 3241-3247 (1984).

57. Zhao, X., Eden, M., and Levitt, M. H. Recoupling of heteronuclear dipolar interactions in solid-state NMR using symmetry-based pulse sequences, *Chem. Phys. Lett.* **342**, 353-361 (2001).

58. Takegoshi, K., Nakamura, S., and Terao, T. C-13-H-1 dipolar-assisted rotational resonance in magic-angle spinning NMR, *Chem. Phys. Lett. 344*, 631-637 (2001).

59. Morcombe, C. R., Gaponenko, V., Byrd, R. A., and Zilm, K. W. Diluting abundant spins by isotope edited radio frequency field assisted diffusion, *J. Am. Chem. Soc. 126*, 7196-7197 (2004).

60. Hing, A., Vega, S., and Schaefer, J. Transferred-echo double-resonance NMR, *J. Magn. Reson.* **96**, 205-209 (1992).

61. Lange, A., Luca, S., and Baldus, M. Structural constraints from proton-mediated rare-spin correlation spectroscopy in rotating solids, *J. Am. Chem. Soc.* **124**, 9704-9705 (2002).

62. Lange, A., Seidel, K., Verdier, L., Luca, S., and Baldus, M. Analysis of proton-proton transfer dynamics in rotating solids and their use for 3D structure determination, *J. Am. Chem. Soc.* **125**, 12640-12648 (2003).

63. Jaroniec, C. P., Filip, C., and Griffin, R. G. 3D TEDOR NMR experiments for the simultaneous measurement of multiple carbon-nitrogen distances in uniformly C-13, N-15-labeled solids, *J. Am. Chem. Soc.* **124**, 10728-10742 (2002).

64. Hauser, H., Pascher, I., and Sundell, S. Preferred Conformation and Dynamics of the Glycerol Backbone in Phospholipids - an NMR and X-ray single-crystal analysis, *Biochemistry* **27**, 9166-9174 (1988).

65. Browning, J. L., and Seelig, J. Bilayers of phosphatidylserine - deuterium and phosphorus nuclear magnetic-resonance study, *Biochemistry* **19**, 1262-1270 (1980).

66. Mattai, J., Hauser, H., Demel, R. A., and Shipley, G. G. Interactions of metal-ions with phosphatidylserine bilayer-membranes - effect of hydrocarbon chain unsaturation, *Biochemistry* **28**, 2322-2330 (1989).

CHAPTER 3

Progress Toward Solid-State NMR Structure of Ca^{2+}-Phosphatidylserine-rich Membrane Binding Domains

3.1 Notes and Acknowledgements

This work was supported by the National Institute of General Medical Sciences, NIH (R01-GM075937 and R01-GM079530 to C.M.R., and R01-GM086749 and R01-GM067887 to E.T.), the National Center for Research Resources, NIH (P41-RR05969 to E.T.), the National Heart Lung and Blood Institute, NIH (R01 HL47014 to J.H.M. and R01 HL103999 to J.H.M. and C.M.R.), and M.C.C. is an American Heart Association Predoctoral Fellow (12PRE12050304). This work was supported by the NIH/NHLBI (R01HL103999).

3.2 Abstract

The asymmetric distribution of phospholipids between the external and cytosolic leaflets of the plasma member is one of the key regulators of membrane structure and function. Exposure of anionic phospholipids like phosphatidylserine (PS) to extracellular calcium concentration is know to induce a lateral reorganization of PS in to locally dense regions on the membrane surface, characterized by the presence to two rigid conformations of the PS headgroup that interact with each other to from a stable complex. These Ca^{2+}-PS rich regions are putative binding sites for vitamin-K dependent coagulation factors that play a critical role in the regulation of blood coagulation reactions. In this study we utilized ^{13}C-^{15}N isotopically labeled PS and magic angle spinning (MAS) solid-state nuclear magnetic resonance (SSNMR) to determine the first atomic resolution structures of Ca^{2+}-PS complexes in mixed PS/

phosphatidylcholine (PC) bilayers. These results represent a critical first step in the determination of atomic resolution phospholipid structures and subsequent improvements in realism of molecular dynamics simulations.

3.3 Introduction

The plasma membrane is one of the most important boundaries in the body. Extending upon the fluid mosaic model first proposed by Singer and Nicolson in 1972,[1] it is the complex interplay among the proteins, lipids, and counter ions that regulate the properties of the membrane. The interactions of the naturally sparse anionic phospholipids such as phosphatidylinositol (PI), phosphatidylserine (PS), phosphatidylglycerol (PG), and phosphatidic acid (PA) are of particular interest because of the role in signal transduction, vesicle fusion, apoptosis, and blood coagulation.[2-7] The sequestration of anionic lipids on the cytosolic membrane, particularly PS, is a defining characteristic of healthy normal cells.[7-9] Exposure of PS on the external leaflet in normal cells only occurs during stress related processes like blood coagulation and apoptosis,[10-12] but PS is also exposed of the surface of the majority of cancer cells.[13]

Exposure of anionic lipids to plasma concentrations of Ca^{2+} and cationic membrane binding peptides and proteins is known to induce a lateral reorganization and immobilization of the PS headgroups. The clustering/aggregation of PS and other anionic lipid induced by calcium produces regions of locally high PS content visible by fluorescence microscopy implying the formation of large Ca-PS complex.[14-16] However, surface absorption studies and molecular dynamics studies show that Ca^{2+} interacts with PS to from a 1:1 or 2:1 complex.[17-21] X-ray diffraction studies demonstrated a reduced area pre lipid and dehydration of the headgroup region upon treatment with Ca^{2+}.[17,18,22,23] The reduced area per lipid is also consistent with the

reduced mobility of the PS headgroup resulting for Ca^{2+} coordination.[24-30] Molecular dynamics simulations have shown that Ca^{2+} interacts preferentially with the serine carboxylate oxygen's and then the phosphate group in PS/ phosphatidylcholine (PC) bilayers.[23,31,32] However, there is very limited high-resolution experimental structural information for phospholipids in general, due to the dynamic nature of the phospholipid membrane.

In our pervious studies (ref. 32) we observed the formation of macroscopically well ordered PS-clusters in which PS headgroups that displayed conformational changes relative to a Ca^{2+} free bilayer. We identified two equally populated rigid conformations of the PS headgroup in studies of U-^{13}C-^{15}N-POPS/POPC Nanodiscs and liposomes. Site-specific dynamics measurements showed that the acyl chains are essentially unaffected by Ca^{2+} coordination while the PS headgroups are rigid, displaying gel phase behavior regardless of the overall phase of the bilayer. Correlation spectra confirmed that the two configurations of the PS headgroup are located within ~ 6 Å indicating a tight packing of PS. Because both configurations of the PS headgroup are essentially equally populated we were able to conclude that Ca^{2+} laterally reorganized PS into oligomeric structures with an even number of subunits.

We propose that the fundamental subunit of the PS-Ca^{2+} clusters is a $Ca(PS)_2$ dimer, which forms larger complexes by coordination of the Ca^{2+} ions to form larger complexes. This would be facilitated by one of the two configurations of the PS headgroup coordinating Ca^{2+} through both its phosphate and carboxylate groups, while the second configuration bridges the oligomeric complexes via coordination of the Ca^{2+} ions between dimer sub units. Such a complex would leave the carboxylate and or phosphate group of the second PS molecule free to interact with other binding partners. Such interactions could resulting in the propagation of the formation of larger Ca^{2+}-PS complex or interactions with proteins.

In this study phospholipid Nanodisc prepared with and isotopically labeled POPS were used to assess PS-Ca oligomerization and determine potential structures of the $Ca(PS)_2$ dimer. We utilized existing dipolar recoupling techniques measure quantitative intra and intermolecular ^{13}C-^{15}N dipolar coupling. These coupling were utilized in simulated annealing structure calculations performed using the XPLOR-NIH computational package,[33] yielding three potential structures of the $Ca(PS)_2$ dimer. These results represent a critical first step in the determination of the atomic resolution structures of phospholipid complexes.

3.4 Materials and Methods

3.4.1 Sample Preparation

Isotopically labeled POPS (1-palmitoyl-2-oleoyl-phosphatidylserine), was prepared as previously described in Boettcher *et al*.[32] using phospholipase D from *Streptomyces*[34,35] (provided by the Takano Laboratory at Tokyo University of Agriculture) to biosynthetically replaced the choline headgroup of POPC (1-palmitoyl-2-oleoyl-phosphatidylcholine, Avanti Polar Lipids, Alabaster, AL) with U-^{13}C,^{15}N-L-Serien U-^{13}C-L-Serien or , ^{15}N-L-serine, (Cambridge Isotopes Laboratories, Andover, MA) to produce U-^{13}C,^{15}N-POPS, U-^{13}C-POPS, and ^{15}N-POPS respectively.

Nanodisc Preparation.

Isotopically enriched POPS is then incorporated in POPC/POPS Nanodisc as described in Boettcher *et al*. using a low salt, 10 mM Tris-HCl pH 7.4 with 1 mM $CaCl_2$, FPLC purification buffer to minimize the amount of excess salt in sample. Samples were concentrated using an Amicon Ultra 10000 NMWL centrifugal filter (Thermo Fisher Scientific, Waltham, MA) to 4-6 mM phospholipid (15-22 μM Nanodiscs). Fura-2 fluorescence analysis[36] of concentrated Nanodisc solutions was used to determine the molar ratio of Ca^{2+} to PS, and Ca^{2+} concentration

adjusted to give a PS:Ca^{2+} mole ratio of ~2:1. The lyoprotectant, trehalose, was added in a 1:1 molar ratio to phospholipid, after which samples were frozen and lyophilized. The powders (~50% Nanodiscs by weight) were packed into 3.2 mm SSNMR rotors, after which water was added (equal to ~50% of the dry weight of packed samples) and centrifuged for 5 minutes at 10,000 rcf prior to sealing the rotor. Samples were stored at 4 °C for a minimum of 48 hours prior to use to allow for full equilibration, and then subsequently stored at -20 °C when not in use.

Liposome Preparation.

Mixtures of dried POPC and U-^{13}C-^{15}N-POPS (10 mg total) were suspended in 30 μL of 50 mM Tris-HCl pH 7.4, 100 mM NaCl, 2.5 mM $CaCl_2$ and sonicated until the solution was visually homogeneous, after which 1 mL of 2.5 mM $CaCl_2$ was added and the solution was sonicated again. Sample preparation in the absence of Ca^{2+} was identical except for the inclusion or addition of $CaCl_2$. Liposomes were collected by ultracentrifugation at 4 °C for 2.5 hours at 250,000 rcf, and the pelleted liposomes were packed into 3.2 mm SSNMR rotors.

3.4.2 SSNMR Spectroscopy

All SSNMR experiments were performed using a 600 MHz InfinityPlus spectrometer (Varian, now a subsidiary of Agilent Technologies, Inc.) equipped with a 3.2 mm T3 HXY MAS probe tuned to ^{1}H-^{31}P-^{13}C, and a 3.2 mm T3 Balun™ ^{1}H-^{13}C-^{15}N probe. Spinning was controlled via a Varian MAS controller to 10 000 ± 2-3 Hz. SPINAL-64 decoupling (~75 to 85 kHz) was used during acquisition periods. The variable temperature gas was maintained at 90±10 scfh flow, and the reported sample temperatures take into account thermocouple calibration and frictional heating due to MAS, as calibrated with ethylene glycol.[37] Data were processed with NMRPipe[38] with back linear prediction and polynomial baseline (frequency domain) correction

applied to the direct dimension, and zero filling and Lorentzian-to-Gaussian apodization applied to each dimension before Fourier transformation; additional processing parameters are located in the figure captions. Chemical shifts are referenced to adamantane, using the IUPAC standard gyromagnetic ratios to indirectly reference ^{15}N and ^{31}P spectra.[39]

^{13}C-^{15}N Band Selective Transfer Echo Double Resonance (BASE-TEDOR)

A series of 2D ^{13}C-^{15}N spectra were collected using the BASE-TEDOR pulse sequence.[40] A 1500 us Gaussian soft pulse was used to selectively recouple the Cα (67 ppm), Cβ (59 ppm), and Cγ (174 ppm) resonances, with a ~80KHz of SPINAL[41] ^{1}H decoupling during acquisition. REDOR dipolar recoupling periods utilized TPPM decoupling with a ^{1}H field strength of ~100 kHz and ^{15}N π-pulse width of ~ 15 μs, the latter set to ~ 30% of ^{1}H nutation frequency to minimize interference. 70% U-^{13}C-^{15}N-POPS and 30% POPC Nanodisc were used to measure intramolecular ^{15}N-^{13}Cα and ^{15}N-^{13}Cβ correlations as well as intermolecular ^{15}N-^{13}Cα distances. 35% U-^{13}C-POPS 35% ^{15}N-POPS and 30% POPC Nanodisc were used to measure intermolecular correlations.

SSNMR Simulations and Data Fitting

All spectra were processed using NMRpipe,[38] and peak intensities extracted using the nlinLS package, resulting in trajectories as a function of dipolar mixing time between 1.6 to 25.6 ms insteps of 1.6 ms. These trajectories were then normalized relative to the maximum observed intensity for a given ^{13}C spin system prior to fitting. SPINEVOLUTION[42] was used to simulate the spin dynamics of BASE-TEDOR with the following assumptions: (1) Each ^{13}C site is coupled to *n* ^{15}N spins that are not coupled to other ^{15}N; (2) the relative orientation of each the *n* ^{13}C-^{15}N couplings can be ignored; (3) the effects of ^{15}N chemical shift anisotropy can be ignored; (4) ^{13}C-^{13}C homonuclear and ^{1}H-^{13}C heteronuclear couplings are sufficiently averaged out by

magic angle spinning and ^{1}H decoupling; (5) perfect selectivity of soft pulse. Spin systems were a clear maximum was observed were fit using an in-house FORTRAN code that utilized MINUIT[43] minimization libraries[43] to minimize the differences between the simulated and experimental trajectories as a function of the dipolar coupling, ^{13}C T_2 relaxation, and scaling factors.

In the case of weak dipolar couplings were a clear maximum is not observed the MINUET routine could not be used. This is due to the deceased dependence on the relative relaxation rate and scaling factor, as the 'curve' is essentially a straight line resulting in a large range of values that result in a 'good fit' and obfuscating the actual value of the dipolar coupling. Therefore, the dipolar coupling was determined by direct comparison of the experimental data to simulated trajectories over a range of dipolar coupling values between 3.0 and 7.0 Å. Because the experimental trajectory is related to the simulated trajectory by:

$$S_{\exp}\left(t_{mix}\right) = \lambda e^{-\Gamma t_{mix}} S_{calc}(t_{mix})$$

where λ and Γ are the scaling and a ^{13}C R_2 relaxation rate respectively. The scaling factor and relaxation rate for each dipolar coupling were then determined by linear regress analysis of the natural log of the ratio of the experimental and theoretical trajectories as a function of mixing time.

3.4.3 XPLOR-NIH Structure Calculations

The XPLOR-NIH computation package[33] was used to perform structure calculations using the experimentally determined NOE type constraints. Structure calculations were carried out on POPS lipids truncated at the first methylene in the hydrocarbon chains, rather just PS headgroup to properly account for orienting effects of the glycerol linker and lipid packing. Given the disordered nature of the acyl chains it was not necessary to measure quantitative

distance constraints for the acyl chains. Rather it is sufficient to use constraints regarding the area per lipid, and hydrocarbon chain lengths determined by x-ray and neutron diffraction studies to constrain the hydrophobic core.[44] By accounting for the relative spacing and vertical distribution of the acyl chains between neighboring POPS monomers structure calculations can be performed in a more computationally efficient manner by considering only the individual molecules rather than a full membrane patch. This was accomplished using the plane distance potential in XPLOR-NIH to maintain vertical orientation and a weak NOE potential positioning the acyl chain methylene carbons within 1-9 Å of each other to mimicking the effects. Finally the CHARMM force filed parameters were adapted for use in the XPLOR-NIH simulated annealing calculations, using only the N-Cβ-Cα-O_1, N-Cβ-Cγ-Oγ$_1$, O_1-P-O_2-C_1, and P-O_2-C_1-C_2 dihedral angles, and improper dihedral angles to define planer double bound character, and chiral centers to prevent biasing of structure calculations.

Calculations were performed using the constraints listed in supplementary Table 3.1 as the dominant potential driving the calculation. A minimum uncertainty of ± 0.1 Å was used even when MINUIT reported smaller variations. Restraints derived from the less quantitative homonuclear correlation methods (DARR and (^{1}H)-^{13}C-(^{1}H-^{1}H)-^{13}C) were assigned a minimum uncertianty of ± 2 Å. Additional ambiguous 2.5 ± 0.5 Å constraint between the carboxylate and phosphate oxygen atoms of the PS headgroups and a Ca^{2+} ion, such that the Ca^{2+} coordinates with at least one of the carboxylate or phosphate oxygen atoms of each headgroup and then a third interaction with the carboxylate or phosphate group of either monomer. Finally, constraints were placed on the P-Cβ and P-Cγ distances so that they occupy a range between 3.0-4.0 Å and 3.5-5.5 Å respectively, consistent with analogous distances observed in crystal structure of phosphorylated amino acids and phosphorylethanolamine.[45-49] This was done to prevent the

potential overlap of the phosphate and carboxylate atoms which in the absence of these constraints where within 2.4 Å of each other.

3.5 Results

3.5.1 Phospholipid Nanodisc and PS Cluster Formation

We first identified the most effective membrane mimetic and composition to use for detailed structure studies. Traditionally liposomes are used in SSNMR studies of lipids to characterize the dynamics of the acyl chains and/or headgroup properties. As previously demonstrated in Boettcher *et al*., ([32]) calcium induces a both a lateral reorganization and rigidification of the PS headgroup resulting in two equally populated configuration of the headgroup in both Nanodisc and liposome systems (Figure 3.1). However, uncomplexed PS is still observed in POPS liposome samples (Figure 3.1a, b), the overlap of these 'free' signals with those corresponding to the Ca^{2+} bound PS hinder structural studies and could contribute the to poor spectral quality above the phase transition. The larger surface area of the liposome increases the lateral and translational diffusion of individual membrane components resulting in increased dipolar averaging hindering structural studies of the headgroup in these and pervious studies.[28,29,50,51] Finally, liposome samples must be prepared with excess sodium in addition to Ca^{2+} to prevent aggregation of PS prior to formation of the liposome. The presence of the excess sodium in the sample increases dielectric loading of the sample. The motion of free ions in pulsed field results in dielectric heating, which causes sample degradation and lose of sensitivity due to temperature gradients across the sample.[52] High power ^{1}H decoupling exacerbates this effect, but is essential to the efficient performance of dipolar based NMR experiments.[52]

The nanodiscs system offers many advantages relative to liposomes, because Nanodiscs can be prepared with specific phospholipid composition.[53-55] We can essentially reconstruct regions with

very specific composition, and the reduced surface area increases the probability of the formation of the PS-Ca^{2+} complex. This is demonstrated in ^{31}P cross-polarization spectra of natural abundance POPS/POPC Nanodisc prepared with 3, 6, 9, 12, 15, 22.5, and 30% POPS. These samples were prepared to aid in the determination of the minimum number of PS molecules required to induce cluster formation. This concentration range results in Nanodisc containing an average of 2, 4, 6, 8, 10, 14, and 18 PS molecules per leaflet. As shown in Figure 3.2a, Nanodisc containing less than 12 % POPS did not produce the signature ^{31}P chemical shifts previously assigned to PS1 (-6.3 ppm) and PS2 (-7.4 ppm). Further more the relative intensity observed in the 12 and 15% POPS Nanodisc was only ~ 50% of that expected intensity if all POPS molecules were complexed by Ca^{2+}+ (Figure 3.2b). Comparison of the relative POPS intensity to the poison distribution of lipids in the 12, 15, 22.5 and 30 % POPS Nanodisc (Figure 3.2c) indicated that between six and eight POPS molecule per leaflet are needed for observation of Ca^{2+}-PS complex. It should be noted that cross-polarization experiments were performed in lieu of the more quantitative direct polarization experiments, due to the long ^{31}P T_1 relaxation (> 60s) of the POPS phosphate groups. This is considerably longer than the average ^{31}P T_1 of 0.6 s observed for mobile POPC bilayers in the absence of divalent cations, and is consistent with the reduced mobility of the PS headgroups in the presence of Ca^{2+}.

There were no significant differences observed in the resonance frequencies or relative peak PS1/PS2 peak intensities in Nanodisc containing 12-70% POPS, therefore the structural

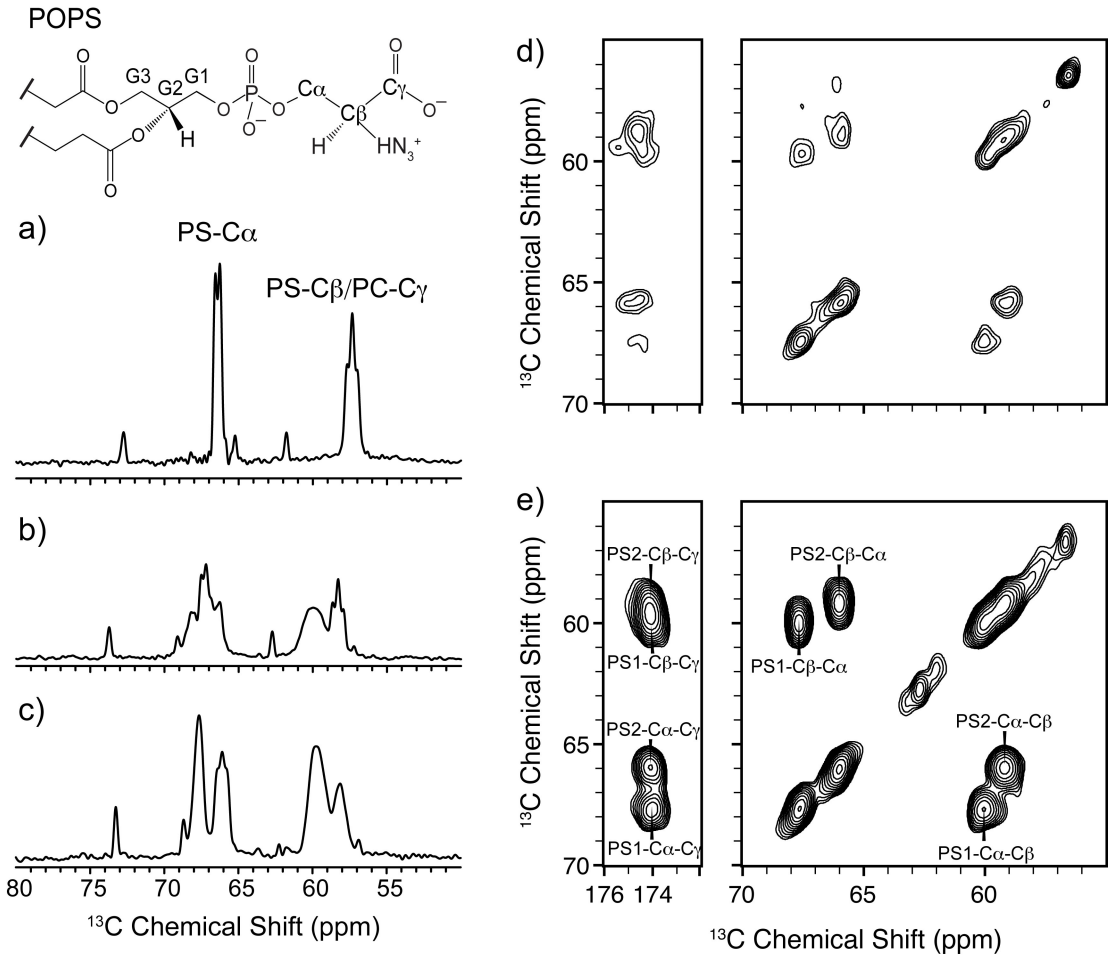

Figure 3.1 Effect of Ca^{2+} on PS Cα and β in Nanodiscs and Liposomes
Cross-polarized ^{13}C one-dimensional Spectra of 30% U-^{13}C-^{15}N-POPS, 70% POPC liposomes were acquired without Ca^{2+} at (a) 10 °C or with 2.5 mM Ca^{2+} at (b) 10 ºC. Spectrum of 30% U-^{13}C-^{15}N-POPS, 70% POPC Nanodiscs with 4 mM Ca^{2+}at (c) 23 °C demonstrate the conformational and changes induced by Ca^{2+} binding, which is further supported by the ^{13}C-^{13}C two-dimensional spectra of: (d) 30% U-^{13}C-^{15}N-POPS 70% POPC MLVs with 2.5 mM Ca^{2+} with 25 ms DARR mixing acquired at -20 °C, acquired 4 weeks after preparation, signal averaged for 18 hours, average signal to noise 15; (e) 30% U-^{13}C-^{15}N-POPS 70% POPC Nanodisc with 4 mM Ca^{2+} with 50 ms DARR mixing acquired at -20 °C, acquired 3 weeks after preparation, signal averaged for 4 hours, average signal to noise 45. Nanodisc samples have both superior signal to noise and sample life time compared to the 30% MLVs which are already showing signs of degradation after 1 month, with the majority of that time spent in storage at -20 °C. Spectra (a), (b), and (d) were acquired with an MAS rate of 11.111 kHz on a 500 MHz (^1H frequency) spectrometer. Spectrum (c) and (e) was acquired with an MAS rate of 10.000 kHz on a 600 MHz (^1H frequency) spectrometer;

studies presented here were conduced using Nanodisc containing 70% POPS 30 % POPC. Because the Ca^{2+} bound PS headgroup conformation is insensitive to the phase of the lipid

chains, structural studies were performed at -20 °C were the motion of any free Ca^{2+} ions in the sample is minimized. This reduced the dielectric heating of the sample and allowed for the application of 105 kHz ^{1}H decoupling during the dipolar mixing periods, improving the ^{13}C T_2 relaxation rates and sensitivity of the experiments.

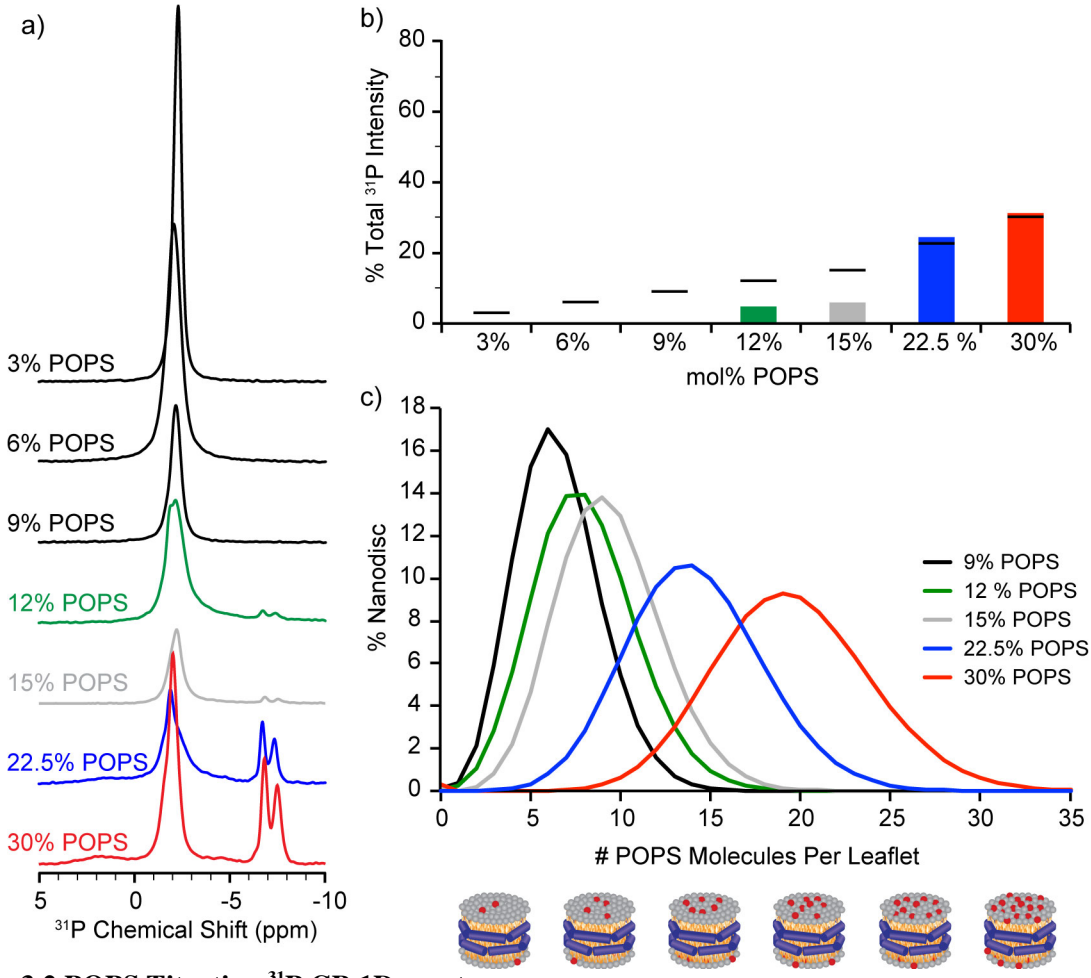

Figure 3.2 POPS Titration ^{31}P CP-1D spectra
(a) Cross-polarized ^{31}P 1D spectra of Nanodisc prepared with 3, 6, 9, 12, 15, 22.5, and 30 % POPS with POPC making up the remainder of the lipids acquired above the bulk phase transition temperature (15-24 °C). There are no distinct signals corresponding to POPS in samples containing less than 12 % POPS. As shown in (b) the relative intensity of the POPS component, expressed as a percentage of the total observed ^{31}P intensity is plotted in as a function of mole % of POPS, with black bars indicate the theoretical intensity. Panel (c) represents the percentage of Nanodisc containing the indicated number of POPS molecules or more per leaflet based on the poison distribution for the leaflets containing 67 lipids per leaflet. Spectra were processed with 40 Hz line broadening (Lorentzian-to-Gaussian apodization) and peak intensities were determined using the spectral deconvolution function included in the Spinsight 3.0 software package. All spectra were acquired on a 600 MHz (^{1}H frequency) spectrometer, at an MAS rate of 10 000 ± 2-3 Hz, with 75 kHz of SPINAL decoupling,[41] with a total of 20,480 scans per spectrum.

3.5.2 Internuclear ^{13}C-^{15}N constraints

The 3D TEDOR experiments developed by Jaroniec *et al*.[40] were developed for the measurement of heteronuclear ^{13}C-^{15}N couplings in a uniformly labeled peptides/proteins. The 3D ZF-TEOR allows for the simultaneous measurement of all ^{13}C-^{15}N dipolar couplings, assuming nominal contributions from ^{15}N chemical shift anisotropy, and the homonuclear ^{13}C-^{13}C scalar couplings (J 30 – 60 Hz) are known. The scalar couplings also modulate the crosspeak intensities, resulting in sever signal dampening when the scalar and dipolar couplings are the same order of magnitude, and obfuscates accurate determination the more interesting weak intra and intermolecular couplings. To insure accurate determination of weak dipolar coupling, that are critical to the determination of the complex, the scalar couplings had to be removed. Therefore, we utilized the less BASE-TEDOR experiment to measure ^{13}C-^{15}N distances as shown in Figure 3.3 and Figure 3.4. The BASE-TEDOR experiment is less efficient in that only couplings to the selected ^{13}C resonances can be detected but the deleterious effects of the homonuclear ^{13}C-^{13}C scalar couplings are removed, and does not require the production of multiple skip labeled samples.

In this study two nanodisc samples contacting 70% POPS 30% POPC were prepared to measure all ^{15}N-^{13}C dipolar couplings. A 70% U-^{13}C-^{15}N-POPS 30% POPC Nanodisc sample was used to determine the intramolecular couplings and unambiguous intermolecular ^{15}N-^{13}C couplings (Figure 3.3). The chemical shift dispersion of the alpha carbons allowed the simultaneous measurement of the both in the intra and intermolecular ^{15}N-$^{13}C\alpha$ dipolar couplings. However, the poor chemical shift dispersion of the PS beta and gamma carbons (Figure 3.4a, b) prevents the measurement of intermolecular constraints. Therefore, a 35% ^{15}N-

POPS 35% U-^{13}C-POPS 30% POPC Nanodisc sample was used to measure intermolecular distances so that only cross peaks resulting form intermolecular ^{15}N-^{13}C contacts could be observed. While the mixed labeled same allowed for the determination of intermolecular contacts it also presented new challenges when determining the dipolar coupling from the dipolar trajectories.

The accurate determination of the T_2 relaxation rate (Γ) and the scaling factor (λ) is essential to the determination of accurate dipolar couplings from experimentally determined TEDOR trajectories. The trajectories of strong one and two bond ^{15}N-^{13}C-dipolar couplings are highly dependent on the scaling factor and relaxation rate. Measuring the ^{13}C T_2 under the same decoupling conditions can approximate the relaxation rate. However, the scaling factor depends on the accurate determination of the maximum intensity. For strong dipolar couplings the trajectory will reach a maximum within a 10 to 12 ms, well within the 25.6 ms mixing time measured in this study. Therefore, it is relatively easy to accurately determine the dipolar coupling, scaling factor, and relaxation rate. However, weak couplings can require more than 30 ms to reach a maximum, which could not be measured due to the dialectic heating of the samples. In the case on the intermolecular ^{15}N-^{13}Cα distances the relaxation rate and scaling factor were fixed by the strong intramolecular couplings measured and fit at the same time. The MINUTE fitting of the intermolecular ^{15}N-^{13}Cβ couplings was unsuccessful because there was no clear maximum intensity observed. Without a clear maximum the dependence of the fit on the scaling factor is nullified, and the minimization routines can no longer converge. Therefore, the relaxation rate and scaling factor were determined for the experimental trajectories over a range of simulated trajectories corresponding to couplings between 3.0 and 7.0 Å in 0.1 Å steps. The best values were selected based on agreement between the experimentally determined relaxation

rate, and the scaling factors determined for the intramolecular N-Cβ couplings which would be a factor of ~5-7 larger than that observed for a strong one or two bond coupling as demonstrated by the relative intensity of the intermolecular N-Cα couplings (Figure 3.3c and d). The results are summarized in Table 3.1 reflect these considerations, and as shown in Figure 3.4 and 3.3 agree well with the experimental data. It is also interesting to note that the relative relaxation rates for the intermolecular N-Cβ dipolar couplings were consistent with the formation of N-Cβ contacts between the two different PS configurations.

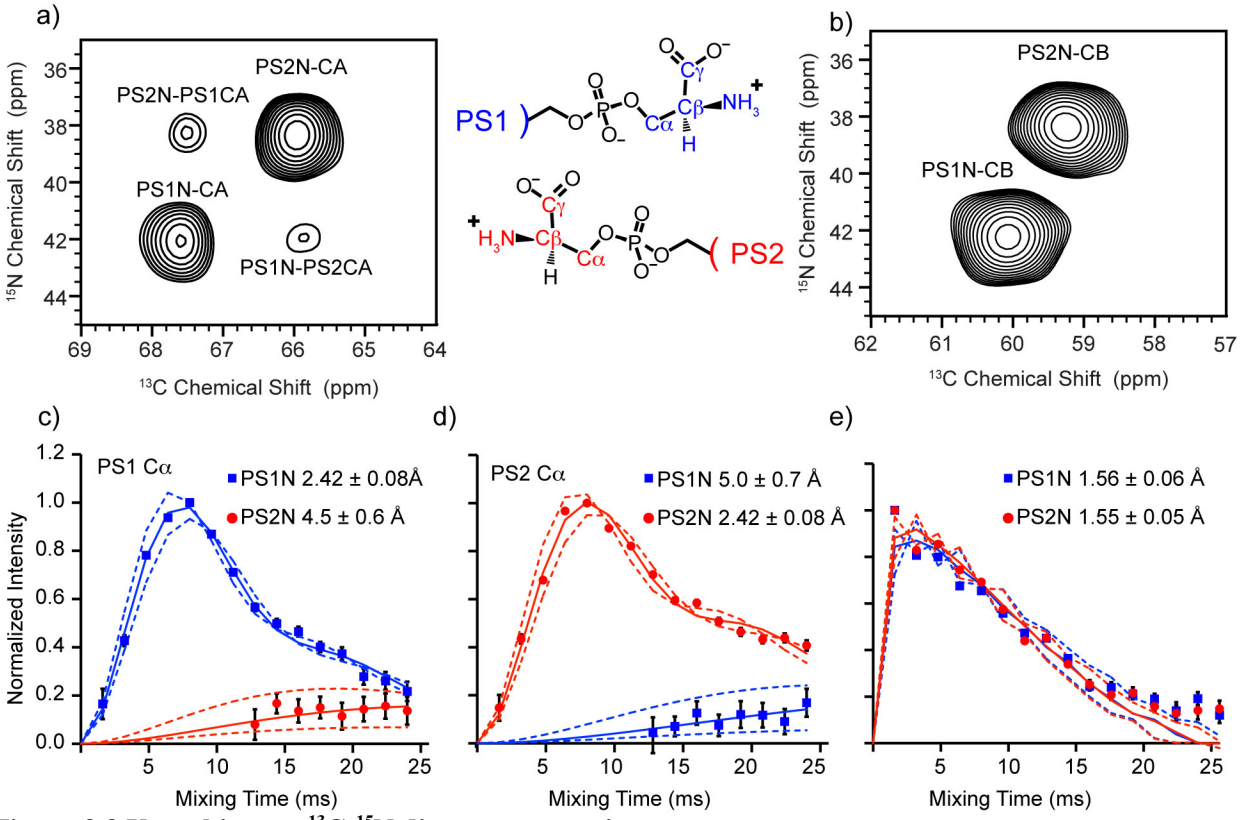

Figure 3.3 Unambiguous ^{13}C-^{15}N distance constraints.
2D ^{15}N-^{13}C plans of 70% U-^{13}C-^{15}N-POPS 30% POPC Nanodisc (a) ^{15}N-Cα BASE-TEDOR with 16 ms and (b) ^{15}N-^{13}Cβ BASE-TEDOR with 1.6 ms mixing. Spectra were processed with 50 Hz net line-broadening (Lorentzian-to-Gaussian apodization) ^{13}C and 15 Hz in ^{15}N. TEDOR trajectories derived form integrated peak volumes form the individual 2D plans at the respective mixing times between 1.6 to 25.6 ms for polarization transfer form PS1-^{15}N (blue squares) and PS2-^{15}N (red circles) to (c) PS1-^{13}Cα, (d) PS2-^{13}Cα and (e) PS1/PS2 ^{13}Cβ. The best-fit trajectories from MINUIT and SPINEVOLUTION fitting are shown as solid lines. The fit are as follows PS1N-Cα 2.42 ± 0.09 Å, PS1N-PS2Cα 4.5 ± 0.6 Å, PS2N-Cα 2.44 ± 0.09 Å, PS2N-PS1Cα 5.0 ± 0.7 Å, PS1N-Cβ 1.56 ± 0.06 Å, and PS2N-Cβ 1.55 ± 0.05 Å. The

intramolecular distances are consistent with those routinely observed for in for one and two bond ^{15}N-^{13}C couplings observed in amino acids.

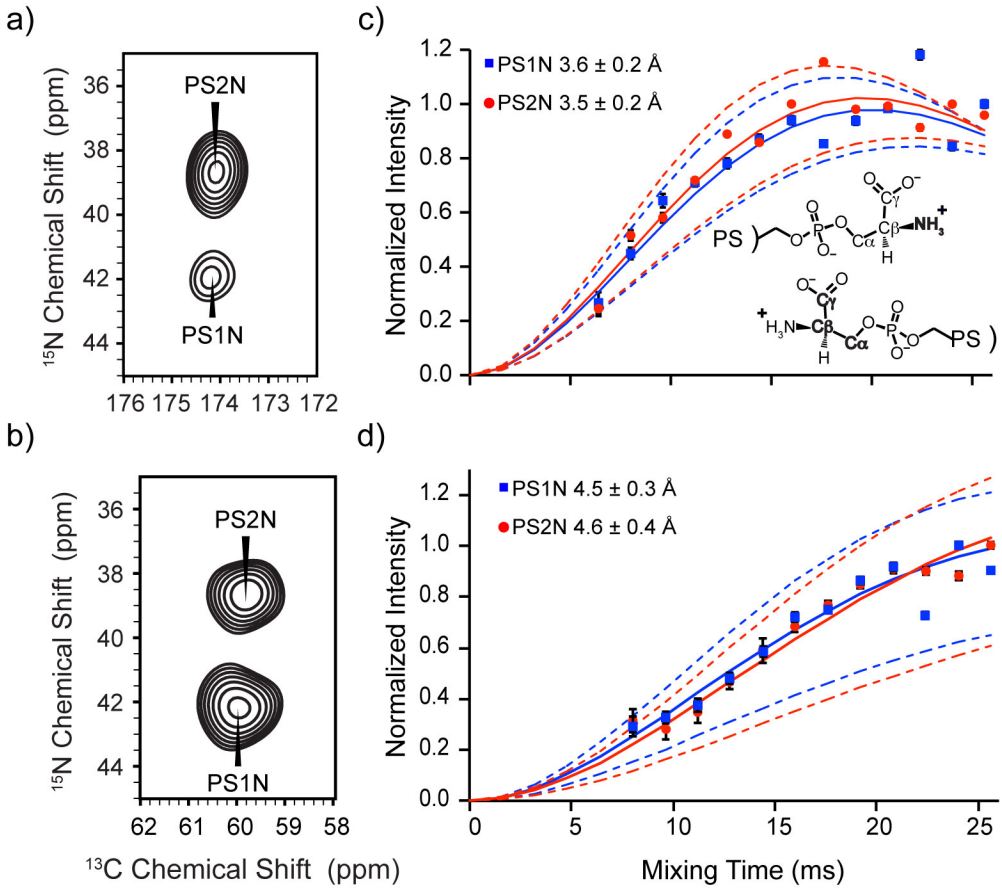

Figure 3.4 Intramolecular ^{13}C-^{15}N constraints

2D ^{15}N-^{13}C plans of 35% U-^{13}C-POPS 35% ^{15}N-POPS 30% POPC Nanodisc (a) ^{15}N-Cγ BASE-TEDOR with 20 ms and (b) ^{15}N-$^{13}C\beta$ BASE-TEDOR with 20 ms mixing. Spectra were processed with 50 Hz net line-broadening (Lorentzian-to-Gaussian apodization) ^{13}C and 15 Hz in ^{15}N. TEDOR trajectories derived form integrated peak volumes form the individual 2D plans at the respective mixing times of 6.4 to 25.6 ms in increments of 1.6 ms for polarization transfer form PS1-^{15}N (blue) and PS2-^{15}N (red) to (c) PS-$^{13}C\beta$ (d) PS1/PS2 $^{13}C\beta$. The best-fit trajectories from MINUIT and SPINEVOLUTION fitting are shown as solid lines. The fit are as follows PS1N-PS-Cβ 3.8 ± 0.6 Å, PS1N-PSCβ 3.8 ± 0.6 Å, PS1N-PS-Cγ 3.6 ± 0.3 Å, and PS2N-PS-Cγ 3.6 ± 0.1 Å. The intermolecular distances are consistent with the tight packing of the headgroups, and the formation of hydrogen bonds between the amino and carboxylate groups.

Table 3.1 ^{13}C-^{15}N BASE-TEDOR Results

Assignment	r (Å)	$R_2(s^{-1})$ Fit	$R_2(s^{-1})$ Exp.	λ
PS1-N-Cα	2.42 ± 0.08	79	71	3.7
PS2-N-PS1-Cα	4.5 ± 0.6	79	71	3.7
PS1-N-Cβ	1.56 ± 0.06	26	51	2.1
PS1-N-PS-Cβ	4.5 ± 0.3	42	48	10.9
PS1-N-PS-Cγ	3.6 ± 0.2	48	28	6.1
PS2-N-Cα	2.42 ± 0.08	53	65	3.1
PS1-N-PS2-Cα	5.0 ± 0.7	53	65	3.1
PS2-N-Cβ	1.55 ± 0.05	32	51	2.3
PS2-N-PS-Cβ	4.6 ± 0.4	34	48	10.2
PS2-N-PS-Cγ	3.5 ± 0.2	45	28	5.6

3.5.3 XPLOR-NIH Structure Calculations

The 10 lowest energy structures (of 500) converged with no violations of the SSNMR constraints (Figure 3.5). The distribution of intermolecular ^{13}C-^{15}N distances and intramolecular ^{13}C-^{31}P and ^{15}N-^{31}P distances are shown in Figure 3.5e and 3.5e respectively. As shown in Figure 3.5e and Table 3.2 there was excellent agreement between the SSNMR restraints and final structures. The primary variations in the final structures relative to the SSNMR constraints were the intermolecular N-Cα distances, which also displayed the largest variation experimentally. There were three dominant configurations of the $Ca(PS)_2$ complex observed in the 10 lowest energy structures typically reported in NMR structure calculations (Figure 3.5). To facilitate discussion of structural results we will define some terminology. Conformations of the PS headgroup with a shorter P-Cγ distance are referred to as gauche while the conformation with a longer P-Cγ distance are referred to as trans. Dimer configurations are referred to in terms PS1-PS2 of gauche and or trans pairs. The gauche-gauche dimer (Figure 3.5a) Ca^{2+} is localized between the carboxylate and phosphate groups of PS2 but dose not interact significantly (> 4. Å) with PS1. The relaxed gauche-trans dimer (Figure 3.5a) Ca^{2+} is localized between the carboxylate and phosphate groups of PS2 but dose not interact significantly (> 4. Å) with PS1.

The gauche-trans dimer (Figure 3.5b) also localized Ca^{2+} among the carboxylate and phosphate groups of PS2 and the phosphate group of PS1. Finally the relaxed gauche-trans dimer (Figure 3.5c) localized Ca^{2+} between the carboxylate group of PS2 and the phosphate group of PS1.

The exact values of the ^{13}C-^{15}N, ^{13}C-^{31}P, and ^{15}N-^{31}P distances observed for each o the configuration of the dimer are summarized in Table 3.2.But in all three conformation of the $Ca(PS)_2$ dimer PS2 subunit is always shorter than the PS1 monomer. There are also clear differences in the intramolecular P-N distances, which could be utilized to differentiate between the three conformations of the $Ca(PS)_2$.

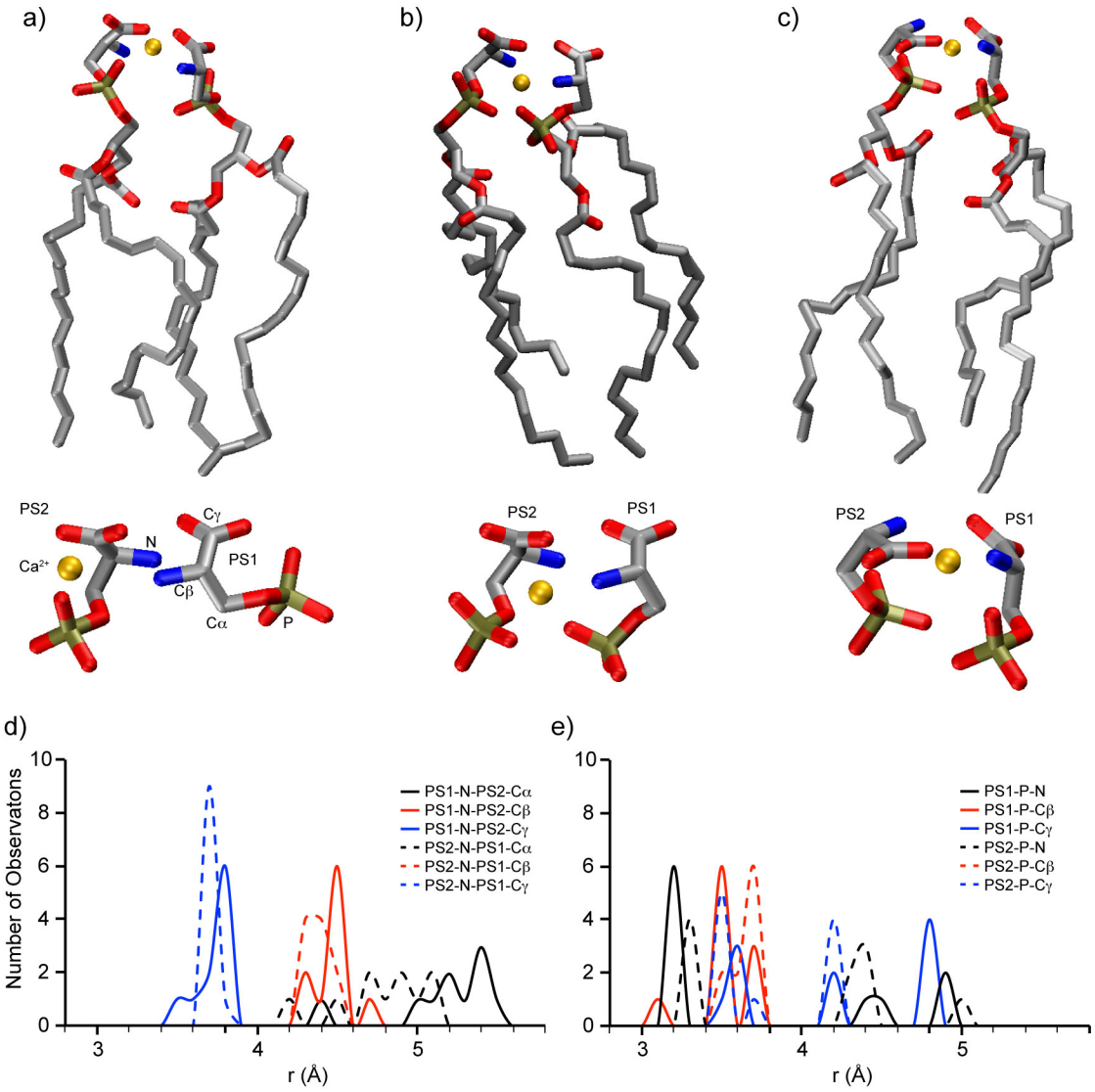

Figure 3.5 $Ca(PS)_2$ dimer structures.
$(PS)_2$-Ca^{2+} dimer structures calculated using ^{13}C-^{15}N TEDOR, ^{13}C-^{13}C DARR, (^1H)-^{13}C-(^1H-^1H)-^{13}C, and ^{31}P-^{31}P DARR constraints summarized in supplementary table 3.1. There were three primary configuration of the $Ca(PS)_2$ dimers observed in the 10 lowest energy structures (of 500): (a) the gauche-gauche dimer; (b) gauche-trans dimer; and (c) the relaxed gauche-trans dimer colored according to following color scheme: carbon, gray; oxygen, red; nitrogen, blue; calcium, yellow. (d) The distribution of intermolecular ^{15}N-^{13}C distances are well within the boundaries of the SSSNMR constraints. (e)The distribution of intramolecular ^{31}P-^{13}C and ^{31}P-^{15}N are the primary source of variation between the three configurations.

Table 3.2 Comparison of Internuclear Distances Observed in XPLOR-NIH $Ca(PS)_2$ Dimer Calculations

		r(Å)		
Assignment	SSNMR	Fig. 3.5a	Fig. 3.5b	Fig. 3.5c
PS1-N-Cα	2.42 ± 0.08	2.5	2.5	2.5
PS1-N-Cβ	1.56 ± 0.06	1.5	1.5	1.5
PS1-N-PS2-Cα	5.0 ± 0.7	4.9	5.0	5.4
PS2-N-Cα	2.42 ± 0.08	2.5	2.5	2.5
PS2-N-Cβ	1.55 ± 0.05	1.5	1.5	1.5
PS2-N-PS1-Cα	4.5 ± 0.6	4.5	4.7	4.9
PS1-N-PS2-Cβ	4.5 ± 0.3	4.5	4.4	4.5
PS2-N-PS1-Cβ	4.6 ± 0.4	4.3	4.3	4.4
PS1-N-PS2-Cγ	3.6 ± 0.2	3.8	3.7	3.7
PS2-N-PS1-Cγ	3.5 ± 0.2	3.7	3.7	3.7
PS1-P-Cβ		3.7	3.4	3.4
PS2-P-Cβ		3.6	3.6	3.5
PS1-P-Cγ		3.54	4.1	4.8
PS2-P-Cγ		3.49	3.5	4.2
PS1-P-N		4.9	3.2	3.2
PS2-P-N		4.3	4.3	3.3
PS1-N-PS2-P		4.3	4.7	5.3
PS2-N-PS1-P		5.2	3.9	6.0
PS1-P-PS2-Cγ		7.1	5.1	5.0
PS2-P-PS1-Cγ		6.2	6.5	4.7

3.6 Discussion

We proposed that the fundamental subunit of the PS-Ca^{2+} clusters is the $Ca(PS)_2$ dimer, in which one of the two configurations of the PS headgroup coordinating Ca^{2+} through both its phosphate and carboxylate groups, while the second configuration interacting via its carboxylate or phosphate group. Such a mechanism of clustering would allow for the formation of both large and small complexes, and explain why in these and our pervious studies the same chemical shifts and correlation spectra are observed over such a wide range of POPS concentrations (Figure 3.1).[32] Titration studies summarized in Figure 3.2 further demonstrate this effect as the same PS1 and PS2 ^{31}P chemical shifts and relative intensities are observed in POPS/POPC Nanodisc with and average of six or more POPS molecules per leaflet. It should be noted that it is possible

that the $Ca(PS)_2$ dimer is still formed at lower concentrations of POPS, as demonstrated by 10% POPS liposomes, but the cross-polarization efficiency or relative intensity of the PS1/PS2 peaks was not sufficient form observation. Further support of the mechanism of cluster formation was derived from our pervious study of the binding of bovine prothrombin fragment 1 to 30% POPS 70% POPC Nanodisc.[6] Where in the presence of saturating levels of fragment 1 we observed the same two equally populated PS1 and PS2 configurations of the headgroups in addition to a new configuration of the PS headgroup.

Two out of the three configurations of the $Ca(PS)_2$ dimer structures directly agree with our hypothesis that Ca^{2+} coordinates both the phosphate and carboxylate groups of one of the PS monomers. In both the gauche-gauche (Figure 3.5a) and gauche-trans (Figure 3.5b) configuration the PS2 monomer adopts a very compact conformation characterized by a shorter P-Cγ distance and localization of Ca^{2+} between its phosphate and carboxylate. In the gauche-gauche configuration the PS1 monomer also adopts a very compact conformation but does not interact with the Ca^{2+} ion. It is easy to visualize the propagation of the larger oligomers, as the PS1 phosphate group extends out leaving it available to coordinate a neighboring Ca^{2+}-ion. In contrast the gauche-trans configuration (Figure 3.5b) PS1 is more extended and the phosphate moiety also interacts with the same Ca^{2+} ion as PS2. In this case it is more difficult to see how $Ca(PS)_2$ dimers would interact with each other, and the exposure of the PS1 amine would prevent coordination of Ca^{2+} ions.

The relaxed gauche-trans configuration presents and interesting alternative mode of dimer formation. In This case the phosphate group of PS1 and the carboxylate group of PS2 coordinate the same Ca^{2+} ion. Again the PS2 configuration has a shorter intramolecular P-Cγ distance the PS1 (Table 3.2), but in this case the PS2 phosphate and PS1 carboxylate moieties are

available for coordination of neighboring $Ca(PS)_2$ dimers. Cocoordination of neighboring $Ca(PS)_2$ dimers could also explain the differences in the relative crosspeak intensities observed in ^{15}N-13Cγ BASE-TEDOR experiments (Figure 3.4a). The hydrogen bond formed between the opposing amino and carboxylate plays a critical role in the formation of the $Ca(PS)_2$ dimers. It helps to bring the two negatively charged headgroups close together, and may even provide a stabilizing effect in the event of Ca^{2+} exchange.

In all three configurations the PS2 subunit coordinates Ca^{2+} via its carboxylate, and has a short intramolecular P-Cγ distances, while the PS1 conformation tends to adopt a more extended conformation that interacts with Ca^{2+} via either its carboxylate or phosphate moiety but never both within the same $Ca(PS)_2$ dimer. Calcium coordination by the PS carboxylate group was the primary mode of interaction observed in molecular dynamics simulations performed by Vernier *et al*.[23] However we observe Ca^{2+} interactions with the PS phosphate groups in all three structures while Vernier *et al*. reported very limited interactions between the Ca^{2+} and the PS phosphate. This could potentially be due to the very 'sticky' nature of Ca^{2+} in molecular dynamics simulations, which does not readily exchange once bound.

The determination of quantitative ^{13}C-^{31}P and ^{31}P-^{15}N distances would greatly enhance these structural studies but present a new set of unique challenges. The majority of dipolar recoupling techniques rely upon the observation of isolated spin pairs, which in the case of ^{13}C-^{15}N couplings is relatively simple. Samples can be prepared with selectively labeled, mixed labeling, and or dilution in natural abundance to simplify the spin matrix, remove scalar couplings, and allow for the measurement of unambiguous intermolecular distances as demonstrated by Nieuwkoop *et al*.[56] and Jaroniec *et al*. [40,57,58], and exploited in this study. This is all possible because of the natural scarcity of the NMR active ^{13}C and ^{15}N isotopes. Further more

in proteins and peptides the natural spacing between molecules with the same chemical shifts is inherently greater than that which is possible in phospholipids. In contrast to ^{13}C and ^{15}N, the NMR active ^{31}P 99% abundant and therefore no isotopic enrichment is necessary, while simultaneously preventing the measurement of unambiguous intermolecular constraints by dilution in natural abundance. This coupled with the high gyromagnetic ratio of ^{31}P present and large chemical shift anisotropy (CSA) make it a very interesting target for NMR studies. In fact Roux *et al*. [28] and Casal *et al*.[25] used the ^{31}P CSA to monitor changes in the phospholipid bilayer in the presence of various counter ions. However it is precisely these features that make measurement of quantitative ^{31}P-^{13}C and ^{31}P-^{15}N distances difficult. The large ^{31}P CSA cannot be ignored when fitting dipolar recoupling trajectories. The tight packing and limited chemical shift dispersion of phospholipid headgroups, means that the assumptions that each ^{13}C-^{31}P coupling represents a single spin pair is no longer valid, as exemplified by the intermolecular P-C distances summarized in Table 3.2 and Supplementary Figure 3.1. Therefore, we are working to develop new dipolar recoupling and fitting methodologies to determine the intra and intermolecular ^{13}C-^{31}P and ^{31}P-^{15}N distances needed for further refinement of the $Ca(PS)_2$ dimer structures.

The three configurations of the $Ca(PS)_2$ dimer presented here represent a critical first step in the determination of the phospholipid structures, and a mechanism for the continued improvement of molecular dynamics simulations of phospholipids and their interactions with membrane proteins. These studies have already provided a number of unique insights including the formation of hydrogen bonds between the amino and carboxylate groups the two PS conformations and the coordination of Ca^{2+} by both the PS phosphate and carboxylate. These

insights have prompted the development of new experiential techniques to account for the unique challenges associated with the measurement of heteronuclear ^{31}P dipolar couplings.

3.7 Supplementary Information

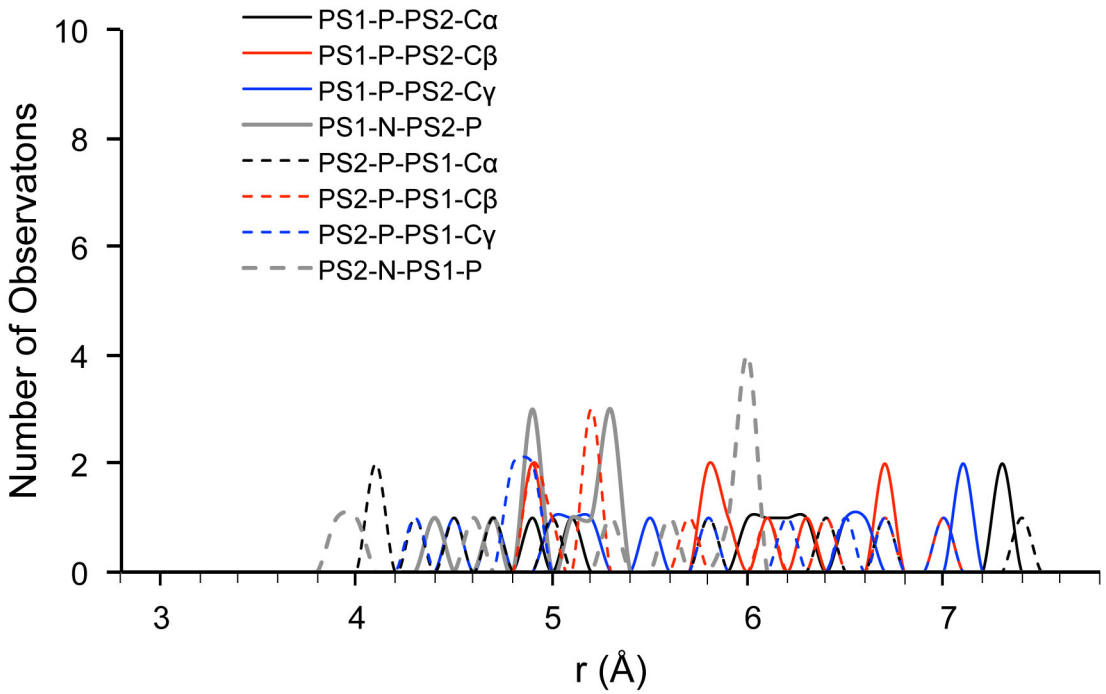

Supplementary Figure 3.1 Distribution of Intramolecular ^{15}N-^{31}P and ^{13}C-^{31}P distance in 10 lowest energy structures of Ca(PS)$_2$ dimers.
Intramolecular P-Cα (black) P-Cβ (red), P-Cγ (blue), and P-N (gray) between PS1-P (solid lines) and PS2-P (dashed lines) observed in the 10 lowest energy structures of the Ca(PS)$_2$ dimers.

Supplementary Table 3.1 List SSNMR Constraints

Assignment	r (Å)
Unambiguous Constraints	
PS1-N-Ca	2.42 ± 0.08
PS1-N-Cb	1.56 ± 0.06
PS1-N-PS2-Ca	5.0 ± 0.7
PS2-N-Ca	2.42 ± 0.08
PS2-N-Cb	1.55 ± 0.05
PS2-N-PS1-Ca	4.5 ± 0.6
PS1-Ca-PS2-Ca	5 ± 2
PS1-Ha- PS2-Hb	5 ± 2
PS1-P-PS2-P	5 ± 3
Ambiguous Intermolecular Constraints	
PS1-N-PS-Cb	4.5 ± 0.3
PS2-N-PS-Cb	4.6 ± 0.4
PS1-N-PS-Cg	3.6 ± 0.2
PS2-N-PS-Cg	3.5 ± 0.2

3.8 References

1 Singer, S. J. & Nicolson, G. L. The fluid mosaic model of the structure of cell membranes. *Science* **175**, 720-731, (1972).

2 Fadok, V. A., Voelker, D. R., Campbell, P. A., Cohen, J. J., Bratton, D. L. & Henson, P. M. Exposure of phosphatidylserine on the surface of apoptotic lymphocytes triggers specific recognition and removal by macrophages. *J. Immunol.* **148**, 2207-2216, (1992).

3 Papahadjopoulos, D., Poste, G., Schaeffer, B. E. & Vail, W. J. Membrane fusion and molecular segregation in phospholipid vesicles. *Biochim. Biophys. Acta* **352**, 10-28, (1974).

4 McLaughlin, S. & Murray, D. Plasma membrane phosphoinositide organization by protein electrostatics. *Nature* **438**, 605-611, (2005).

5 Berridge, M. J. & Irvine, R. F. Inositol trisphosphate, a novel second messenger in cellular signal transduction. *Nature* **312**, 315-321, (1984).

6 Tavoosi, N., Davis-Harrison, R. L., Pogorelov, T. V., Ohkubo, Y. Z., Arcario, M. J., Clay, M. C., Rienstra, C. M., Tajkhorshid, E. & Morrissey, J. H. Molecular determinants of phospholipid synergy in blood clotting. *J. Biol. Chem.* **286**, 23247-23253, (2011).

7 Phillips, R., Ursell, T., Wiggins, P. & Sens, P. Emerging roles for lipids in shaping membrane-protein function. *Nature* **459**, 379-385, (2009).

8 Paterson, J. K., Renkema, K., Burden, L., Halleck, M. S., Schlegel, R. A., Williamson, P. & Daleke, D. L. Lipid specific activation of the murine P4-ATPase Atp8a1 (ATPase II). *Biochemistry* **45**, 5367-5376, (2006).

9 Gordesky, S. E. & Marinetti, G. V. The asymetric arrangement of phospholipids in the human erythrocyte membrane. *Biochem. Biophys. Res. Commun.* **50**, 1027-1031, (1973).

10 Zwaal, R. F. & Schroit, A. J. Pathophysiologic implications of membrane phospholipid asymmetry in blood cells. *Blood* **89**, 1121-1132, (1997).

11 Zwaal, R. F., Comfurius, P. & Bevers, E. M. Surface exposure of phosphatidylserine in pathological cells. *Cell. Mol. Life Sci.* **62**, 971-988, (2005).

12 Leventis, P. A. & Grinstein, S. The distribution and function of phosphatidylserine in cellular membranes. *Annu Rev Biophys* **39**, 407-427, (2010).

13 Riedl, S., Zweytick, D. & Lohner, K. Membrane-active host defense peptides--challenges and perspectives for the development of novel anticancer drugs. *Chem. Phys. Lipids* **164**, 766-781, (2011).

14 Yang, L. & Glaser, M. Formation of membrane domains during the activation of protein kinase C. *Biochemistry* **35**, 13966-13974, (1996).

15 Haverstick, D. M. & Glaser, M. Visualization of Ca^{2+}-induced phospholipid domains. *Proc. Natl. Acad. Sci. USA* **84**, 4475-4479, (1987).

16 Yeung, T., Gilbert, G. E., Shi, J., Silvius, J., Kapus, A. & Grinstein, S. Membrane phosphatidylserine regulates surface charge and protein localization. *Science* **319**, 210-213, (2008).

17 Newton, C., Pangborn, W., Nir, S. & Papahadjopoulos, D. Specificity of Ca^{2+} and Mg^{2+} binding to phosphatidylserine vesicles and resultant phase changes of bilayer membrane structure. *Biochim. Biophys. Acta* **506**, 281-287, (1978).

18 Hauser, H., Darke, A. & Phillips, M. C. Ion-binding to phospholipids. Interaction of calcium with phosphatidylserine. *Eur. J. Biochem.* **62**, 335-344, (1976).

19 Hauser, H., Phillips, M. C., Levine, B. A. & Williams, R. J. Ion-binding to phospholipids. Interaction of calcium and lanthanide ions with phosphatidylcholine (lecithin). *Eur. J. Biochem.* **58**, 133-144, (1975).

20 Feigenson, G. W. On the Nature of Calcium-Ion Binding between Phosphatidylserine Lamellae. *Biochemistry* **25**, 5819-5825, (1986).

21 McLaughlin, S., Mulrine, N., Gresalfi, T., Vaio, G. & McLaughlin, A. Adsorption of divalent cations to bilayer membranes containing phosphatidylserine. *J. Gen. Physiol.* **77**, 445-473, (1981).

22 Pandit, S. A. & Berkowitz, M. L. Molecular dynamics simulation of dipalmitoylphosphatidylserine (DPPS) bilayer with mono and divalent cations. *Biophys. J.* **82**, 489A-489A, (2002).

23 Vernier, P. T., Ziegler, M. J. & Dimova, R. Calcium binding and head group dipole angle in phosphatidylserine-phosphatidylcholine bilayers. *Langmuir* **25**, 1020-1027, (2009).

24 Casal, H. L., Mantsch, H. H. & Hauser, H. Infrared studies of fully hydrated saturated phosphatidylserine bilayers. Effect of Li+ and Ca2+. *Biochemistry* **26**, 4408-4416, (1987).

25 Casal, H. L., Mantsch, H. H., Paltauf, F. & Hauser, H. Infrared and 31P-NMR studies of the effect of Li+ and Ca2+ on phosphatidylserines. *Biochim. Biophys. Acta* **919**, 275-286, (1987).

26 Roux, M. & Bloom, M. Ca^{2+}, Mg^{2+}, Li^{+}, Na^{+}, and K^{+} distributions in the headgroup region of binary membranes of phosphatidylcholine and phosphatidylserine as seen by deuterium NMR. *Biochemistry* **29**, 7077-7089, (1990).

27 Roux, M. & Bloom, M. Calcium binding by phosphatidylserine headgroups. Deuterium NMR study. *Biophys. J.* **60**, 38-44, (1991).

28 Roux, M., Neumann, J. M., Bloom, M. & Devaux, P. F. 2H and 31P NMR study of pentalysine interaction with headgroup deuterated phosphatidylcholine and phosphatidylserine. *European biophysics journal : Eur. Biophys. J.* **16**, 267-273, (1988).

29 Browning, J. L. & Seelig, J. Bilayers of phosphatidylserine: a deuterium and phosphorus nuclear magnetic resonance study. *Biochemistry* **19**, 1262-1270, (1980).

30 Sinn, C. G., Antonietti, M. & Dimova, R. Binding of calcium to phosphatidylcholine-phosphatidylserine membranes. *Colloid Surface A* **282**, 410-419, (2006).

31 Pedersen, U. R., Leidy, C., Westh, P. & Peters, G. H. The effect of calcium on the properties of charged phospholipid bilayers. *Biochem. Biophys. Aacta-Biomembranes* **1758**, 573-582, (2006).

32 Boettcher, J. M., Davis-Harrison, R. L., Clay, M. C., Nieuwkoop, A. J., Ohkubo, Y. Z., Tajkhorshid, E., Morrissey, J. H. & Rienstra, C. M. Atomic view of calcium-induced clustering of phosphatidylserine in mixed lipid bilayers. *Biochemistry* **50**, 2264-2273, (2011).

33 Schwieters, C. D., Kuszewski, J. J., Tjandra, N. & Clore, G. M. The Xplor-NIH NMR molecular structure determination package. *J. Magn. Reson.* **160**, 65-73, (2003).

34 Nakazawa, Y., Sagane, Y., Sakurai, S., Uchino, M., Sato, H., Toeda, K. & Takano, K. Large-scale production of phospholipase D from Streptomyces racemochromogenes and its application to soybean lecithin modification. *Applied Biochemistry and Biotechnology* **165**, 1494-1506, (2011).

35 Nakazawa, Y., Sagane, Y., Kikuchi, T., Uchino, M., Nagai, T., Sato, H., Toeda, K. & Takano, K. Purification, biochemical characterization, and cloning of phospholipase D from Streptomyces racemochromogenes strain 10-3. *Protein J.* **29**, 598-608, (2010).

36 Martinezzaguilan, R., Martinez, G. M., Lattanzio, F. & Gillies, R. J. Simultaneous measurement of intracellular Ph and Ca^{2+} using the fluorescence of Snarf-1 and Fura-2. *Am. J. Physiol.* **260**, C297-C307, (1991).

37 Van Geet, A. L. Calibration of the methanol and glycol nuclear magnetic resonance thermometers with a static thermistor probe. *Anal. Chem.* **42**, 2227, (1968).

38 Delaglio, F., Grzesiek, S., Vuister, G. W., Zhu, G., Pfeifer, J. & Bax, A. Nmrpipe - a multidimensional spectral processing system based on unix pipes. *J. Biomol. NMR* **6**, 277-293, (1995).

39 Morcombe, C. R. & Zilm, K. W. Chemical shift referencing in MAS solid state NMR. *J. Magn. Reson.* **162**, 479-486, (2003).

40 Jaroniec, C. P., Filip, C. & Griffin, R. G. 3D TEDOR NMR experiments for the simultaneous measurement of multiple carbon-nitrogen distances in uniformly ^{13}C,^{15}N-labeled solids. *J. Am. Chem. Soc.* **124**, 10728-10742, (2002).

41 Comellas, G., Lopez, J. J., Nieuwkoop, A. J., Lemkau, L. R. & Rienstra, C. M. Straightforward, effective calibration of SPINAL-64 decoupling results in the enhancement of sensitivity and resolution of biomolecular solid-state NMR. *J. Magn. Reson.* **209**, 131-135, (2011).

42 Veshtort, M. & Griffin, R. G. SPINEVOLUTION: A powerful tool for the simulation of solid and liquid state NMR experiments. *J. Magn. Reson.* **178**, 248-282, (2006).

43 James, F. & Roos, M. Minuit - system for function minimization and analysis of parameter errors and correlations. *Comput. Phys. Commun.* **10**, 343-367, (1975).

44 Pan, J., Cheng, X., Monticelli, L., Heberle, F.A., Kucerka, N., Tieleman, D. P. & Katsaras, J. The molecular structure of a phosphatidylserine bilayer determined by scattering and molecular dynamics simulations. *Soft matter* **10**, 3716-3725, (2014).

45 Suga, T., Inubushi, C. & Okabe, N. O-Phospho-L-tyrosine. *Acta Cryst.* **C54**, 83-85, (1998).

46 Suga, T. & Okabe, N. Aqua(L-O-serine phosphato)calicum(II). *Acta Cryst.* **C52**, 1894-1896, (1996).

47 Sundaralingam, M. & Putkey, E. F. Molecular Structures of Amino Adds and Peptides. II. A Redetermlnation of the Crystal Structure of L-O-Serine Phosphate. A Very Short Phosphate-Carboxyl Hydrogen Bond. *Acta Cryst.* **B26**, 790, (1970).

48 Bryndal, I., Picur, B. & Lis, T. The structure of O-phospho-l-threonine in different chemical environments. *J. Mol. Struct.* **647**, 295-310, (2003).

49 Weber, H. P., McMullan, R. K., Swaminathan, S. & Craven, B. M. The Structure and Thermal Motion of Phosphorylethanolamine at 122 K from Neutron Diffraction. *Acta Cryst.* **B40**, 506-511, (1984).

50 Roux, M. & Bloom, M. Ca^{2+}, Mg^{2+}, Li^{+}, Na^{+}, and K^{+} Distributions in the Headgroup Region of Binary Membranes of Phosphatidylcholine and Phosphatidylserine as Seen by Deuterium Nmr. *Biochemistry* **29**, 7077-7089, (1990).

51 Roux, M. & Bloom, M. Calcium-Binding by Phosphatidylserine Headgroups - Deuterium Nmr-Study. *Biophys. J.* **60**, 38-44, (1991).

52 Stringer, J. A., Bronnimann, C. E., Mullen, C. G., Zhou, D. H., Stellfox, S. A., Li, Y., Williams, E. H. & Rienstra, C. M. Reduction of RF-induced sample heating with a scroll coil resonator structure for solid-state NMR probes. *J. Magn. Reson.* **173**, 40-48, (2005).

53 Bayburt, T. H., Grinkova, Y. V. & Sligar, S. G. Self-assembly of discoidal phospholipid bilayer nanoparticles with membrane scaffold proteins. *Nano. Lett.* **2**, 853-856, (2002).

54 Bayburt, T. H. & Sligar, S. G. Self-assembly of single integral membrane proteins into soluble nanoscale phospholipid bilayers. *Protein Sci.* **12**, 2476-2481, (2003).

55 Nath, A., Atkins, W. M. & Sligar, S. G. Applications of phospholipid bilayer nanodiscs in the study of membranes and membrane proteins. *Biochemistry* **46**, 2059-2069, (2007).

56 Nieuwkoop, A. J., Wylie, B. J., Franks, W. T., Shah, G. J. & Rienstra, C. M. Atomic resolution protein structure determination by three-dimensional transferred echo double resonance solid-state nuclear magnetic resonance spectroscopy. *J. Chem. Phys.* **131**, 095101, (2009).

57 Jaroniec, C. P., Tounge, B. A., Herzfeld, J. & Griffin, R. G. Frequency selective heteronuclear dipolar recoupling in rotating solids: Accurate ^{13}C-^{15}N distance measurements in uniformly ^{13}C,^{15}N-labeled peptides. *J. Am. Chem. Soc.* **123**, 3507-3519, (2001).

58 Jaroniec, C. P., Tounge, B. A., Rienstra, C. M., Herzfeld, J. & Griffin, R. G. Recoupling of heteronuclear dipolar interactions with rotational-echo double-resonance at high magic-angle spinning frequencies. *J. Magn. Reson.* **146**, 132-139 (2000).

CHAPTER 4

Molecular Determinants of Phospholipid Synergy in Blood Clotting[1]

4.1 Notes and Acknowledgements

This chapter is adapted from "Molecular Determinants of Phospholipid Synergy in Blood Clotting." *Journal of Biological Chemistry* 286, 23247-23253, (2011), Autors: Narjes Tavoosi[‡], Rebecca L. Davis-Harrison, Taras V. Pogorelov, Y. Zenmei Ohkubo, Mark J. Arcario, **Mary C. Clay**, Chad M. Rienstra, Emad Tajkhorshid, and James H. Morrissey. We thank Julie Collins and Jessica Luzwick for excellent technical contributions, Dr. John Boettcher for help with NMR experiments, and Dr. Stephen G. Sligar for kindly providing membrane scaffold protein. This work was supported by the National Institute of General Medical Sciences, NIH (R01-GM075937 and R01-GM079530 to C.M.R., and R01-GM086749 and R01-GM067887 to E.T.), the National Center for Research Resources, NIH (P41-RR05969 to E.T.), the National Heart Lung and Blood Institute, NIH (R01 HL47014 to J.H.M. and R01 HL103999 to J.H.M. and C.M.R.), and by the American Heart Association (0920045G to R.D.H.).

4.2 Abstract

Many regulatory processes in biology involve reversible association of proteins with membranes. Clotting proteins bind to phosphatidylserine (PS) on cell surfaces, but a clear picture of this interaction has yet to emerge. We present a novel explanation for membrane binding by GLA domains of clotting proteins, supported by biochemical studies, solid-state NMR analyses,

---

[1] This project was published in Journal of Biological Chemistry, in July 2011. Copyright owner has provided

Narjes Tavoosi[‡], Rebecca L. Davis-Harrison[‡], Taras V. Pogorelov[‡,§], Y. Zenmei Ohkubo[‡,§], Mark J. Arcario[§,¶], Mary C. Clay[‖], Chad M. Rienstra[¶,‖], Emad Tajkhorshid[‡,§,¶], and James H. Morrissey[‡,1]

From the [‡]Department of Biochemistry, [§]Beckman Institute for Advanced Science and Technology, [¶]Center for Biophysics and Computational Biology, and [‖]Department of Chemistry, University of Illinois, Urbana, IL 61801

and molecular dynamics simulations. The model invokes a single "phospho-L-serine-specific" interaction and multiple "phosphate-specific" interactions. In the latter, the phosphates in phospholipids interact with tightly bound Ca^{2+} in GLA domains. We show that phospholipids with any headgroup other than choline strongly synergize with PS to enhance factor X activation. We propose that phosphatidylcholine and sphingomyelin (the major external phospholipids of healthy cells) are anticoagulant primarily because their bulky choline headgroups sterically hinder access to their phosphates. Following cell damage or activation, exposed PS and phosphatidylethanolamine collaborate to bind GLA domains by providing phospho-L-serine-specific and phosphate-specific interactions, respectively.

4.3 Introduction

Proteins that bind to phosphatidylserine (PS)[2] are implicated in diverse processes such as intracellular signal transduction cascades; vesicle fusion and neurotransmitter release; plasma membrane-cytoskeleton interactions; phagocytosis of apoptotic cells; and blood clotting [2]. Indeed, most of the steps in the coagulation cascade require the reversible, Ca^{2+}-dependent association of clotting proteins with membrane bilayers containing exposed PS [3]. Releasing these proteins from the membrane surface renders them thousands of times less active. An exemplar is the initiation of clotting, triggered when the plasma protease, factor VIIa (fVIIa), binds to the integral membrane protein, tissue factor (TF). The resulting TF:fVIIa complex activates two membrane-bound zymogens, factors IX (fIX) and X (fX), by limited proteolysis [4]. FVIIa, fIX and fX are homologous proteins that interact with PS-containing membranes via their GLA domains, so-named because they are rich in gamma-carboxyglutamate (Gla). GLA domains are the most common membrane-binding motif in blood clotting [3], but in spite of their importance, we lack a detailed understanding of their interaction with the membrane at atomic resolution.

This study provides a new view of how lipids collaborate to promote the binding of GLA domains to membrane surfaces and trigger blood clotting.

A puzzling feature of TF:fVIIa is its requirement for unphysiologically high PS levels (~30% PS) for optimal procoagulant activity when TF is incorporated into liposomes with mixtures of PS and phosphatidylcholine (PC). The answer may come from phosphatidylethanolamine (PE). By itself, PE (in PE/PC liposomes) supports little to no clotting activity, but when PE is incorporated into PS/PC liposomes, it dramatically decreases the PS requirement for optimal activity of membrane-bound protease blood clotting reactions, including proteolytic activation of fX by the TF:fVIIa complex [5], inactivation of fVa by activated protein C [6], activation of prothrombin by the fVa:fXa (prothrombinase) complex [7] and activation of fX by the fVIIIa:fIXa (intrinsic tenase) complex [8]. Of the four major plasma membrane phospholipids, PC and sphingomyelin are abundant on the outer surface while PS and PE are actively sequestered to the inner leaflet (Figure 4.1A). Cell lysis, damage or activation causes externalization of PS and PE, which promotes clotting reactions [9]. PE is considerably more abundant than PS, so the ability of small amounts of PS to support blood clotting reactions in the presence of larger amounts of PE represents a more physiologic environment for assembling clotting reactions.

How PE "synergizes" with PS is not known, but Zwaal et al. [3] and Gilbert & Arena [8] have summarized the following hypotheses from the literature: **PE-1:** PE, being a non-lamellar phospholipid, induces the formation of PS-rich microdomains which are more efficient in supporting clotting reactions. **PE-2:** Clotting proteins contain binding site(s) for PE (or a combination of PE and PS). **PE-3:** PE has hydrogen bond donors but PC does not; when PE forms hydrogen bonds with adjacent PS molecules it induces PS headgroup conformations that

are more favorable for binding to clotting proteins. **PE-4:** The PC headgroup is so bulky and highly hydrated [10,11] that it sterically hinders access of GLA domains to adjacent PS molecules.

Our previous studies demonstrated approximately one fX membrane-binding site for every 6 to 8 PS molecules, which is about equal to a GLA domain's membrane footprint [15]. Here we present a novel, general explanation for GLA domain interactions with membranes which we term the *Anything But Choline (ABC)* hypothesis, triggered by detailed molecular dynamics (MD) simulations of GLA domains associating with PS-containing bilayers (Figure 4.1B) [13,16]. The ABC hypothesis proposes two key types of GLA domain-phospholipid interactions: A single "phospho-L-serine-specific" binding site per GLA domain (Figure 4.1C,D), and multiple "phosphate-specific" interactions, in which phospholipid headgroups bend to allow their phosphates to form coordination complexes with tightly bound Ca^{2+} in the GLA domain (Figure 4.1E). The unique "phospho-L-serine-specific" binding site was independently identified in the crystal structure of lyso-PS bound to the prothrombin GLA domain (Figure 4.1C) [14] and in MD simulations of fVIIa GLA domain binding to PS-bilayers (Figure 4.1D) [13]. The proposed "phosphate-specific" interactions have been repeatedly observed in our MD simulations of GLA domains associating with PS-containing bilayers [13,16]. We propose that PS can provide both interactions, while PC can provide neither (because its bulky choline headgroup sterically hinders access of proteins to its own phosphate moiety). PE can provide phosphate-specific but not phospho-L-serine-specific interactions, explaining why PE/PC bilayers poorly support clotting, while PE synergizes with small amounts of PS.

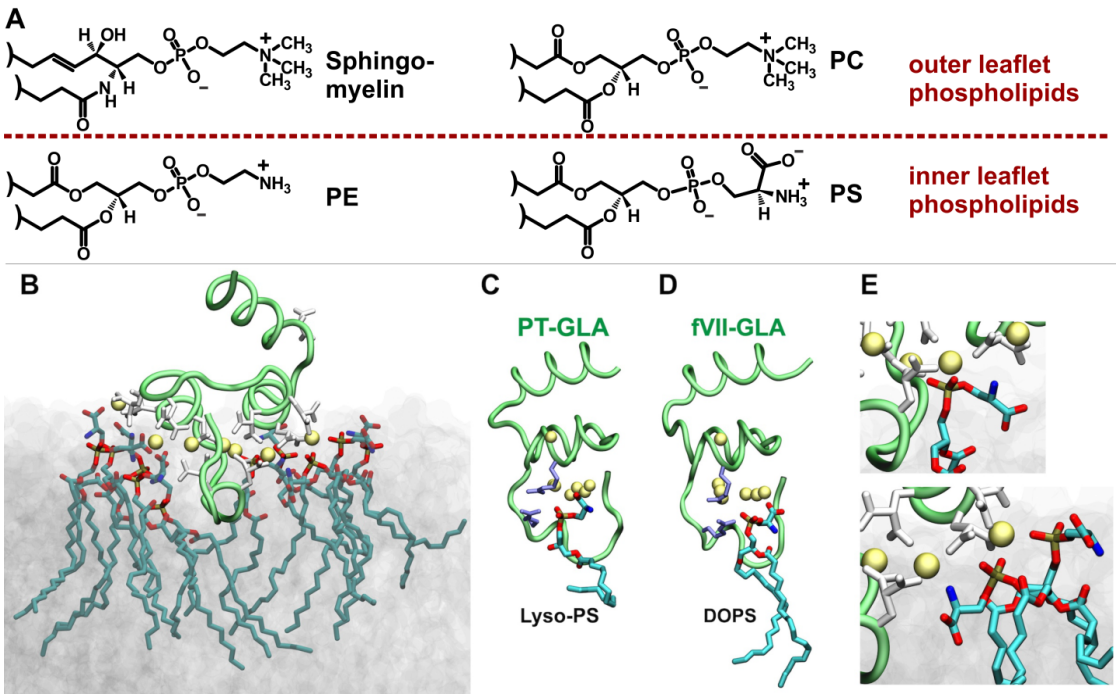

Figure 4.1 GLA domain-PS interactions.
(*A*) Depicted are the four most abundant plasma membrane phospholipids. Sphingomyelin and PC are abundant in the outer leaflet, while PS and PE are largely restricted to the inner leaflet; this membrane asymmetry is lost following platelet activation or cellular trauma [12]. (*B*) Membrane-bound model of the human fVII GLA domain obtained from MD simulations on the surface of a PS bilayer [13]. GLA domain backbone is a green tube, Gla residues are white, tightly bound Ca^{2+} are yellow spheres, and interacting PS are in stick representation. (*C*,*D*) The proposed phospho-L-serine-specific binding site independently observed in (*C*) the crystal structure of bovine prothrombin fragment 1 (PDB 1NL2 [14]) and (*D*) our MD simulations of the fVIIa GLA domain-membrane complex [13].). In *C* and *D*, two Arg contributing to the site are purple sticks and the uniquely bound lyso-PS and DOPS molecules are drawn using stick representations. (*E*) Examples of two phosphate-specific interactions from *B*.

A strong prediction of the ABC hypothesis is that there is nothing unique about the ethanolamine headgroup in PE other than that it is not as bulky as PC. Thus, any phospholipid whose headgroup can bend to allow its phosphate to contribute phosphate-specific interactions with GLA domains should synergize with PS, a prediction inconsistent with the PE-specific hypotheses outlined above. In this study, we use a combination of biochemical techniques, solid-state NMR (SSNMR) analyses and MD simulations to compare the predictions of the ABC hypothesis versus PE-specific hypotheses to explain how phospholipids synergize to support fX activation by TF:fVIIa.

4.4 Materials and Methods

4.4.1 Materials

Diacylglycerol (DAG) and phospholipids (except for D-PS and PS*) were from Avanti Polar Lipids (Alabaster, AL); Bio-Beads® SM-2 adsorbent was from Bio-Rad (Hercules, CA); D-serine was from Sigma-Aldrich (St. Louis, MO); U-^{13}C,^{15}N-L-serine was from Cambridge Isotope Laboratories (Andover, MA); human fVIIa was from American Diagnostica (Stamford, CT); bovine prothrombin was from Haematologic Technologies (Essex Junction, VT); human fX and α-thrombin were from Enzyme Research Laboratories (South Bend, IN); and NTA Biacore sensor chips were from GE Healthcare Bio-Sciences (Piscataway, NJ). Recombinant, membrane-anchored TF [15] and the membrane scaffold protein for Nanodisc production [17] were expressed in *E. coli* and purified as described. PS with D-serine (D-PS) and PS* were synthesized from natural isotopic abundance POPC via phospholipase D-catalyzed headgroup exchange, using either D-serine (for D-PS) or U-^{13}C,^{15}N-L-serine (for PS*), as previously described [18]. Prothrombin fragment 1 was prepared by digestion of bovine prothrombin with human α-thrombin and purified by ion-exchange and size-exclusion chromatography essentially as described [19].

4.4.2 TF-Liposome Preparation and Measurement of FX Activation

TF was incorporated into liposomes of varying phospholipid composition as described previously [20] using Bio-Beads® SM-2 and 20mM sodium deoxycholate. Initial rates of fX activation by TF:fVIIa assembled on TF-liposomes were quantified as described previously [15,21], typically using 100 nM fX, 5 pM fVIIa, and 500 pM TF.

4.4.3 SPR Analyses of FX Binding to Nanoscale Bilayers

TF-free Nanodiscs of varying phospholipid composition were prepared as described [15]. FX binding affinities for nanoscale bilayers were quantified using SPR analyses (on a Biacore 3000 instrument) as described, with Nanodiscs immobilized on Ni^{2+}-NTA sensor chips via the oligohistidine tag on the membrane scaffold protein [15]. As previously reported, binding isotherms were plotted from maximal, steady-state RU values versus the fX concentration flowed over the chip surface, from which K_d values were derived by fitting the single-site ligand binding equation to the data [15].

4.4.4 MAS-SSNMR Spectroscopy

SSNMR studies were performed on Varian (Fort Collins, CO) InfinityPlus spectrometers. POPS*/POPC Nanodisc spectra were acquired at 600 MHz with a Varian T3 HXY 3.2 mm probe at an MAS rate of 10,000 ± 3 Hz or 13,333 ± 2 Hz. The variable temperature gas was maintained at 90 ± 10 scfh flow, and the reported sample temperatures take into account thermocouple calibration and frictional heating due to MAS, calibrated with ethylene glycol [22]. All experiments utilized tangent ramped cross-polarization[23] with TPPM decoupling[24] at ~80 kHz nutation frequency.

4.4.5 MD Simulation

Four bilayers each composed of 1,188 lipids and solvated by water at approximately a 43:1 water/lipid ratio were simulated. The bilayers were all composed of palmitoyloleoyl (PO) phospholipids, but with different headgroups, namely PE, CH_3-PE, $(CH_3)_2$-PE, and PC, respectively. All simulations were performed using NAMD2[25], utilizing the CHARMM22 force field with ϕ/ψ cross term map (CMAP) corrections[26] for proteins and CHARMM36 parameters for lipids[27]. The TIP3 model[28] was used for water. All simulations were performed using an NPT

ensemble at 1.0 atm and 298 K, and with a time step of 2 fs. Constant pressure was maintained using the Nosé-Hoover Langevin piston method [29,30], while constant temperature was maintained by Langevin dynamics using a damping coefficient γ of 0.5 ps^{-1} applied to all heavy atoms. Non-bonded interactions were cut off after 12 Å with a smoothing function applied after 10 Å. The particle mesh Ewald (PME) method[31] was used for long-range electrostatic calculations with a grid density greater than 1 $Å^{-3}$. As a measure of accessibility, solvent accessible surface area (SASA) of the lipid phosphates was calculated in VMD [32], where a probe of a specified radius representing molecular species of various sizes is rolled over the phosphate groups and the surface available for direct contact with the probe is integrated. Molecular images were generated using VMD [32].

4.5 Results

4.5.1 Many Phospholipids Synergize with PS to Enhance FX Activation by TF:FVIIa

The ABC hypothesis predicts that many phospholipids can synergize with PS to enhance fX activation by TF:fVIIa, while PE-centric hypotheses rely on specific properties of the ethanolamine headgroup. (Here we refer to PS with the usual L-serine in its headgroup as L-PS, and PS with D-serine as D-PS.) To test these hypotheses, we measured rates of fX activation by TF:fVIIa on TF-liposomes containing binary lipid mixtures (0-30% L-PS; balance = PC), or ternary lipid mixtures in which the sum of L-PS plus the other test lipid equaled 30% (balance = 70% PC). Lipids tested included PE, phosphatidylglycerol (PG), phosphatidylinositol (PI), phosphatidic acid (PA) and D-PS.

Consistent with our previous report [5], PE strongly synergized with L-PS to support fX activation, left-shifting the L-PS response relative to L-PS/PC liposomes (Figure 4.2A). PG also strongly synergized with L-PS while supporting very low rates of fX activation in the absence of

L-PS (figure 3.2A). On the other hand, PE did not synergize with PG, as the effects of these lipids were strictly additive (Figure 4.2B). This is consistent with the ABC hypothesis, which predicts the same role for PE and PG — i.e., providing phosphate-specific interactions. Figs. 2A and B employed dioleoyl (DO-) phospholipids to ensure that they were always above the phase transition, since palmitoyloleoyl PE (POPE) has a relatively high transition temperature. For other phospholipid mixtures, we used palmitoyloleoyl (PO-) phospholipids; the results (cf. Figs. 2A and 2C) confirm that PG synergizes with L-PS equally well whether PO- or DO-phospholipids were employed. Phospholipid synergy is thus independent of any subtle bilayer packing differences due to DO- versus PO-phospholipids. PA and PI also strongly synergized with L-PS while supporting very low rates of fX activation in the absence of L-PS (Figure 4.2C). Taken together, these results demonstrate that PE's ethanolamine moiety is not required for phospholipid synergy, as lipids with very different headgroups synergized equally well with L-PS

Components of the prothrombinase and fVIIIa:fIXa complexes bind much more weakly to membranes if L-PS is replaced by D-PS (reviewed by Zwaal et al. 3). To our knowledge, PS headgroup stereospecificity has not been examined for fX activation by TF:fVIIa. We prepared TF-liposomes with binary lipid mixtures (0-30% L-PS, balance = PC), or ternary lipid mixtures of a total of 30% L-PS + D-PS (balance = 70% PC). D-PS poorly supported fX activation on its own, but it strongly synergized with L-PS (Figure 4.2C). This is fully consistent with the ABC hypothesis, since D-PS should not support phospho-L-serine specific interactions but should provide phosphate-specific interactions with GLA domains.

4.5.2 PG and D–PS Synergize with L–PS to Enhance FX Binding to Membranes

Multiple protein-phospholipid interactions are present when TF:fVIIa activates fX, but the dominant membrane contribution to catalysis appears to be fX binding to membranes

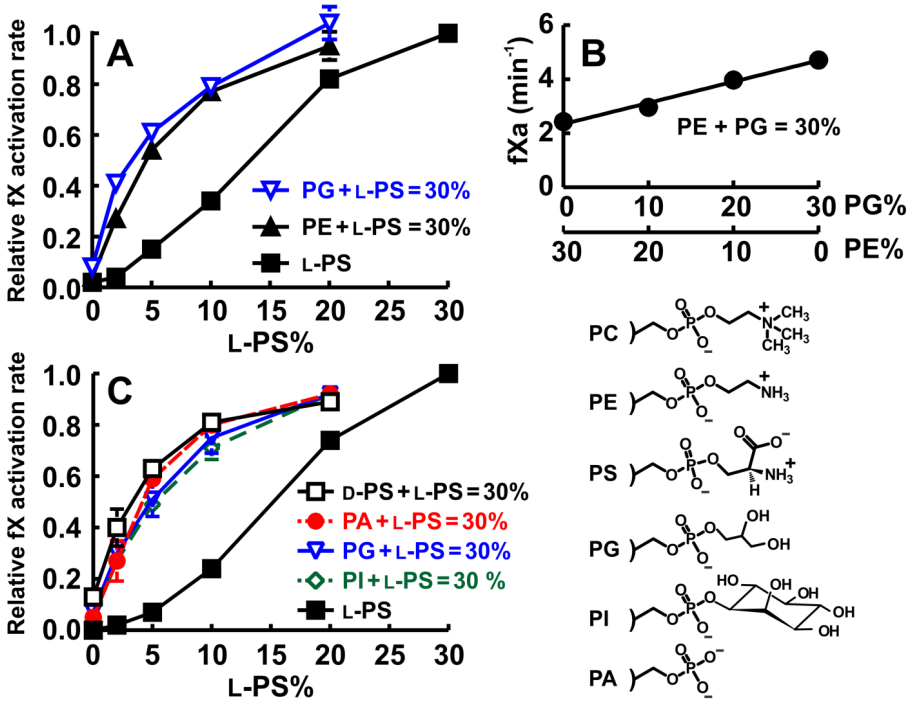

Figure 4.2 All tested glycerophospholipids synergize with L-PS to enhance fX activation by TF:fVIIa on liposomes, but PE does not synergize with PG.
(*A*) Normalized rates of fX activation by fVIIa on TF-liposomes prepared with binary lipid mixtures (0-30% L-DOPS; balance = DOPC), or ternary lipid mixtures in which the sum of L-DOPS plus DOPE or DOPG equaled 30% (balance = 70% DOPC). (*B*) Rates of fX activation by fVIIa on TF-liposomes prepared with ternary lipid mixtures in which the sum of DOPG + DOPE equaled 30% (balance = 70% DOPC). (*C*) Normalized rates of fX activation by fVIIa on TF-liposomes prepared with binary lipid mixtures (0-30% L-POPS; balance = POPC), or ternary lipid mixtures in which the sum of L-POPS plus the other test lipid equaled 30% (balance = 70% POPC). Lipids tested included phosphatidylglycerol (POPG), phosphatidylinositol (POPI), phosphatidic acid (POPA) and D-POPS. FX activation rates for each TF-liposome preparation in panels A and C were normalized to the rate with 30% L-PS/70% PC. Data are mean ± standard error; n = 3 to 10. Headgroup structures for lipids in this experiment are included on the right.

adjacent to TF:fVIIa [15]. We therefore quantified fX binding to nanobilayers using surface plasmon resonance (SPR) as described [15]. Consistent with our previous findings, the K_d for fX binding to Nanodiscs decreased with increasing L-PS content. The L-PS dose-response was left-shifted in the presence of 40% PG (Figure 4.3A), demonstrating that PG synergizes with L-PS to

support fX binding to bilayers. We also examined fX binding to nanobilayers containing either 50% L-PS, 50% D-PS, or 25% L-PS + 25% D-PS (balance in all cases = 50% PC; Figure 4.3B). FX bound less to bilayers with 50% D-PS compared to 50% L-PS, while bilayers with 25% L-PS + 25% D-PS performed as well as those with 50% L-PS. Thus, D-PS synergizes with L-PS to enhance membrane binding of fX.

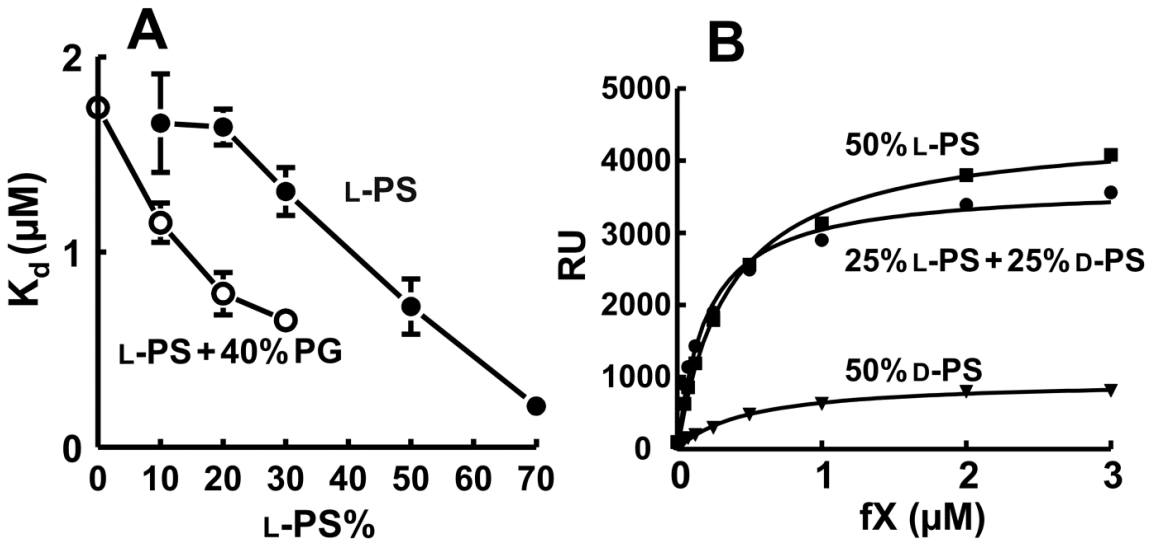

Figure 4.3 PG and D-PS synergize with L-PS to enhance fX membrane binding.
(*A*) Binding affinities of fX to Nanodiscs with varying L-POPS content with or without 40% POPG (balance = POPC). Nanodiscs were immobilized on Biacore sensorchips, after which steady-state levels of fX binding were quantified; K_d values were derived from the resulting binding isotherms. Data are mean ± standard error; $n = 3$. (*B*) Steady-state binding of fX to nanoscale bilayers, quantified by SPR, using Nanodiscs with 50% POPC and either 50% L-POPS, 50% D-POPS, or 25% L-POPS + 25% D-POPS.

4.5.3 Methylation of PE Headgroups Diminishes Synergy

PC differs from PE by three N-methyl groups (cf. Figure 4.4). We therefore asked how the presence of one or two N-methyl groups on PE would affect synergy with L-PS, using TF-liposomes containing binary lipid mixtures (0-30% L-PS, balance = PC), or ternary lipid mixtures of 0-30% L-PS plus either 30% PE, 30% N-monomethyl PE or 30% N-dimethyl PE

(balance = PC). The results (Figure 4.4A) show a progressive diminution in synergy when one or two N-methyl groups are added to PE.

4.5.4 Importance of the Phosphate Groups of Phospholipids for Synergy

The experiment in Figure 4.2C showed that PA synergized well with L-PS to support fX activation. We next asked whether PA's phosphate is required, by comparing the ability of PA and diacylglycerol (DAG) to synergize with L-PS to enhance fX activation by TF:fVIIa. TF-liposomes were prepared containing binary lipid mixtures (0-30% L-PS, balance = PC), or ternary lipid mixtures of either a total of 30% PA + L-PS, or a total of 30% DAG + L-PS (balance = PC). DAG, which lacks a phosphate group, weakly synergized with L-PS compared to robust synergy with PA (Figure 4.4B).

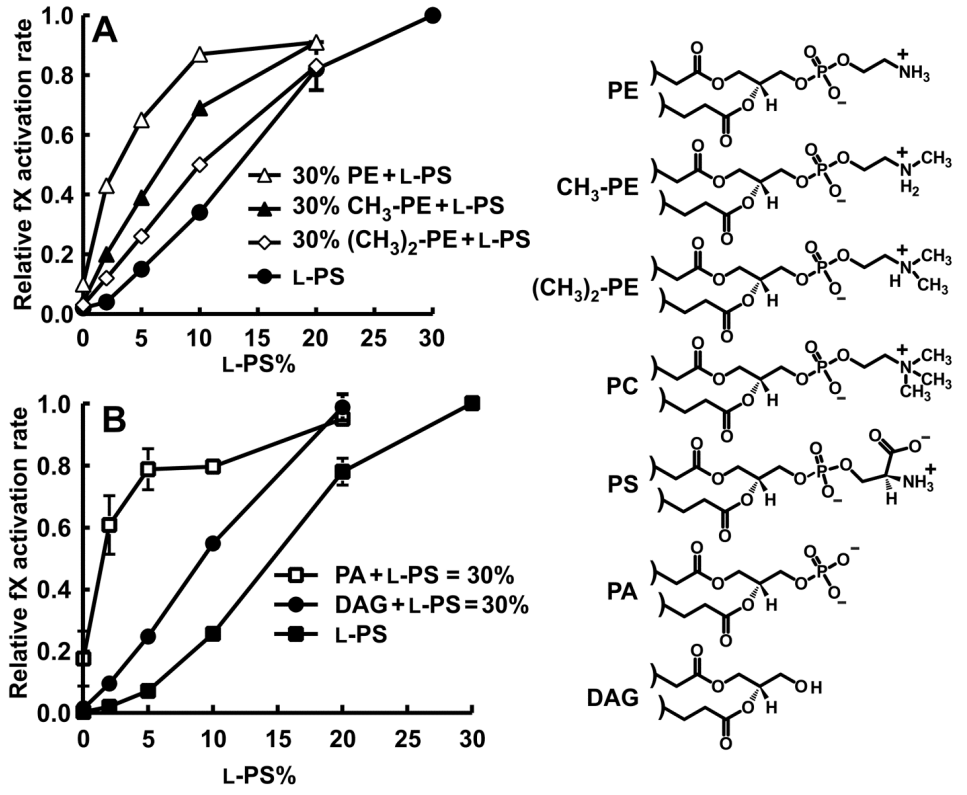

Figure 4.4 Influence of PC methyl groups and PA phosphate on fX activation by TF:fVIIa.

(A) Rates of fX activation by fVIIa on TF-liposomes prepared with varying L-DOPS and either no DOPE, 30% DOPE, 30% CH_3-DOPE or 30% $(CH_3)_2$-DOPE (balance = DOPC). (*B*) Rates of fX activation by fVIIa on TF-liposomes prepared with binary lipid mixtures (0-30% L-POPS; balance = POPC), or ternary lipid mixtures in which the sum of L-POPS plus either POPA or DAG equaled 30% (balance = 70% PC). (DAG had palmitoyloleoyl acyl chains.) In both panels, fX activation rates for each TF-liposome preparation were normalized to the rate with 30% L-PS/70% PC; data are mean ± standard error; n = 3 to 7. Headgroup structures for lipids in this experiment are included on the right. (B)

4.5.5 MD Simulations of Phosphate Accessibility in Bilayers

To investigate the molecular basis of phospholipid synergy, especially in terms of the accessibility of lipid phosphate groups, four independent 40 ns MD simulations of bilayers were performed in which the lipid headgroups were progressively transformed from PE to N-monomethyl PE, N-dimethyl PE and PC, paralleling the experimental setting in Figure 4.4. Each simulation included 1,188 lipids distributed equally in the two leaflets to provide statistically meaningful data. Analyses of solvent accessible surface areas (SASA; Figure 4.5) clearly show that each N-methyl group diminished the accessibility of the phosphate group for all probes with radii >1.5 Å (approximately the size of water), with the difference in phosphate exposure also being evident from top-view snapshots shown for representative frames taken from the simulations (Figure 4.5, bottom). Although protein binding to membranes may induce lipid rearrangement, these measurements clearly show that the choline headgroup of PC sterically hinders access to PC's phosphate group.

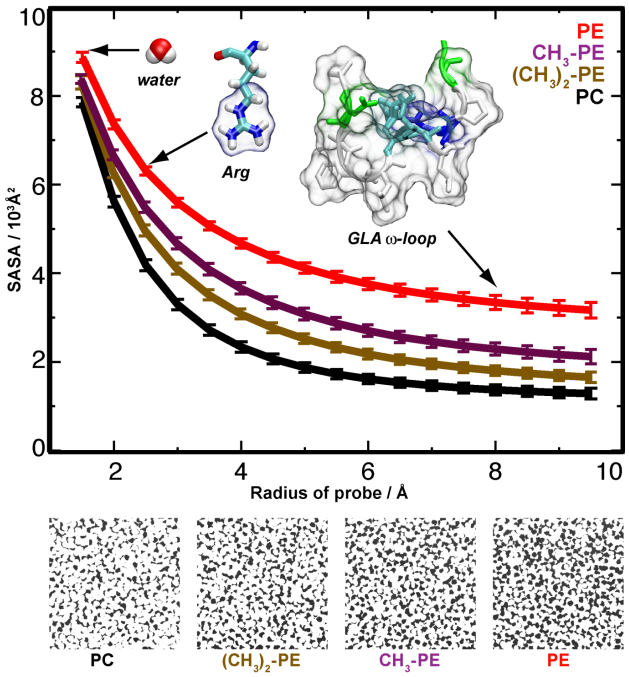

Figure 4.5 MD simulations show that PC has restricted phosphate accessibility.
(*Top*) MD simulations showing that adding N-methyl groups to PE reduces the solvent-accessible surface areas (SASA) of the phosphate group: PE (red), CH_3-PE (magenta), $(CH_3)_2$-PE (brown), and PC (black). SASA are calculated using varying probe radii for the last 20 ns of 40 ns MD simulations of 1,188 lipids. For comparison, water (radius 1.4 Å), Arg (guanidinium group radius ~2.5 Å), and the fVIIa GLA domain ω-loop (radius ~8 Å) are shown, in order to compare the results to the approximate size of functional groups that could interact with the phosphate groups. (*Bottom*) Visual comparison of phosphate exposure in the bilayer simulations (phosphate is black; remainder of the lipid is white).

4.5.6 SSNMR Evidence for a New PS Chemical Environment Induced by GLA Domains

We recently showed, using magic angle spinning SSNMR, that Ca^{2+} induces two distinct, equally populated conformations of L-PS headgroups in close spatial proximity, consistent with Ca^{2+} promoting L-PS clusters [18]. In the present study, we employed this approach to investigate PS-GLA domain binding interactions, using PS with uniformly ^{13}C,^{15}N labeled L-serine (termed PS*) incorporated into Nanodiscs. When L-PS engages a GLA domain's proposed phospho-L-serine-specific binding site, its headgroup should take up a unique conformation observable by SSNMR. 2-D ^{13}C-^{13}C spectra were acquired of 30% PS*/70% PC Nanodiscs prepared with Ca^{2+} in the absence (Figure 4.6, blue trace) or presence (red trace) of saturating levels of prothrombin fragment 1 (which contains the GLA domain).

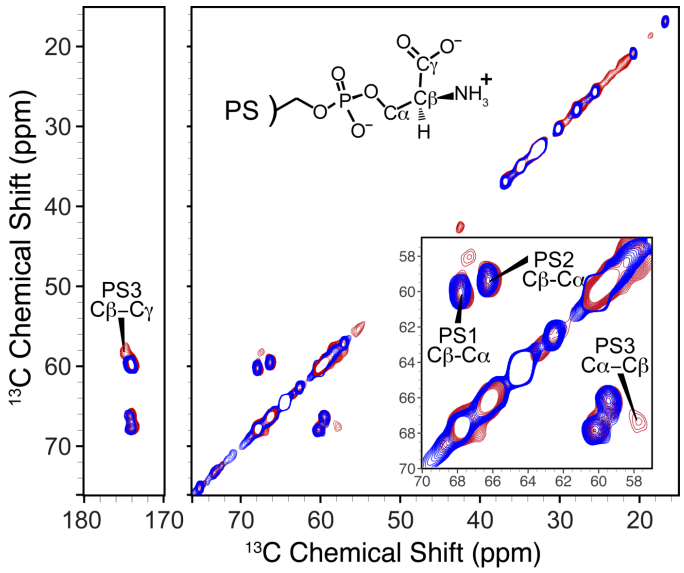

Figure 4.6 SSNMR spectroscopy demonstrates a novel PS headgroup environment induced upon GLA domain binding to bilayers.
A ^{13}C-^{13}C 2-D SSNMR spectrum in *blue* of 30% POPS*/70%POPC Nanodiscs (25 ms DARR mixing; 2.6 hr at 13 °C; 13.333 kHz MAS rate). Overlaid in *red* is a spectrum of 30% POPS*/70% POPC Nanodiscs in the presence of prothrombin fragment 1 (50 ms DARR mixing; 50 hr at 13 °C; 10.000 kHz MAS rate). Both spectra were acquired on a 600 MHz (^{1}H frequency) spectrometer. Insert is an expansion of serine Cα-Cβ regions. PS1 and PS2 represent equally abundant chemical environments for PS headgroups in the presence of Ca^{2+}, while PS3 represents a novel PS headgroup environment induced by Ca^{2+} plus prothrombin fragment 1.

In the presence of fragment 1, we observed a new correlation pattern at 58, 67, and 175 ppm, corresponding to a new chemical environment for L-PS headgroups (termed PS3 in Figure 4.6). This is in addition to the two nearly equally populated, Ca^{2+}-induced headgroup configurations termed PS1 and PS2 that we also observed in our previous study [18]. The individual cross-peaks made up the following fractions of the total L-PS intensities: PS1, 42±3%; PS2, 41±2%; and PS3, 17±2%. SPR studies and MD simulations suggest that 6-8 L-PS molecules constitute a GLA domain binding site [13,15]. The observation that 17±2% of the L-PS headgroups are found in the PS3 chemical environment upon GLA domain binding is consistent with the idea that one L-PS molecule per GLA domain is involved in the phospho-L-serine-specific binding interaction, with the rest of the PS molecules participating in phosphate-specific interactions (as depicted in Figure 4.1).

4.6 Discussion

The impetus for this study was to explain why PE, a relatively abundant plasma membrane phospholipid, poorly supports clotting reactions in bilayers composed of binary mixtures of PE and PC, but strongly promotes clotting reactions when small amounts of PS are also included. We reasoned that solving this conundrum would allow us to develop a general mechanism for how GLA domains interact with PS-containing membranes. To investigate this question, we studied fX activation by TF:fVIIa assembled on liposomes with a wide variety of lipid compositions. Existing hypotheses to explain PE/PS synergy (PE-1 to PE-4, above) focus on specific properties of PE's ethanolamine headgroup. In contrast, the ABC hypothesis proposes that GLA domains bind to bilayers via a single phospho-L-serine-specific binding interaction together with multiple phosphate-specific interactions. In binary PS/PC mixtures, PS has to provide both types of interaction since the bulky choline moiety of PC sterically hinders GLA domains from interacting with its own phosphate group. (The same situation would also apply to sphingomyelin, whose phosphocholine headgroup is identical to that of PC. Since PC and sphingomyelin are the predominant phospholipids on the outer leaflet of the plasma membrane, and since PS is sequestered to the inner leaflet, this explains the generally anticoagulant surface of healthy, intact cells.) PE collaborates with PS to create membrane binding sites for GLA domains because PE provides the more numerous phosphate-specific interactions, freeing up limited amounts of PS to engage in the single phospho-L-serine-specific interaction per GLA domain. We tested these hypotheses by examining how various phospholipids synergize with PS to enhance fX binding to bilayers, and to enhance fX activation by TF:fVIIa in liposomes. Glycerophospholipids with a wide variety of different headgroups were fully as effective as PE in synergizing with PS, including those with *myo*-inositol (PI),

glycerol (PG), D-serine (D-PS), or even just a bare phosphate (PA). We also found that PE did not synergize with PG in the absence of L-PS; instead, the effects of PE and PG were strictly additive. This is consistent with the ABC hypothesis, which predicts that while PE and PG can both provide phosphate-specific interactions, they cannot provide the essential phospho-L-serine-specific interaction. The fact that TF-liposomes containing binary mixtures of D-PS and PC poorly supported fX activation by TF:fVIIa recapitulates similar findings with prothrombinase and fVIIIa:fIXa [3]. On the other hand, D-PS synergized strongly with L-PS to support TF:fVIIa activity, which is fully consistent with the ABC hypothesis, since D-PS should retain the ability to enter into phosphate-specific interactions with GLA domains.

Hypotheses PE-1 to PE-4 are inconsistent with our findings: 1) PE-1 (i.e., non-lamellar PE promotes PS-rich microdomains) cannot explain our results since both lamellar and non-lamellar phospholipids synergized with PS. Furthermore, the nanoscale bilayers in Nanodiscs preclude long-range clustering of PS into microdomains, yet they strongly supported PG/PS and D-PS/L-PS synergy for fX binding. 2) PE-2 (i.e., PE-specific binding sites in GLA domains) likewise cannot explain our finding that phospholipids with headgroups structurally unrelated to ethanolamine all strongly synergized with PS. In addition, progressive diminution of PE/PS synergy as one or two N-methyl groups were added to PE (by progressively inhibiting access to its own phosphate) is consistent with the ABC hypothesis but inconsistent with PE-2, which predicts an abrupt loss of synergy when the PE ethanolamine is chemically altered. We also showed, using MD simulations, that accessibility of the phosphate groups to objects the size of amino acids or the ω-loop of GLA domains is progressively diminished as the ethanolamine moiety of PE contains one, two or three N-methyl groups. 3) PE-3 (i.e., hydrogen-bonding between PE and adjacent phospholipids alters PS headgroup conformations) is also inconsistent

with our findings, since the various PS-synergizing headgroups tested cannot engage in the same kind of hydrogen bonding interactions that ethanolamine can. 4) PE-4 is the most similar to the ABC hypothesis, the chief difference being that PE-4 proposes that bulky PC sterically hinders access of GLA domains to adjacent PS molecules, while the ABC hypothesis proposes that the PC headgroup sterically hinders access of GLA domains to PC's own phosphate. PE-4 is not completely ruled out by many of the experiments presented here, but DAG (which contains no phosphate group) synergized weakly with PS, compared with full synergy observed with PA. Weak PS synergy with DAG is consistent with the notion that simply removing the bulky choline reduces some steric hindrance to the bilayer in general. However, this experiment argues that lipids need to retain their phosphate moieties in order to synergize fully with PS, in agreement with the ABC hypothesis.

Electrostatics *per se* cannot explain PE/PS synergy, since we observed identical PS synergy with phospholipids having very different net charges, including PE (neutral); D-PS, PI and PG (-1); and PA (-1 to -2). Nor is it necessary for the synergizing phospholipid to be zwitterionic or even to have an amino group, as PA, PI, and PG lack these features. The common feature required for a phospholipid to synergize with PS appears to be a phosphate unshielded by a bulky headgroup.

It is possible that when L-PS engages the phospho-L-serine-specific binding site in a GLA domain, it induces a conformational change in the GLA domain that promotes the phosphate-specific interactions (and in fact PS has been proposed to be an allosteric regulator of clotting protein function [33]). This may help explain why GLA domains bind so weakly to membranes containing relatively high amounts of anionic phospholipids other than L-PS.

Our SSNMR results provide direct evidence for a unique PS headgroup environment induced when a GLA domain binds to PS-containing bilayers. The finding that approximately 1/6 of the total PS* signal intensity is in this chemical environment is fully consistent with the ABC hypothesis, which predicts that about this fraction of the PS molecules in a PS/PC bilayer will be engaged in the single phospho-L-serine-specific binding interaction per GLA domain, provided that a GLA domain binding site consists of about 6 or so PS molecules, a notion which is supported by both our MD simulations (Fig. 3.1B) [13,16] and SPR-based binding studies [15]. Based on these stoichiometries from Nanodisc-based studies, one might expect maximal rates of fX activation on liposomes with approximately 5% L-PS + 25% synergistic phospholipid. When we examined fX activation by TF:fVIIa on TF-liposomes, maximal fX activation generally required somewhat more than 5% L-PS in combination with non-PC phospholipids. One explanation could be that L-PS is more readily clustered into nanodomains in the presence of Ca^{2+} than are other non-PC phospholipids.

This study provides a new explanation for how plasma membrane phospholipids synergize to create binding sites for GLA domain-containing blood clotting proteins, using fX activation by TF:fVIIa as the exemplar. In future studies, it will be interesting to test the predictions of the ABC hypothesis versus PE-specific hypotheses on other membrane-dependent clotting reactions, e.g., activities of the prothrombinase, fVIIIa:fIXa and protein S-activated protein C complexes. The nature of the proposed phospho-L-serine-specific and phosphate-specific binding sites deserve considerably greater scrutiny and are the subject of our ongoing studies aimed at achieving an atomic-scale understanding of the binding of GLA domains to membrane bilayers.

4.7 References

1 Tavoosi, N. *et al*. Molecular Determinants of Phospholipid Synergy in Blood Clotting. *J. Biol. Chem.* **286**, 23247-23253 (2011).

2 Zwaal, R. F., Bevers, E. M. & Rosing, J. Regulation and function of transbilayer movement of phosphatidylserine in activated blood platelets and sickle cells. *Prog. Clin. Biol. Res.* **282**, 181-192 (1988).

3 Zwaal, R. F. A., Comfurius, P. & Bevers, E. M. Lipid-protein interactions in blood coagulation. *Biochim. Biophys. Acta* **1376**, 433-453, (1998).

4 Morrissey, J. H. Tissue factor: a key molecule in hemostatic and nonhemostatic systems. *Int. J. Hematol.* **79**, 103-108 (2004).

5 Neuenschwander, P. F., Bianco-Fisher, E., Rezaie, A. R. & Morrissey, J. H. Phosphatidylethanolamine augments factor VIIa-tissue factor activity: Enhancement of sensitivity to phosphatidylserine. *Biochemistry* **34**, 13988-13993, (1995).

6 Smirnov, M. D. & Esmon, C. T. Phosphatidylethanolamine incorporation into vesicles selectively enhances factor Va inactivation by activated protein C. *J. Biol. Chem.* **269**, 816-819 (1994).

7 Smeets, E. F., Comfurius, P., Bevers, E. M. & Zwaal, R. F. A. Contribution of different phospholipid classes to the prothrombin converting capacity of sonicated lipid vesicles. *Thromb. Res.* **81**, 419-426 (1996).

8 Gilbert, G. E. & Arena, A. A. Phosphatidylethanolamine induces high affinity binding sites for factor VIII on membranes containing phosphatidyl-L-serine. *J. Biol. Chem.* **270**, 18500-18505 (1995).

9 Zwaal, R. F., Comfurius, P. & Bevers, E. M. Surface exposure of phosphatidylserine in pathological cells. *Cell Mol. Life Sci.* **62**, 971-988 (2005).

10 Burgess, S. W., McIntosh, T. J. & Lentz, B. R. Modulation of poly(ethylene glycol)-induced fusion by membrane hydration: importance of interbilayer separation. *Biochemistry* **31**, 2653-2661 (1992).

11 Murzyn, K., Zhao, W., Karttunen, M., Kurdziel, M. & Rog, T. Dynamics of water at membrane surfaces: Effect of headgroup structure. *Biointerphases* **1**, 98-105 (2006).

12 Schroit, A. J. & Zwaal, R. F. Transbilayer movement of phospholipids in red cell and platelet membranes. *Biochim. Biophys. Acta* **1071**, 313-329 (1991).

13 Ohkubo, Y. Z. & Tajkhorshid, E. Distinct structural and adhesive roles of Ca^{2+} in membrane binding of blood coagulation factors. *Structure* **16**, 72-81 (2008).

14 Huang, M. *et al*. Structural basis of membrane binding by Gla domains of vitamin K-dependent proteins. *Nat. Struct. Biol.* **10**, 751-756 (2003).

15 Shaw, A. W., Pureza, V. S., Sligar, S. G. & Morrissey, J. H. The local phospholipid environment modulates the activation of blood clotting. *J. Biol. Chem.* **282**, 6556-6563 (2007).

16 Ohkubo, Y. Z., Morrissey, J. H. & Tajkhorshid, E. Dynamical view of membrane binding and complex formation of human factor VIIa and tissue factor. *J. Thromb. Haemost.* **8**, 1044-1053 (2010).

17 Bayburt, T. H., Grinkova, Y. V. & Sligar, S. G. Self-assembly of discoidal phospholipid bilayer nanoparticles with membrane scaffold proteins. *Nano Lett.* **2**, 853-856 (2002).

18 Boettcher, J. M., Davis-Harrison, R. L., Clay, M. C., Nieuwkoop, A. J., Ohkubo, Y. Z., Tajkhorshid, E., Morrissey, J. H. & Rienstra, C. M. Atomic view of calcium-induced clustering of phosphatidylserine in mixed lipid bilayers. *Biochemistry* **50**, 2264-2273 (2011).

19 McDonald, J. F. *et al*. Comparison of Naturally Occurring Vitamin K-Dependent Proteins: Correlation of Amino Acid Sequences and Membrane Binding Properties Suggests a Membrane Contact Site†. *Biochemistry* **36**, 5120-5127 (1997).

20 Smith, S. A. & Morrissey, J. H. Rapid and efficient incorporation of tissue factor into liposomes. *J Thromb Haemost* **2**, 1155-1162 (2004).

21 Waters, E. K. & Morrissey, J. H. Restoring full biological activity to the isolated ectodomain of an integral membrane protein. *Biochemistry* **45**, 3769-3774 (2006).

22 Shin, J. J. H. & Loewen, C. J. R. Putting the pH into phosphatidic acid signaling. *BMC Biol.* **9**, doi:Artn 85Doi 10.1186/1741-7007-9-85 (2011).

23 Young, B. P. *et al*. Phosphatidic Acid Is a pH Biosensor That Links Membrane Biogenesis to Metabolism. *Science* **329**, 1085-1088 (2010).

24 Nelsestuen, G. L. Enhancement of Vitamin-K-Dependent Protein Function by Modification of the γ-Carboxyglutamic Acid Domain: Studies of Protein C and Factor VII. *Trends Cardiovasc. Med.* **9**, 162-167 (1999).

25 Smirnov, M. D. & Esmon, C. T. Phosphatidylethanolamine incorporation into vesicles selectively enhances factor Va inactivation by activated protein C. *J. Biol. Chem.* **269**, 816-819 (1994).

26 Zwaal, R. F., Comfurius, P. & Bevers, E. M. Lipid-protein interactions in blood coagulation. *Biochim. Biophys. Acta* **1376**, 433-453 (1998).

27 Bevers, E. M., Comfurius, P., Dekkers, D. W., Harmsma, M. & Zwaal, R. F. Transmembrane phospholipid distribution in blood cells: control mechanisms and pathophysiological significance. *Biol. Chem.* **379**, 973-986 (1998).

28 van Dieijen, G., Tans, G., Rosing, J. & Hemker, H. C. The role of phospholipid and factor VIIIa in the activation of bovine factor X. *J. Biol. Chem.* **256**, 3433-3442 (1981).

29 Rosing, J., Tans, G., Govers-Riemslag, J. W., Zwaal, R. F. & Hemker, H. C. The role of phospholipids and factor Va in the prothrombinase complex. *J. Biol. Chem.* **255**, 274-283 (1980).

30 Gerads, I., Govers-Riemslag, J. W., Tans, G., Zwaal, R. F. & Rosing, J. Prothrombin activation on membranes with anionic lipids containing phosphate, sulfate, and/or carboxyl groups. *Biochemistry* **29**, 7967-7974 (1990).

31 Rosing, J., Tans, G., Speijer, H. & Zwaal, R. F. Calcium-independent activation of prothrombin on membranes with positively charged lipids. *Biochemistry* **27**, 9048-9055 (1988).

32 Shah, A. M., Kisiel, W., Foster, D. C. & Nelsestuen, G. L. Manipulation of the membrane binding site of vitamin K-dependent proteins: Enhanced biological function of human factor VII. *Proceedings of the National Academy of Sciences* **95**, 4229-4234 (1998).

33 Rosing, J., Speijer, H. & Zwaal, R. F. Prothrombin activation on phospholipid membranes with positive electrostatic potential. *Biochemistry* **27**, 8-11 (1988).

CHAPTER 5

Amphotericin Forms an Extramembranous and Fungicidal Sterol Sponge

5.1 Notes and Acknowledgements

This chapter is adapted from "Amphotericin forms an extramembranous and fungicidal sterol sponge." *Nature Chemical Biology*, volume 10, 2014, pages 400 – 406, authors: Anderson, T. M.*; **Clay.M. C.***; Cioffi, A. G.; Diaz, K. A.; Hisao, G. S.; Tuttle, M. D.; Nieuwkoop, A. J.; Comellas, G.; Maryum, N.; Wang, S.; Uno, B. E.; Wildeman, E. L.; Gonen, T.,; Rienstra, C. M.; Burke, M. D. (* These authors contributed equally to this work). Portions of this work were supported by the NIH (R01GM080436, F30DK081272), the University of Illinois at Urbana-Champaign (Centennial Scholar Award to C.M.R.). M.D.B. is an HHMI Early Career Scientist. M.C.C. is an American Heart Association Predoctoral Fellow. T.M.A. is a Ruth L. Kirchstein NIH NRSA Predoctoral Fellow. The Gonen lab is funded by the Howard Hughes Medical Institute. Paul J. Hergenrother and Eric Oldfield are gratefully acknowledged for helpful discussions, and Dr. Jakob J. Lopez is thanked for preliminary spin diffusion SSNMR experiments.

5.2 Abstract

Amphotericin has remained the powerful but highly toxic last line of defense in treating life-threatening fungal infections in humans for over 50 years with minimal development of microbial resistance. Understanding how this small molecule kills yeast is thus critical for guiding development of derivatives with an improved therapeutic index and other resistance-refractory antimicrobial agents. In the widely accepted ion channel model for its mechanism of

cytocidal action, amphotericin forms aggregates inside lipid bilayers that permeabilize and kill cells. In contrast, we report that amphotericin exists primarily in the form of large, extramembranous aggregates that kill yeast by extracting ergosterol from lipid bilayers. These findings reveal that extraction of a polyfunctional lipid underlies the resistance-refractory antimicrobial action of amphotericin and suggests a roadmap for separating its cytocidal and membrane-permeabilizing activities. This new mechanistic understanding is also guiding development of the first derivatives of amphotericin that kill yeast but not human cells.

5.3 Introduction

The incidence of life-threatening systemic fungal infections continues to rise in parallel with expanding populations of immunocompromised patients.[1] Substantially exacerbating this problem is the concomitant rise in pathogen resistance to almost all clinically approved antifungal agents. In contrast, amphotericin B (AmB) (Fig. 5.1a) has served as the gold standard treatment for systemic fungal infections for over five decades with minimal development of clinically significant microbial resistance.[2] This exceptional track record reveals that resistance-refractory modes of antimicrobial action exist, and the mechanism by which AmB kills yeast is one of them. However, because of the often dose-limiting toxicity of this natural product, mortality rates for systemic fungal infections persist near 50%.[3] Improving the notoriously poor therapeutic index of this drug and the development of other resistance-refractory antimicrobial agents thus represent two critically important objectives that stand to benefit from a clarified molecular description of the biological activities of AmB. Moreover, an advanced understanding of the biophysical interactions of this natural product within living systems would enable more effective utilization of its remarkable capacity to perform ion channel-like functions.

For decades, the prevailing theory has been that AmB primarily exists in the form of

small ion channel aggregates that are inserted into lipid bilayers and thereby permeabilize and kill yeast cells (Fig. 5.1b).[4-23] An extensive series of structural and biophysical studies, including those employing planar lipid bilayers,[4-10] liposome permeability,[9-13,17] Corey-Pauling-Kulton (CPK) modeling,[7-9] UV/Vis spectroscopy,[9-11,13,21] circular dichroism,[10,11,13,21] fluorescence spectroscopy,[9,11] Raman spectroscopy,[10] differential scanning calorimetry,[9,10,21] chemical modifications,[11-14,17] atomic force microscopy,[21] transmission electron microscopy,[20] computer modeling,[11,15] electron paramagnetic resonance,[10] surface plasmon resonance,[22] solution NMR spectroscopy,[11] and solid-state NMR (SSNMR)[16-19] spectroscopy have been interpreted through the lens of this ion channel model. Importantly, this model suggests that the path to an improved therapeutic index requires selective formation of ion channels in yeast versus human cells,[10-20] that the search for other resistance-refractory antimicrobials should focus on membrane-permeabilizing compounds,[24] and that the ion channel-forming and cytotoxic activities of AmB cannot be separated.

Recent studies show that the channel forming capacity of AmB is not required for fungicidal activity, whereas binding ergosterol (Erg) (Fig. 5.1a) is essential.[25-27] However, the structural and biophysical underpinnings of this rare type of small molecule-small molecule interaction and its connection to cell killing all remained unclear. Sterols, including Erg in yeast, play many essential roles in eukaryotic cell physiology, including functional regulation of membrane proteins, microdomain formation, endocytosis, vacuole fusion, cell division, and cell signaling.[28-31] We thus hypothesized that sequestering Erg and thereby concomitantly precluding its participation in multiple cellular functions may underlie the fungicidal action of AmB.

Guided by this hypothesis, we considered three possible models for the primary structure and function of AmB in the presence of Erg-containing phospholipid membranes (Fig. 5.1b-d):

(i) In the classic channel model, AmB primarily exists in the form of small (~1 nm) ion channel aggregates inserted into the membrane, perpendicular to the membrane surface, with Erg molecules interdigitated between AmB molecules (Fig. 1b).[7-9,11,12,15-19,22,23] (ii) In an alternative surface adsorption model, AmB is primarily positioned in the intermediate/headgroup region,

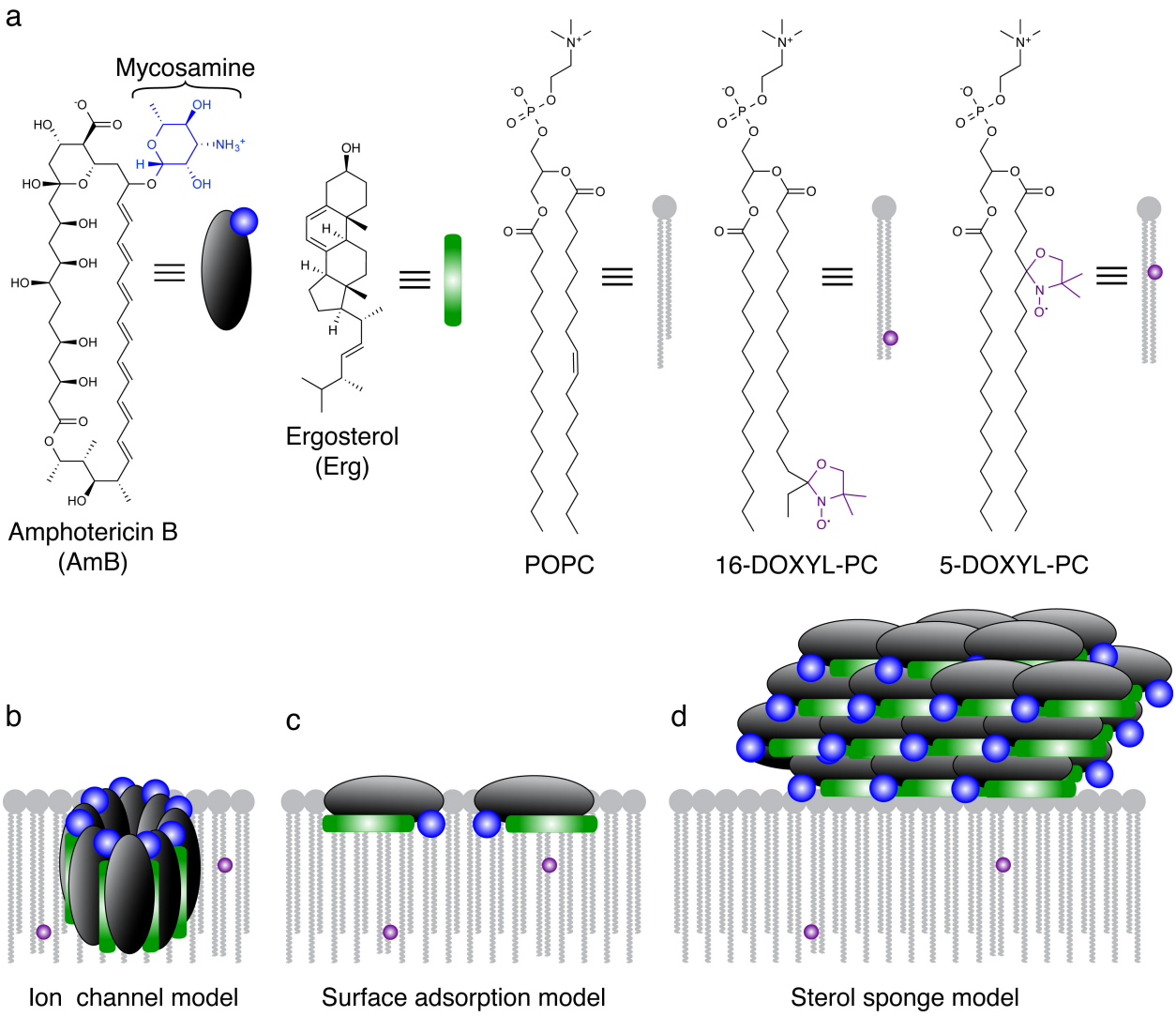

Figure 5.1 Models for the structure and function of AmB in the presence of lipid bilayers.
a, Structures of AmB, Erg, POPC, and paramagnetic probes 5-DOXYL-PC and 16-DOXYL-PC. 5-DOXYL and 16-DOXYL position a paramagnetic functional group at depths of ~12 and ~25 Å within the lipid bilayer, respectively. **b**, The classic ion channel model for the structure and function of AmB. **c**, Surface adsorption model. **d**, A new sterol sponge model, in which AmB primarily exists in the form of large extramembranous aggregates that extract Erg from lipid bilayers.

oriented parallel to the plane of the membrane, sequestering Erg to the membrane surface (Fig.

5.1c).[9,22] (iii) In a new sterol sponge model, AmB primarily exists as large extramembranous aggregates that extract Erg from lipid bilayers (Fig. 5.1d). In the latter two models, we envisioned that membrane-permeabilizing ion channels represent relatively minor contributors to both the structure and cytocidal activity of AmB. Here we report an extensive series of SSNMR, transmission electron microscopy (TEM), and cell-based experiments that all support the new sterol sponge model (Fig. 1d).

5.4 Materials and Methods

5.4.1 General Methods

Materials

Commercially available materials were purchased from Sigma-Aldrich, Alfa Aesar, Avanti Polar Lipids, Cambridge Isotope Laboratories, or Fisher Scientific and were used without further purification unless stated otherwise. Natural abundance amphotericin (AmB) was purchased from Sigma-Aldrich or a gift from Bristol-Myers Squibb Company. Unless stated otherwise, all solvents were dispensed from a solvent purification system that passes solvents through packed columns according to the method of Pangborn and coworkers[52] (THF, Et_2O, CH_2Cl_2, toluene, dioxane, hexanes: dry neutral alumina; DMSO, DMF, CH_3OH: activated molecular sieves). Water was dispensed from a MilliQ water purification system (Millipore Corporation, Billerica, MA).

Purification and Analysis

Preparative scale HPLC purification was performed using an Agilent 1260 series instrument equipped with a multiple-wavelength detector and a Waters SunFire Prep C18 OBD 5 μm 30 x 150 mm column at a flow rate of 25 mL/min. All HPLC solvents were filtered through

0.2 mm Millipore filters prior to use. UV/Vis analyses were performed on a Shimadzu PharmaSpec UV-1700 spectrophotometer. Electrospray ionization mass spectra (ESI-MS) were obtained at the University of Illinois mass spectrometry facility.

Amphotericin and Amphoteronolide B

Due to light and air sensitivity of polyenes, all manipulations of AmB and amphoteronolide B (AmdeB) were carried out under low-light conditions and compounds were stored under a dry argon atmosphere at -20 ºC. AmdeB was prepared synthetically from natural abundance AmB as previously described.[25-27] All AmB and AmdeB used for current experiments were purified by preparative scale HPLC. All manipulations of HPLC-purified AmB and AmdeB were performed using either Optima MeOH, 0.2 μm-filtered HPLC grade solvents, or solvents dispensed from a solvent purification system.[52]

For purification, solid AmB was dissolved in DMSO (10 mg/mL), filtered through Celite 545 and purified (100 μL injections) with gradient of 5% to 65% MeCN / 5 mM ammonium acetate (NH_4OAc) over 12 minutes with detection at 406 nm. The column was subsequently flushed with isocratic 95% MeCN / 5 mM NH_4OAc for 2 min and re-equilibrated to 5% MeCN / 5 mM NH_4OAc prior to the next injection. The combined AmB solution was concentrated *in vacuo*, with filtered (0.2 μm) MeCN added back to the flask as needed for azeotropic removal of water. The resulting yellow solid was suspended via bath sonication in 1:1 MeCN:toluene and again concentrated *in vacuo* for azeotropic removal of residual NH_4OAc. Residual solvent was removed under high vacuum for ≥ 8 h to furnish a pale yellow solid, which was stored under argon at -20 ºC.

AmdeB was dissolved in DMF, filtered (Celite 545), injected, and eluted with a mobile phase gradient of 5% to 95% MeCN / 5 mM NH_4OAc over 25 min.

Ergosterol

Natural abundance ergosterol (Erg) was purchased from Sigma-Aldrich and recrystallized from EtOH before use. Stock solutions of 4 mg/mL Erg in $CHCl_3$ were stored under argon at -20 °C for up to one month. ^{13}C-skip-labeled Erg (^{13}C-Erg) was prepared biosynthetically using the method previously described.[19,51]

5.4.2 Biosynthesis and Characterization of U-^{13}C-Amphotericin

Biosynthesis

U-^{13}C-Amphotericin (U-^{13}C-AmB) (was prepared biosynthetically from cultures of the bacterium *Streptomyces nodosus* (American Type Culture Collection [ATCC], Manassas, VA, cell line 14899) using a modified version of the protocol previously reported.[18] In our modified protocol, the "FCA" medium[61] was used, with substitution of U-^{13}C-Glucose (U-^{13}C-Glc) for natural abundance fructose. Inoculation of culture medium and pulse feeding U-^{13}C-Glc were carried out in a Labconco Clean Bench (Labconco, Kansas City, MO) sterilized with 70% EtOH before and after each inoculation/feeding. *S. nodosus* starter cultures were prepared from ATCC 14899 as previously described.[61] Nine 250 mL baffled culture flasks, each containing 20 mL of the U-^{13}C-Glc-enriched medium in 250 mL baffled flasks were inoculated with *S. nodosus* starter culture. Pulse feeding of cultures was done according to the schedule previously described,[18] but with140 μL of aqueous 50% w/v U-^{13}C-Glc added to each baffled flask.

Purification

After work-up of the U-^{13}C-AmB as previously described,[18] if there remained any sign of residual Aliquat 336 (strong odor of Aliquat 336, dark yellow solid, sticky solid, not free flowing), then this material was further purified via C18 reverse phase flash chromatography as follows: AmB was dissolved in a minimum amount of DMF and Celite 545 was added to form a

slurry. This slurry was concentrated *in vacuo*, thus adsorbing the AmB onto the Celite. This solid was loaded onto a flash column loaded with Silicycle C18 silica gel and equilibrated with 20% MeCN / 5 mM ammonium acetate. Purification proceeded with a gradient of 20% MeCN / 5 mM NH_4OAc to 100% MeCN followed by 100% Optima MeOH (Fisher Scientific). The resulting yellow fractions were concentrated *in vacuo* and analyzed via ^1H NMR in DMF-*d*7 for presence of residual Aliquat 336. If Aliquat 336 was still present, the material was purified again by C18 flash column using the above protocol. Once removal of Aliquat 336 was confirmed, U-^{13}C-AmB was purified by preparative scale HPLC as described in General Methods above (Section 5.4.1). Prior to each experiment involving U-^{13}C-AmB, the purity of the compound was confirmed by analytical HPLC (see representative chromatogram below).

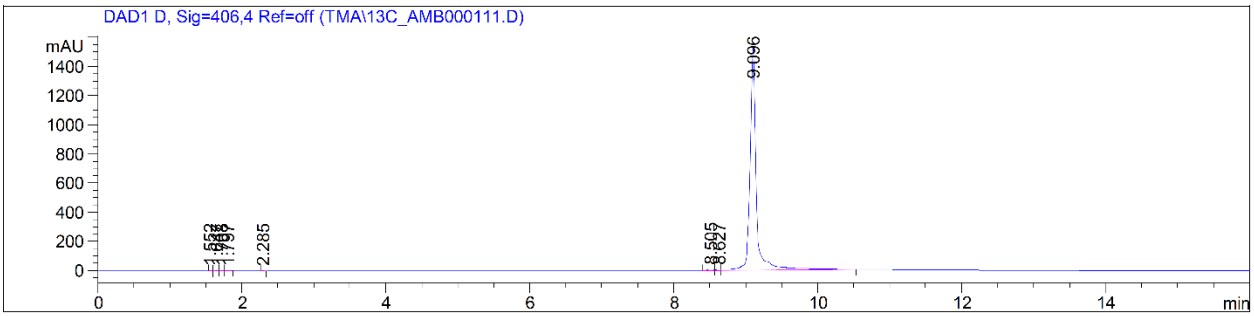

Isotopic enrichment

For natural abundance AmB, the calculated mass for $C_{47}H_{74}NO_{17}$ $(M+H)^+$ is 924.49. Average isotopic enrichment of U-^{13}C-AmB was calculated from ESI-MS peak intensities. The average *m/z* $(M+H)^+$ was 965.8. Thus, on average, 41 of the 47 carbon atoms of AmB were ^{13}C-enriched and the overall enrichment was thus approx. 87% ($41/47 \approx 0.87$).

5.4.3 Solid-State NMR Spectroscopy

SSNMR experiments were performed using a 600 MHz InfinityPlus spectrometer (Varian, now a subsidiary of Agilent Technologies, Inc.) equipped with a 3.2 mm T3 HXY MAS probe tuned to ^{1}H-^{31}P-^{13}C mode. Pulse widths (p/2) for ^{1}H, ^{13}C, and ^{31}P were 2-2.5 μs, 3.2 μs, and 3.2 μs, respectively. Spinning was controlled with a Varian MAS controller to 10,000 ± 2 Hz. SPINAL-64 decoupling (~75 to 80 kHz) was used during evolution and acquisition periods.[53] The flow rate of sample cooling gas was maintained at 100 scfh at 20 °C, resulting in a calibrated sample temperature of 19.2±1 °C. Chemical shifts were referenced externally with adamantane, with the downfield ^{13}C resonance referenced to 40.48 ppm.[54]

^{13}C T_1 and PRE Experiments

T_1 values were measured using standard T_1 inversion recovery pulse sequence with a 5 second pulse delay. Data were processed and fit with Varian Spinsight software version 4.3.2. For each of the resolved methine and methylene in U-^{13}C-labeled amphotericin (U-^{13}C-AmB) and ^{13}C skip labeled ergosterol (^{13}C-Erg) the longitudinal ^{13}C PRE was obtained by calculating the difference between the ^{13}C R_1 values for sample with and without 5 mol% of the DOXYL lipids, determined by modeling the individual relaxation trajectories as single exponential decays. T_1 trajectories were fit using the integrated volume of a given peak as a function of delay time (tau_1); integration boundaries were set to at the linewidth half height. The average line width observed for POPC is ~40-60 Hz. The average linewidth observed for Erg in the absence of AmB is ~50 Hz, and 127 Hz in the presence of AmB (see Supplementary Table 5.3). The average linewidth observed for AmB is ~187 Hz.

^{1}H-^{13}C Spin-Diffusion Experiments

We performed ^{1}H-^{13}C spin-diffusion correlation experiments as previously described[41] using a 1 ms T_2 filter, to detect interactions between the mobile ^{1}H signals of lipid acyl chains (1.35 ppm) and/or water (4.7 ppm) with the U-^{13}C-AmB, and ^{13}C-Erg in the presence and absence of AmB. ^{1}H-^{13}C polarization transfer trajectories were extracted from ^{1}H-^{13}C 2D spectra collected with ^{1}H-^{13}C mixing times ranging from 1 ms to 625 ms, by fitting peaks with a minimum signal to noise of 5, using a box integration method in Sparky. Trajectories were then normalized based on maximum observed intensity for a single resolved water or lipid ^{1}H-^{13}C cross peak after correction for ^{1}H T_1 relaxation, which was measured in a separate T_1 inversion recovery experiment. Error bars are derived from the signal-to-noise ratios observed for each crosspeak.

Order Parameters from ^{1}H-^{13}C Dipolar Couplings

Dipolar order parameters (S) were measured using the T-MREV pulse sequence[44] at an MAS rate of 8.333 kHz (N=4 condition, 100 kHz ^{1}H decoupling nutation frequency, 2.5 μs ^{1}H $\pi/2$ pulse length). The T-MREV ^{13}C-^{1}H dephasing was incremented by 30 μs and a total of 25 increments were recorded in t_1. Fortran fitting routines[55] were used to determine the ^{13}C-^{1}H dipolar coupling, taking into account the effects of relaxation and contributions from weaker couplings from neighboring protons. We calibrated the scaling factor of the T-MREV sequence by measuring the ^{13}C-^{1}H dipolar coupling for crystalline *N*-acetyl-L-valine under the identical experimental conditions.

(^{1}H)-^{13}C-(^{1}H-^{1}H)-^{13}C Correlation Spectra

(^{1}H)-^{13}C-(^{1}H-^{1}H)-^{13}C SSNMR experiments to yield performed at 10 °C, at an MAS rate 11.628 kHz, with the heteronuclear contact time (t_{HC}) set to 400 μs, and ^{1}H-^{1}H mixing time of 400 μs. These conditions reveal cross peaks for internuclear ^{13}C-^{13}C distances of ~4-6 Å. In

order to properly identify new intermolecular AmB-Erg cross peaks the (^{1}H)-^{13}C-(^{1}H-^{1}H)-^{13}C spectra were acquired back-to-back under identical conditions and signal averaged to approximately the same extent, adjusting the total measurement time based on the amount of material packed in each SSNMR rotor. The rotors of POPC:U-^{13}C-AmB:Erg (10:1:1 molar ratio) and POPC:U-^{13}C -AmB:^{13}C-Erg (10:1:1 molar ratio) were packed with ~25 mg and the spectra signal averaged for 7.8 days each. The 10:1:1 POPC:AmB:^{13}C-Erg sample was ~16 mg and therefore signal averaged for 13.6 days. The three spectra were all processed identically, with 40 and 75 Hz ^{13}C line broadening applied in the direct and indirect dimensions, respectively.

5.4.4 Preparation of Samples for SSNMR

A fresh stock solution of HPLC-purified AmB (natural abundance or U-^{13}C-AmB) was prepared for each experiment by dissolving AmB in a large volume of Optima methanol, typically 75-100 mL for 10 mg of AmB. Stock solution concentration was measured in triplicate by dilution in MeOH and measuring absorbance at 406 nm (e_{406} = 146000 M^{-1} cm^{-1}).[26] Unused stock solution was concentrated *in vacuo* and stored under a dry argon atmosphere at -20 ºC.

Stock solutions of Erg were prepared by dissolving recrystallized (commercial) or HPLC-purified (biosynthetic ^{13}C-Erg) Erg in a minimum volume of $CHCl_3$ and the concentration determined by UV/Vis spectroscopy in a manner analogous to that used for AmB (e_{282} = 10,400 M^{-1} cm^{-1}).[27] Erg stock solutions were stored in I-Chem vials under a dry argon atmosphere at -20 ºC for up to 1 month.

Phospholipids were purchased as stock solutions in $CHCl_3$ and these solutions were used directly for liposome preparation. Unused phospholipid solutions were stored in vials/bottles under a dry argon atmosphere at -20 ºC. Stock solutions of unsaturated phospholipids were discarded after 1 month.

Preparation of liposome vesicles for SSNMR.

Liposomes were prepared using a modified version of the protocol previously reported.[18] A suspension of POPC/Erg/AmB in 1:1 $CHCl_3$/MeOH was prepared as follows: The desired amount of AmB stock solution (typically 30-40 mL) was concentrated *in vacuo* to 2-3 mL and transferred to a 7 mL Wheaton vial, with three Optima MeOH washes to ensure complete transfer. This resulting AmB suspension was concentrated *in vacuo*. The desired amounts of stock solutions of phospholipid and Erg were then added via Hamilton gastight syringe, and an equivalent volume of Optima MeOH was added to resuspend the AmB. The vial was capped and this suspension was briefly vortexed and bath-sonicated until no AmB remained adherent to the sides of the vial (2-3 cycles). Solvent was removed under a gentle stream of nitrogen gas. Residual solvent was removed under high vacuum for ≥8 h.

To the dried solid was added filter-sterilized 0.3 mM HEPES buffer, pH 7.0 to yield a final phospholipid concentration of 40 mM. This aqueous suspension was vortexed and sonicated 3 times or until a homogeneous suspension was observed. Samples were then submitted to 5 freeze/thaw cycles (liquid nitrogen, lukewarm tap water). Samples were again frozen in liquid nitrogen and lyophilized for ≥8 h. The lyophilization chamber was then back-filled with dry Ar to prevent samples from absorbing ambient water. Samples were immediately capped and packed into rotors for SSNMR as soon as possible.

Dry samples were packed in 3.2 mm diameter limited speed SSNMR rotors (Agilent Technologies, Inc.) and hydrated with 8-10 mL of MilliQ H_2O. Rubber discs were used in the rotors to maintain hydration levels by creating a seal against which the rotor cap and drive tip were placed. Samples were placed at 4 °C for at least 24 hours to allow water to equilibrate.

5.4.5 Electron Microscopy

General Information

LUVs were prepared by the method reported previously,[25,27] and AmB was added to the LUV suspension as a freshly-prepared DMSO stock solution. Microscopy was performed using a 120-keV FEI Spirit Transmission Electron Microscope. Images were recorded using a bottom mount TVIPS CMOS based camera system at nominal magnifications of 23,000-49,000x at the specimen level. Measurements were taken in ImageJ32 (v 1.47).

Sample Preparation

AmB was prepared as a stock DMSO solution (8.82 mM). 5 μL of the stock AmB solution was added to 95 μL of the 50x-diluted LUV solutions. For AmB-free samples, 5 μL of DMSO was added to 95 μL of the 50x-diluted LUV solutions. Samples were vortexed gently for 5 seconds then incubated at 37 °C for 1 hour. EM samples were prepared as previously described[56] with the following modifications. A 4 μL drop of the sample was applied to a negatively charged carbon-coated copper grid (Gilder 200 mesh, Ted Pella, Inc., Redding CA) for 30 seconds. Subsequently, two drops of freshly prepared 2% uranyl acetate were added to the sample and incubated for 1 minute before drying via aspiration. Samples were then screened on the electron microscope.

5.4.6 In Vivo Sterol Extraction Studies and Membrane Isolation.

Growth Conditions for *S. cerevisiae*

S. cerevisiae was grown in autoclave-sterilized yeast peptone dextrose (YPD) media consisting of 10 g/L yeast extract, 20 g/L peptone and 20 g/L of filter-sterilized dextrose added as a sterile 40% w/v solution in water. Solid media was prepared by pouring sterile media containing agar (20 g/L) onto Corning (Corning, NY) 100 x 20 mm polystyrene plates. Liquid

cultures were incubated at 30 °C on a rotary shaker and solid cultures were maintained at 30 °C in an incubator.

Sample Preparation

750 mL overnight cultures of *S. cerevisiae* were grown to stationary phase (OD_{600} of ~1.7 as measured with a Shimadzu PharmaSpec UV-1700 UV/Vis spectrophotometer). This culture was divided equally into 50 mL Falcon centrifuge tubes.

Stock solutions of AmdeB, AmB, and Erg were prepared in DMSO. Methyl-beta-cyclodextrin (MBCD) were added directly to the liquid culture. Cells were treated with either a DMSO only control, 5 mM AmdeB, or 5 mM AmB for 1, 30, 60, or 120 minutes. Cells were treated with DMSO control, 500 mM MBCD, 25 mM Erg control, and the 5 mM AmB:25 mM Erg complex (Section VII) for 120 minutes. Treated tubes were incubated on the rotary shaker (200 rpm) at 30 °C for the time of exposure.

For the quantification of colony forming units (CFUs), at the end of exposure, aliquots were taken from the samples, diluted, and plated on YPD agar plates. The plates were then incubated for 48 hours at 30 °C and colony-forming units were counted.

For the quantification of percent ergosterol remaining, yeast membranes were isolated using a modified version of Haas' spheroplasting and isosmotic cell lysis protocol and simple differential ultracentrifugation.[45] At the end of the exposure time, tubes were removed from the shaker and centrifuged for 5 minutes at 3000·g at room temperature. The supernatant was poured off and 5 mL of wash buffer (dH_2O, 1M DTT, 1M Tris-HCl, pH 9.4) was added. The tubes were vortexed to resuspend and incubated in a 30 °C water bath for 10 minutes. Tubes were then centrifuged again for 5 minutes at 3000·g and the supernatant poured off.

1 mL of spheroplasting buffer (1M KPi, YPD media, 4M Sorbitol) and 100 mL of a 5 mg/mL solution of lyticase from *Arthrobacter luteus* (L2524 Sigma-Aldrich) was added to each tube, and each tube was then vortexed to resuspend. Tubes were incubated in a 30 °C water bath for 30 minutes, with occasional swirling. After incubation, tubes were centrifuged for 10 minutes at 1080·g at 4 °C and the supernatant poured off.

1 mL of PBS buffer and 20 mL of a 0.4 mg/ml dextran in 8% Ficoll solution was added to each tube, mixed very gently to resuspend. This suspension was placed on ice for 4 minutes and then heat-shocked in a 30 °C water bath for 3 minutes.

The suspensions were then transferred to Eppendorf tubes, vortexed to ensure complete lysis, and centrifuged at 15000·g at 4 °C for 15 minutes to remove un-lysed cells and cell debris. The resulting supernatants were transferred to thick-wall polycarbonate ultracentrifuge tubes (3.5 mL, 13 x 51 mm, 349622 Beckman Coulter) and spun for 1 hour at 100,000·g at 4ºC in a Beckman Coulter TLA-100.3 fixed-angle rotor in a Beckman TL-100 Ultracentrifuge. The supernatant was poured off. The remaining membrane pellet was resuspended in 1 mL PBS buffer and stored at -80 °C until further analysis.

Gas chromatography quantification of sterols.

750 mL of each membrane pellet sample and 20 mL of internal standard (4 mg/mL cholesterol in chloroform) were dissolved in 3 mL 2.5% ethanolic KOH in a 7 mL vial, which was then vortexed gently, capped, and heated in a heat block on a hot plate at 90ºC for 1 hour. The vials were then removed from the heat source and allowed to cool to room temperature. 1 mL of brine was added to the contents of each vial. Extraction was performed twice, each with 3 mL of hexane. Organic layers were removed in both extractions, dried over magnesium sulfate,

filtered through Celite® 545 (Sigma-Aldrich), and transferred to another 7 mL vial. The contents of the vial were then concentrated *in vacuo* in a 30ºC water bath.

The resulting sterol films were resuspended in 100 mL pyridine and 100 mL *N*,*O*-Bis-(trimethylsilyl)-trifluoroacetamide with 1% trimethylchlorosilane (T6381-10AMP Sigma-Aldrich) by vortexing gently.[57] This solution was heated at 60 ºC for 1 hour. The vials were placed on ice and the solvent was evaporated off by nitrogen stream. Vials must be kept at a low temperature to prevent evaporation of the sterol TMS ethers along with the solvent. The resulting films were resuspended in 100 mL of decane, filtered and transferred to a GC vial insert for analysis.

Gas chromatography analysis was carried out on an Agilent 7890A gas chromatograph equipped with a FID, an Agilent GC 7693 Autosampler, and a Dell computer running Microsoft XP that utilizes ChemStation v.B.04.02 SP1. Samples were separated on a 30 m, 0.320 mm ID, 0.25 um film HP-5 capillary column (19091J-413 Agilent). Hydrogen was employed as a carrier gas with an average velocity of 84.8 cm/s. Nitrogen make-up gas, hydrogen and compressed air were used for the FID. A split/splitless injector was used in a 20:1 split. The injector volume was 2 mL. The column temperature was initially held at 250 ºC for 0.5 min, then ramped to 265 ºC at a rate of 10 ºC /min with a final hold time of 12.5 min. The injector and detector temperature were maintained at 270 ºC and 290 ºC, respectively. The value reported for each time point was calculated by dividing the value for the treatment group by the value for the DMSO control at the same time point, and then normalizing the DMSO control to 100%.

5.4.7 Preparation of an Amphotericin/Ergosterol Complex

Erg was prepared as a stock solution, 4 mg/mL in $CHCl_3$, and the solvent removed under a gentle stream of nitrogen gas. Residual solvent was removed under high vacuum for at least 8

h. A DMSO solution of 5 mM AmB was then added to this solid Erg (25 mM final Erg concentration, 5:1 mole ratio Erg:AmB). The resulting suspension was gently vortexed and then heated to 80 ºC for one hour in an aluminum heating block to allow Erg to fully dissolve. The resulting AmB/Erg solution was then allowed to cool to room temperature. This solution was left to complex at room temperature for another hour before use.

The absorbance spectra of the two types of aggregate, (1) 5 mM AmB only in PBS buffer, (2) 5 mM AmB:25 mM Erg complex in PBS buffer, and the monomeric form of AmB (AmB in 25% PBS buffer, 75% methanol) were investigated using a Shimadzu PharmaSpec UV-1700 UV/Vis spectrophotometer.[58] Supplementary Fig. 5.15 shows the distinct shift in UV spectra between the different forms of AmB and AmB bound to Erg in a complex.

5.5 Results

5.5.1 SSNMR Paramagnetic Relaxation Enhancement Experiments

Distinguishing among the aforementioned structural and functional models (Fig. 5.1b-d) required determining the location of AmB relative to lipid bilayers and the corresponding location of Erg in the absence and presence of AmB. Making these determinations turned out to be exceptionally challenging due to the lack of high-resolution methods for probing small molecule/membrane interactions.[9-13,15,17-21] We thus developed an experiment based on the NMR paramagnetic relaxation enhancement (PRE) of ^{13}C nuclei caused by lipid-appended spin labels.[32-34] ^{13}C nuclei proximal to a stable radical, such as 4,4-dimethyloxazolidine-*N*-oxyl (DOXYL), experience large enhancements of their longitudinal relaxation rates ($R_1 = 1/T_1$). Due to the high gyromagnetic ratio of the electron spin, the PRE is detectable for distances up to ~20 Å. Harnessing this phenomenon, we designed a magic-angle spinning (MAS) SSNMR PRE experiment based on 16-DOXYL-PC and 5-DOXYL-PC to interrogate proximity to the

hydrophobic core and intermediate/headgroup region, respectively (Fig. 5.1a). Importantly, the three models under consideration (Fig. 5.1b-d) predict distinct PRE effects for AmB. The ion channel model predicts large PREs with both spin labels; the surface adsorption model predicts large PREs only with 5-DOXYL-PC; and the sterol sponge model predicts little or no PRE effects with either spin label.

To execute this experiment with maximized signal-to-noise ratio, we prepared highly enriched uniformly ^{13}C-labeled AmB (U-^{13}C-AmB) via development of an improved biosynthetic protocol.[18] By using uniformly ^{13}C-labeled glucose (U-^{13}C-glucose) as the primary carbon source, we developed a robust procedure for attaining >80% ^{13}C incorporation, the highest ^{13}C enrichment yet reported for this natural product (Materials and Methods Section 5.4.2). This highly enriched U-^{13}C-AmB enabled confident assignment of ^{13}C resonances and high sensitivity PRE measurements even at high lipid-to-AmB ratios.

We next identified a physiologically relevant lipid bilayer system in which we could execute the targeted experiments. Recent structure-function studies with AmB reveal that, in contrast to liposomes comprised of fully saturated lipids, liposomes derived from monounsaturated 1-palmitoyl-2-oleoyl-*sn*-glycero-3-phosphocholine (POPC) and Erg yield results that mirror those obtained with live yeast cells.[25,27] Also, unlike membranes derived from fully saturated lipids, the plasma membranes of yeast and bilayers derived from POPC:Erg are both in the liquid crystalline state at 23 °C.[35,36] In yeast, POPC is highly abundant, and Erg is the most common sterol.[37] Moreover, at the minimum inhibitory concentration for AmB against both *Saccharomyces cerevisiae* and *Candida albicans*, there is at least as much AmB as there is Erg.[25]

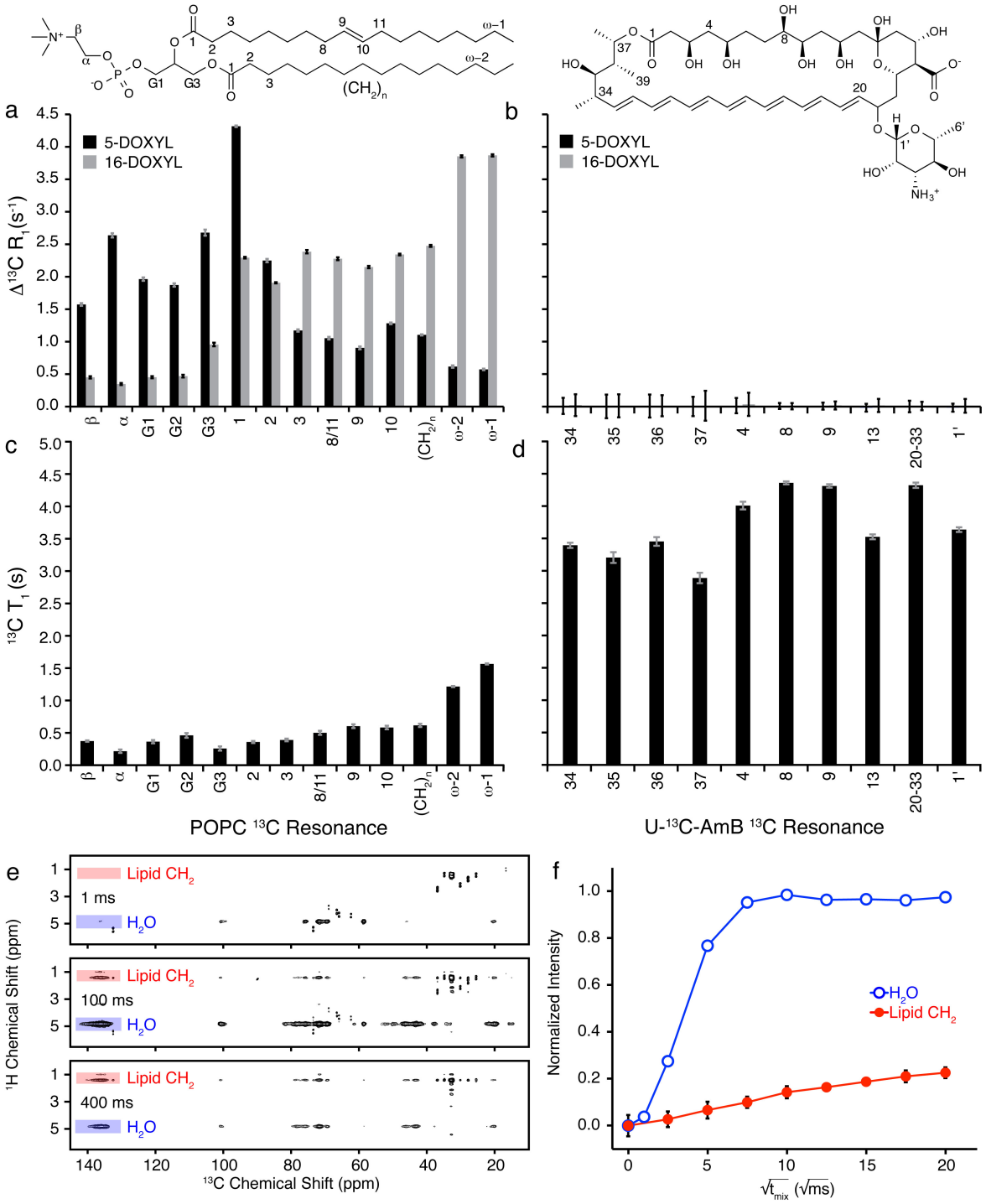

Figure 5.2 AmB primarily exists as large extramembranous aggregates.
a, Paramagnetic relaxation enhancements (PREs) have magnitude proportional to $1/r^6$ where r is the distance from spin label to NMR-detected nucleus. POPC controls demonstrated this proportionality in the presence of 5 mol% 5-DOXYL-PC (black) or 16-DOXYL-PC (gray). **b**, U-^{13}C-AmB demonstrated no significant PRE effects (> 0.1 s^{-1}) in the presence of either 5-DOXYL-PC (black) or 16-DOXYL-PC (gray) paramagnetic probes. **c**,**d**, Substantial differences were observed between longitudinal (T_1) ^{13}C relaxation times for sites in (**c**) POPC and (**d**) AmB. **e**, Selected ^{1}H-^{13}C 2D spectra were collected with 1

ms T_2 filter, and ^{1}H-^{1}H spin diffusion times of 1 ms, 100 ms, and 400 ms; cross peaks from lipid acyl chains (red) and water (blue) to U-^{13}C-AmB polyene region. **f**, The polarization transfer was quantified as a function of spin diffusion time from water and lipid to U-^{13}C-AmB polyene. PRE values were derived from the difference between ^{13}C R_1 relaxation rates measured via inversion recovery for diamagnetic samples and samples containing 5- and 16-DOXYL-PC. Error bars were determined by chi-squared analysis. ^{1}H-^{13}C spin diffusion data were normalized relative to maximum intensity observed for both lipid and water cross peaks for a given ^{13}C site after correcting for ^{1}H T_1 relaxation. Error bars were derived from signal-to-noise of the observed cross peak. Spectra were acquired at 14.1 T (600 MHz 1H frequency) at 20 °C, 10 kHz MAS.

We thus prepared lipid bilayer samples throughout this study with molar ratios of at least 10:1 POPC:Erg; for those samples containing AmB, we used at least 1 equivalent of AmB (relative to Erg). These bilayers exhibited proper phase behavior and retained this behavior upon addition of DOXYL spin labels (Supplementary Fig. 5.1).

To first confirm the position of each spin label in the bilayer, we determined the respective PREs on ^{13}C resonances in natural abundance POPC lipids with 5 mol% of each DOXYL spin label (Fig. 2a). Consistent with the structure of POPC membranes,[35] bilayers doped with 5% 16-DOXYL-PC demonstrated a maximal PRE at the termini of the POPC fatty acid chains, and the PRE decreased as the distance from the center of the membrane increased (Fig. 5.2a). The incorporation of 5-DOXYL-PC alternatively yielded maximal PREs in the intermediate and headgroup regions of the lipid bilayer and much smaller, yet still readily observable, effects at the membrane interior. Thus, these two spin label probes enabled confident and complementary interrogation of the innermost and outermost regions of a lipid bilayer in a straightforward SSNMR experiment.

We next prepared samples with U-^{13}C-AmB in POPC/Erg bilayers and used a series of ^{13}C chemical shift correlation experiments (including CTUC-COSY,[38] DARR,[39] and SPC5 recoupling[40]) to assign *de novo* the ^{13}C resonances of AmB (Material and Methods Section 5.4.3, Supplementary Fig. 5.2 and 5.3, Supplementary Table 5.1, and Material and Methods Section

5.4.2). We then performed PRE measurements in the presence of 16-DOXYL-PC or 5-DOXYL-PC spin probes. The results were striking and unambiguous. As predicted by the extramembranous sterol sponge model, and inconsistent with both the membrane-inserted ion channel and surface adsorption models, we observed no significant PREs to any ^{13}C resonances of AmB with either probe (Fig. 5.2b). Thus, the majority of AmB in these samples was >20 Å away from the membrane-embedded spin labels.

5.5.2 AmB Primarily Exists as Large Extramembranous Aggregates

A series of additional SSNMR experiments further revealed that AmB exists in the form of large aggregates that are more closely associated with water than lipids. The longitudinal relaxation times (T_1 values) for AmB were substantially longer than those of the lipids, consistent with large and relatively immobile aggregates of AmB (Fig. 5.2c, 5.2d, Supplementary Table 5.2). SSNMR spin-diffusion experiments, designed for the purpose of probing membrane protein topology,[41] revealed that lipid-AmB correlations reached maximum intensity only at very long mixing times (~400 ms) for all resolvable carbons on AmB (Fig. 5.2e, 5.2f, Supplementary Fig. 5.4), indicating that the majority of the lipids were >15 Å away from the AmB. In contrast, we observed strong correlations between water and AmB within just 25 ms, consistent with intimate proximity of the AmB aggregates to water.

To further probe these aggregates and distinguish between an intramembranous vs. extramembranous location, we also performed transmission electron microscopy analysis of large unilamellar vesicles (LUVs) comprised of the same ratio of POPC:Erg ± AmB. In the absence of added AmB, we observed well-formed LUVs (Fig. 5.3a, Supplementary Fig. 5.5a). When AmB was added, we observed large extramembranous aggregates (Fig. 5.3b, Supplementary Fig. 5.5b). These aggregates were associated with one or more LUVs, suggesting

an interaction between the surfaces of the aggregate and the lipid bilayer. When we added the same amount of AmB to the same volume of buffer devoid of LUVs, similar aggregates of AmB were observed (Fig. 5.3c, Supplementary Fig. 5.5c). These observations are consistent with the spontaneous formation in aqueous buffer of large AmB aggregates that externally associate with the surface of lipid bilayers.

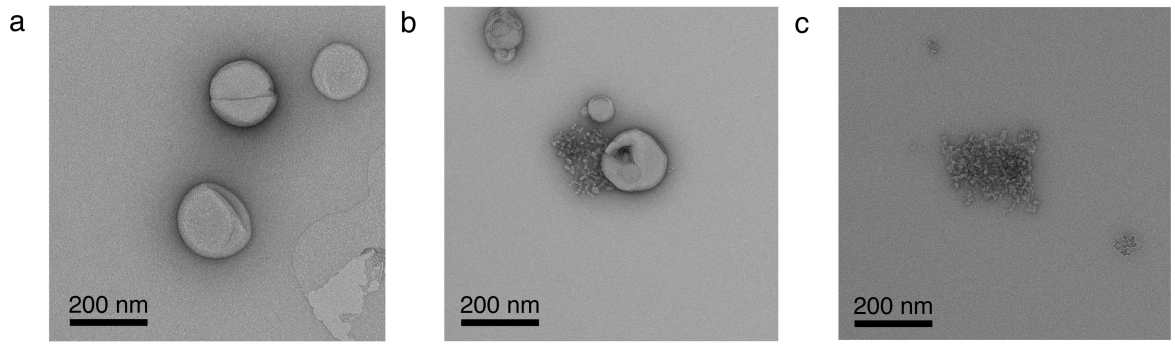

Figure 5.3 Direct visualization of large extramembranous aggregates of AmB by transmission election microscopy.
a, (supplementary Fig. 5.5a), POPC:Erg 10:1 liposomes. **b** (supplementary Fig. 5.5b), POPC:Erg 10:1 liposomes with 1 equivalent (relative to Erg) of added AmB. **c** (supplementary Fig. 5.5c), AmB only.

Importantly, parallel potassium efflux experiments revealed readily observable membrane permeabilization upon adding the same concentration of AmB to suspensions of the same POPC:Erg LUVs (Supplementary Fig. 5.6). This observation was consistent with a minor fraction of AmB existing in the form of membrane-permeabilizing ion channels that are too small to be visualized by TEM. This analysis was also consistent with all of our SSNMR data, in which the limits of detection permit up to 5% of the AmB existing in the membrane (Materials and Methods Section 5.4.3).

5.5.3 Extramembranous Aggregates of AmB Extract Ergosterol From Lipid Bilayers

With the structural aspects of the sterol sponge model confirmed, we aimed to test the functional prediction that these large extramembranous aggregates of AmB extract Erg from lipid bilayers. We first performed a modified SSNMR PRE experiment in which we analyzed ^{13}C-skip-labeled Erg (^{13}C-Erg, Fig. 5.4a)[19] in spin label-containing bilayers as a function of AmB:^{13}C-Erg ratio (Fig. 5.4a). This labeling pattern provided sufficient sensitivity that the ratio of POPC to Erg was increased to 40:1, readily enabling titrations of the AmB:Erg molar ratio while retaining the biophysical properties of the lipid bilayer. Thus, we prepared bilayers comprised of POPC:^{13}C-Erg 40:1 ± 5 mol% 16-DOXYL without or with increasing amounts of natural abundance AmB. AmB had minimal effect on the POPC PRE (Supplementary Fig. 5.7). In contrast, we observed a progressive decrease in the ^{13}C-Erg PRE as the amount of AmB increased, indicating that Erg increasingly occupied a position outside the lipid bilayer (Fig. 5.4a, Supplementary Fig. 5.7a). In the absence of AmB (AmB:^{13}C-Erg 0:1), we observed substantial PREs for the resolved ^{13}C signals of ^{13}C-Erg; for several sites, such as Erg-18, Erg-21, Erg-22, Erg-24 and Erg-26/27, the PRE was ~1.5 s^{-1} or greater, and the ^{13}C T_1 values were relatively short (<1.5 s) (Supplementary Fig. 5.7b). These findings are consistent with the structure of Erg-containing membranes in which the Erg was inserted into the hydrophobic core of the bilayer,[35] with the isopropyl tail most deeply inserted and therefore most proximate to the 16-DOXYL label. These conformation-specific PREs for ^{13}C-Erg decreased markedly upon the addition of AmB (Fig. 5.4a, Supplementary Fig. 5.7a). Specifically, with increasing amounts of natural abundance AmB (AmB:^{13}C-Erg ratios of 1:1, 4:1, 8:1), we observed a progressive decrease, with

at least a three-fold reduction in observed PRE in the AmB:^{13}C-Erg 8:1 sample. These results

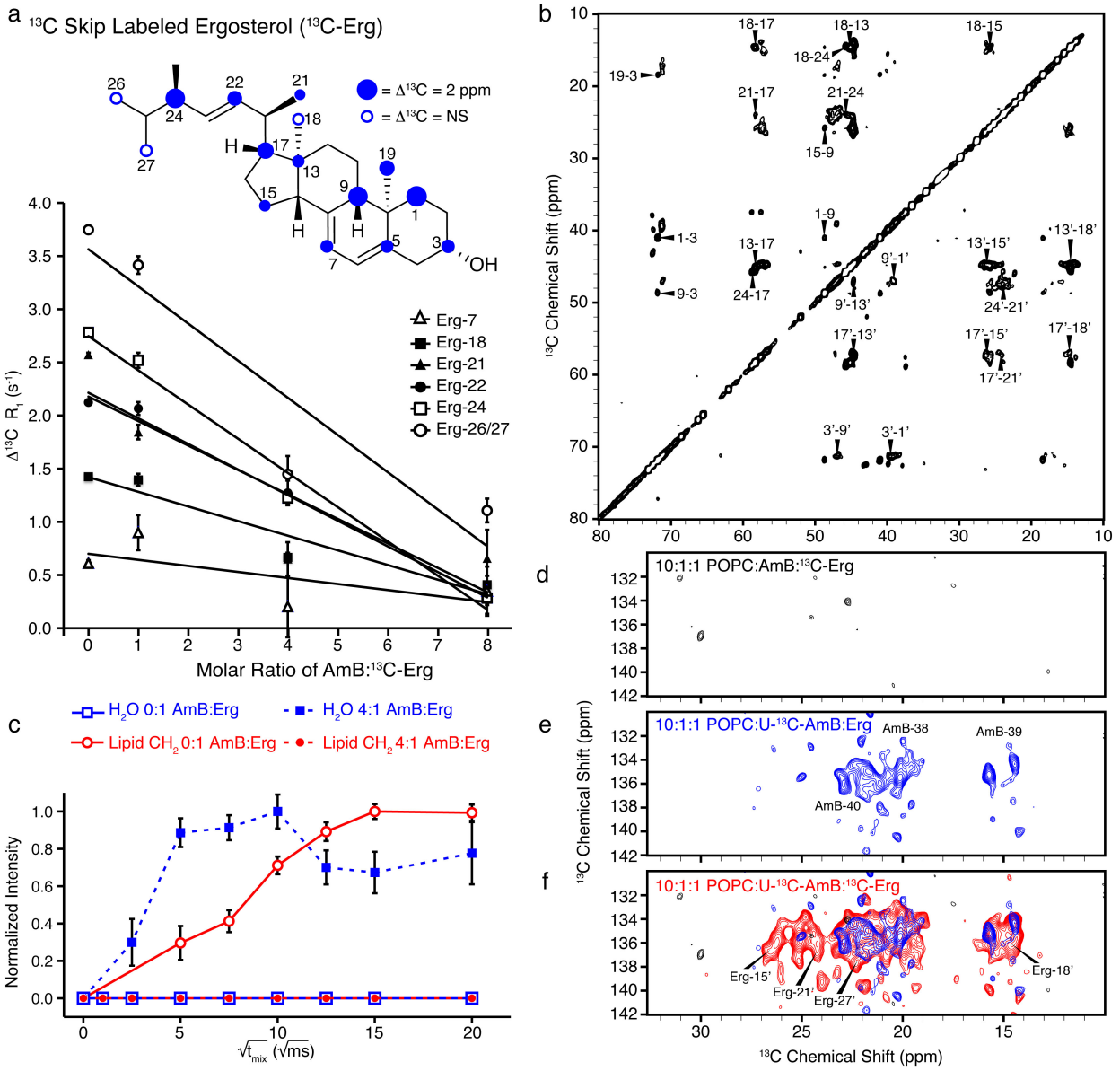

Figure 5.4 AmB extracts Erg from lipid bilayers.
a, Samples prepared using 40:1 POPC:^{13}C-skip-labeled Erg (^{13}C-Erg) ± 5 mol% 16-DOXYL-PC displayed progressive decrease in PRE effects of resolved Erg resonances as the ratio of AmB:^{13}C-Erg increased. **b**, The 2D ^{13}C-^{13}C DARR spectrum of ^{13}C-Erg (250 ms mixing, 10:1:1 POPC:AmB:^{13}C-Erg) changed upon addition of AmB, exhibiting new cross peaks. **c**, The ^{1}H-^{13}C polarization transfers from water (blue) and lipid (red) to Erg-7 were substantially different in the absence (closed circles/squares, dashed line) and presence (open circles/squares, solid line) of AmB. **d**-**f**, Expansions of the olefin-to-methyl spectral region for 2D (^{1}H)-^{13}C-(^{1}H-^{1}H)-^{13}C spectra[42,43] of (**d**) only ^{13}C-Erg (328 h signal averaging time), (**e**) only U-^{13}C-AmB (187 hr), and (**f**) both ^{13}C-Erg and U-^{13}C-AmB (187 hr). Error bars in (a) were derived from chi-squared analysis of inversion recovery trajectories. The ^{1}H-^{13}C spin diffusion data in (c) were normalized relative to maximum intensity observed for both lipid and water cross peaks for a given ^{13}C site after correcting for ^{1}H T$_1$ relaxation, and error bars were derived from signal-to-noise of the

observed cross peak. Spectra were acquired at 14.1 T (600 MHz ^{1}H frequency). Panels (a, b and c) were acquired at 10 kHz MAS, at 20 °C and 10° C, respectively. The (^{1}H)-^{13}C-(^{1}H-^{1}H)-^{13}C spectra (d-f) were acquired at 10 °C, 11.628 kHz MAS, processed with 40 and 75 Hz linebroadening in the direct and indirect dimensions, respectively, and were drawn with contour threshold set to four times the root mean square noise.

support the interpretation that, in the presence of increasing amounts of AmB, Erg increasingly occupied a position outside the lipid bilayer membrane.

Additional SSNMR experiments also supported this conclusion and further demonstrated that the extracted Erg is physically bound to the extramembranous aggregates of AmB. As the ratio of AmB:^{13}C-Erg increased, Erg resonances, but not those of POPC, demonstrated inhomogeneous broadening,[19] consistent with a transition from a mobile state to an immobile state (Supplementary Fig. 5.8). The average ^{13}C T_1 relaxation values for ^{13}C-Erg also followed the expected trend, increasing with the AmB:^{13}C-Erg ratio (Supplementary Fig. 5.7b). 2D ^{13}C-^{13}C correlation spectra further revealed several ^{13}C-Erg resonances that shifted significantly upon the addition of AmB (Fig. 5.4b, and Supplementary Table 5.3), and resolved bound state resonances exhibited significantly higher linewidth and T_1 values than those of the corresponding unbound state (Supplementary Fig. 5.9). In the absence of AmB, we observed very strong lipid-Erg correlations and no water-Erg correlations (Fig. 5.4c, Supplementary Fig. 5.10),[41] whereas in the presence of AmB we observed strong water correlations to all resolved Erg sites, with polarization transfer rates similar to those observed for AmB (Fig. 5.4c, Supplementary Fig. 5.11). We also repeated 1D and 2D chemical shift, linewidth, and T_1 analyses of ^{13}C-Erg in the presence of amphoteronolide B (AmdeB), a synthesized derivative of AmB that lacks the mycosamine appendage and does not bind Erg,[25,27] and observed no ^{13}C-Erg chemical shift perturbations and only very small changes in linewidths and T_1 values (Supplementary Fig. 5.12).

To definitively probe whether the extracted Erg is bound to the AmB aggregate, we prepared an additional series of samples in which ^{13}C labels were placed on (i) only Erg (Fig. 5.4d), (ii) only AmB (Fig. 5.4e), and (iii) both AmB and Erg (Fig. 5.4f). (^{1}H)-^{13}C-(^{1}H-^{1}H)-^{13}C spectra[42,43] for the first two samples showed only the anticipated intramolecular correlations (Fig. 5.4d, 5.4e), while the sample containing labels on both AmB and Erg revealed many new intermolecular AmB-Erg cross peaks (Fig. 5.4f), consistent with Erg aligned parallel to the polyene region of AmB and directly confirming the formation of a small molecule-small molecule complex. We also measured the ^{1}H-^{13}C dipolar couplings for resolved sites in both AmB and Erg using the T-MREV recoupling sequence[44] (Online Methods Section II, Supplementary Fig. 5.13) and Erg (Supplementary. Fig 5.14) to determine the relative mobility of these sites. In the absence of AmB, Erg was mobile as evidenced by the low order parameters, but in the presence of AmB, the order parameters shifted to the same rigid lattice limit observed for AmB (Supplementary Table 5.2). Furthermore, we observed line widths of >110 Hz for both AmB and Erg in the sterol sponge (Supplementary Table 5.2). Thus, AmB extracts Erg from lipid bilayers into large, extramembranous aggregates.

5.5.4 AmB Extracts Ergosterol From and Thereby Kills Yeast Cells

Finally, we tested the validity of the sterol sponge model in cells. First, we probed whether AmB extracts Erg from the cell membrane of yeast by adapting an ultracentrifugation-based membrane isolation assay[45] to quantify the amount of Erg in the membranes of live *Saccharomyces cerevisiae* cells in the absence and presence of AmB (Material and Methods Section 5.4.6). As shown in Fig. 5.5a, AmB very effectively extracted Erg in a time-dependent fashion. In contrast, we observed no Erg extracting effects with the non-Erg-binding derivative AmdeB.

Further experiments demonstrated that the Erg-extracting activity of AmB was responsible for its cell killing effects. As shown in Fig. 5.5b, we observed no cell killing with DMSO or AmdeB, whereas AmB promoted robust cell killing with a time course that paralleled

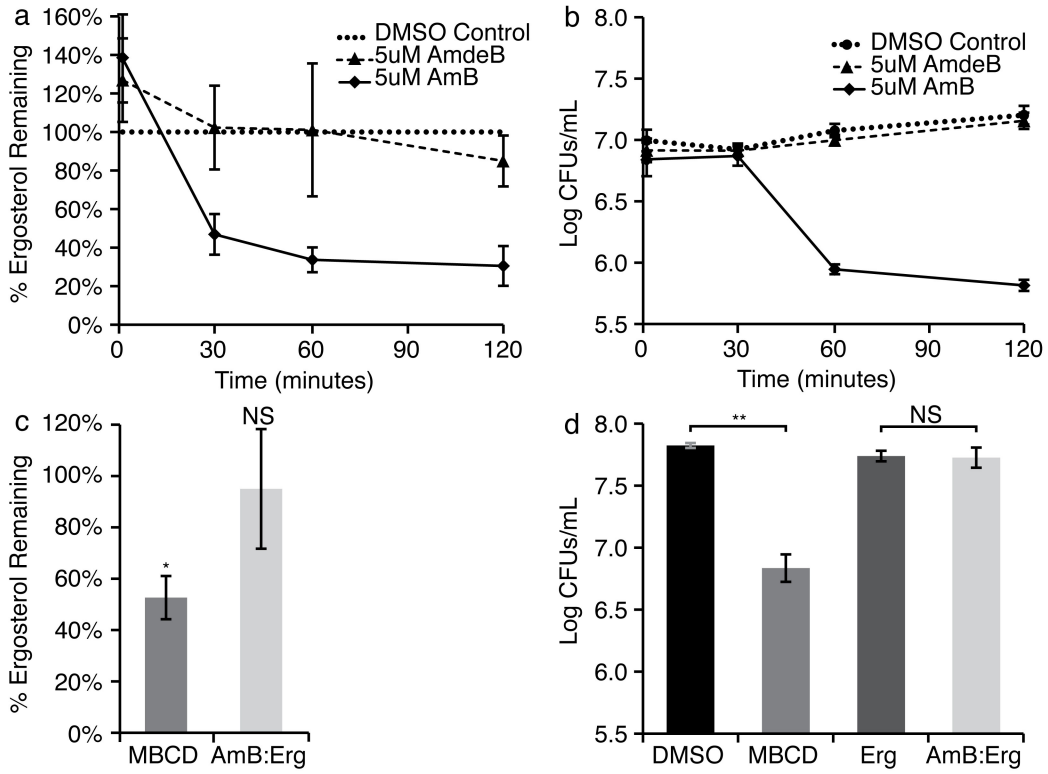

Figure 5.5 AmB extracts Erg from and thereby kills yeast cells.
a, AmB extracted Erg from the membranes of *S. cerevisiae* cells in a time-dependent manner, while the non-Erg-binding derivative AmdeB showed no Erg-extracting activity. The percentage of Erg remaining in the cell membranes was normalized to DMSO-only treated controls. **b**, Cell killing paralleled Erg extraction in AmB-treated cells. The non-Erg-extracting derivative, AmdeB showed no cell killing effects. **c**, Erg extraction after 120 minutes of incubation. 500 mM MBCD extracted Erg from the membranes of *S. cerevisiae* cells, whereas a pre-formed 5 mM AmB:25 mM Erg complex did not. The percentage of Erg remaining in the cell membranes was normalized to DMSO-only and 25 mM Erg in DMSO-only treated controls, respectively. **d**, Cell killing after 120 minutes incubation was observed for yeast treated 500 mM MBCD, but not for yeast treated with 5 mM AmB:25 mM Erg complex. Averages ± s.e.m. for at least 3 independent experiments. * $P < 0.02$, ** $P < 0.002$, NS not significant.

Erg extraction. In addition, methyl-beta-cyclodextrin (MBCD), a cyclic oligosaccharide known to extract sterols from membranes,[46] similarly demonstrated both Erg extracting and cell killing activities (Fig. 5.5c and 5.5d). Finally, the sterol sponge model predicts that AmB aggregates pre-saturated with Erg will lose the ability to extract Erg from membranes and kill yeast. Enabling this hypothesis to be tested, we found conditions that promoted the formation of stable and soluble aggregates of AmB and Erg (Material and Methods Section 5.4.7). As predicted, treating cells with this pre-formed AmB/Erg complex resulted in no Erg extraction (Fig. 5.5c), and no cell killing (Fig. 5.5d).

5.6 Discussion

For decades, scientists have widely accepted that membrane-spanning ion channels primarily contribute to the structure and antifungal activity of AmB (Fig. 5.1b).[4-23] In contrast, we found that AmB primarily forms large extramembranous aggregates that extract Erg from lipid bilayers and thereby kill yeast. Membrane-inserted ion channels are relatively minor contributors, both structurally and functionally, to the antifungal action of this natural product. While previous studies have reported large aggregates of AmB or its derivatives,[17,21] the interpretation of these findings has been in terms of the ion channel model. Here we described PRE (Fig. 5.2b and 5.2d), ^{1}H spin diffusion trajectory (Fig. 5.2f and 5.4c, Supplementary Fig. 5.4, 5.10, 5.11), and TEM studies (Fig. 5.3a-c, Supplementary Fig. 5.5) that collectively demonstrated that AmB primarily exists in the form of large extramembranous aggregates. Moreover, changes in PREs, ^{1}H spin diffusion trajectories, T_1 relaxation, order parameters, line widths, and chemical shift perturbations, as well as the observation of direct intermolecular cross peaks and the results of cell-based ergosterol extraction experiments demonstrated that extramembranous aggregates of AmB directly bind Erg. We further confirmed that the AmB

aggregates we observed in our SSNMR, TEM, and cell-based experiments were similar (Supplementary Fig. 5.15). Collectively, these results strongly support the proposed sterol sponge model in which extramembranous aggregates of AmB extract ergosterol from phospholipid bilayers and thereby kill yeast.

The sterol sponge model provides a new foundation for better understanding and more effectively harnessing the unique biophysical, biological, and medicinal properties of this small molecule natural product. Based on the classic ion channel model, many efforts over the past several decades to improve the therapeutic index of AmB focused on selectively permeabilizing yeast versus human cells.[11,13] This approach has not yielded a clinically viable derivative of the natural product. The sterol sponge model suggests that an alternative approach will be more effective. Specifically, analogous to the now clarified mechanism of antifungal activity, the extraction of cholesterol by large extramembranous aggregates of AmB may be primarily responsible for toxicity to human cells. This, in turn, suggests that the goal should be to maximize the relative binding affinity of AmB aggregates for Erg versus cholesterol. This insight is already guiding development of the first derivatives of AmB that are toxic to yeast cells but not human cells and thus hold exceptional promise for yielding an improved therapeutic index.[47]

A high-resolution structure of the large, extramembranous AmB aggregate, with and without bound ergosterol and cholesterol, would powerfully enable the discovery and/or further development of such derivatives. Importantly, the results described herein provide a strong platform for determining such a structure. Specifically, the large extramembranous aggregate of AmB, confirmed to reproducibly and stably form in the presence of POPC bilayers (Supplementary Fig. 5.2, 5.15), represents an excellent substrate for SSNMR analysis, and the common relaxation properties of AmB and Erg are consistent with the existence of a stable

complex. Moreover, the 2D (^{1}H)-^{13}C-(^{1}H-^{1}H)-^{13}C spectra of the complex derived from U-^{13}C-AmB and ^{13}C-Erg (Fig. 5.4f) exhibited intermolecular AmB-Erg correlations with intensities indicating internuclear distances of ~6 Å or less. We further note that comparison of ^{13}C-^{13}C 2D spectra of 10:1:0 POPC:U-^{13}C-AmB:Erg and 10:1:1 POPC:U-^{13}C-AmB:Erg (Supplementary Fig. 5.2) showed that the structures of the AmB aggregates in the absence and presence of Erg were very similar. There were, however, some intriguing changes in the AmB resonances corresponding to the mycosamine appendage upon the binding of ergosterol (Supplementary Fig. 5.3), which will be the subject of future investigations.

We anticipate that further SSNMR studies, including those applied to derivatives of AmB and/or Erg/cholesterol with site-specific or skip-pattern isotopic labels, will enable us to define in high resolution the structure of this extramembranous aggregate and the interface between these small molecules. Such information may reveal the structural underpinnings of the small preference of AmB to bind Erg over cholesterol and further guide the development of derivatives of AmB that maximize this binding preference and thus the therapeutic index.[47] In this vein, we note that the pattern of chemical shift perturbations observed for Erg in the absence and presence of AmB are consistent with tight association between AmB and the A and B rings of the sterol. Interestingly, the B ring of cholesterol, to which AmB binds but less strongly than Erg,[27,47] is more sterically bulky than that of Erg, because it possesses an extra degree of saturation. Moreover, lanosterol, to which AmB does not bind,[27] possesses both the same extra degree of saturation in the B ring and a sterically bulky gem dimethyl group on the A ring. While further studies are required to provide a detailed picture, our current data begin to support a structural rationale for the differential binding of AmB to Erg (strong), cholesterol (weak), and lanosterol (no binding). More broadly, relative to small molecules that bind proteins, small molecules that

bind other small molecules in a biologically relevant fashion are very rare. A high-resolution structure of this prototypical AmB-Erg complex may enable rational pursuit and study of other biologically important small molecule-small molecule interactions.

The sterol sponge model also offers a new rationale for the paucity of clinically relevant microbial resistance that is a hallmark of AmB as a therapeutic. Because the extraction of Erg renders yeast membranes Erg-deficient, AmB may simultaneously perturb all cellular processes that depend on membrane Erg.[28-31,48] This likely includes many different membrane proteins that directly bind Erg,[28-31] and simultaneous mutation of all such proteins in a manner that alleviates this Erg dependence is highly improbable. It has also remained unclear why, in contrast to the rarity with which AmB resistant mutants are found in patients, it is relatively easy to generate AmB-resistant yeast mutants in cell culture experiments.[49] The sterol sponge model provides a rationale for this dichotomy. AmB-resistant mutants generated in cell culture generally possess modified sterols in their membranes, e.g., lanosterol[50] (and/or other biosynthetic precursors to Erg) to which AmB does not bind (see above).[27] It was previously assumed that such changes in sterol content minimize antifungal potency by minimizing membrane-permeabilizing activity.[9,10,13,49] The sterol sponge model alternatively suggests that, because AmB does not bind or extract lanosterol, this modified sterol remains in the membrane to serve as a surrogate binding partner for sterol-dependent proteins. Due to the structural differences between lanosterol and Erg described above, however, the former is likely only a minimally effective substitute, resulting in reduced activity of many proteins that require specific interactions with Erg to function properly. This, in turn, may translate into substantially reduced pathogenicity of the resulting yeast mutants. Consistent with this notion, strains of yeast with modified sterol content have markedly reduced pathogenicity in animal models.[49] Such strains may routinely

emerge in patients treated with AmB, but, due to their reduced pathogenicity, cannot thrive and/or are rapidly cleared by the immune system of the host. A recently reported alternative series of studies provide complementary support for these conclusions.[49]

The clarified picture of the structural and functional underpinnings of AmB activity provided by the sterol sponge model also illuminates a rational roadmap for separating the ion channel forming and cytotoxic activities of AmB. Small, membrane-spanning ion channel aggregates likely exist as minor components in equilibrium with the large extramembranous assemblies of AmB characterized herein. This proposal is consistent with the weak AmB-lipid correlations observed in the SSNMR spin diffusion experiments, and the limits of detection of the SSNMR PRE and TEM studies. As we have previously demonstrated, binding ergosterol in the absence of channel activity is sufficient for cell killing.[25] Specifically, the capacity for channel formation can be selectively eliminated while preserving the capacity for both Erg binding and cell killing via deleting the C35 hydroxyl group appended to AmB.[25] In the sterol sponge model, this result can be rationalized by invoking a selectively destabilizing influence of this functional group deletion on the smaller membrane-inserted channel aggregates. Future studies will aim to determine whether this putative equilibrium between large extramembranous and small membrane-spanning aggregates can be alternatively shifted to favor ion channel formation, thereby maximizing potentially useful membrane-permeabilizing functions[25] while minimizing cytotoxic sterol extracting activity.

In summary, for more than half a century, the classic ion channel model has dominated the conceptual framework through which scientists have perceived and studied the structure and function of AmB in lipid bilayers. In contrast to this classic model, AmB primarily exists in the form of large, extramembranous aggregates that physically extract Erg from lipid bilayers and

thereby kill yeast. This new sterol sponge model stands to more effectively guide the understanding, optimization, and clinical utilization of this prototypical small molecule natural product, as well as other small molecules that similarly interface with living systems.

5.7 Supplementary Figures

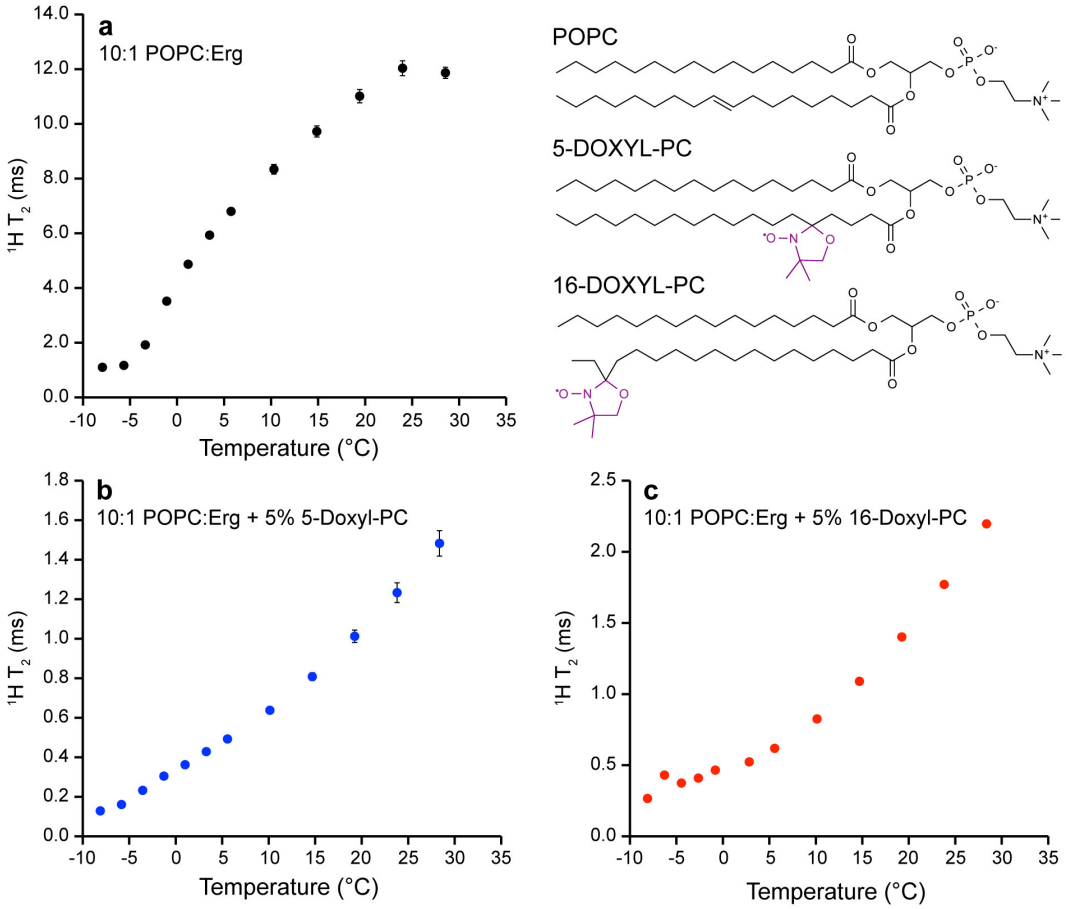

Supplementary Figure 5.1 Phase transition behavior of 5% 5 and 16-DXYL-PC
^{1}H T_2 values of the bulk fatty acyl CH_2 peaks of molar ratios of (a) 10:1 POPC:Ergosterol (b) 10:1 POPC:Ergosterol + 5% 5-Doxyl-PC and (c) 10:1 POPC:Ergosterol + 5% 16-Doxyl-PC liposomes as a function of temperature. The data were acquired on a 600 MHz spectrometer over a calibrated temperature range of -8 to 28 °C.

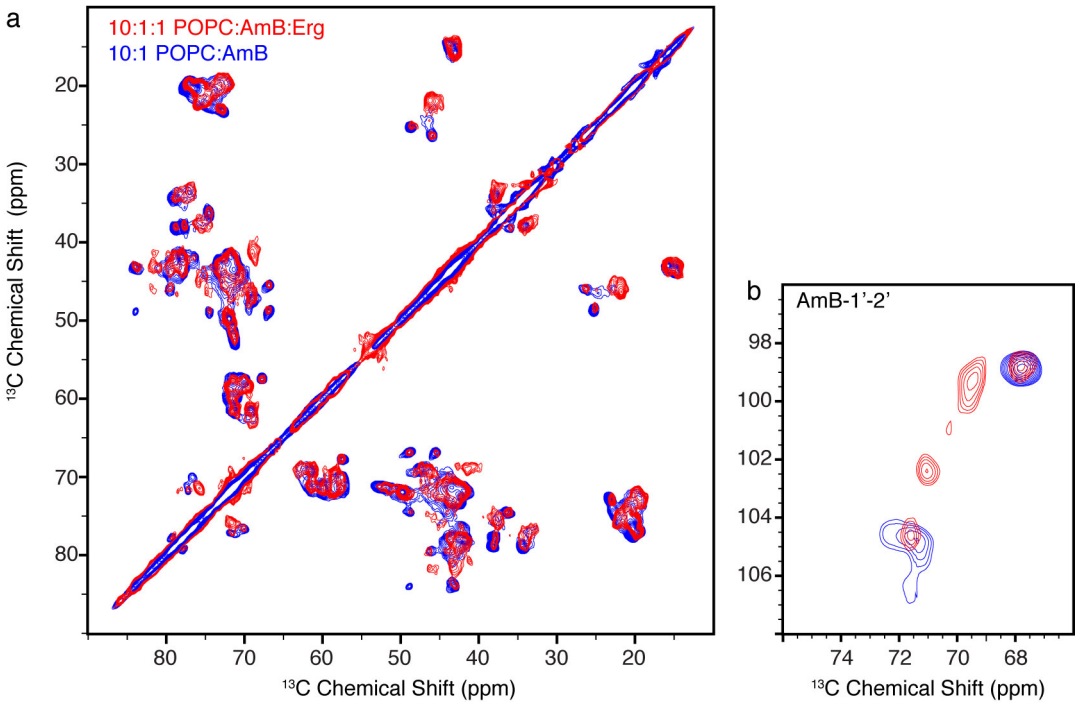

Supplementary Figure 5.2 CC2D of AmB with and without ergosterol

^{13}C-^{13}C 2D spectra of (1.44 ms SPC5$_3$ mixing) of 10:1:1 POPC:U-^{13}C-AmB:Erg (red) and 10:1:0 POPC:U-^{13}C-AmB:Erg (blue) at 600 MHz with SPINAL ^{1}H decoupling.[53] Irrespective of the presence of Erg, the peak positions do not change substantially. However, as shown in panel b, some interesting changes in the mycosamine resonances upon the binding of Erg are noted.

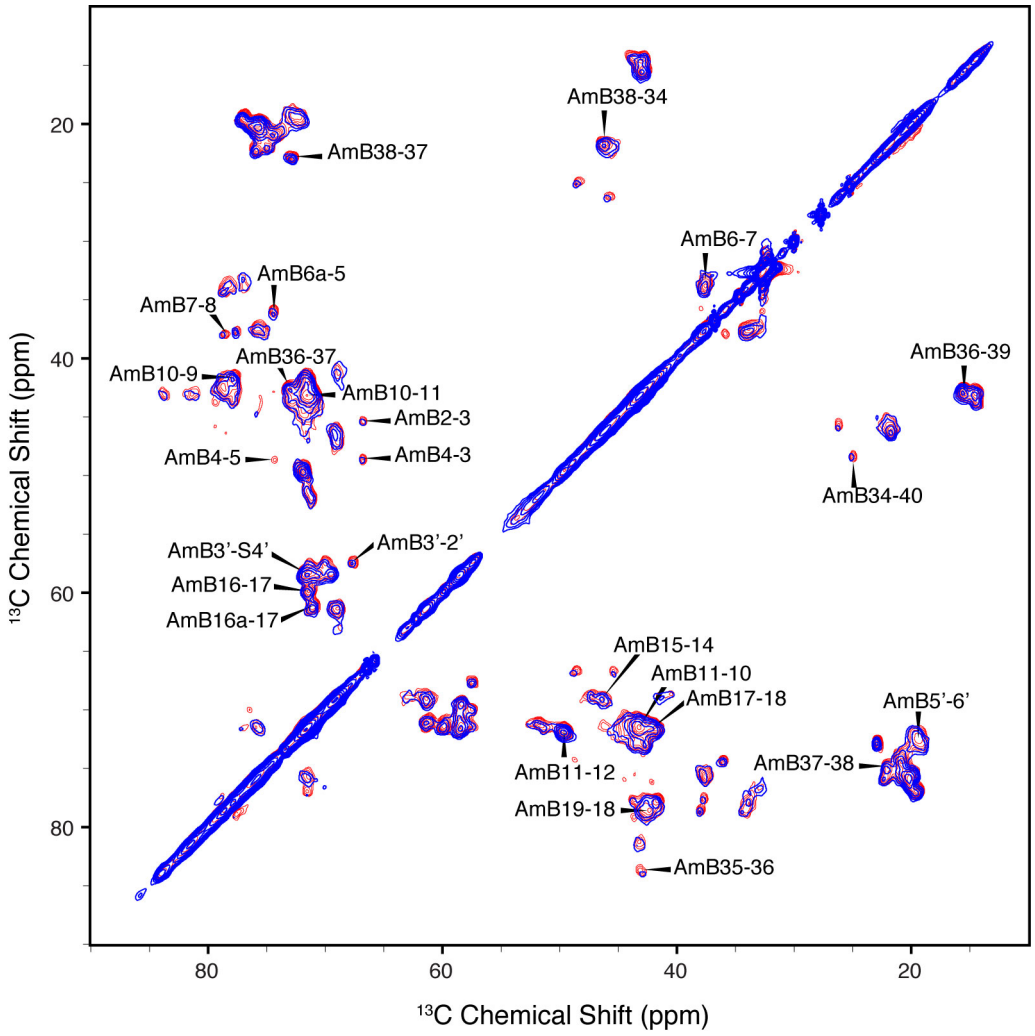

Supplementary Figure 5.3 CC2Ds AmB with and without 5-DOXYL-PC

^{13}C-^{13}C 2D spectra of (1.44 ms SPC5 mixing) of 10:1:1 POPC:U-^{13}C-AmB:Erg (red) and 10:1:1 POPC:U-^{13}C-AmB:Erg with 5 mol% 5-DOXYL-PC used to make site-specific assignments of the AmB and confirm that the addition of the DOXYL spin labels has no significant effect on AmB. Spectrum was acquired on a 600 MHz spectrometer, at 20 °C with and MAS rate of 10 kHz, and 75 kHz SPINAL ^{1}H decoupling.[53]

Supplementary Table 5.1 ^{13}C resonance assignments for AmB

Carbon atoms are numbered sequentially starting with the macrolactone carbonyl, denoted "AmB-1." The mycosamine appendage is numbered starting with "AmB-1' " carbon atoms 20 to 33 are identified as "AmB-Polyene". Asterisk (*) indicates resonances that overlap with lipid resonances and therefore were excluded from PRE and line shape analysis.

Assignment	^{13}C Chemical Shift (ppm)					
AmB-1	174.6	175.4				
AmB-	45.5	40.6	44.2			
AmB-3 *	66.8	68.6	73.2			
AmB-4	48.8	42.6				
AmB-5	74.4	78.9	74.6	77.9	75.7	
AmB-6 *	37.8	36.1	34.4	33.0	33.9	
AmB-7 *	33.9	34.1	38.1	37.9	37.7	
AmB-8	78.0	77.8	78.8	78.4		
AmB-9	77.8	77.9	79.4	78.9		
AmB-10	41.8	44.2	43.7	42.5		
AmB-11	71.8	71.6	71.3	71.7		
AmB-12	49.7	51.8	51.3	52.7		
AmB-13	99.9	100.4	100.7	100.2	101.3	99.6
AmB-14	46.4	46.9	47.4	47.9		
AmB-15 *	69.0	69.1	69.2			
AmB-16 *	61.2	59.9	61.5	63.0		
AmB-17	71.5	71.0	71.3	71.6		
AmB-18	43.2	42.2	43.3			
AmB-19	78.5	79.3				
AmB-Polyene	134.5-141.1					
AmB-34	46.2	48.7	46.0	45.2		
AmB-35	81.5	83.9	84.0	79.5	83.5	
AmB-36	43.1	42.9	43.8	43.4	42.1	
AmB-37 *	72.7	73.0	76.5	74.2	74.9	75.9
AmB-38	22.9	22.3	21.8	23.2	21.2	19.5
AmB-39	15.5 *	14.6	14.6			
AmB-40 *	25.1	26.3	21.8	22.2		
AmB-41	182.1	183.9	182.0	184.8		
AmB-1'	102.3	104.6	98.7	106.4	99.2	99.9
AmB-2' *	71.5	67.7	70.9	69.6	69.4	
AmB-3'	58.4	57.5	61.2	59.8		
AmB-4'	71.5	69.2	70.1	70.8	69.6	
AmB-5'	75.6	75.8	76.1	76.8	77.1	
AmB-6'	20.3	19.6	22.4	20.0	20.1	

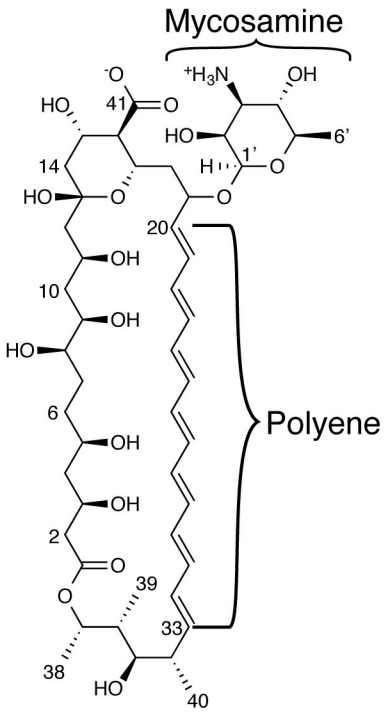

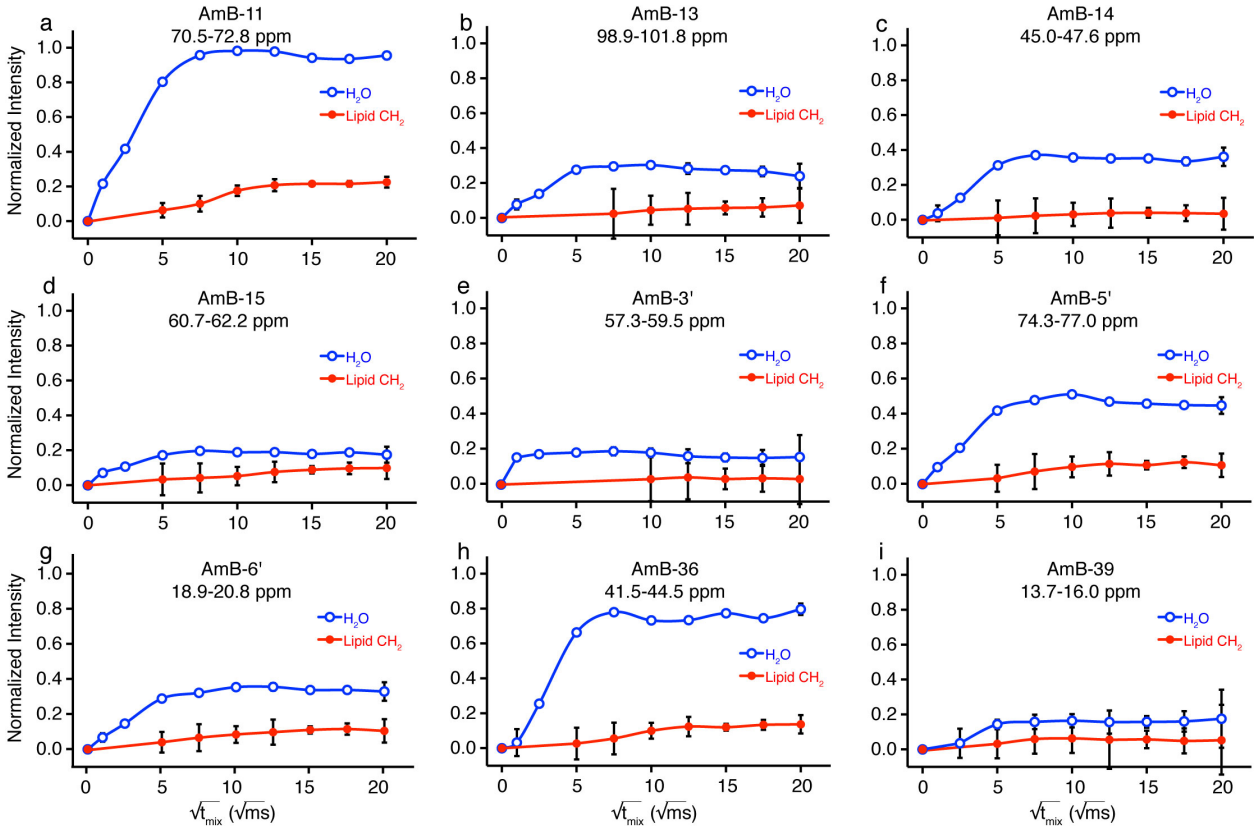

Supplementary Figure 5.4 AmB ^{1}H spin diffusion

T_2-filtered (1 ms) spin diffusion studies of 10:1:1 POPC:U-^{13}C-AmB:Erg MLVs show rapid transfer from lipid ^{1}H to lipid ^{13}C signals and from water to U-^{13}C-AmB, but much slower transfer of lipid polarization to AmB. The selected ^{1}H-^{13}C correlations were collected with 1 ms T_2 filter and ^{1}H-^{1}H spin diffusion times of 1 ms to 400 ms. Cross peaks from the lipid acyl chain CH_2 protons (~1.35 ppm) and water (~4.7 ppm) to the various regions on U-^{13}C-AmB are shown in red and blue, respectively. The rates show that the majority of the AmB is closely associated with water and >15-20 Å from the lipid acyl chains.[28] The polarization transfer is normalized based on the maximum observed intensity after correction of the ^{1}H T_1 relaxation. Spectra were acquired on a 600 MHz spectrometer, at 20 °C with and MAS rate of 10 kHz, and 75 kHz SPINAL ^{1}H decoupling.[53]

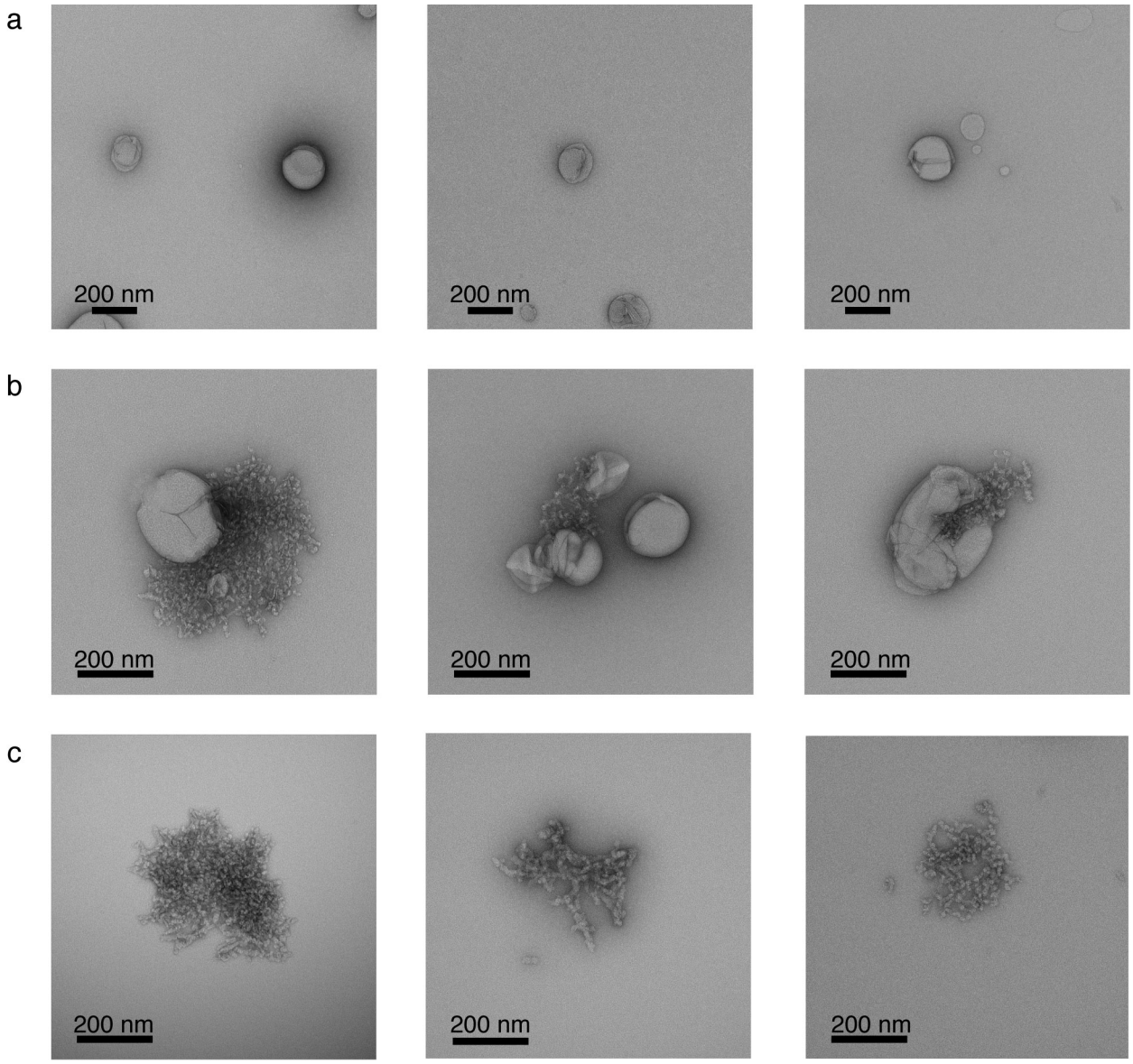

Supplementary Figure 5.5 Supplemental transmission electron microscopy images.
a) 10:1 POPC:Erg liposomes. Average LUV size was ≈ 200 nm b) POPC:Erg 10:1 liposomes with 1 equivalent of added AmB. The average LUV size was ≈ 200 nm. c) 1 equivalent AmB added in HEPES Buffer.

Supplementary Table 5.2 ^{13}C Line widths and order parameters

	- AmB	
Peak Assignment	Line Width (Hz)	S
Erg-1	41	0.443
Erg-3	42	0.412
Erg-7	45	0.219
Erg-9	45	0.456
Erg-17	60	0.414
Erg-19	43	0.393
Erg-22	45	0.377
Erg-24	57	0.287
	+ AmB	
Erg-1	153	0.943
Erg-3	149	0.938
Erg-7	167	0.976
Erg-9	179	0.948
Erg-17	176	0.989
Erg-19	184	0.803
Erg-22	207	0.912
Erg-24	228	0.921
A1'	110	0.981
A1'	138	0.988
AmB-Polyene		0.981
A8	111	0.988
A9	158	0.994
A11, A17	140	0.999
A35	161	0.994

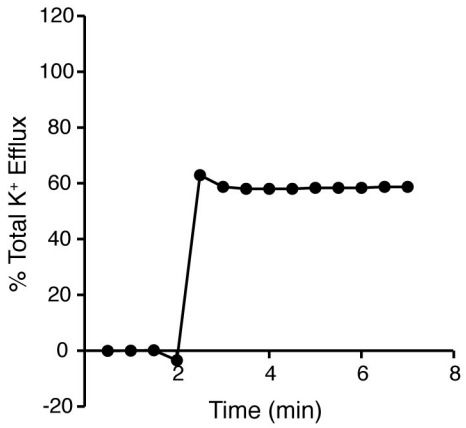

Supplementary Figure 5.6 AmB potassium efflux

AmB promotes robust K^+ efflux from 200 mm LUV's composed of 10:1 POPC:Erg. This activity mirrors both the *in vitro* and *in vivo* efflux activity of AmB previously reported by our laboratories.[25,27] 10 mol% AmB was added as a DMSO solution (final AmB concentration of 1 mM) at t = 1.5 min, and efflux is reported as a percentage of total efflux observed upon addition of Triton X-100. The observed plateau at 60% efflux is likely reflective of equilibrium between the bulk solution and the vesicle interior.

Supplementary Table 5.3 ^{13}C Chemical Shifts of ^{13}C Skip Labeled Ergosterol (^{13}C-Erg)

	- AmB	+ AmB	
Assignments	^{13}C (ppm)	^{13}C (ppm)	Δ^{13}C (ppm)
Erg-1	41.2	39.3	1.9
Erg-3	72.0	71.5	0.6
Erg-5	143.7	144.3	-0.6
Erg-7	119.7	120.1	-0.4
Erg-9	48.9	47.2	1.7
Erg-13	45.3	45.0	0.3
Erg-15	26.0	26.2	-0.2
Erg-17	58.5	57.4	1.1
Erg-18	14.7	14.7	0.0
Erg-19	18.6	17.8	0.8
Erg-21	24.0	24.2	-0.2
Erg-22	138.4	139.4	-0.9
Erg-24	45.9	47.5	-1.6
Erg-26	20.3	20.3	0.0
Erg-27	22.4	22.4	0.0

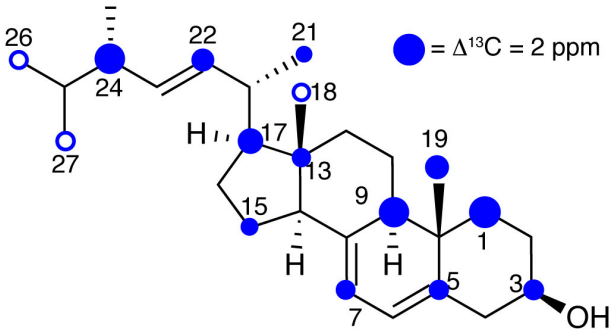

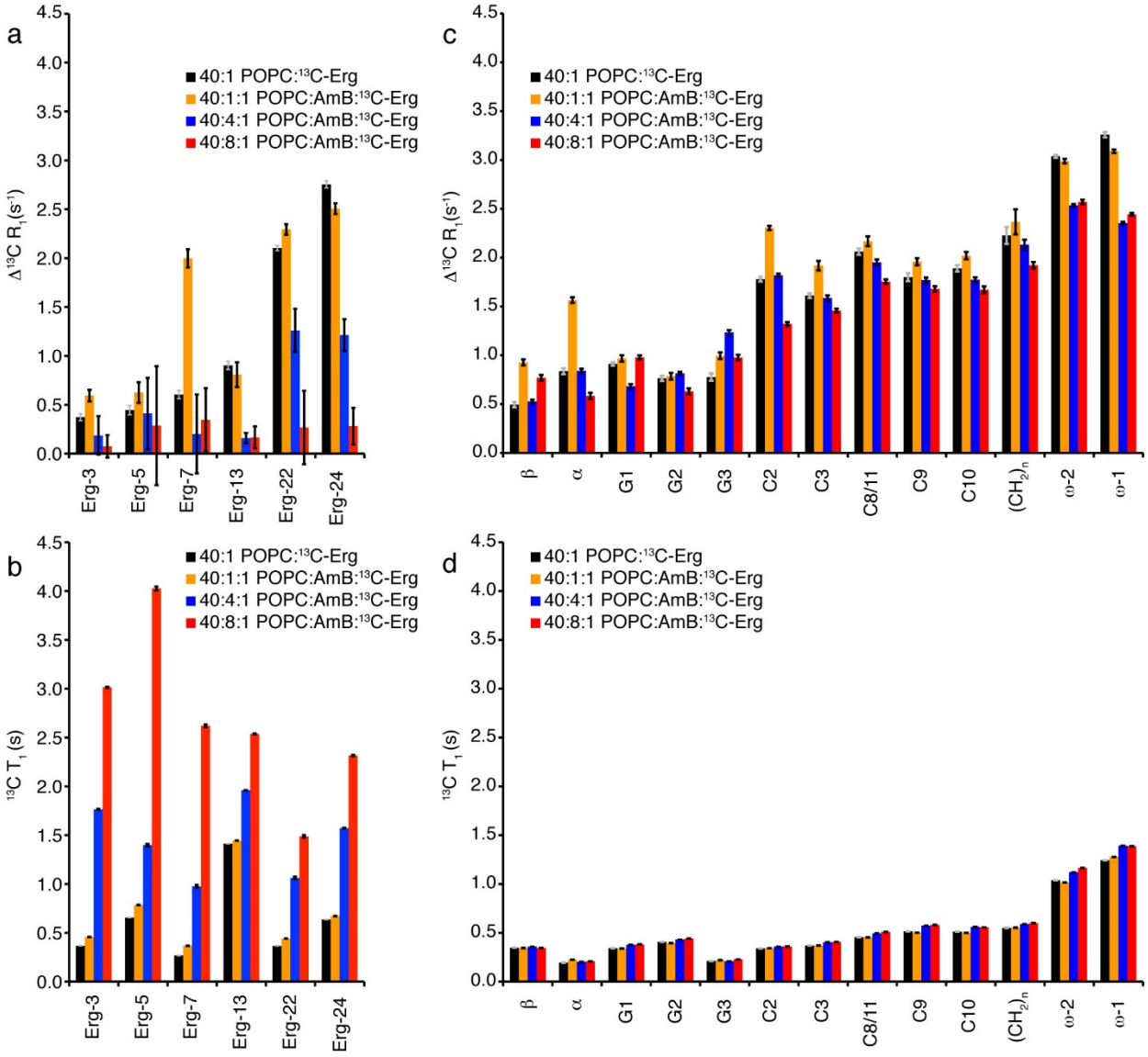

Supplementary Figure 5.7 16-DOXYL PRE effects

The addition of AmB to POPC:Erg liposomes has a large effect on Erg, but a relatively small effect on POPC. The combination of the decrease in (a) PRE and substantial increase in the (b) longitudinal relaxation times (T_1) of Erg are consistent with the formation of an AmB:Erg complex that is separated from the lipid bilayer. Note the small relative change in the POPC (c) PRE (~20% on average) and (d) ^{13}C T_1 values (~ 10% on average). (40:1 POPC:^{13}C-Erg (black), 40:1:1 POPC:AmB:^{13}C-Erg (orange), 40:4:1 POPC:AmB:^{13}C-Erg (blue), and 40:8:1 POPC:AmB:^{13}C-Erg (red) liposomes ± 5 mol% 16-DOXYL-PC.) Only methine (CH) and methylene (CH_2) sites that do not shift significantly (< 0.5 ppm) upon addition of AmB are shown. SSNMR experiments were performed on a 600 MHz spectrometer, at 20 °C with an MAS rate of 10 kHz and 75 kHz ^{1}H decoupling.[53]

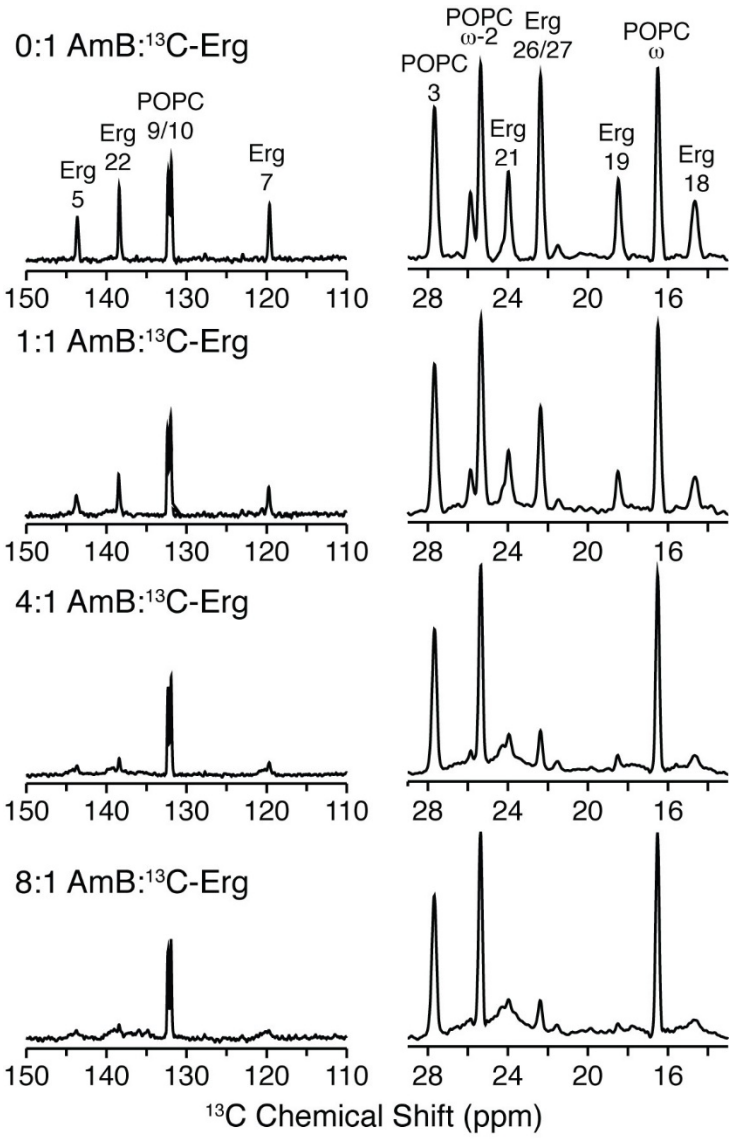

Supplementary Figure 5.8 AmB extracts Erg from lipid bilayers.
1D ^{13}C spectra of ^{13}C-Erg titrated with natural abundance AmB. As a function of AmB:Erg ratio, the ^{13}C-Erg resonances broaden from an average linewidth of 0.3 ppm to >1.0 ppm, consistent with formation of an AmB-Erg complex Spectra were acquired at 14.1 T (600 MHz ^{1}H frequency), at 20 °C and 10 kHz MAS rate.

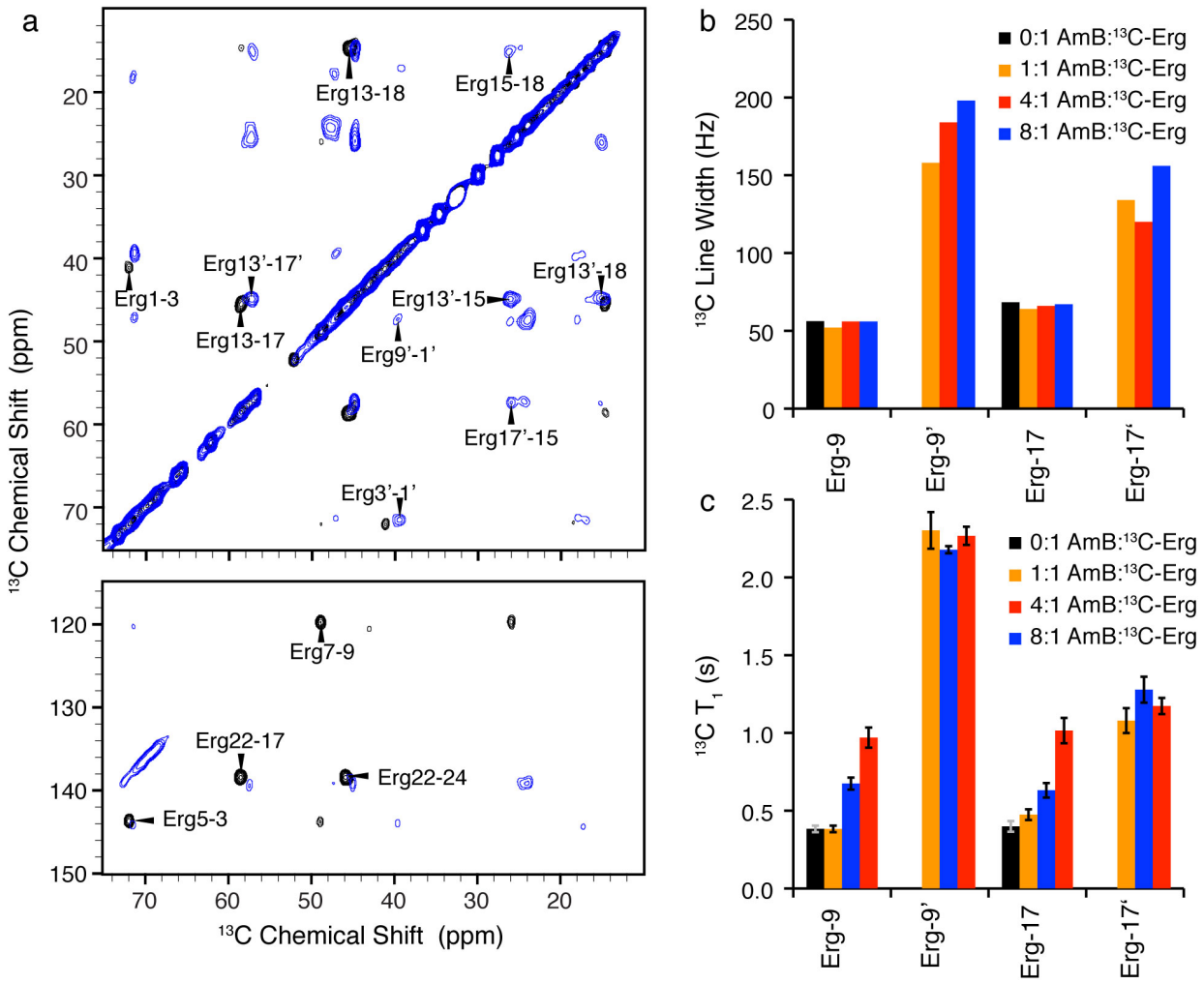

Supplementary Figure 5.9 Effects of AmB of Erg linewidth, T1, and CC2D.
The addition of increasing amounts of AmB to 40:1 POPC:^{13}C-Erg membranes induces substantial changes in the spectroscopic properties of Erg. (a) The ^{13}C-^{13}C 2D DARR spectra (500 ms mixing) of POPC:^{13}C-Erg (black) and 40:8:1 POPC:AmB:^{13}C-Erg (blue) show dramatic changes in not only the postion but number of cross peaks. This coupled with the increase in (b) line width (c) ^{13}C T_1 values for the bound state (denoted with a ') versus the free state indicates a large reduction in the mobility of Erg in the presence of AmB, consistent with the formation of an AmB:Erg complex. (40:1 POPC:^{13}C-Erg (black), 40:1:1 POPC:AmB:^{13}C-Erg (orange), 40:4:1 POPC:AmB:^{13}C-Erg (blue), and 40:8:1 POPC:AmB:^{13}C-Erg (red) liposomes.) Spectra were acquired on a 600 MHz frequency spectrometer, at 20 °C with an MAS rate of 10 kHz and 75 kHz ^{1}H decoupling.[53]

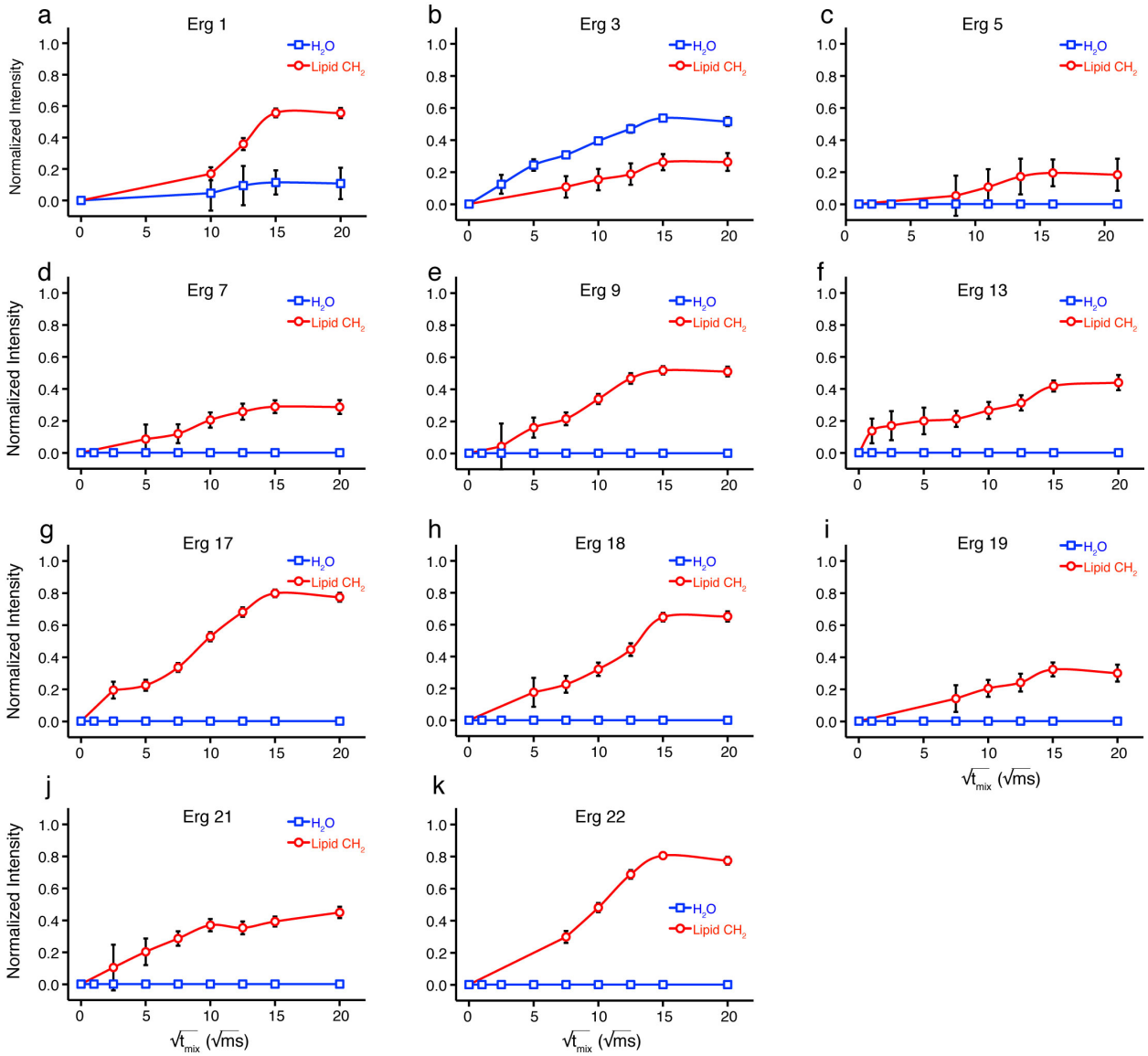

Supplementary Figure 5.10 ^{1}H spin diffusion to Erg in absence of AmB

T_2-filtered (1 ms) spin diffusion studies of 40:0:1 POPC:AmB:^{13}C-Erg MLVs show that in the absence of AmB Erg is embedded in the lipid membrane, with the C3 site on the A ring located close to the membrane water interface. The selected ^{1}H-^{13}C correlations were collected with 1 ms T_2 filter and ^{1}H-^{1}H spin diffusion times of 1 ms to 400 ms. Cross peaks from the lipid acyl chain CH_2 protons (~1.35 ppm) and water (~4.7 ppm) to all resolved sites of ^{13}C-Erg are shown in red and blue, respectively. The polarization transfer is normalized based on the maximum observed intensity after correction of the ^{1}H T_1 relaxation. Spectra was acquired on a 600 MHz spectrometer, at 20 °C with and MAS rate of 10 kHz, and 75 kHz SPINAL ^{1}H decoupling.[53]

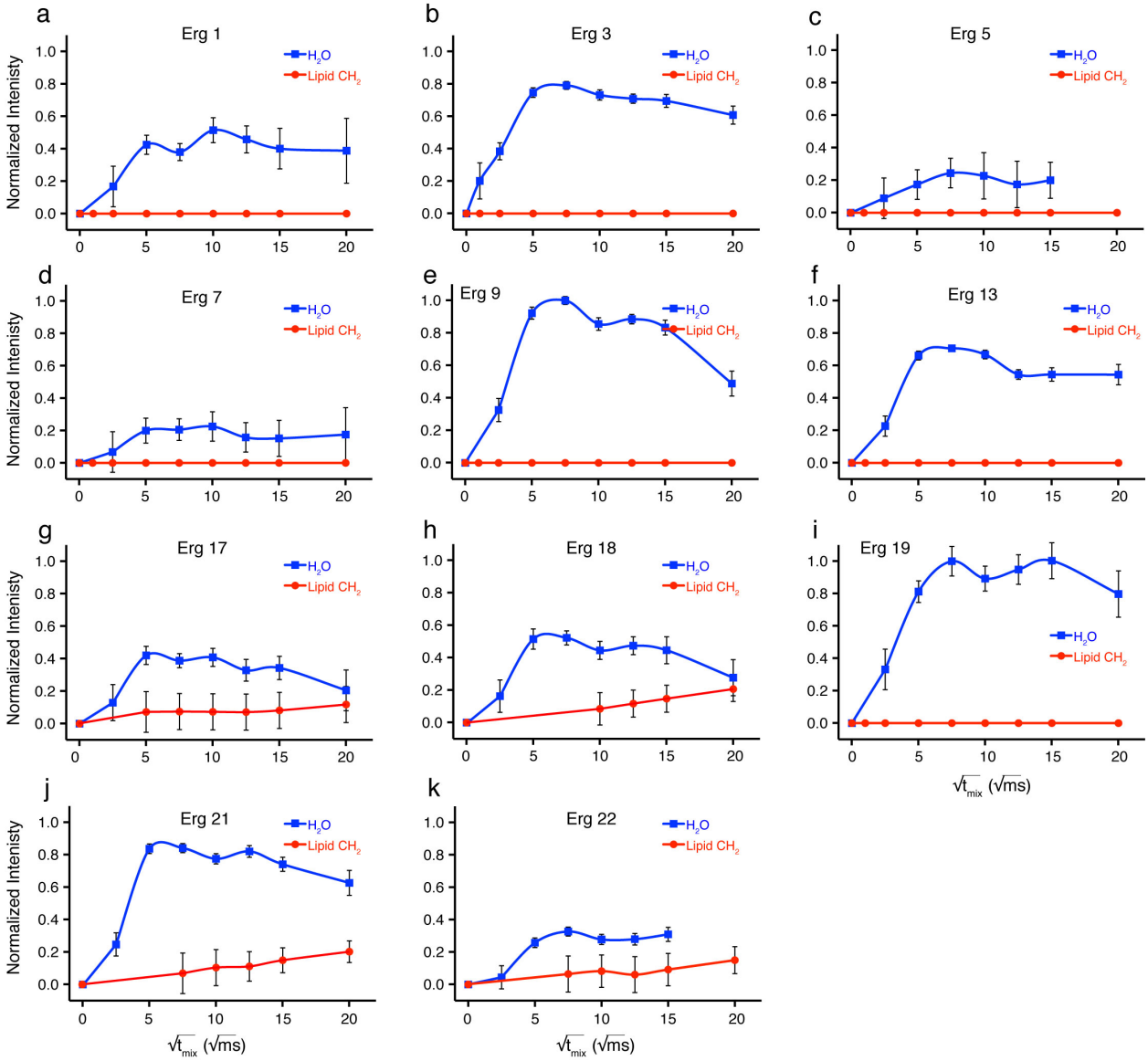

Supplementary Figure 5.11 ^{1}H spin diffusion to Erg in presence of AmB

T_2-filtered (1 ms) spin diffusion studies of 40:4:1 POPC:AmB:^{13}C-Erg MLVs show that in the presence of AmB Erg has been removed from the lipid bilayer, with the majority of Erg located more than 15-20 Å away from the lipid acyl chains. The polarization transfer from water is very similar to that observed for AmB (Supplementary Information Fig. 4, Fig. 2f), supporting the fact that the Erg has been absorbed by the AmB sterol sponge. The selected ^{1}H-^{13}C correlations were collected with 1 ms T_2 filter and ^{1}H-^{1}H spin diffusion times of 1 ms to 625 ms. Cross peaks from the lipid acyl chain CH_2 protons (~1.35 ppm) and water (~4.7 ppm) to all resolved sites of ^{13}C-Erg are shown in red and blue, respectively. The polarization transfer is normalized based on the maximum observed intensity after correction of the ^{1}H T_1 relaxation. Spectra was acquired on a 600 MHz spectrometer, at 20 °C with and MAS rate of 10 kHz, and 75 kHz SPINAL ^{1}H decoupling.[53]

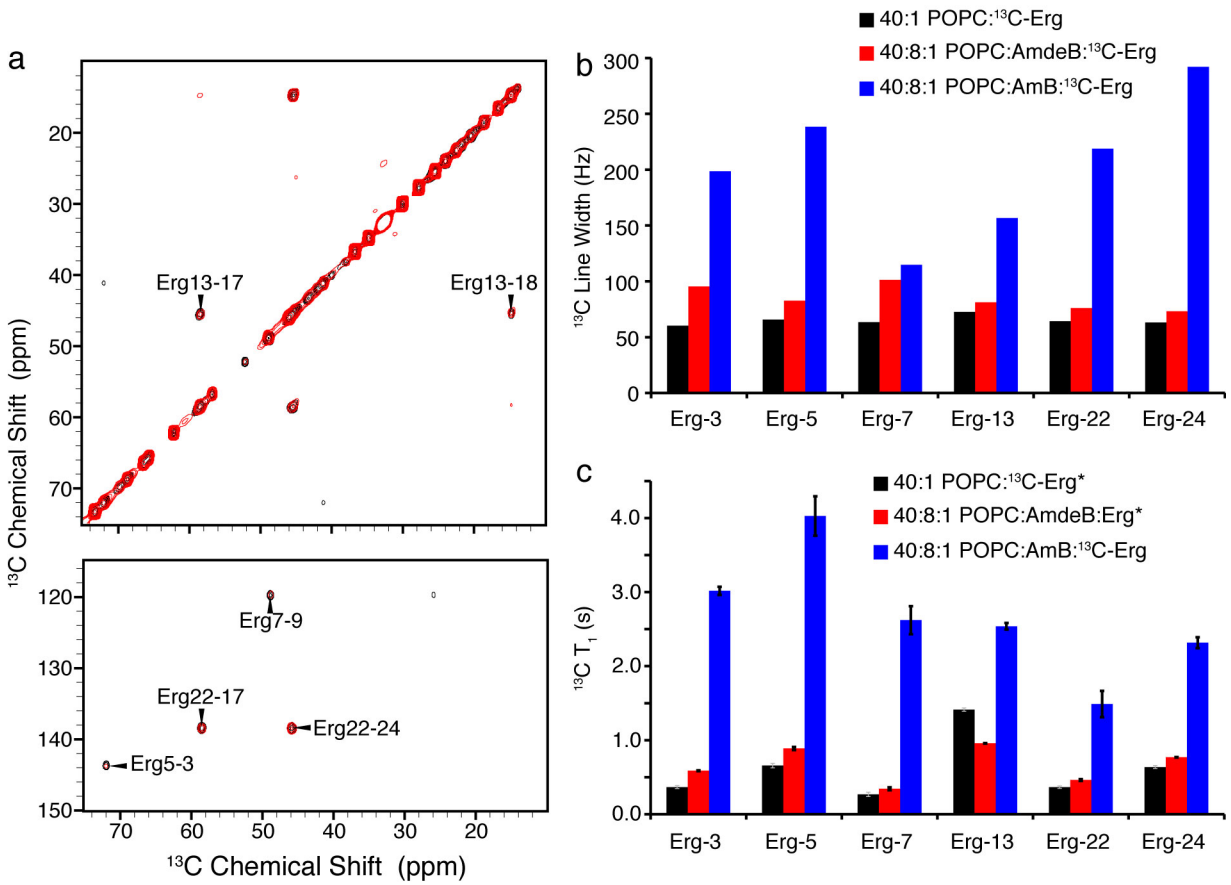

Supplementary Figure 5.12 Effects of AmdeB of Erg linewidth, T_1, and CC2D
As a control experiment we also examined the effect of AmdeB, a derivative of AmB lacking the mycosamine appendage that does not bind Erg.[25,27] There were no chemical shift perturbations observed upon the addition of AmdeB, as shown in (a) the over lay of ^{13}C-^{13}C 2D DARR (500ms mixing) spectra of 40:1 POPC:^{13}C-Erg (black), 40:8:1 POPC:AmdeB:^{13}C-Erg (red). This is in stark contrast to the dramatic changes observed with the addition of AmB to POPC:^{13}C-Erg membranes, as shown in Supplementary Fig. 4a. Furthermore there were only slight perturbations of the (b) ^{13}C linewidth, and (c) ^{13}C longitudinal (T_1) relaxation times in comparison to those changes induced by the addition of an equivalent amount of AmB (40:8:1 POPC:AmB:^{13}C-Erg (blue)). Spectra were acquired on a 14.1 T (600 MHz ^{1}H frequency) spectrometer, at 20 °C with an MAS rate of 10 kHz and 75 kHz ^{1}H decoupling.[53]

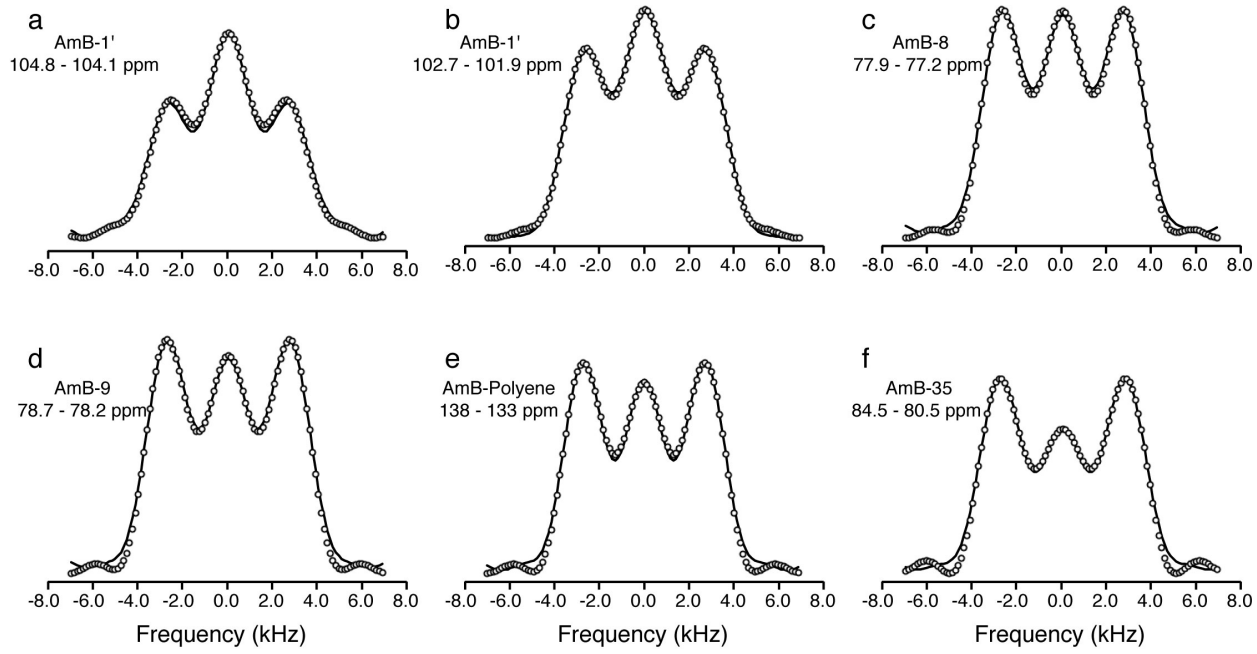

Supplementary Figure 5.13 AmB T-MREV dipolar lines shapes and order parameters
The T-MREV dipolar lines shapes and order parameter measured select AmB resonances in 10:1:1 POPC:U-^{13}C-AmB:Erg MLVs (black, experimental solid line, simulation open circle) confirm that sterol sponge is rigid. Spectra was acquired on a 600 MHz spectrometer, at 20 °C with and MAS rate of 8.333 kHz, and 85 kHz TPPM ^{1}H decoupling[59], using N=4 T-MREV.[44]

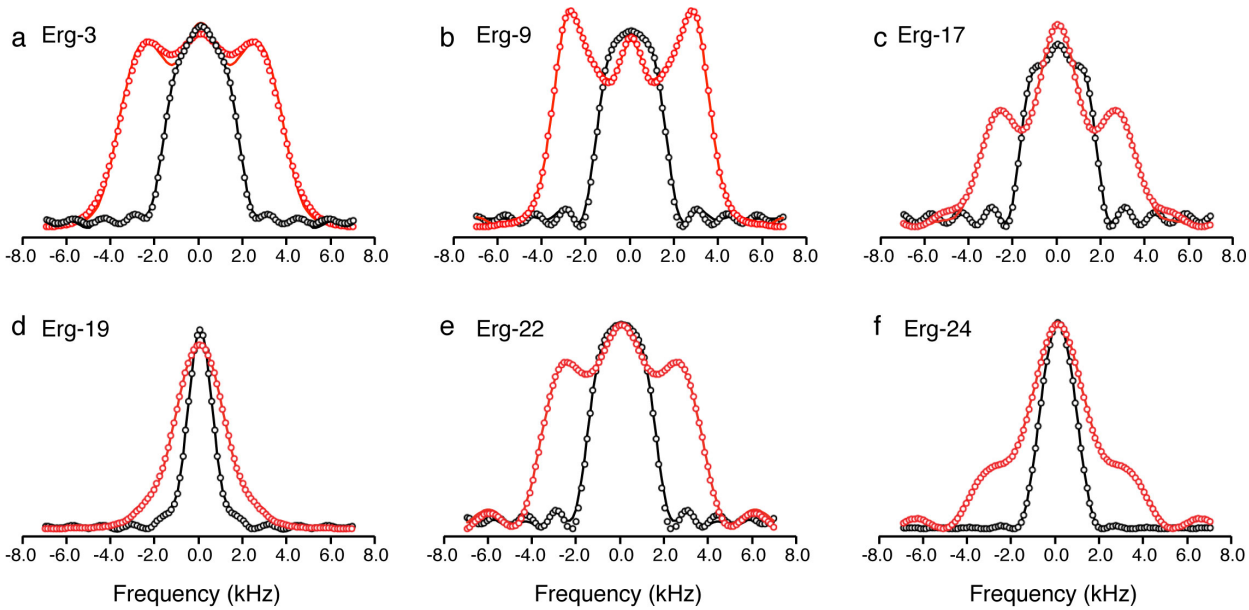

Supplementary Figure 5.14 Erg T-MREV dipolar lines shapes and order parameters
The substantial broadening of the T-MREV dipolar lines shapes and order parameter measured for select Erg resonances in 40:0:1 (black, experimental solid line, simulation open circle) and 40:4:1 POPC:AmB:^{13}C-Erg (red, experimental solid line, simulation open circle) further confirms the absorption

of Erg by the AmB Sterol sponge. Spectra was acquired on a 600 MHz spectrometer, at 20 °C with and MAS rate of 8.333 kHz, and 85 kHz TPPM ^{1}H decoupling,[59] N=4 T-MREV.[44]

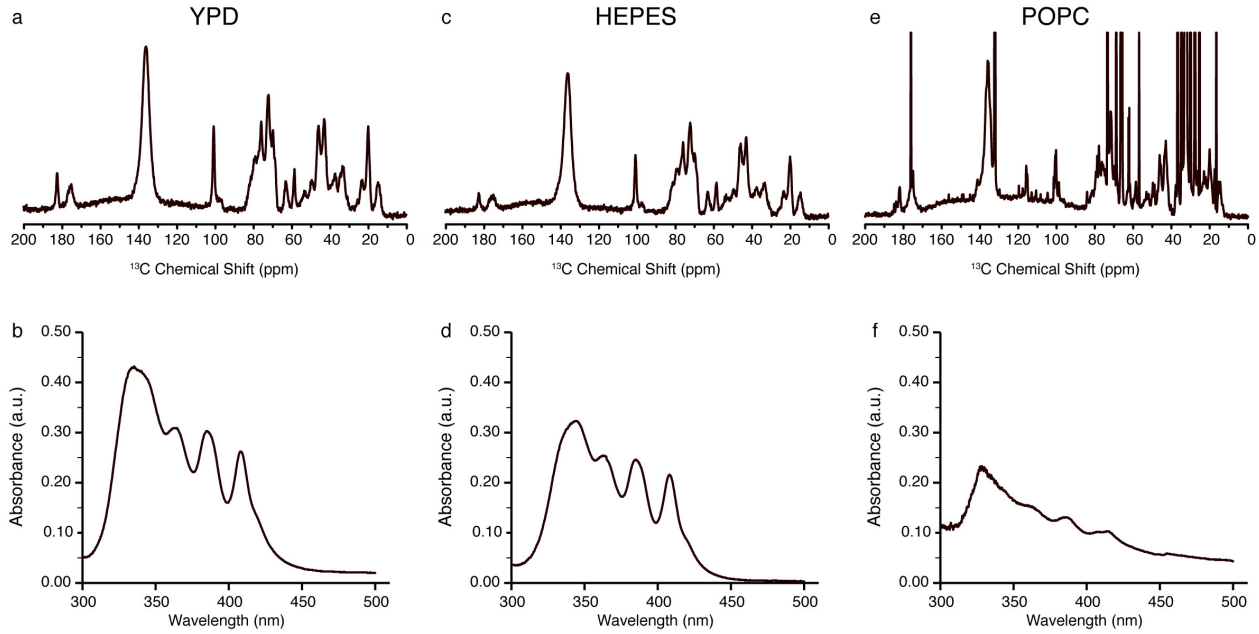

Supplementary Figure 5.15 ^{13}C1D and UV-Vis spectra of AmB preparations

^{13}C NMR and UV-Vis spectra of (a, b) AmB precipitated in YPD buffer used for *in vivo* studies, (c,d) AmB precipitated in HEPES buffer used for TEM studies, and (e, f) 10:1 mole ratio of POPC:AmB MLVs lyophilized and rehydrated for SSNMR studies.

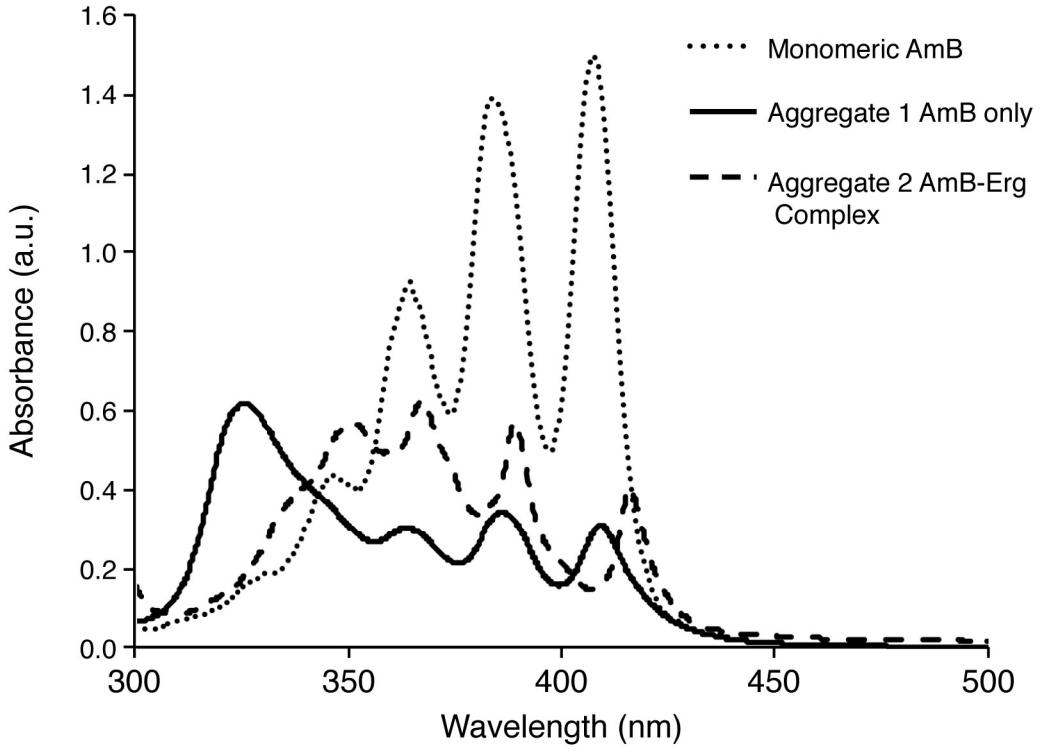

Supplementary Figure 5.16 Monomeric AmB in PBS:methanol and AmB aggregate in PBS buffer demonstrate spectral signatures by UV spectroscopy.[60]

5.8 References

1 Cannon, R. D., Lamping, E., Holmes, A. R., Niimi, K., Tanabe, K., Niimi, M. & Monk, B. C. *Candida albicans* drug resistance - another way to cope with stress. *Microbiology* **153**, 3211-3217 (2007).

2 Mora-Duarte, J., Betts, R., Rotstein, C., Colombo, A. L., Thompson-Moya, L., Smietana, J., Lupinacci, R., Sable, C., Kartsonis, N. & Perfect, J. Comparison of caspofungin and amphotericin B for invasive candidiasis. *New. Engl. J. Med.* **347**, 2020-2029 (2002).

3 Monk, B. C. & Goffeau, A. Outwitting multidrug resistance to antifungals. *Science* **321**, 367-369 (2008).

4 Ermishkin, L. N., Kasumov, K. M. & Potzeluyev, V. M. Single ionic channels induced in lipid bilayers by polyene antibiotics amphotericin-B and nystatine. *Nature* **262**, 698-699 (1976).

5 Andreoli, T. E. & Monahan, M. The interaction of polyene antibiotics with thin lipid membranes. *J. Gen. Physiol.* **52**, 300-325 (1968).

6 Cass, A., Finkelstein, A. & Krespi, V. The ion permeability induced in thin lipid membranes by the polyene antibiotics nystatin and amphotericin B. *J. Gen. Physiol.* **56**, 100-124 (1970).

7 Finkelstein, A. & Holz, R. Aqueous pores created in thin lipid membranes by the polyene antibiotics nystatin and amphotericin B. *Membranes* **2**, 377-408 (1973).

8 Andreoli, T. E. Structure and function of amphotericin B-cholesterol pores in lipid bilayer membranes. *Ann. N.Y. Acad. Sci.* **235**, 448-468 (1974).

9 de Kruijf, B. & Demel, R. A. Polyene antibiotic-sterol interactions in membranes of acholeplasma-laidlawii cells and lecithin liposomes. 3. molecular-structure of polyene sntibiotic-cholesterol complexes. *Biochim. Biophys. Acta* **339**, 57-70 (1974).

10 Bolard, J. How do the polyene macrolide antibiotics affect the cellular membrane-properties. *Biochim. Biophys. Acta* **864**, 257-304 (1986).

11 Volmer, A. A., Szpilman, A. M. & Carreira, E. M. Synthesis and biological evaluation of amphotericin B derivatives. *Nat. Prod. Rep.* **27**, 1329-1349 (2010).

12 Cereghetti, D. M. & Carreira, E. M. Amphotericin B: 50 years of chemistry and biochemistry. *Synthesis-Stuttgart* 914-942 (2006).

13 Cheron, M., Cybulska, B., Mazerski, J., Grzybowska, J., Czerwinski, A. & Borowski, E. Quantitative structure-activity relationships in amphotericin B derivatives. *Biochem. Pharmacol.* **37**, 827-836 (1988).

14 Croatt, M. P. & Carreira, E. M. Probing the role of the mycosamine C2'-OH on the activity of amphotericin B. *Org. Lett.* **13**, 1390-1393 (2011).

15 Baginski, M., Resat, H. & Borowski, E. Comparative molecular dynamics simulations of amphotericin B-cholesterol/ergosterol membrane channels. *Biochim. Biophys. Acta* **1567**, 63-78 (2002).

16 Murata, M., Kasai, Y., Umegawa, Y., Matsushita, N., Tsuchikawa, H., Matsumori, N. & Oishi, T. Ion channel complex of antibiotics as viewed by NMR. *Pure Appl. Chem.* **81**, 1123-1129 (2009).

17 Matsumori, N., Sawada, Y. & Murata, M. Large molecular assembly of amphotericin B formed in ergosterol-containing membrane evidenced by solid-state NMR of intramolecular bridged derivative. *J. Am. Chem. Soc.* **128**, 11977-11984 (2006).

18 Matsuoka, S., Ikeuchi, H., Umegawa, Y., Matsumori, N. & Murata, M. Membrane interaction of amphotericin B as single-length assembly examined by solid state NMR for uniformly ^{13}C-enriched agent. *Bioorg. Med. Chem.* **14**, 6608-6614 (2006).

19 Umegawa, Y., Nakagawa, Y., Tahara, K., Tsuchikawa, H., Matsumori, N., Oishi, T. & Murata, M. Head-to-tail interaction between amphotericin B and ergosterol occurs in hydrated phospholipid membrane. *Biochemistry* **51**, 83-89 (2012).

20 Verkleij, A. J., Dekruijf.B, Gerritse.Wf, Demel, R. A., Vandeene.Ll & Ververga.Ph. Freeze-Etch Electron-Microscopy of erythrocytes, acholeplasma-laidlawii cells and liposomal membranes after action of filipin and amphotericin-B. *Biochim. Biophys. Acta* **291**, 577-581 (1973).

21 Milhaud, J., Ponsinet, V., Takashi, M. & Michels, B. Interactions of the drug amphotericin B with phospholipid membranes containing or not ergosterol: New insight, into them role of ergosterol. *Biocehm. Biophys. Acta-Biomembranes* **1558**, 95-108 (2002).

22 Mouri, R., Konoki, K., Matsumori, N., Oishi, T. & Murata, M. Complex formation of amphotericin B in sterol-containing membranes as evidenced by surface plasmon resonance. *Biochemistry* **47**, 7807-7815 (2008).

23 Katzung, B. G., Masters, S. B. & Trevor, A. J. *Basic and Clinical Pharmacology* 12th edn, (McGraw-Hill Education, Europe, 2012).

24 Fernandez-Lopez, S., Kim, H. S., Choi, E. C., Delgado, M., Granja, J. R., Khasanov, A., Kraehenbuehl, K., Long, G., Weinberger, D. A., Wilcoxen, K. M. & Ghadiri, M. R. Antibacterial agents based on the cyclic D,L-alpha-peptide architecture. *Nature* **412**, 452-455 (2001).

25 Gray, K. C., Palacios, D. S., Dailey, I., Endo, M. M., Uno, B. E., Wilcock, B. C. & Burke, M. D. Amphotericin primarily kills yeast by simply binding ergosterol. *Proc. Natl. Acad. Sci. USA* **109**, 2234-2239 (2012).

26 Palacios, D. S., Anderson, T. M. & Burke, M. D. A post-PKS oxidation of the amphotericin B skeleton predicted to be critical for channel formation is not required for potent antifungal activity. *J. Am. Chem. Soc.* **129**, 13804-13805 (2007).

27 Palacios, D. S., Dailey, I., Siebert, D. M., Wilcock, B. C. & Burke, M. D. Synthesis-enabled functional group deletions reveal key underpinnings of amphotericin B ion channel and antifungal activities. *Proc. Natl. Acad. Sci. USA* **108**, 6733-6738 (2011).

28 Jin, H., McCaffery, J. M. & Grote, E. Ergosterol promotes pheromone signaling and plasma membrane fusion in mating yeast. *J. Cell Biol.* **180**, 813-826 (2008).

29 Kato, M. & Wickner, W. Ergosterol is required for the Sec18/ATP-dependent priming step of homotypic vacuole fusion. *EMBO J.* **20**, 4035-4040 (2001).

30 Heese-Peck, A., Pichler, H., Zanolari, B., Watanabe, R., Daum, G. & Riezman, H. Multiple functions of sterols in yeast endocytosis. *Mol. Biol. Cell* **13**, 2664-2680 (2002).

31 te Welscher, Y. M., van Leeuwen, M. R., de Kruijff, B., Dijksterhuis, J. & Breukink, E. Polyene antibiotic that inhibits membrane transport proteins. *Proc. Natl. Acad. Sci. USA* **109**, 11156-11159 (2012).

32 Solomon, I. Relaxation processes in a system of 2 spins. *Phys. Rev.* **99**, 559-565 (1955).

33 Nadaud, P. S., Helmus, J. J., Hofer, N. & Jaroniec, C. P. Long-range structural restraints in spin-labeled proteins probed by solid-state nuclear magnetic resonance spectroscopy. *J. Am. Chem. Soc.* **129**, 7502-7503 (2007).

34 Sankaram, M. B. & Thompson, T. E. Cholesterol-induced fluid-phase immiscibility in membranes. *Proc. Natl. Acad. Sci. USA* **88**, 8686-8690 (1991).

35 Hsueh, Y. W., Chen, M. T., Patty, P. J., Code, C., Cheng, J., Frisken, B. J., Zuckermann, M. & Thewalt, J. Ergosterol in POPC membranes: Physical properties and comparison with structurally similar sterols. *Biophys. J.* **92**, 1606-1615 (2007).

36 Watson, K., Bertoli, E. & Griffiths, D. E. Phase-transitions in yeast mitochondrial-membranes - effect of temperature on energies of activation of respiratory enzymes of *saccharomyces-cerevisiae*. *Biochem. J.* **146**, 401-407 (1975).

37 Ejsing, C. S., Sampaio, J. L., Surendranath, V., Duchoslav, E., Ekroos, K., Klemm, R. W., Simons, K. & Shevchenko, A. Global analysis of the yeast lipidome by quantitative shotgun mass spectrometry. *Proc. Natl. Acad. Sci. USA* **106**, 2136-2141 (2009).

38 Chen, L. L., Olsen, R. A., Elliott, D. W., Boettcher, J. M., Zhou, D. H. H., Rienstra, C. M. & Mueller, L. J. Constant-time through-bond ^{13}C correlation spectroscopy for assigning protein resonances with solid-state NMR spectroscopy. *J. Am. Chem. Soc.* **128**, 9992-9993 (2006).

39 Takegoshi, K., Nakamura, S. & Terao, T. ^{13}C-^{1}H dipolar-assisted rotational resonance in magic-angle spinning NMR. *Chem. Phys. Lett.* **344**, 631-637 (2001).

40 Hohwy, M., Rienstra, C. M., Jaroniec, C. P. & Griffin, R. G. Fivefold symmetric homonuclear dipolar recoupling in rotating solids: Application to double quantum spectroscopy. *J. Chem. Phys.* **110**, 7983-7992 (1999).

41 Huster, D., Yao, X. L. & Hong, M. Membrane protein topology probed by ^{1}H spin diffusion from lipids using solid-state NMR spectroscopy. *J. Am. Chem. Soc.* **124**, 874-883 (2002).

42 Lange, A., Luca, S. & Baldus, M. Structural constraints from proton-mediated rare-spin correlation spectroscopy in rotating solids. *J. Am. Chem. Soc.* **124**, 9704-9705 (2002).

43 Tang, M., Waring, A. J. & Hong, M. Intermolecular packing and alignment in an ordered beta-hairpin antimicrobial peptide aggregate from 2D solid-state NMR. *J. Am. Chem. Soc.* **127**, 13919-13927 (2005).

44 Hohwy, M., Jaroniec, C. P., Reif, B., Rienstra, C. M. & Griffin, R. G. Local structure and relaxation in solid-state NMR: Accurate measurement of amide N-H bond lengths and H-N-H bond angles. *J. Am. Chem. Soc.* **122**, 3218-3219 (2000).

45 Haas, A. A quantitative assay to measure homotypic vacuole fusion in vitro. *Methods Cell Sci.* **17**, 283-294 (1995).

46 Yancey, P. G., Rodriqueza, W. V., Kilsdonk, E. P. C., Stoudt, G. W., Johnson, W. J., Phillips, M. C. & Rothblat, G. H. Cellular cholesterol effect mediated by cyclodextrins - Demonstration of kinetic pools and mechanism of efflux. *J. Biol. Chem.* **271**, 16026-16034 (1996).

47 Wilcock, B. C., Endo, M. M., Uno, B. E. & Burke, M. D. C2′-OH of amphotericin B plays an important role in binding the primary sterol of human cells but not yeast cells. *J. Am. Chem. Soc.* **135**, 8488-8491 (2013).

48 Kang, C. K., Yamada, K., Usuki, Y., Ogita, A., Fujita, K. & Tanaka, T. Visualization analysis of the vacuole-targeting fungicidal activity of amphotericin B against the parent strain and an ergosterol-less mutant of Saccharomyces cerevisiae. *Microbiology* **159**, 939-947 (2013).

49 Vincent, B. M., Lancaster, A. K., Scherz-Shouval, R., Whitesell, L. & Lindquist, S. Fitness trade-offs restrict the evolution of resistance to amphotericin B. *PLoS Biol.* **11**, e1001692 (2013).

50 Sanglard, D., Ischer, F., Parkinson, T., Falconer, D. & Bille, J. Candida albicans mutations in the ergosterol biosynthetic pathway and resistance to several antifungal agents. *Antimicrob. Agents Chemother.* **47**, 2404-2412 (2003).

51 Seo, S., Uomori, A., Yoshimura, Y., Takeda, K., Seto, H., Ebizuka, Y., Noguchi, H. & Sankawa, U. Biosynthesis of sitosterol, cycloartenol, and 24-methylenecycloartanol in tissue-cultures of higher-plants and of ergosterol in yeast from [1,2-$^{13}C_2$]-Acetate and [2-^{13}C-$^{2}H_3$]-Acetate and [5-^{13}C-$^{2}H_2$] MVA. *J. Chem. Soc., Perkin. Trans. 1* 2407-2414 (1988).

52 Pangborn, A. B., Giardello, M. A., Grubbs, R. H., Rosen, R. K. & Timmers, F. J. Safe and convenient procedure for solvent purification. *Organometallics* **15**, 1518-1520 (1996).

53 Comellas, G., Lopez, J. J., Nieuwkoop, A. J., Lemkau, L. R. & Rienstra, C. M. Straightforward, effective calibration of SPINAL-64 decoupling results in the

enhancement of sensitivity and resolution of biomolecular solid-state NMR. *J. Magn. Reson.* **209**, 131-135 (2011).

54 Morcombe, C. R. & Zilm, K. W. Chemical shift referencing in MAS solid state NMR. *J. Magn. Reson.* **162**, 479-486 (2003).

55 Rienstra, C. M., Hohwy, M., Mueller, L. J., Jaroniec, C. P., Reif, B. & Griffin, R. G. Determination of multiple torsion-angle constraints in U-^{13}C,^{15}N-labeled peptides: 3D ^{1}H-^{15}N-^{13}C-^{1}H dipolar chemical shift NMR spectroscopy in rotating solids. *J. Am. Chem. Soc.* **124**, 11908-11922 (2002).

56 Ohi, M., Li, Y., Cheng, Y. & Walz, T. Negative staining and image classification - powerful tools in modern electron microscopy. *Biol. Proced. Online* **6**, 23-34 (2004).

57 Winkler, J. K., Rennick, K. A., Eller, F. J. & Vaughn, S. F. Phytosterol and tocopherol components in extracts of corn distiller's dried grain. *J. Agric. Food. Chem.* **55**, 6482-6486 (2007).

58 Shervani, Z., Etori, H., Taga, K., Yoshida, T. & Okabayashi, H. Aggregation of polyene antibiotics as studied by electronic absorption and circular dichroism spectroscopies. *Colloid. Surface. B* **7**, 31-38 (1996).

59 Fung, B. M., Khitrin, A. K. & Ermolaev, K. An improved broadband decoupling sequence for liquid crystals and solids. *J. Magn. Reson.* **142**, 97-101 (2000).

60 Shervani, Z., Etori, H., Taga, K., Yoshida, T. & Okabayashi, H. Aggregation of polyene antibiotics as studied by electronic absorption and circular dichroism spectroscopies. *Colloid. Surface. B* **7**, 31-38 (1996).

61 McNamara, C. M., Box, S., Crawforth, J. M., Hickman, B. S., Norwood, T. J., & Rawlings, B. J. Biosynthesis of amphotericin B. *J. Chem. Soc. Perk. T.* **1**, 83-87, (1998).